

https://dspace.org/

Fabrication of porous structures using cold gas dynamic spray technology

Hamweendo, Agripa

2017

https://hdl.handle.net/10539/24014

Hamweendo, Agripa (2017) Fabrication of porous structures using cold gas dynamic spray technology, University of the Witwatersrand, Johannesburg, <http://hdl.handle.net/10539/24014>

Downloaded from a DSpace repository. https://dspace.org/

FABRICATION OF POROUS STRUCTURES USING COLD GAS DYNAMIC SPRAY TECHNOLOGY

Agripa Hamweendo

A thesis submitted to the Faculty of Engineering and the Built Environment, University of the Witwatersrand, Johannesburg, in fulfilment of the requirements for the degree of Doctor of Philosophy.

Johannesburg, August 2017

Declaration

I declare that this thesis is my own, unaided work, except where otherwise acknowledged. It is being submitted for the degree of Doctor of Philosophy at the University of the Witwatersrand, Johannesburg. It has not been submitted before for any degree or examination at any other University.

Signed this __ day of _____ 20__

_____

Agripa Hamweendo.

Acknowledgements

I sincerely acknowledge Professor Ionel Botef for his support, inspiration and guidance through out the work of my thesis.

I also appreciate the support of the academic, administrative and technical staff of the school of Mechanical, Industrial and Aeronautical Engineering at the University of the Witwatersrand, Johannesburg.

The support of the DST-NRF Centre of Excellence in Strong Materials (CoE-SM) towards this research is hereby acknowledged. Opinions expressed and conclusions arrived at in this thesis, are those of the author and are not necessarily to be attributed to the CoE-SM.

I wish to thank my wife Mutinta and my children: Claire, Carter, Caster, Castra, Clara and Carister for their patient, encouragement, and understanding during this study.

Abstract

Porous structures are increasingly becoming important engineering materials in aerospace, health, cooling of electronics, and several other areas. However, the supply of porous structures in these areas is still not being met because the conventional methods of manufacturing porous structures lack the modern requirements of competitiveness, quality, and flexibility. Therefore, new methods are required. One of these methods is the cold spray technology. However, studies do not give clear indications on how the cold spray technology could be used to fabricate porous structures. Consequently, this thesis uses various methods such as the control of cold spray parameters, powder mixtures, and the integration of the cold spray with alloy-de-alloy process to investigate the capability of cold spray technology to manufacture porous structures. The results of this investigation proved that the cold spray technology can be used to fabricate porous structures with varied amount of porosity for a number of applications.

Published Work

Aspects of this thesis have been published in the following references:

- A. Hamweendo, and I. Botef , Method for Manufacturing an Object with Microchannels - Patent Application Number PCT IB2015 057821, World Intellectual Property Organization WIPO, April **2016**.
- A. Hamweendo, T. Malama, and I. Botef, Titanium-Nickel Alloys for Bone Tissue Engineering Application via Cold Spray, International Conference on Competitive Manufacturing COMA16, **Vol. 2016**, Stellenbosch, South Africa, pp. 273279, January **2016**.
- A. Hamweendo, L. Moloisane, and I. Botef, Bio-Mechanical Compatibility Assessment of Titanium-Nickel Alloy Fabricated Using Cold Spray Process, Materials Science Forum, **Vol. 828-829**, South Africa, pp. 351 356, November **2015**.
- A. Hamweendo, and I. Botef, A novel Process for Fabricating Alu- minium Alloy Porous Structure for Possible Application in Antimicrobial Filtration, Materials Science Forum, **Vol. 828-829**, South Africa, pp. 359-365, November **2015**.
- A. Hamweendo , P. A. I. Popoola , and I. Botef, Computational Modelling and Simulation Analysis of Trapezoidal Channeled Micro Heat Sinks Fabricated using Cold Spray Process, Mathematical Methods in Science and Engineering, MMCTSC, Athens, Greece, pp. 186190, November **2014**.
- A. Hamweendo , P. A. I. Popoola , and I. Botef, Mathematical Model for Predicting Process Parameters in Cold Spray of Porous Ti Coatings, Mathematical Methods in Science and Engineering, MMCTSC, Athens, Greece, pp. 225229, November **2014**.

Contents

Declaration i

Acknowledgements ii

Abstract iii

Published Work iv

Contents v

List of Figures xi

List of Tables xvii

List of Acronyms xxvii

1 INTRODUCTION 1

1.1 Background of the Research 1

1.2 Justification of the Research 3

1.3 Research Question 3

1.4 Delimitation of Scope 4

1.5 Research Hypotheses 5

1.6 Source of Data and Methodologies 5

1.7 Contributions of the Research 5

1.8 Definitions 6

1.9 Outline of the Thesis 7

1.10 Conclusion 8

2 REVIEW OF LITERATURE 9

2.1 Porous Structures 9

2.2 Application of Porous Structures 12

2.3 Limitations of Fabrication Methods 14

2.4 Cold Spray Process 16

2.5 Conclusions 18

3 RESEARCH METHODOLOGY 19

3.1 Definitions 19

3.2 Research Question and Hypotheses 20

3.3 Experimental Procedures 20

3.3.1 Strategy 1: Control of Spray Parameters 21

3.3.2 Strategy 2: Coatings from Powder Mixtures 25

3.3.3 Strategy 3: CS Process and Alloy-De-Alloy 27

3.4 Conclusions 31

4 RESULTS, ANALYSIS AND DISCUSSION **32**

4.1 Porous Structures through Control of Spray Parameters 33

4.1.1 Feedstock Powders 33

4.1.2 The Coatings 35

4.1.3 Analysis and Discussion 37

4.1.4 Applications 40

4.2 Porous Structures through Powder Mixtures 41

4.2.1 Feedstock Powder Mixtures 41

4.2.2 The Coatings 43

4.2.3 Analysis and Discussion 47

4.2.4 Applications 50

4.3 Porous Structures through CS and Alloy-De-Alloy 52

4.3.1 Feedstock Powders 52

4.3.2 Coatings from CS and Alloy-De-Alloy 52

4.3.3 Analysis and Discussion 53

4.3.4 Applications of the Coatings 58

4.4 Conclusions 58

5 CONCLUSION **60**

5.1 Introduction 60

5.2 A Brief Overview of Previous Chapters 60

5.3 Conclusions About the Research Question 63

5.4 Contributions of the Research 64

5.5 Research Limitations 65

5.6 Further Recommendations and Suggestions 66

REFERENCES **67**

I APPENDICES **95**

A Glossary **96**

B : Classification Criteria for Porous Structures **102**

C : Porous Structures for Cooling of Electronics **104**

D : Porous Structures for Medical Implants **109**

E : Porous Structures for Medical Filters **112**

F : Porous Structures for Gas Sensors **115**

G : Additional Advantages of Porous Structures **118**

H : Fabrication of Porous Structures **120**

H.1 Porous Structures Fabrication Principles 120

H.2 Porous Structures Fabrication Methods 123

I : Introduction to Cold Spray Process **131**

I.1 Evolution of CS (CS) process 132

I.2 CS Systems 133

I.3 Deposition by CS Process 135

I.4 Bonding Mechanisms in CS Process 135

I.5 Research Works on CS Process 137

J : Methodological Processes **140**

J.1 Selection of Powders and Equipment 140

J.2 Mixing of Powders 142

J.3 Calculation of Spray Parameters 143

J.4 Optimisation of Spray Parameters 146

J.5 Fabrication of Microchannels 147

J.6 Fabrication of Antimicrobial Filters 150

K : Isentropic Gas Models **152**

L : Cold Spray Parameters **156**

L.1 Analysis of Spray Parameters 156

L.2 Description of Spray Parameters 158

M : Parameters Selection Tools **171**

N : Tables of Parameters **174**

O : Analysis and Validation of Data **177**

O.1 Calculation of Tensile Strength and Young's Modulus 177

O.2 Evaluation of Micro Heat Sink 178

O.3 Modelling of CS Parameters 188

P : Graphs and Pictures **191**

P.1 Powder Size Distributions 191

P.2 EDX Spectra for Powders 194

P.3 Coatings 195

P.4 EDX Spectra for Coatings 195

List of Figures

1.1 Organization of thesis' chapters 7

2.1 Application Vs. pore architecture. 10

2.2 Nature of porous structures 11

2.3 Pore structures 11

2.4 Powder metallurgy process. 14

2.5 Alloy-de-alloy process. 16

2.6 Self propagating synthesis process. 17

2.7 Downstream injection CS process. 17

3.1 Experimental methodology flow chart. 21

3.2 Tensile test substrate. 22

3.3 Gas sensing layer 26

3.4 Pyramidal fins fabrication. 26

3.5 Fabrication of microchannels. 29

3.6 Process for antimicrobial filters. 30

3.7 Simulation models. 30

4.1 Chapter 4's map. 32

4.2 Morphology of aluminium and copper powders. 33

4.3 Morphology of titanium and zinc powders. 33

4.4 Size distributions of powders for strategy 1. 34

4.5 EDX spectrum for titanium. 35

4.6 Coatings under sub-optimised conditions. 35

4.7 Surface porosity for copper and zinc coating. 36

4.8 Titanium coating under optimised conditions. 36

4.9 Measured Vs. predicted porosity for titanium. 39

4.10 Morphology of powder mixtures. 42

4.11 Tin-oxide-copper agglomerates. 43

4.12 Titanium-nickel coatings 43

4.13 Microhardness graphs for coatings. 45

4.14 Tin-oxide-copper coating. 45

4.15 Surface porosity of gas sensing layer. 46

4.16 EDX spectra for gas sensing layer. 46

4.17 EDX spectra for gas sensing layer. 46

4.18 Gas sensors. 47

4.19 Graph for gas sensor sample 1. 49

4.20 Graph for gas sensor sample 2. 49

4.21 Sensitivity variation with gas concentration. 50

4.22 Antimicrobial filters. 52

4.23 Microchannels. 53

4.24 Microchannels dimension and model. 54

4.25 Graph of temperature Vs. heat flux. 54

4.26 Simulated temperature profile for micro heat sink. 55

4.27 Simulated stress profile for micro heat sink. 56

4.28 Thermal resistance graphs. 57

4.29 Proofs for hypotheses. 59

5.1 Chapter 5's map. 61

5.2 Hypotheses loop. 62

5.3 Research contributions. 65

B.1 Classification of porous structures. 103

C.1 Thermal solutions hierarchy. 105

C.2 Microfluidic cooling architecture. 105

C.3 Heat transfer coefficients. 106

C.4 Non-circular shapes for microchannels. 107

C.5 Heat exchange rate Vs. Re for water cooling. 107

C.6 Heat exchange rate Vs. Re for nanofluid cooling. 108

D.1 Demand for bone implants. 110

D.2 Porous coated bone implants. 110

E.1 Antimicrobial capability of metals. 113

E.2 Antimicrobial capability of CS coatings. 114

F.1 Gas sensor configuration. 115

F.2 Gas sensing mechanism. 116

F.3 Effects of electrodes position. 117

H.1 Loosely packing of aggregates 121

H.2 Subtraction of aggregates. 121

H.3 Selected pore structures 122

H.4 Sol-gel method. 123

H.5 Powder metallurgy process. 124

H.6 Thermal spray process. 124

H.7 Plasma spray process. 125

H.8 Plasma spray coating 126

H.9 HVOF process 126

H.10 Chemical etching method. 127

H.11 Micro-mechanical and laser cutting. 128

H.12 3D-printing process. 129

H.13 Electron beam and selective laser melting. 129

I.1 Comparison between CS and thermal spray processes. 131

I.2 Wind tunnel test 132

I.3 CS process configuration. 134

I.4 Particle evolution during bonding 136

I.5 Porosity minimisation in CS coatings. 139

J.1 Enlarged particles. 143

J.2 Response surface 146

J.3 Cold spray through mask 148

J.4 Fabrication process for microchannels. 149

K.1 Converging-diverging supersonic nozzle 153

L.1 Effect of stagnation gas temperature. 158

L.2 Optimal CS conditions. 159

L.3 Critical velocity Vs. process gas temperature. 160

L.4 Effect of gas pressure. 161

L.5 Effect of standoff distance on deposition. 161

L.6 Comparison of particle velocities. 163

L.7 Critical velocity Vs. deposition efficiency. 163

L.8 Calculated and experimental critical velocities 165

L.9 Variation of particle temperature. 166

L.10 Particle velocity Vs. nozzle diameter. 167

L.11 Variation of Mach with nozzle expansion. 168

L.12 Particle velocity Vs. particle diameter. 168

L.13 Particle morphology. 169

L.14 Deposition efficiency Vs. melting temperature. 170

O.1 Thermal physical data schedules. 181

O.2 Thermal physical data for water-alumina nanofluids. 184

O.3 Thermal physical data for water-copper nanofluids. 185

O.4 Variation of thermal resistance for alumina nanofluids. 186

O.5 Variation of thermal resistance for copper nanofluids. 187

P.1 Particle size distributions for aluminum-alumina 191

P.2 Particle size distributions for chromium powder 192

P.3 Particle size distribution for zinc powder 192

P.4 Particle size distribution for magnesium Powder 193

P.5 Particle size distribution for nickel powder. 193

P.6 EDX spectrum for copper powder. 194

P.7 EDX spectra for magnesium powder. 194

P.8 EDX spectra for nickel powders. 195

P.9 Mixed powder coatings. 196

P.10 Coatings for individual powders. 197

P.11 EDX Spectrum for titanium-nickel coatings. 198

List of Tables

3.1 Powder mixtures. 25

4.1 Tensile behaviour of cold sprayed coatings. 40

4.2 Sensor response for sample 1. 47

4.3 Sensor response for sample 2. 47

4.4 Geometric dimensions for microchannels. 53

4.5 Simulation temperature distribution for micro heat sink. 54

I.1 Operation parameters for CS systems 134

J.1 Selected powders. 141

J.2 Selected equipment and software. 141

J.3 Powder mixtures. 142

J.4 Steps in fabrication of microchannels. 149

J.5 Optimised CS parameters for antimicrobial filters. 151

J.6 Steps in fabrication of antimicrobial filters. 151

L.1 Analysis of CS process parameters. 157

N.1 Spray parameters for aluminum-alumina. 174

N.2 Spray parameters for copper. 175

N.3 Spray parameters for titanium. 175

N.4 Spray parameters for zinc. 175

N.5 Optimised spray parameters for powder mixtures. 176

N.6 Optimised spray parameters for microchannels. 176

N.7 Optimised spray parameters for antimicrobial filters. 176

O.1 Porosity and microhardness values for coatings. 190

O.2 Standard deviation for microhardness. 190

List of Symbols

A nozzle cross-sectional area (m^2)

A_e nozzle exit cross-sectional area (m^2)

$A*$ nozzle throat cross-sectional area (m^2)

C specific heat (J/kgMol)

c_p particle heat capacity (J/kg)

C_p gas heat capacity at constant pressure (J/kg K)

C_v gas heat capacity at constant volume (J/kg K)

c_g gas heat capacity (J/kg)

C_{npf} specific heat capacity of nanofluid

C_{pbf} specific heat capacity of base fluid

C_{pnp} specific heat capacity of nanoparticle

d diameter (m)

d_h hydraulic diameter (m)

d_e nozzle exit diameter (m)

d_f equivalent diameter of fluid molecule (m)

d_p diameter of the particle (μm)

$fr1$ fraction distribution for powder number 1

$fr2$ fraction distribution for powder number 2

h convective heat transfer coefficient

k thermal conductivity (W/mK)

k_b Boltzmann constant

k_{eff} effective thermal conductivity (W/mK)

k_f thermal conductivity of the base fluid (W/mK)

k_{hs} thermal conductivity of heat sink (W/mK)

k_p thermal conductivity of nanoparticle (W/mK)

l_0 original length (m)

m mass (kg)

M local Mach number

M_w molecular weight (Kg/Mol)

M_e nozzle exit Mach number (K)

m_p average powder particle mass (kg)

Nu Nusselt number

N Avogadro number

P perimeter (m)

P pressure (Pa)

P_{ang} powder angularity

P_e nozzle exit pressure (Pa)

P_g gas pressure (Pa)

P_o stagnation gas pressure (Pa)

P_s downstream shock pressure (Pa)

P^* nozzle throat gas pressure (Pa)

P_r Prandtl number

R specific gas constant (J/kmol K)

R_a resistance of the layer in air (Ω)

R_g resistance of the layer in gas (Ω)

$R_{capa.}$ capacitive thermal resistance (K/W)

$R_{const.}$ constrictive thermal resistance

$R_{cond.}$ conductive thermal resistance (K/W)

$R_{conv.}$ convective thermal resistance (K/W)

Re' Reynolds number for nanoparticles

R_e gas-particle Reynolds number

R_{th} total thermal resistance (K/W)

Se sensitivity of the sensing layer

S standoff distance (mm)

SOD_{GM} standoff distance between gun and mask (mm)

SOD_{MS} standoff distance between mask substrate (mm)

SOD_{GS} standoff distance between gun and substrate (mm)

t time (s)

T temperature (K)

T_e nozzle exit temperature (K)

T_{fr} freezing point of the base liquid (K)

T_g gas temperature (K)

T_i particle impact temperature (K)

T_m melting temperature (K)

T_o stagnation gas temperature (K)

T_p particle temperature (K)

T_R ambient temperature (K)

T_{sub} temperature of substrate

T^* nozzle throat gas temperature (K) (K)

v velocity (m/s)

v_{crit} critical impact velocity (m/s)

$v_{crit.1}$ critical velocity for constituent powder number 1

$v_{crit.2}$ critical velocity for constituent powder number 2

v_{critm} mean critical velocity for the powder mixture

v_g gas velocity (m/s)

v_e nozzle exit gas velocity (m/s)

v_{impact} particle impact velocity (m/s)

v_p particle velocity (m/s)

V_p total volume of the pores in the structure (m^3)

v_s speed of sound in materials (m/s)

V_s total volume of the structure (m^3)

$v*$ nozzle throat gas velocity (m/s)

w width of the micro heat sink (m)

w_c width of microchannel (m)

w_w width of the wall for microchannel (m)

x axial position measured from the nozzle throat(m)

X process parameter

X_i coded level for process parameter

X_{max} maximum value of process parameter

X_{min} minimum value of process parameters

Y Young's Modulus (Gpa)

Greek Symbols

ρ density (kg/m^3)

ρ_o stagnation gas density (kg/m^3)

ρ_g gas density (kg/m^3)

ρ_p particle density (kg/m^3)

$\rho*$ nozzle throat gas density (kg/m^3)

ρ_e nozzle exit gas density (kg/m^3)

ρ_m theoretical density of the material

ρ_s bulk density (kg/m^3)

ρ_{bf} density of the base fluid

ρ_{nf} density of the nanofluid

ρ_{np} density of nanoparticles

φ volume fraction of nanoparticles in base fluid is

Δl elastic extension

ϵ strain

μ viscosity (Pas)

μ_f dynamic viscosity of base fluid

μ_{eff} effective dynamic viscosity of the nanofluid

γ ratio of gas specific heats C_p/C_v

σ tensile strength of material (MN/m^2)

σ_p tensile strength at porosity p (MN/m^2)

σ_0 tensile strength of dense material (MN/m^2)

Subscripts

bf base fluid

const constrictive

cond conductive

conv convective

capa capacitive

crit critical

e nozzle exit conditions

eff effective

fr freezing

g gas

GM gun to mask

GS gun to substrate

hs heat sink

i impact

m melting

max maximum

min minimum

MS mask to substrate

np nanoparticle

o stagnation conditions

p particle conditions

s post shock conditions

th thermal

v volume

Superscripts

* nozzle throat conditions

List of Acronyms

Al Aluminium

AMF Antimicrobial filtration

BI Bone implants

CAD Computer aided design

CCDOE Central composite design of experiment

CD Convergent divergent

CGDS Cold gas dynamic spray

CS Cold spraying

Cr Chromium

Cu Copper

DE Deposition efficiency

DNA Deoxyribonucleic acid

DSM Design structures matrix

EBM Electron beam melting

EC Electronic cooling

EDX Energy dispersive x-ray spectroscope

FESEM Field emission scanning electron microscope

HVOF High velocity oxy-fuel

HP-CS High pressure cold spray

LP-CS Low pressure cold spray

LPA Loosely packing of aggregates

MEMS Micro-electromechanical systems

MFCS Microfluidic cooling systems

MHS Micro heat sink

Mg Magnesium

Ni Nickel

PBR Powder to ball mass ratio

PM Powder metallurgy

PS Plasma spray

PSD Particle size distribution

SOD_{GM} Standoff distance between the spray gun and mask

SOD_{GS} Standoff distance between the spray gun and substrate

SOD_{MS} Standoff distance between the mask and substrate

SLM Selective laser melting

SST Supersonic spray technology

Ti Titanium

TOADE Taguch orthogonal array design of experiments

TS Thermal spray

ULSIC Ultra-large-scale-integrated-circuit

Zn Zinc

1 INTRODUCTION

This chapter lays the foundation for this thesis. It introduces the background, problem, and hypotheses of the research. It then outlines the methodologies used to answer the hypotheses, which are briefly described and justified. The definitions, and contributions of the research are also highlighted. And, finally, the outline of the thesis is presented.

1.1 Background of the Research

Porous structures are increasingly being applied in aerospace, health, energy generation, noise filtration, and cooling of electronic components (Ryan et al., 2006; Carey and Inderwildi, 2009; Arenas and Crocker, 2010; Liang and Weimer, 2015). The increased demand for porous structures in these applications is as a result of their favourable properties that include large surface area to volume ratios and lightweight, to name a few (Levy et al., 1996; Luyten et al., 2010; Lu and Zhao, 2011).

However, the existing methods for fabrication of porous structures are still challenging and not cost effective, and so new methods are required (Prakash and Kumar, 2014; Zhou et al., 2014). For example, the conventional powder metallurgy process used to fabricate porous metals led to products with deteriorated properties, and the pore size, pore shape, pore volume fraction, and pore distribution were difficult to control (Krishna et al., 2008).

Similarly, the most recent methods of manufacturing such as $3D$-printing, chemical etching, laser and micro-mechanical machining have limitations such as low productivity, longer processing time, inflexibility, inaccuracy, and high

costs. As such, it has been difficult to use these methods to fabricate porous products that could be applied in micro heat exchangers, cooling of electronic components, and other areas (Prakash and Kumar, 2014; OConnor et al., 2014; Zhou et al., 2014). Other methods such as plasma arc, electron beam, and laser beam welding are still unsuitable for production of porous structures due to creation of small heat-affected zones that result in unsatisfactory physical properties such as cracks, residual stresses, brittleness, intermetallic compounds, arising from differences in fusion points and thermal expansion coefficients of the materials (Maev and Leshchynsky, 2008; Peerawatt et al., 2011; Sidambe, 2014).

Likewise, the possibility of using thermal spray processes to fabricate porous structures was hampered by large quantity of heat applied to the feedstock powders that melted the particles, and splashed across the surface of the substrate resulted in contraction of the splats, and creation of stresses and flaws within the coatings. In addition, this large quantity of heat led to defects such as oxidization, decomposition, loss of constituents, and other defects with detrimental effects to the microstructure of the coatings (Hanson and Settles, 2003; Papyrin, 2006; Cadney et al., 2008; Peerawatt et al., 2011; Hardwicke and Lau, 2013).

Consequently, the Cold Gas Dynamic Spray (CGDS) technology, or simply Cold Spray (CS) as it shall be called from here onwards, was believed to be an alternative method for fabrication of porous structures that could offer solutions to some of the limitations for the methods presented above (Zahiri, Antonio and M.Jahedi, 2008; Julio, 2014; Adebiyi et al., 2016). However, the survey of literature indicated that the studies on the CS process focused on elimination of porosity in the structures (Zahiri et al., 2006; Zahiri, Antonio and M.Jahedi, 2008; Koivuluoto et al., 2012). As such, there is limited information about the capability of the CS process to fabricate porous structures. For example, it is not well established if the CS process can fabricate porous coatings by either control of spray parameters, use of mixed feedstock powders or both of these (Zahiri, Antonio and M.Jahedi, 2008; Lioma et al., 2015). In addition, the prospects of using the CS process together with new methods such as alloy-de-alloy to fabricate porous structures need to be investigated (Papyrin, 2006; Sova et al., 2013; Jo et al., 2014).

1.2 Justification of the Research

There are several important theoretical and practical grounds for pursuing research on porous structures. For instance, literature survey has shown that porous structures are used in many areas of science and engineering as stated earlier (Lu and Zhao, 2011; Li et al., 2015). Therefore, the research on porous structures could increase the knowledge about their properties, methods of manufacturing, and new areas of application (Klemperer and Maharaj, 2009; Singh et al., 2009; Vasquez et al., 2009). In addition, the actual methods used to manufacture porous structures no longer meet the modern requirements, and so, new, efficient, and cost effective methods are necessary (OConnor et al., 2014; Zhou et al., 2014; Prakash and Kumar, 2014). Consequently, this research is justified to investigate how suitable the CS process is for fabrication of porous structures using the following three strategies:

- control of the CS process parameters in order to create structures with different percentages of porosity,
- use a variety of mixtures of feedstock powders so as to create heterogeneous structures with enhanced porosity, and,
- develop new ways of using CS process in conjunction with other methods such as alloy-de-alloy.

Based on this justification, the following research question was developed.

1.3 Research Question

The research question addressed in this thesis is:

Could the CS technology be practically and efficiently used in the fabrication of porous materials?

Based on this research, essentially it is argued that CS can be used to achieve porous structures in an efficient way, but could also be used to manufacture uni-directional pores such as microchannels for various high-tech applications.

1.4 Delimitation of Scope

This thesis aims to:

- develop a CS process for the fabrication of structures with different percentages of porosity,
- validate the developed CS process on a number of selected porous products such as the micro heat sinks, and
- based on the CS experiments, correlated with various application requirements, evaluate the performance of fabricated porous products.

However, this thesis has specific limitations as follows:

- the pressure of the CS equipment was limited to between 5.5 bar and 17.2 bar due to the available spray equipment,
- the gas temperature was limited to between 20 °C and 550 °C due to the same reason given above,
- only selected feedstock powders such as aluminium, alumina, copper, chromium, magnesium, nickel, titanium, zinc, and mixtures of these were used to fabricate porous structures,
- the selected and evaluated performance criteria included the porosity, tensile strength, microhardness, and where necessary, the thermal performance.
- the bonding tests between the cold sprayed coatings and the substrates, in accordance to standard ASTM C633, will not be carried out because the majority of the applications such as sensors and micro heat sinks developed in this thesis do not need this test.
- the computational methods were used to test the heat transfer capability of specimens with large pores such as microchannels (see O)will be used only for micro heat sink development.

1.5 Research Hypotheses

To find answers to the research question stated above, a number of hypotheses were formulated in order to gather the data and so, satisfactorily solve the research problem. Some of these hypotheses, discussed more in depth in Chapter 3 and answered in Chapter 4 are as follows:

Hypothesis 1: CS process could be used to fabricate porous structures through controlling the spray parameters.

Hypothesis 2: CS process could fabricate porous structures when feedstock powders of different mixtures are used.

Hypothesis 3: CS process could fabricate porous structures with controlled porosity using new methods such as alloying followed by de-alloying.

1.6 Source of Data and Methodologies

The source of data used in this thesis is mainly based on the research literature published by reputable international journals and relevant books.

Furthermore, the chosen methodologies, described and justified in far more detail in Chapter 3, could be classified into three categories, namely:

1. methodologies used to identify research issues,
2. methodologies used to support various decisions, and
3. methodologies used for assessing the results.

1.7 Contributions of the Research

The fact that new, efficient, and cost effective methods for manufacturing porous structures are needed necessitated this study to establish the suitability

of CS process for this purpose. On this basis, this thesis makes the following contributions to knowledge:

- a unitary general approach of making porous structures using CS process,
- a patented method, based on CS process, for fabrication of microchannels with trapezoidal shape necessary in the micro heat sink for cooling of electronic components,
- new method for agglomeration of metal-oxide nanoparticles to make them suitable for CS process,
- a new method for adaptation of the planetary ball mill, type Retsch PM400 MA, into a powder mixer.
- a new approach for deposition of titanium-nickel, tin-oxide-copper, and magnessium-titanium powder mixtures using CS process,
- a new empirical mathematical model for predicting spray parameters and porosity of titanium coatings fabricated by CS process, and
- application of the central composite design of experiment in determination of CS process parameters.

1.8 Definitions

This section gives definitions of the key terms used in this thesis. These definitions are based on the literature, and more information about these terms is presented in Chapter 2 and Chapter 3.

Porous structures are part of solid materials made up of empty spaces such as pores, cavities or interstices, whose shapes can be regular or irregular, and are arranged in isolated, partially interconnected, interconnected, reticulated, cellular or foamed manner according to required performance.

Cold Spray is a process which deposits metal or composite powders on a metallic or dielectric substrate using a high velocity (300 to 1200 m/s) jet of small

($5\ \mu m$ to $50\ \mu m$) particles injected in a stream of preheated and compressed gas passing through a specially designed nozzle.

Microchannels are flow passages of uniform cross section, each with an equivalent circular diameter of between 10 μm and 200 μm.

1.9 Outline of the Thesis

This thesis is organised into five chapters which are structured, unified, and focused on solving one research problem, as illustrated in Figure 1.1. Each chapter, which stands practically alone, has an introductory section which outlines its aim and organisation, the main body of the chapter, and a concluding summary section which outlines the major themes established within it.

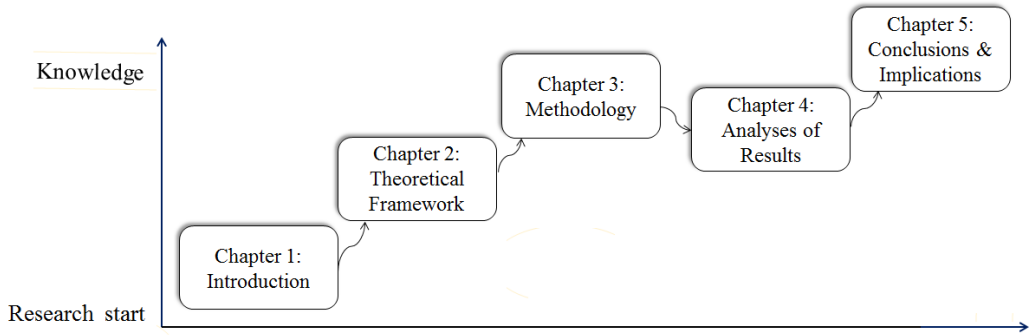


Figure 1.1: Organization of thesis' chapters

The first chapter sets the scene by introducing the core research problem and outlining the path that the reader will travel towards its conclusion. The research itself is described in Chapters 2 to 5. So, Chapter 2 identifies, from the existing body of knowledge, the research gaps. Then, by using various methods, Chapter 3 advances the hypotheses and then, these are practically demonstrated in Chapter 4. After that, Chapter 5 draws conclusions about the hypotheses and research question, and finally highlights the theoretical and practical implications of the research.

1.10 Conclusion

This chapter has laid the foundations for this thesis. It has introduced the research problem, research question, and hypotheses of the thesis. Then the definitions were presented, the methodologies were briefly described and justified, the contributions highlighted and finally, the thesis was outlined. On these foundations, the thesis proceeds with a detailed description of the research issues in Chapter 2.

2 REVIEW OF LITERATURE

This chapter provides the theoretical framework for this thesis. It identifies areas of controversy or gaps which were not previously answered, and thus need to be researched. The chapter starts by defining, describing and classifying the porous structures. This is followed by the review of the properties and areas of application for porous structures and selected applications of CS process are presented. Then, the chapter examines the current methods for fabrication of porous structures and highlights their capabilities and limitations. Finally, the chapter introduces the CS process, and then closes with the conclusion.

2.1 Porous Structures

Porous structures have favorable properties such as high specific area and high permeability (Singh et al., 2009; Lu and Zhao, 2011), consequently, they are used in many applications such as aerospace, energy, medical, electronics, and chemical industries (Yuan et al., 2012; Ludovic et al., 2013; Podshivalov et al., 2013). The architecture of the pores has major influence upon the choice of specific area of application for porous structures.

In this respect, Figure 2.1 shows that porous structures with open pore architecture were considered to be more suitable for functional than structural requirements, while those with closed pore architecture were more appropriate for structural than functional applications. Then, porous structures with partially open pore architecture had wider scope of application because they tend to meet both the structural and functional requirements (Banhart, 2001; Carey and Inderwildi, 2009).

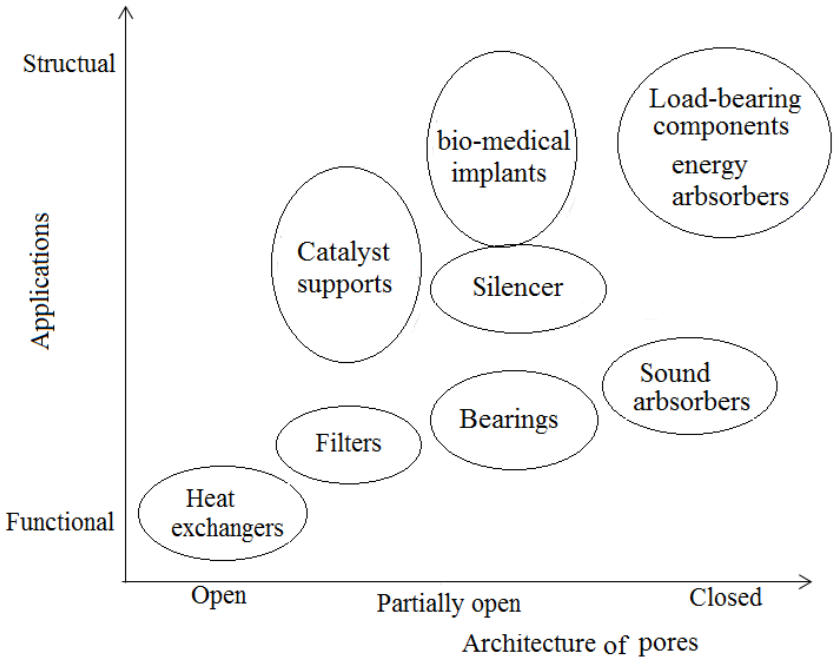


Figure 2.1: Application Vs. pore architecture.
Source: (Banhart, 2001).

Accordingly, porous structures referred to porous materials, were defined as natural or artificial solids with closed or open pores, voids, cavities, channels or interstices with varying shapes (Rouquerol et al., 1994). The morphology and architecture of the pores determine their properties and areas of application (Ashby and Medalist, 1983; Korner and Singer, 2000; Banhart, 2001; Sarkisov, 2012; Liang et al., 2013; Yang et al., 2013). In this respect, porous structures were described as: *open pore* or *through pore* when their pores were connected to each other and permeable to fluids; *blind pore* when the pores were open only on one side; and *close pore* if the pores were completely isolated from each other and impermeable to fluid (Rouquerol et al., 1994; Ryan et al., 2006). All these are illustrated in Figure 2.2.

In case the pores are open on both sides, without definite shapes and arranged as random network of bubbles, the structure was described as: *reticulated pore* (Ackermann et al., 2014). In the *isotropic pore structure*, the pores are oriented so as to give same physical properties in all directions, where as in *anisotropic pore* the pores are oriented to give varying physical properties in all directions (Song and Viskanta, 1994; Heaney et al., 2005; Li et al., 2015). All these are illustrated in Figure 2.3.

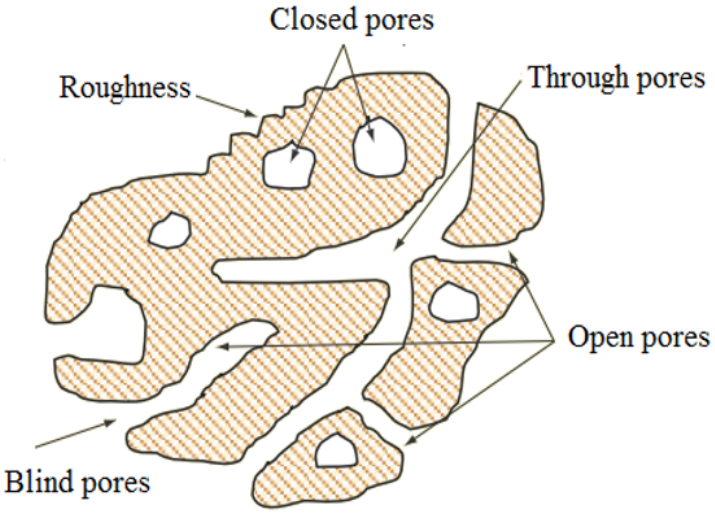


Figure 2.2: Nature of porous structures .
Source: (Arenas and Crocker, 2010).

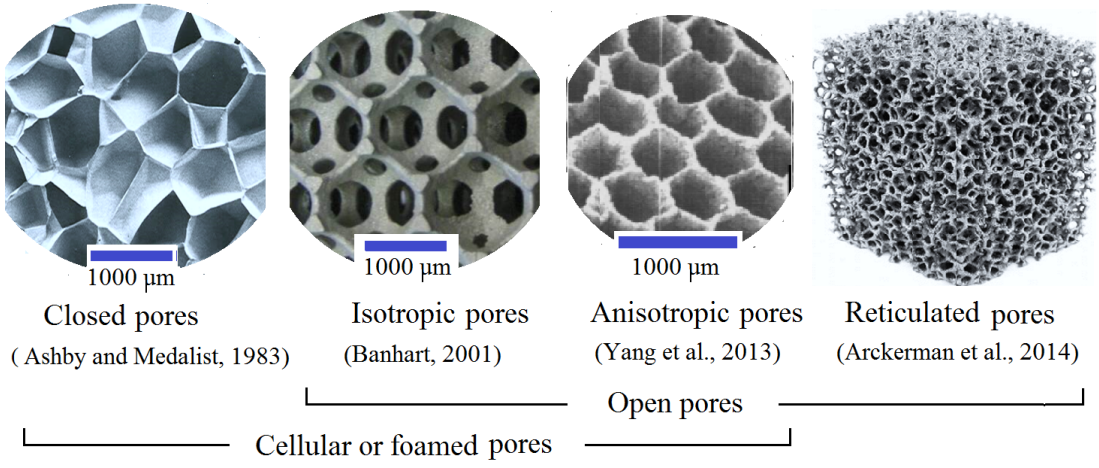


Figure 2.3: Pore structures

Finally, porous structures were categorised as *porous* if their porosity vary between 20 % and 70 %, and as *foamed* or *cellular* when their porosity vary between 70 % and 95 % (Ashby and Medalist, 1983; Nakajima et al., 2004). In this context, porosity was defined as the the ratio of the total volume of the pores to the total volume of the material and expressed by the equation (2.1).

$$p = V_p/V_s * 100 = (1 - \rho_s/\rho_m) * 100 \tag{2.1}$$

where p is the porosity V_p is the total volume of the pores in the structure, V_s is the total volume of the structure, ρ_s is the bulk density of the porous structure, and ρ_m is the theoretical density of the material used to make the porous structure.

Also, the areas of application of porous structures considered the architecture of pores, size of pores, origin of pores, and material used during manufacturing (Ashby and Medalist, 1983; Zdravkov et al., 2007). On this basis, subgroups for porous structures found in literature are presented in the taxonomy (Ackermann et al., 2014; King et al., 2015) shown in Figure B.1. In this taxonomy indicates two main sub-groups specifically, the architecture of pores and the origin of pores. More information about the classification criteria for porous structures is presented in Appendix B.

2.2 Application of Porous Structures

The presence of pores in the structures renders them several advantages for specific applications (Nakajima, 2007). For example, pores such as the microchannels in micro heat sinks (MHSs) confer them high fluid penetration, large surface area to volume ratio, and enhanced heat exchange capability, to mention a few. This characteristics are important in cooling high density electronic components such as microprocessors (Gautam et al., 2011; Thakre et al., 2014; Xia et al., 2015) illustrated in Appendix C. Lack of cost effective method of manufacturing MHSs hampers their wide scale application in this area (Prakash and Kumar, 2014).

Similarly, titanium alloys porous structures have advantages such as high specific strength, high corrosion resistance, super-elasticity, low elastic modulus,

and bio-inertness that make them ideal for bone implants vital for repair of the skeletal system (Elahinia et al., 2012; Sidambe, 2014). The demand for bone implants in orthopaedic surgery is hampered by the lack of cost effective manufacturing processes (Zahiri et al., 2009; Li et al., 2014) as clarified further in Appendix D.

Likewise, the benefits of high surface area to volume ratio and greater fluid permeability characterising the porous antimicrobial metals foams make them ideal for decontamination of drinking water for rural communities where modern water reticulation facilities are scarce due to lack of capital and technological know-how (Varkey, 2010; Sanpo et al., 2009; Zang et al., 2013). The demand for porous metal filters with enhanced antimicrobial capability is high in rural communities, but their supply is limited by the lack of low cost methods of manufacturing. Therefore, the research on fabrication techniques for porous metal foams with antimicrobial ability is urgently needed(Hemin et al., 2008; Champagne and Helfritch, 2013). Additional information on antimicrobial metals is presented in Appendix E

Also, the high gas sensitivity, selectivity and reactivity associated with porous semi-conductive metal oxide coatings make them suitable for gas sensing layers required in the detection of toxic gases in the pollution control and in environmental management systems as illustrated in Appendix F (Edelman et al., 2000). Because of increasing need to monitor environmental pollution, new methods of manufacturing porous gas sensing layers are required (Tiemann, 2007; Korotcenkov and Cho, 2011).

The application of porous structures in cooling electronics, health care, antimicrobial filtration and gas sensors were selected in this study because of their importance in industry and health. However, Appendix G indicates additional areas of application for porous structures but these are not discussed further in this thesis.

Nonetheless, there are some disadvantages associated with porous structures such as reduced mechanical strength, low Youngs Modulus, low corrosion resistance and less thermal and electrical conductivity which limits their application in specific areas (Nakajima et al., 2004; Venkatesh et al., 2013; Yang et al., 2011; Vincent et al., 2012; Xie et al., 2013).

2.3 Limitations of Fabrication Methods

Fabrication of porous structures has been practiced for a long time and several methods have been developed. The basic principles behind these methods included loosely packing of aggregates, removal of material, enclosing of material around space, and self-evolution. The fabrication methods based on the principle of loosely packing of aggregates included the sol-gel, powder metallurgy, and thermal spray. The fabrication methods based on the principle of removing of materials were the chemical etching, micro-mechanical cutting, laser cutting, and alloy-de-alloy. The two common methods based on the principle of self-evolution are the gas bubbling and self propagation high-temperature synthesis. The process steps followed in each of these methods contribute to their respective limitations as presented in the following paragraphs.

In the sol-gel method, the essential steps are: synthesis of gel, deposition of gel, and finally heating to dry and consolidate the gel. This method was proved in many industrial applications, but it failed to achieve maximal adhesion of the coatings to the substrate and, due to the heat during consolidation, the porosity was degraded (Shilova, 2005; Korotcenkov and Cho, 2011). In addition, the powder metallurgy method depicted in Figure H.5 has the following basic steps: mixing of feedstock powders, compaction, and sintering.

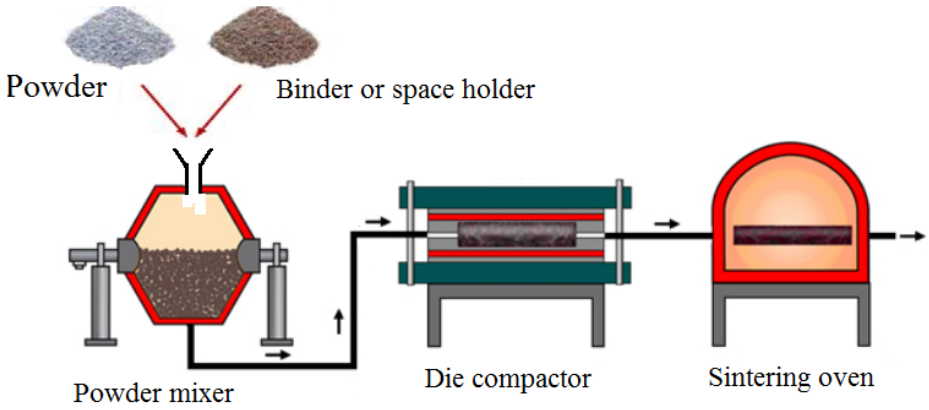


Figure 2.4: Powder metallurgy process.
Source: (HEAT, 2010).

Though the powder metallurgy method was successful in industry, it proved to be costly and, due to high pressure and temperature during compaction and sintering, it produced brittle products with poor workability. This method

also proved unsuitable for the fabrication of porous coatings on surfaces that are delicate or with complex geometries (Ryan et al., 2006; Sidambe, 2014). In the thermal spray processes, the feedstock powders were heated to high temperatures, melted and accelerated towards a substrate to build a coating. As a result, this method has limitations such as high oxidisation, decomposition, decarburisation, and delamination of the coatings, to mention a few. These limitations, made this method unsuitable for fabrication of temperature sensitive materials such as Titanium (Papyrin, 2006; Peerawatt et al., 2011; Bolelli et al., 2014).

Furthermore, the chemical etching method forms pores in the material by dissolution of the unmasked surfaces using common acids. However, this method proved to be slow and unable to control the shape and surface roughness of the pores (Wang, Zheng, Lim, Wang and Lam, 2011; Prakash and Kumar, 2014; OConnor et al., 2014). The micro-mechanical cutting process uses cutting tools to make pores such as microchannels in the material (Pan et al., 2009). However, this method proved to be unsuitable for mass production of porous structures due to high tool and setup costs (OConnor et al., 2014; Prakash and Kumar, 2014). Similarly, the laser cutting that applies a collimated laser beam to fabricate microchannels, proved to be uneconomical because of slowness of the process and the inconsistent interaction between the laser jet and the material that resulted in the pores with irregular topographies (Wang, Zheng, Lim, Wang and Lam, 2011; Zhou et al., 2014; OConnor et al., 2014). Lastly, the alloy-de-alloy method, illustrated in Figure 2.5, is an emerging method for production of porous structures. Its critical steps included, mixing of feedstock powders, alloying through chemical or physical means, and de-alloying using melt-spun and chemical leaching (**?**). Although this method fabricated special porous structures, it is less understood and so, not yet integrated in commercial production of porous products (Gottlieb et al., 2013; Jo et al., 2014; Song et al., 2015).

In addition, in the $3D$ printing method, the pattern is transferred from the model to the object using a laser beam scanner and a reactive liquid polymer to create the pores. However, this method proved to be slow and had high initial costs (Arjun, 2014; OConnor et al., 2014; Zhou et al., 2014). The electron beam melting method, that involves melting and layer-by-layer deposition of metal powders using a magnetically directed beam of electrons, exhibited high setup

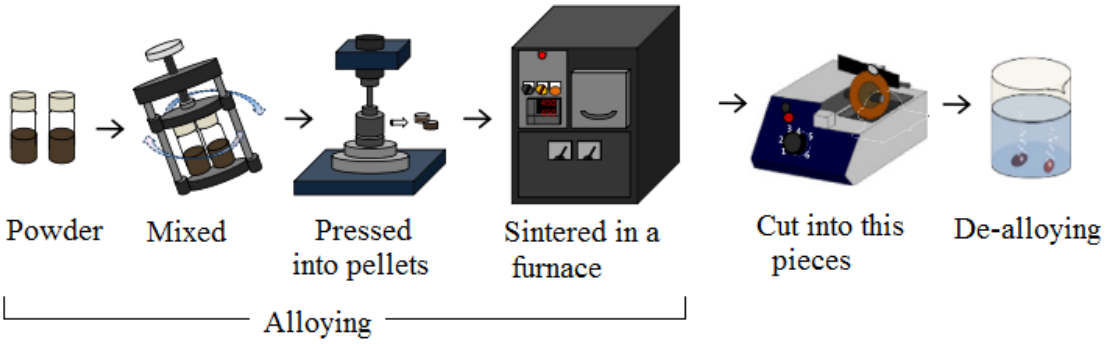


Figure 2.5: Alloy-de-alloy process.
Source:(Jo et al., 2014).

costs due to the requirement of high vacuum atmosphere around the beam of electrons. Similarly, the selective laser melting deposits the materials by completely melting the powders using a high-power laser beam. Although this methods was proved in the laboratory trials it exhibited high setup costs due to the requirement of advanced cooling systems (Bartolo, 2010; Sidambe, 2014).

Finally, in the gas bubbling method the pores are created in the structures by bubbling the gas in the materials. The major challenges with this method was its inflexibility during processing and it only manufactured porous solids, and not coatings (Nakajima, 2007). Similarly, the self propagation high-temperature synthesis, depicted in Figure 2.6, involves mixing of reagents, cold compaction and finally, ignition to initiate combustion. Although this method was cheap it produced undesirable inter-metallic compounds due to high temperature reaction between reagents (Biswas, 2005; Arakawa et al., 2012).

The paragraphs above shown that the methods for fabrication of porous structures have limitations and do not meet the modern manufacturing requirements of high efficiency and cost effectiveness. Hence, new methods need to be developed (Prakash and Kumar, 2014). More information about the methods for fabrication of porous structures is presented in Appendix H.

2.4 Cold Spray Process

Cold spray (CS) process, schematically shown in Figure 2.7, a downstream injection type, was proposed as a method for fabrication of porous structures

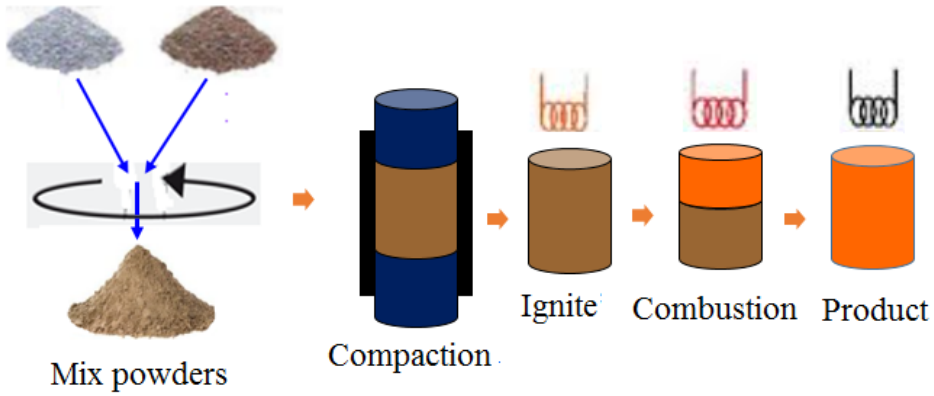


Figure 2.6: Self propagating synthesis process.
Source: (Pacheco, 2007)

due to its advantages over the existing methods presented above (Zahiri et al., 2006; Zahiri et al., 2009). This process can deposit metal or composite powders on a metallic or dielectric substrate using a high velocity (300 to 1200 m/s) jet of small (5 μm to 50 μm) particles injected in a stream of preheated and compressed gas passing through a specially designed nozzle.

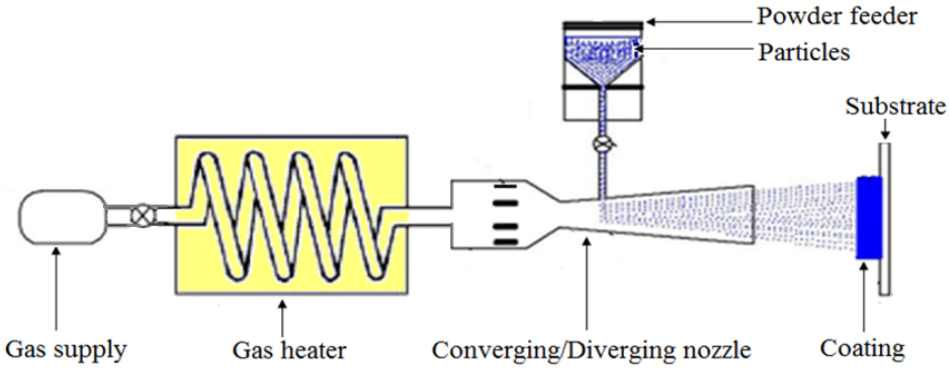


Figure 2.7: Downstream injection CS process.
Source: (Pacheco, 2007)

In the downstream injection cold spray, the spray powder is injected into the nozzle tube downstream of the throat where, in the upstream injection cold spray, the spray powder is injected into the nozzle tube upstream of the throat (Julio, 2014).

The advantages of downstream injection CS process compared to the upstream injection CS process include lower operational costs, avoids clogging of the throat, and better preservation of the nozzle.

However, this low pressure CS process is limited to spray ductile metal powders and mixtures of ceramics and a soft matrix. However, recent developments indicate that the low pressure CS could deposit sub-micron ceramic particles but withing a very narrow window of parameters.

Consequently, the downstream injection CS process was investigated to establish its spray parameters necessary to minimise the porosity in the sprayed coatings. The results of these investigations indicated that the increase in gas temperature and pressure and reduction in standoff distance and size of particles resulted in the reduction of the porosity, as explained in detail in Appendix I. However, studies on the spray conditions necessary to enhance the porosity of the cold sprayed coatings are rare in literature (Zahiri et al., 2006; Zahiri et al., 2009).

2.5 Conclusions

This chapter presented the relevant literature covering porous structures, fabrication methods, and CS process. Highlighting the limitations of the existing methods for fabrication of porous structures, the chapter justifies the need for the development of new methods using the CS process. Consequently, Chapter 3 presents the methods used to accomplish this objective.

3 RESEARCH METHODOLOGY

This chapter describes the methodology used to generate the data necessary to advance the hypotheses and provide the answer to the research question. The chapter begins by defining terms applicable in this thesis, followed by description of the experimental methods used to generate, analyse, and validate the data. Finally, the chapter closes with a conclusion.

3.1 Definitions

The following definitions apply in this thesis:

Porous structures are porous materials characterised with empty spaces or voids such as pores, cavities and interstices whose shapes could be regular or irregular and arranged in isolated, partially interconnected, fully interconnected, reticulated, cellular or foamed manner in accordance to performance requirements.

*Cold spray is a process that can deposit metal or composite powders on metallic or dielectric substrates using a high velocity (*300 *to* 1200 m/s*) jet of small (*5 μm *to* 50 μm*) particles injected in a stream of preheated and compressed gas passing through a specially designed nozzle.*

Microchannels are fluid flow passages with straight or wavy path and uniform cross sections each with an equivalent circular diameter of between 10 μm *and* 200 μm.

3.2 Research Question and Hypotheses

The research question presented in Chapter 1 is repeated here for the sake of clarity of the hypotheses presented below.

Could the CS technology be practically and efficiently used in the fabrication of porous materials?

To answer this question, three hypotheses were formulated.

Hypothesis 1*: CS process could be used to fabricate porous structures through controlling the spray parameters.*

Hypothesis 2*: CS process could fabricate porous structures when feedstock powders of different mixtures are used.*

Hypothesis 3*: The CS process could fabricate porous structures with controlled porosity using the method such as alloy-de-alloy.*

In order to provide answers to the above research question and hypotheses, the following experimental procedures are presented below.

3.3 Experimental Procedures

The developed experimental procedures include: preparation of experiments, fabrication of specimens, characterisation and testing of specimens and, analysis and validation of results. These, alongside their inputs, were organised as shown in the experimental methodology flow chart in Figure 3.1.

This methodology was implemented along with the following three strategies:

- Strategy 1: Control of spray parameters during fabrication of porous structures using individual powders,
- Strategy 2: Using a variety of powder mixtures so as to create heterogeneous structures with different percentage of porosity, and

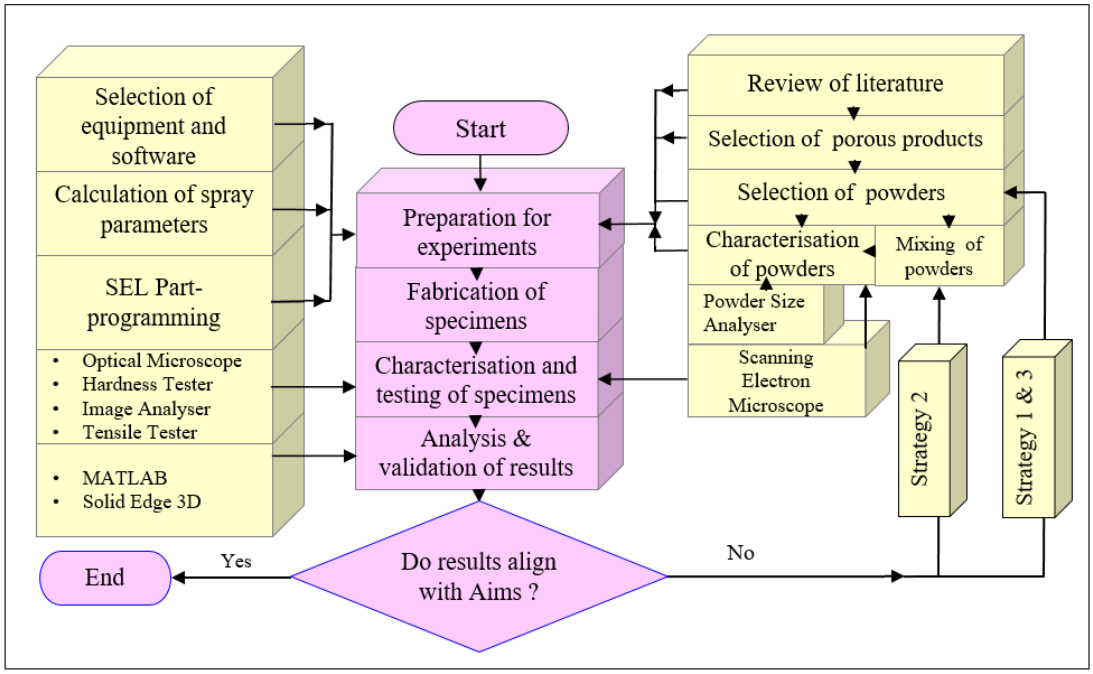


Figure 3.1: Experimental methodology flow chart.

- Strategy 3: Application of the CS process and the alloy-de-alloy method to fabricate porous structures.

3.3.1 Strategy 1: Control of Spray Parameters

Materials and equipment. The feedstock powders used in this strategy were alumina, aluminium-alumina, copper, titanium and zinc. These powders were used to fabricate coatings and, when was necessary, make tensile tests. Information about these powders and equipment used is summarised in Appendix J.1. The substrates used to fabricate copper and zinc coatings were cut from aluminium slabs while the substrates for titanium coatings were from mild steel.

The substrates dimensions for porosity, microstructure, and microhardness examination were 20 mm long, 20 mm wide, and 5mm thick and those for tensile tests were 100 mm long, 10 mm thick, and with the profile shown in Figure 3.2 in accordance with the standard ASTM E−8/E8M−11 for tensile testing of specimens with microscopic cross sections (ASTM-International, 2012). The equipment used for characterisation of powders, fabrication of coatings, testing

of specimens, and the software are presented in Appendix J.1.

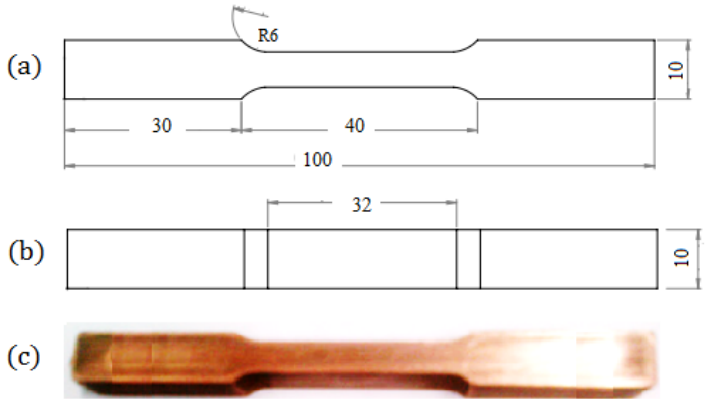


Figure 3.2: Tensile test substrate.
(a) Top view, (b) front view, and (c) actual.

Characterisation of powers. The as-received feedstock powders were characterised for morphology and particle size distributions using the Field Emmission Scanning Electron Microscope (FESEM), type Carl Zeis SIGMA, and the Particle Size Distribution (PSD) Analyser, type Marven Mastersizer−2000, respectively. Then, the oxygen content of the powder was measured using the Oxford Energy Dispersive X-ray Spectroscope (EDX) detector coupled with the FESEM. The results from this characterisation process are presented in Chapter 4.

Calculation of spray parameters. The temperature and pressure of the gas (air) were calculated using the equation (L.1) for the velocity of the particles and the critical velocity of the powder was calculated using the equation (L.3) for individual powders. For mixed powders, the mean critical velocity was calculated using equation (L.4) in which the percentage distribution of critical velocities for constituent powders were accounted (see Appendix L). Then equation (L.1) was equated to equation (L.3) or (L.4) to indicate the commencement of bonding of the particles, and the values for the temperature and pressure were calculated using iterations in the excel spread sheet. The additional equations used in these calculations were from the isentropic gas flow models given in Appendix K. Then, the values for the standoff distance and powder feed rate, which were obtained from the technical data sheets for respective powders, were grouped with the calculated values for the temperature and pressure using the Taguchi method explained in Appendix M. Thereafter, the cold spray deposition trials were carried out to select the groups that

resulted in rapid build up of the coatings. These groups of parameters are presented in Appendix N. Finally, in cases where the CS process was required to deposit coatings for validation, the central composite design of experiment-response surface methodology was used to calculate the spray parameters as explained in Appendix J.

Fabrication of coatings. This process started by entering the spray parameters (temperature, pressure, and powder feed rate) in the control console of the CS system (see Figure I.3), followed by offsetting the nozzle to the required standoff distance. The nozzle used in this process was converging/diverging (CD) type with its diverging length, throat and exit diameters of 120 mm, 2.5 mm and 6.5 mm, respectively. Then, the feedstock powders were fed to the CS system via the external integrated gravitational vibratory bowl feeders. The particles from the powder were injected in the supersonic stream of compressed and preheated gas and accelerated towards the substrate where they bonded due to impact and plastic deformation. The spray gun was automatically moved by the robot according to the velocity and the path specified in the Sel Programme. Through this process, the surface of each substrate was initially activated by grit blasting using alumina powder, followed by actual coating using relevant feedstock powders. However, during the fabrication of specimens for tensile test, a thin layer of aluminium-alumina powder was deposited between the substrate and each coating, which was later dipped in dilute hydrochloric acid to dissolve the aluminium-alumina layer to delaminate the specimens. In addition, during deposition of the powders, the consistence of the vibratory powder feeder may not have been optimal and this could account for the variations in the microstructure and build-up of the coatings as discussed in Chapter 4.

Characterisation and testing of coatings. Each coating was initially cross-sectioned, hot mounted using Struers machine type OPAL 410 and Polyfast conductive resin, ground using the Struers Tegramin−30 machine fitted with grinding discs type MD-Piano grit size 220 μm and MD-Largo $3-9$ μm, and polished using MD-Dac cloth grit size 3 μm, and 1 μm diamond suspension finish. Then, the polished specimens were observed under Optical Microscope (OM), model LEICA CTR 6000, and the FESEM to acquire images that were used to study the microstructure and porosity.

The porosity was measured using image analysis software, ImageJ 1.45, in which five images of each of the coatings were initially cropped and later uploaded into the toolkit. Then, the gray-scale of each of the uploaded images was converted to bit-64, followed by adjustment of the colour threshold to highlight the contrast between the pores and the matrix. The area covered by the pores was calculated automatically by the adjustment of the colour contrast of the two regions. Finally, the percentage area covered by the pores compared to the total area of the coating under analysis was the measured porosity for each of the coating type, and the standard deviation of the porosity measurement for each type of coating was calculated and recorded.

Also, the microhardness values of these specimens were measured using the Vickers Hardness Tester, type FM−700, set to 300 gf load with an automatic loading cycle of 10 seconds. The indentation was carried out on the cross section of each of the coatings, whose thickness exceeded the 76.2 μm minimum required. In this case a total of 12 indentations were made per coating type such that the next indentation was spaced at a distance of at least four times the diagonal of the previous indentation in accordance to the standard ASTM C1327 to avoid the effect of cracking and strain hardening. If the majority of the microhardness values were nearly equal, then three or more measurements with different values were averaged. If the measurement were all scattered, then these were averaged and recorded. The standard deviation of the microhardness value for each type of coating were also calculated and recorded.

Finally, the tensile tests were carried out using a Shimadzu Autograph−20kN/50kNIC machine. The specimens were firmly clamped in the jaws of the tensile tester grips that were placed at an initialisation spaced of 100 mm. Then the testing process was set to increase the tensile load and gauge displacement such that their values were automatically sampled every 50 ms (0.05s) until the specimen fractured. The break point of each of the specimen was detected upon which the testing machine automatically stopped and the cross head restored to its original position. In this way, the displacement of the grips was as a result of the deformation (extension) of the specimen since the machine was able to measure the gauge length on specimens accurately. The results for the tensile tests were automatically recorded in the force-extension report.

Analysis and validation of results. This process was carried out as explained in Appendix O.

The results from the above characterisation, testing, analysis and validation processes are presented and discussed in Chapter 4.

3.3.2 Strategy 2: Coatings from Powder Mixtures

Materials and equipment. The powder mixtures, expressed as percentages by mass, and the substrates used in this strategy are presented in Table 3.1. The powders were mixed as described in Appendix J followed by their characterisation for morphology and oxygen content using the equipment described in section 3.3.1.

Table 3.1: Powder mixtures.

Mixture	Percentage	Application	Substrate
Aluminium:alumina:copper	50 : 30 : 20	Antimicrobial	Copper
Aluminium:alumina:zinc	50 : 30 : 20	Antimicrobial	Aluminium
Copper:chromium	80 : 20	Micro heat sink	Copper
Tin-oxide:copper	70 : 30	Gas sensors	Alumina
Titanium:nickel(at.wt.)	50 : 50	Bone implant	Copper
Magnessium:titanium	60 : 40	Bone implant	Mild steel

Note: for titanium:nickel the 'at.wt.' means atomic weight ratio.

Spray parameters. These are summarised in Table N.5.

Fabrication of coatings. The coatings for porosity, microstructure and tensile tests were fabricated as explained in section 3.3.1. However, the coatings for gas sensing layers were fabricated on top of the aluminium-alumina electrodes that were deposited on the grit blasted alumina substrate, and their arrangement is shown in Figure 3.3.

To enhance the surface porosity of the device, the sensing layers were fabricated on top of the pyramidal fins. The pyramidal fins were fabricated on top of the electrodes using copper power and a mask. In this case, the spray gun, mask and substrate were arranged as shown in Figure 3.4.

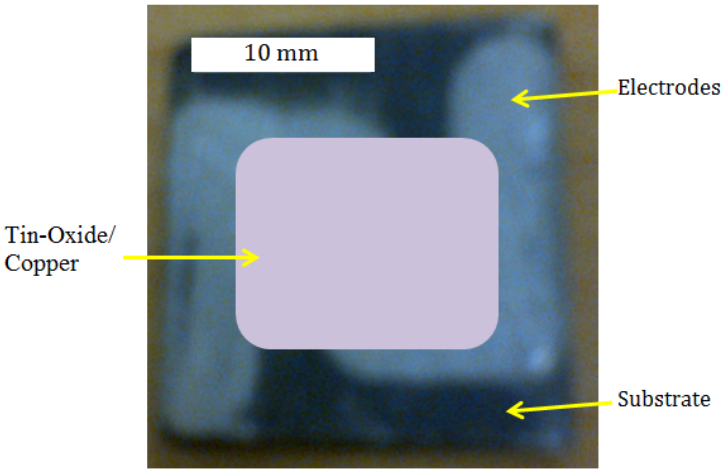


Figure 3.3: Gas sensing layer

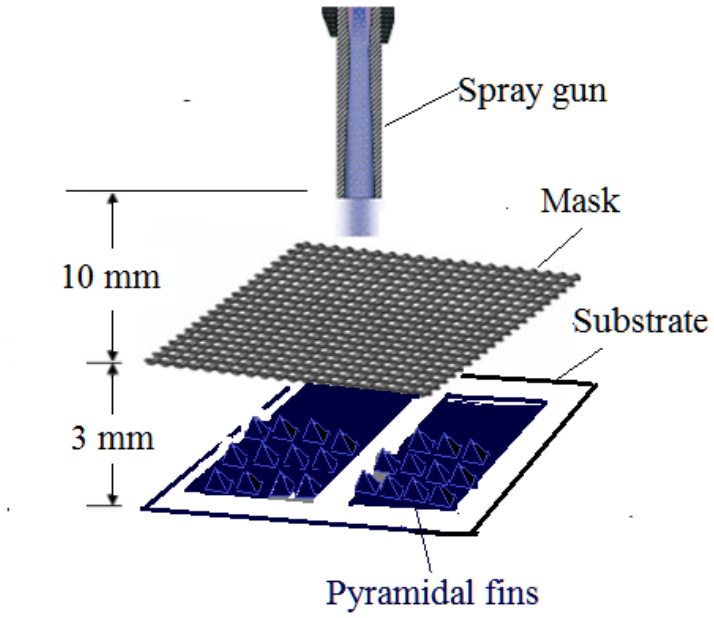


Figure 3.4: Pyramidal fins fabrication.

Characterisation and testing of coatings. The coatings for porosity, microstructure, tensile, and microhardness were prepared, tested and their oxygen content measured as explained in section 3.3.1. The tin-oxide-copper coatings were tested for gas sensitivity by exposing them to Nitrogen dioxide prepared by reacting copper powder with nitric acid in the ESCO fume hood. During this test, the gas sensing layers were heated to between 20 °C and 300 °C using soldering iron and their surface temperature was measured using laser thermometer gun. The results from the characterisation of the powder mixtures, coatings, and tests are presented and discussed in Chapter 4.

3.3.3 Strategy 3: CS Process and Alloy-De-Alloy

In this strategy, the various CS coatings were fabricated followed by de-alloying using common acids. This strategy resulted in microchannels with trapezoidal shapes and an international patent application number $WIPO/PCT$ IB2015057821 was made for this method (Hamweendo and Botef, 2016). Also, the method was used to fabricate porous structures for possible antimicrobial application. The processes used to make these structures are explained below.

Materials and equipment. The feedstock powders used in this strategy were alumina, aluminium-alumina and copper. These powders were mixed as described in Appendix J. The substrates used were copper and aluminium slabs each with 40 mm length, 40 mm width, and 5 mm thickness. The mask used for fabrication of microchannels was made from mild steel and its dimensions were 60 mm length, 50 mm width, and 5 mm thickness. This mask was slotted with straight slits of 600 μm width that were spaced at 400 μm apart. Similarly, the mask used for fabrication of antimicrobial filter was a mild steel with thickness of 0.5 mm and perforated with round holes of radius 400 μm whose centres were spaced at 1484 μm. The equipment used in this strategy is similar to that in section 3.3.1.

Spray parameters. These are summarised in Table N.6 and Table N.7.

Fabrication of microchannels. During this process, the copper and aluminium-alumina powders were deposited alternately according to the following steps:

1. Grit blast the substrate using alumina powder,
2. spray thin layer of aluminium-alumina to create a delamination base,
3. spray three layers of copper powder to create micro heat sink base,
4. through a mask, spray one layer of aluminium-alumina to create ridges,
5. without a mask, spray 3 layers of copper to embed the ridges,
6. grind off the protruding tips of the ridges,
7. repeat steps 3 to 6 for three times to embed 3 layers of ridges,
8. without a mask, spray 3 layers of copper to cover the ridges,
9. lightly grind the cross section of the specimen to expose the ridges,
10. dip specimen in dilute hydrochloric acid to de-alloy aluminium-alumina,
11. repeat step 9 until through microchannels are created and delaminated, and
12. rinse the specimen in distilled water and dry it in air.

These steps are illustrated in Figure 3.5 and explained further in Appendix J.

Fabrication of the antimicrobial filters. The steps for this process are summarised as follows:

1. Grit blast the substrate using alumina powder,
2. spray a thin layer of copper powder to create a delamination base,
3. through a mask spray 3 layers of copper to make discs,
4. without mask, spray 1 layer of powder mixture to cover 3/4 of the discs,
5. repeat steps 3 to 4 to achieve between 2 mm and 3 mm thickness,
6. dip specimen in dilute nitric acid to leach copper discs and delaminate,
7. rinse the specimen in distilled water and dry it in air,
8. dip specimen in dilute hydrochloric acid for 5 seconds to expose copper,

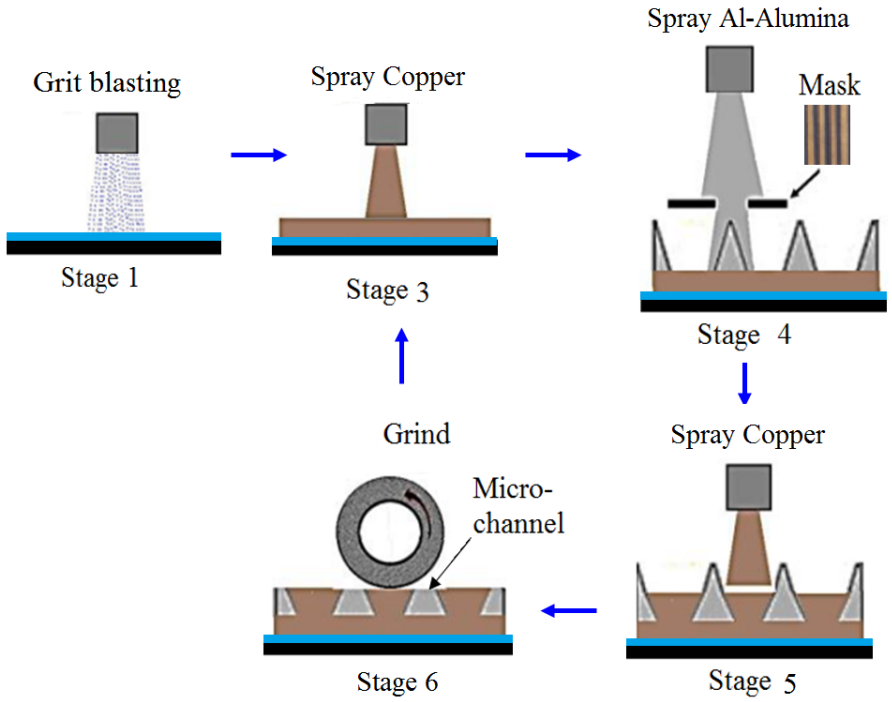


Figure 3.5: Fabrication of microchannels.

9. rinse the specimen in distilled water and dry in air.

These steps are illustrated in Figure 3.6 and explained further in Appendix J.

Characterisation. The fabricated microchannels and antimicrobial filter were characterised for porosity and microstructure, and the results are presented and discussed in Chapter 4.

Performance testing of microchannels. The microchannels were tested for thermal-mechanical and thermal-hydraulic performance using computational modeling and simulation analysis, and analytical methods, respectively. During the test for thermal-mechanical performance, Solid Edge $3D$ modeler software was used. In this case, a wire frame model and the computational domain for the micro heat sink were as shown in Figure 3.7. The input parameters in the simulation window were: ambient temperature of 20 °C, pressure drop of cooling liquid ranging between 0 bar to 1 bar in steps of 0.2 bars, heat flux ranging between 100 W/cm^2 and 500 W/cm^2 in steps of 100 W/cm^2, and the convective heat transfer coefficient of $7,242$ W/m^2K. The cooling liquid was assumed to be de-ionised water. The Reynolds number was varied between 100 and 1700 in steps of 400 and the velocity of the fluid flowing through

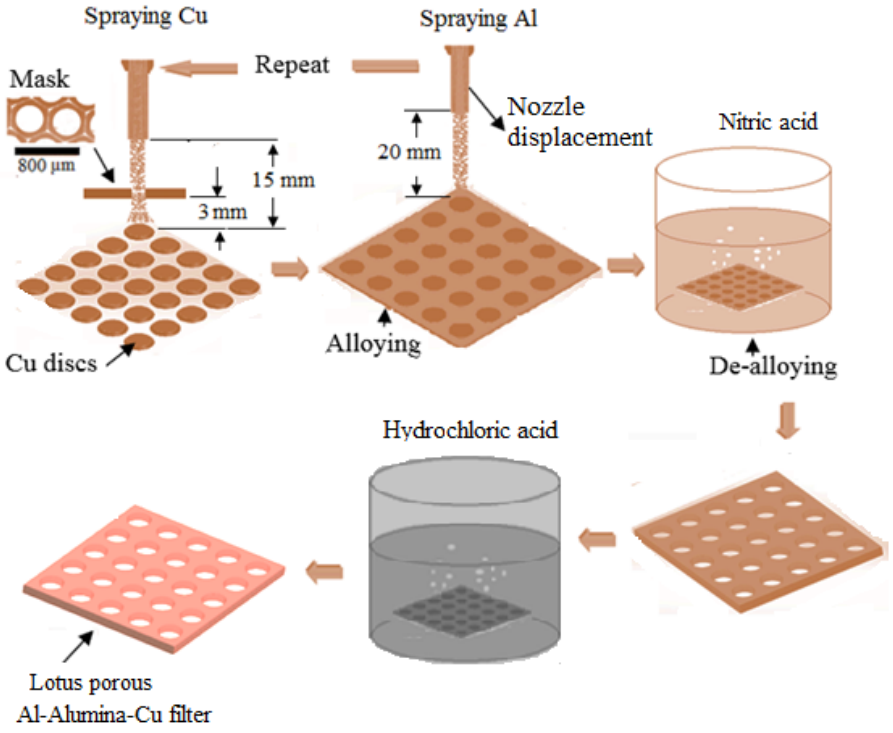


Figure 3.6: Process for antimicrobial filters.

the microchannels was varied between 0.01 m/s and 0.03 m/s according to (Zhang et al., 2014). Finally, the Nusselt number was set at 3.87 (Incropera et al., 2006).

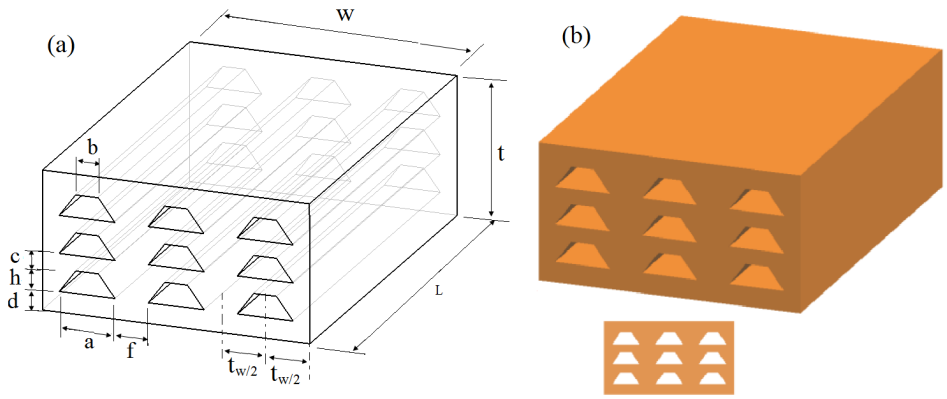


Figure 3.7: Simulation models.
(a) Wire frame (b) Computational domain.

Also, the thermal-hydraulic performance of the microchannels was analytically evaluated using nanofluids that comprised the de-ionised water and alumina or copper nanoparticles of sizes assumed to be 36 μm and 50 μm, respectively (Lee et al., 2007a; Wusiman et al., 2013). The volume fraction of these

nanoparticles in the base fluid was varied between 1 % and 5 % in steps of 1 % (Pak and Cho, 1998; Corcione, 2011). In this case, the objective was to minimise the thermal resistance of the microchannels. The Reynolds number was varied between 100 and 1700 in steps of 400, and the microfluidic flow in the microchannels was assumed to be fully developed laminar (Zhang et al., 2014). In this evaluation, the thermal resistance was calculated using the empirical equation (4.4). The results from the above evaluation methods are presented and discussed in Chapter 4.

3.4 Conclusions

This chapter presented the research question and hypotheses and the methodologies used to provide the necessary answers. The results from this chapter are demonstrated in Chapter 4.

4 RESULTS, ANALYSIS AND DISCUSSION

This chapter presents the results and their analyses for the porous structures fabricated according to the methods presented in Chapter 3. Each analysis is followed by the discussion that highlights its significance in the context of the research question and hypotheses. For an easy way to navigate this chapter, Figure 4.1 shows its mapping. Finally, the Chapter closes with a conclusion.

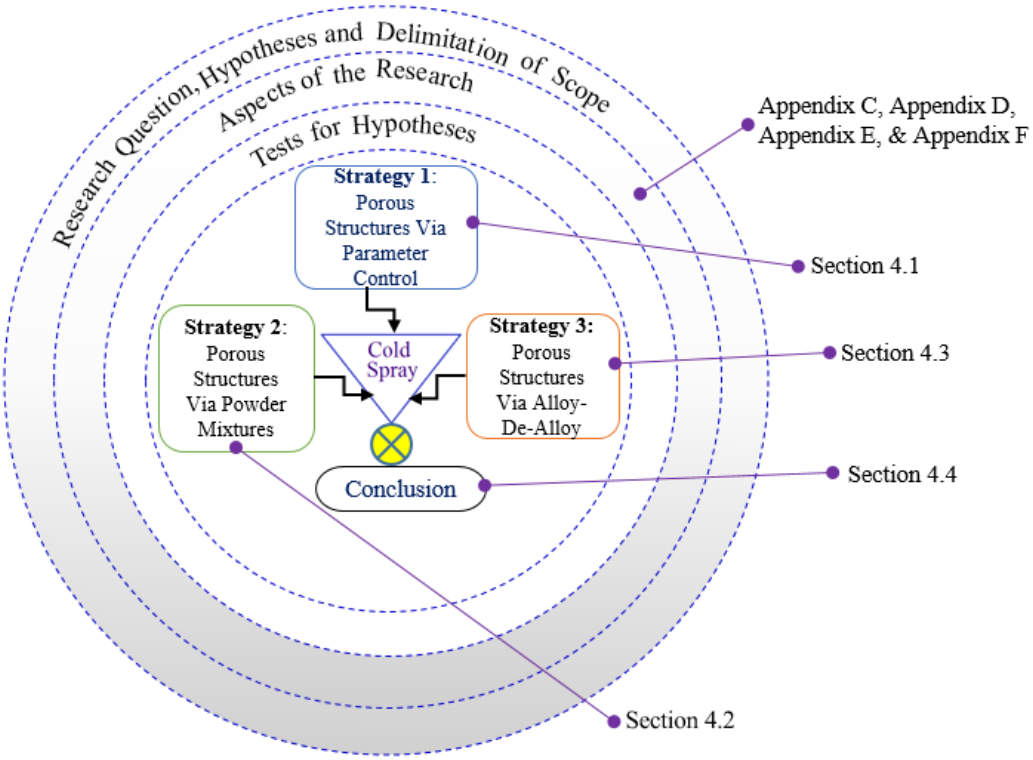


Figure 4.1: Chapter 4's map.

4.1 Porous Structures through Control of Spray Parameters

4.1.1 Feedstock Powders

The feedstock powders used in this strategy were aluminium-alumina, copper, zinc and titanium. These powders were sourced from Centerline, Canada, under the product codes A0050, C5003, Z5001 and T5001. The morphologies of these powders are shown in Figure 4.2 and Figure 4.3.

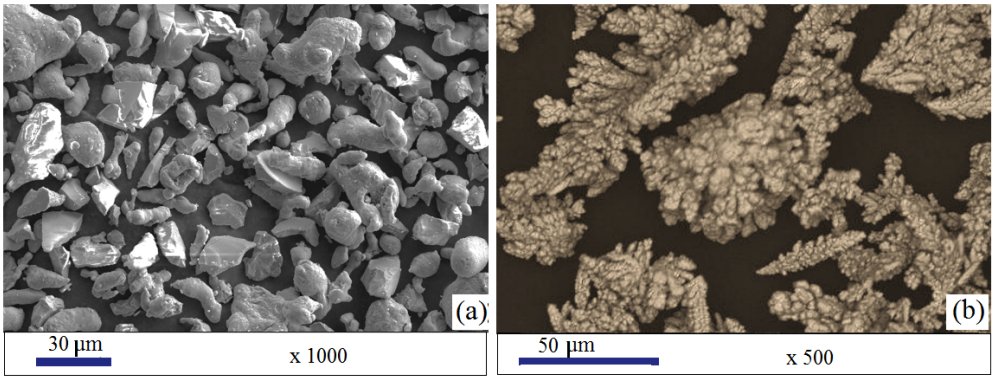


Figure 4.2: Morphology of aluminium and copper powders.
(a) Aluminium-alumina, (b) copper.

As seen in Figure 4.2, the aluminium and copper powders were ovoid and dendritic, respectively.

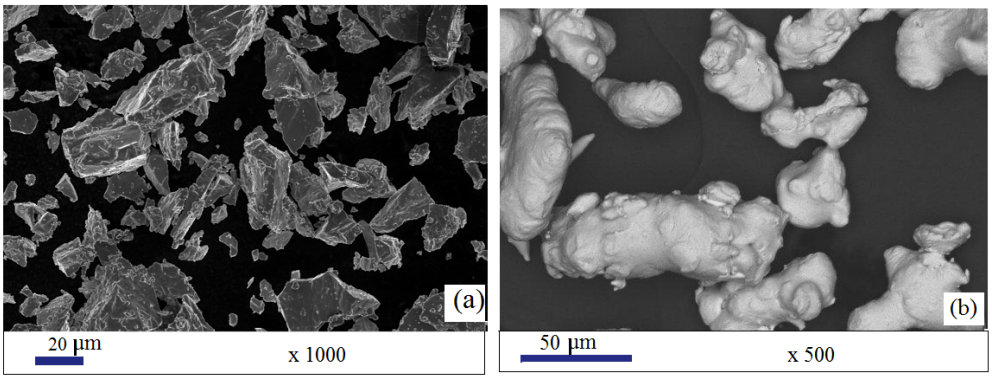


Figure 4.3: Morphology of titanium and zinc powders.
(a) Titanium and (b) zinc.

Similarly, the titanium and zinc powders shown in Figure 4.3 were angular and acircular, respectively.

Then, the particle size distributions (PSDs) of these powders were measured in order to determine their mean sizes and the spread of the distribution. This information was necessary for planning and design of deposition process and to establish if the size of the particles in the powders was within the sprayable limits of the LP-CS equipment. The PSDs for these powders are shown in Figure 4.4.

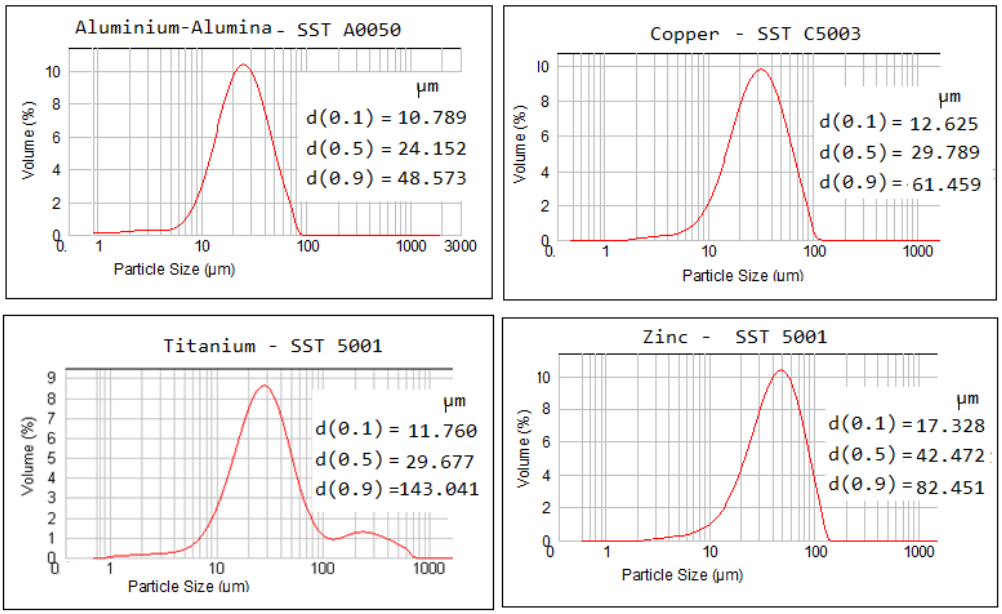


Figure 4.4: Size distributions of powders for strategy 1.

As one can see in above figure, the size distribution for the aluminium-alumina, copper and zinc powders were normal, broad and their mean size of particles ($d_{0.5}$) were within the sprayable limits of 5 μ and 50 μ for the LP-CS equipment. With these powders, the coating would have bridged particles resulting in inter-particle voids (Zahiri et al., 2006). However, the titanium powder exhibited a bi-modal and a broader distribution than the powders earlier mentioned. Thus, when deposited, the titanium powder was expected to produce a heterogeneous microstructure (Cinca et al., 2010). The oxygen content for temperature sensitive titanium powder was measured using the energy dispersion x-ray spectroscope (EDX) and the spectrum is shown in Figure 4.5. This spectrum shows no peaks for oxygen. This means that there was no oxygen in the titanium feedstock powder.

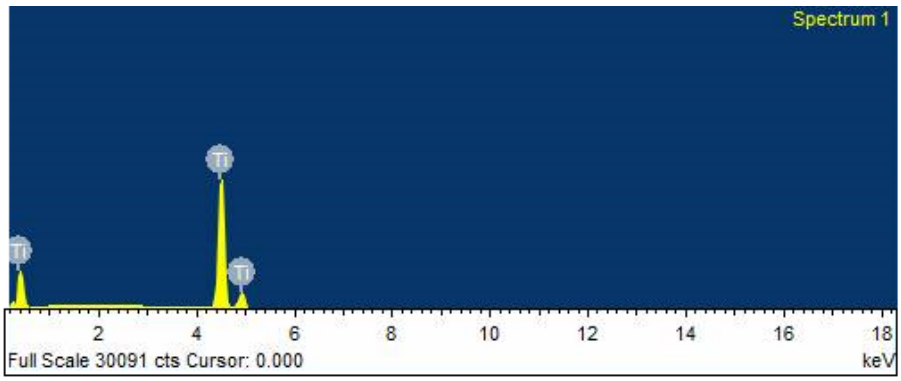


Figure 4.5: EDX spectrum for titanium.

4.1.2 The Coatings

The coatings achieved in this strategy were fabricated using varied conditions. For instance, using sub-optimised spray parameters, the stagnation temperature (T_0) and pressure (P_0) of the gas were set at lower values compared to the optimum levels, and the standoff distance (S) was set at a higher value so that the particles in the powders could reach the substrate with limited impact and deformation in order to achieve porous coatings (Zahiri et al., 2006). So, Figure 4.6 (a) shows the aluminium-alumina coating achieved under this sub-optimised spray condition.

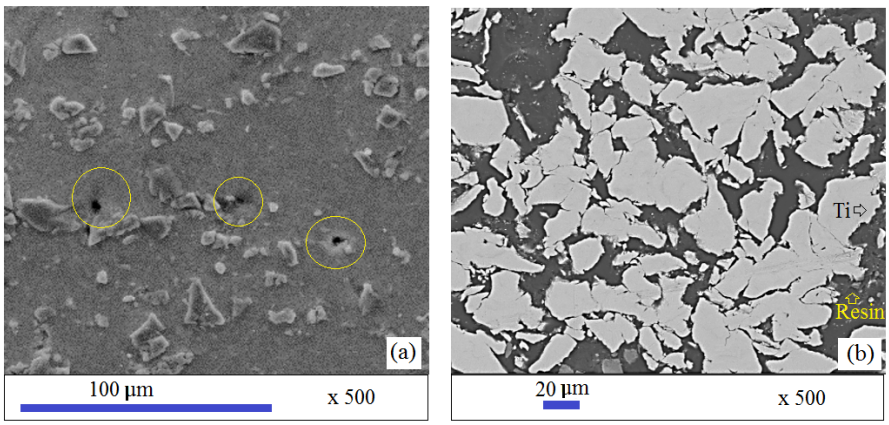


Figure 4.6: Coatings under sub-optimised conditions.
(a) Aluminium-alumina, (b) titanium

As seen in this figure, the aluminium-alumina coating shows very low porosity (less than 1.0 %) since only small holes occurred in the matrix and are

randomly distributed. As such, this structure is impermeable to fluids. Similar structure was reported in literature (Irissou et al., 2007). However, under similar sub-optimised spray parameter conditions, the titanium coating shown in Figure 4.6 (b) showed high porosity of up to 31.5 %. Also, under similar conditions, the coatings fabricated using the copper and zinc powders seen in Figure 4.7 exhibited porosity only on their top surfaces. However, when the optimised spray parameter conditions were used, the aluminium-alumina, copper and zinc coatings were dense as shown in Figure P.10.

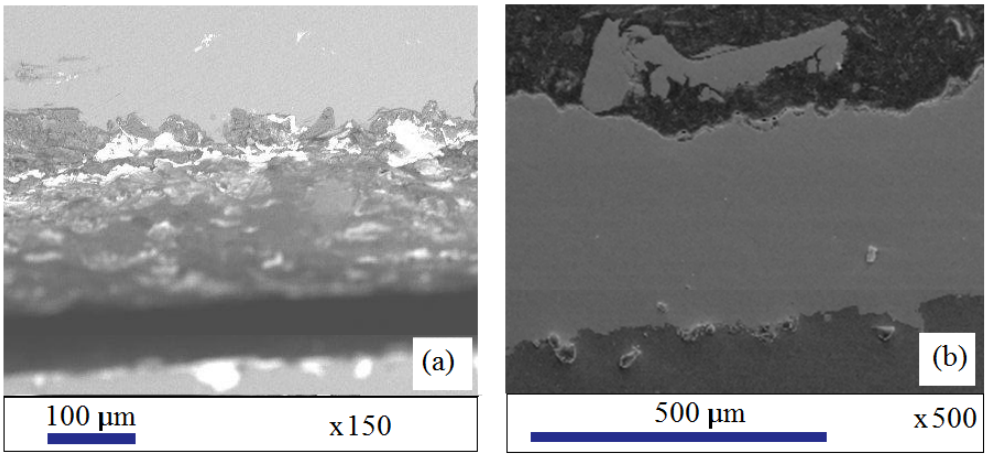


Figure 4.7: Surface porosity for copper and zinc coating.
(a) Copper, (b) zinc coatings.

Then, the titanium coating, shown in Figure 4.8 and achieved using optimised parameters, was dense due to a repeated hammering of the oncoming spray particles (Ghelichi and Guagliano, 2009) and exposed a thin porous layer of about 60 μm on its top surface.

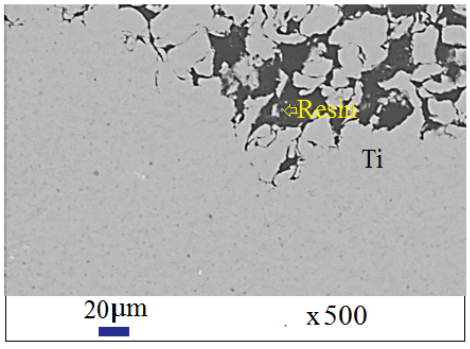


Figure 4.8: Titanium coating under optimised conditions.

4.1.3 Analysis and Discussion

The morphology and the type of the feedstock powders and the variation of spray conditions affected the porosity formation in the coatings. For example, under sub-optimised spray conditions, the angular titanium particles produced porous coatings while under similar conditions, the spherical aluminium and dendritic copper particles produced dense coatings. These results appeared to be contrary to the belief that angular particles produce dense coatings while the spherical or dendritic particles produce porous coatings (Ning et al., 2007; Koivuluoto and Vuoristo, 2010; Assadi et al., 2011). This difference in microstructure of the coatings fabricated under sub-optimised spray conditions was attributed to the following explanation.

When the spray conditions of the LP-CS system were sub-optimised, the titanium particles attained less energy at impact and their deformation was limited. So, nano-recrystallisation at areas of contact could have dominated the cohesion of particles. This mechanism could have been supported by the formation of splats and micro-jets that resulted in a strong structure and a strong bond. As such, the less deformed titanium particles tended to wedge and created large inter-particle voids. Consequently, the mechanical interlocking of the particles due to deformation was less prominent under sub-optimised spray conditions of the LP-CS that resulted in more porous structure. However, the deposition of titanium powder resulted in dense coatings under optimised spray conditions of the LP-CS system because, beside the nano-recrystallisation that took place in the inter-particle contact regions, the particles impacted the target with high energy and their deformation predominated the cohesion.

On the other hand, the aluminium, copper and zinc powders, when deposited under sub-optimised spray conditions of the LP-CS process achieved thin coatings that had less porosity. This could be attributed to a compromise between cohesion and bouncing back of the particles. However, when the spray condition of the LP-CS process were optimised, the particles of these powders acquired enough energy such that upon impact there was plastic deformation at localised thin regions of contact where the thermal-softening effects occurred and caused the adiabatic shear instability. This resulted in the ejection of an interfacial jet that consisted of highly deformed materials, and removed the

oxide films from the surfaces of the substrate or particles that enabled intimate contact of clean metallic surfaces and hence promoting particle-substrate or particle-particle bonding. During this process, the growth of the metal jet at the point of contact progressed from the initial point of contact to the other regions of the particle. Consequently, the thermal softening effect and deformation predominated the bonding mechanism and created compact structures. This type of bonding mechanism could have contributed significantly to the failure to produce porous structures using the strategy of control of spray parameters in the aluminium, copper and zinc powders deposition (see 4.1).

Due to varied porosity of the coatings created using the titanium powder, an empirical mathematical model shown in equation (4.1) that relates the porosity of the titanium coating to the spray parameters, was developed as explained in Appendix O. The porosity of this coating was measured using image analysis software as explained in Chapter 3.

$$Porosity = 11.6656 + A - B \tag{4.1}$$

where A and B are given by equation (4.2) and equation (4.3), respectively.

$$A = 299.8704P + 11.0097S + 0.0333S^2 + 1.3389TP \tag{4.2}$$

$$B = 0.2866T + 0.00057T^2 + 788.452P^2 + 0.01014TS + 4.4700PS \tag{4.3}$$

where, the temperature of the gas is T (K), pressure of the gas is P (bars), and the standoff distance is S (mm).

The porosity values predicted by equation (4.1) and the corresponding measured values presented in Table O.1 were plotted and produced a linear regression graph shown in Figure 4.9. The correlation coefficient for this graph is 98.3 % and signifies a strong positive correlation between the theoretical and practical results (Hamweendo et al., 2014b).

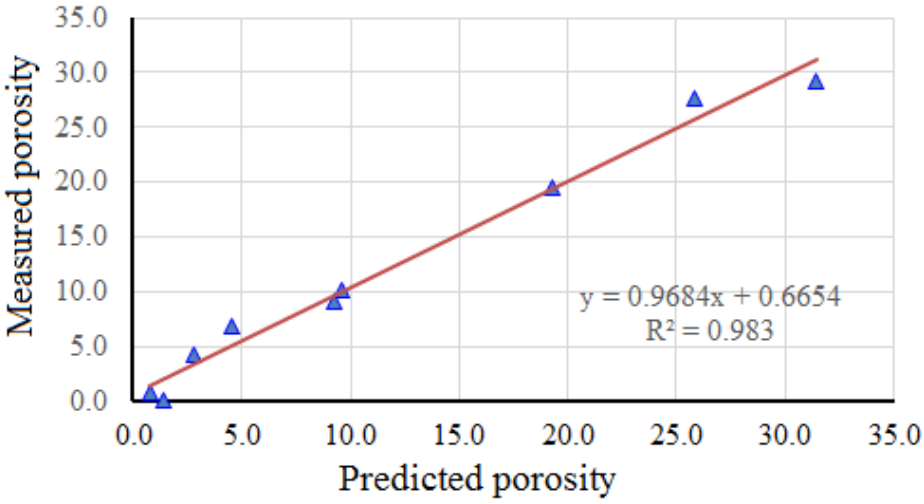


Figure 4.9: Measured Vs. predicted porosity for titanium.

The tensile tests of the cold sprayed titanium (Ti), titanium-nickel and copper-chromium and coatings were carried out according to the standard ASTM E−8/E8M−11 for tensile testing of specimens with microscopic cross sections (ASTM-International, 2012). The results of these tests and their analysis are summarised in Table 4.1. Note that the values for the strain, Young's Moduli, and tensile strength presented in this table were calculated as explained in Appendix O. Also in this table, the labels for titanium specimens correspond to those in Table N.3 for spray parameters of titanium.

As seen in Table 4.1, the calculated tensile strength for titanium specimens varied between 204.0 MPa and 410.0 MPa and their Young's Moduli varied between 49.7 GPa and 99.6 GPa, respectively. These variations are outside the range of 0.14 MPa and 200.0 MPa, and 0.16 GPa and 40.0 GPa recommended for bone implants (Edwards et al., 1997; Keaveny et al., 2004; Yang et al., 2011). Also, it is worth noting that the tensile strength for titanium coatings reduced as the porosity increased. This variation is in agreement with the observation made in literature (Nakajima, 2007). However, the elastic limits for titanium coatings were similar to those of the trabecular bone for the bovine and titanium alloys used in biomedical application (Kaplan et al., 1985; Cordeiro and Barao, 2017). Based on this analysis, it could be concluded that the change in the cold spray parameters resulted in porous structures with different characteristics that could be suitable for specific applications.

Table 4.1: Tensile behaviour of cold sprayed coatings.

Specimen	Measd.Porosity for Ti	Area μm^2	Extens.(mm)	Strain(ϵ)	F_{max} (N)	σ (MPa)	Y (GPa)
$Ti-1$	9.1	169884966	0.8	0.008	80	359.0	90.0
$Ti-2$	9.6	20716966	1.2	0.012	260	355.0	89.0
$Ti-3$	2.8	5193172	0.7	0.002	75	410.0	103.6
$Ti-4$	25.8	25869103	0.2	0.002	25	239.0	58.8
$Ti-5$	19.3	34941185	0.8	0.008	135	283.0	70.1
$Ti-6$	31.5	27924914	1.1	0.011	100	204.0	49.7
$Ti-7$	4.6	23515543	0.9	0.009	120	395.0	99.6
$Ti-Ni$	26.7	6672102	0.2	0.002	8	54.0	14.6
$Cu-Cr$	0.01	19798930	2.5	0.025	470	379.0	117

Finally, the results from 4.1 proved hypothesis 1 that the CS process could be used to fabricate porous structures through the control of spray parameters.

4.1.4 Applications

Bone Implants. The titanium structure achieved in this study could be used for surface coating of bone implants due to its porosity. The other favourable properties of titanium coating (not tested in this study) include low elastic modulus, bio-inertness, high specific strength, low electrical conductivity, low electrochemical oxidation that resulted in the formation of a thin passive oxide layer and excellent corrosion resistance. The other field of application for porous titanium coatings include orthopaedic and orthodontics repair (Zahiri et al., 2006; Sun et al., 2008; Zahiri et al., 2009; Sidambe, 2014; Hamweendo et al., 2015).

Aerospace and Marine. Dense titanium coatings have high tensile strength to density ratio, high corrosion and fatigue resistance, high crack resistance,

and ability to withstand moderately high temperatures without creeping. Consequently, these coatings could be be used in spacecraft and armor plating, naval ships and missile building and repair (Zahiri, Mayo and Jahedi, 2008; Zahiri et al., 2009; Cinca et al., 2010; Julio, 2014).

Gas Sensors. Coatings of zinc and copper powders or their oxides when characterised with surface porosity could be used in the fabrication porous surface coated gas sensors (Galdikas et al., 1997; Tamaekong et al., 2010).

4.2 Porous Structures through Powder Mixtures

4.2.1 Feedstock Powder Mixtures

The morphology of the powder mixtures used in this strategy is shown in Figure 4.10 and Figure 4.11. As seen in Figure 4.10 (a) and (b), the constituent particles in the aluminium-alumina-copper (Al-Alumina-Cu) and titanium-nickel (Ti-Ni) powder mixtures were evenly dispersed though the nickel particles appeared to have been deformed and this could have contributed towards the observed poor flow of the Ti-Ni powder mixture through the powder feeding system during cold spray trials. The aluminium-alumina-zinc (Al-Alumina-Zn) powder mixture in (c) do not show the distinct constituent particles as these appeared to have been crushed into smaller sizes and then agglomerated into larger balls while the titanium-magnesium (Ti-Mg) powder mixture in (d) shows the titanium particles (greyish) and the magnesium counterparts (whitish) as aggregates of the balls.

Consequently, these powder mixtures exhibited very poor flow through the powder feeding system during cold spray trials and so were sieved to improve their flowability during cold spray trials. Similarly, Figure 4.11(a) shows the agglomerated tin-oxide-copper powder. As seen in this figure, these agglomerates were ovoid and their mean size was between 5 μm and 50 μm, while their mixture with copper powder shown in (b) had an excellent distribution of the constituent particles that improved their adhesion during deposition and their

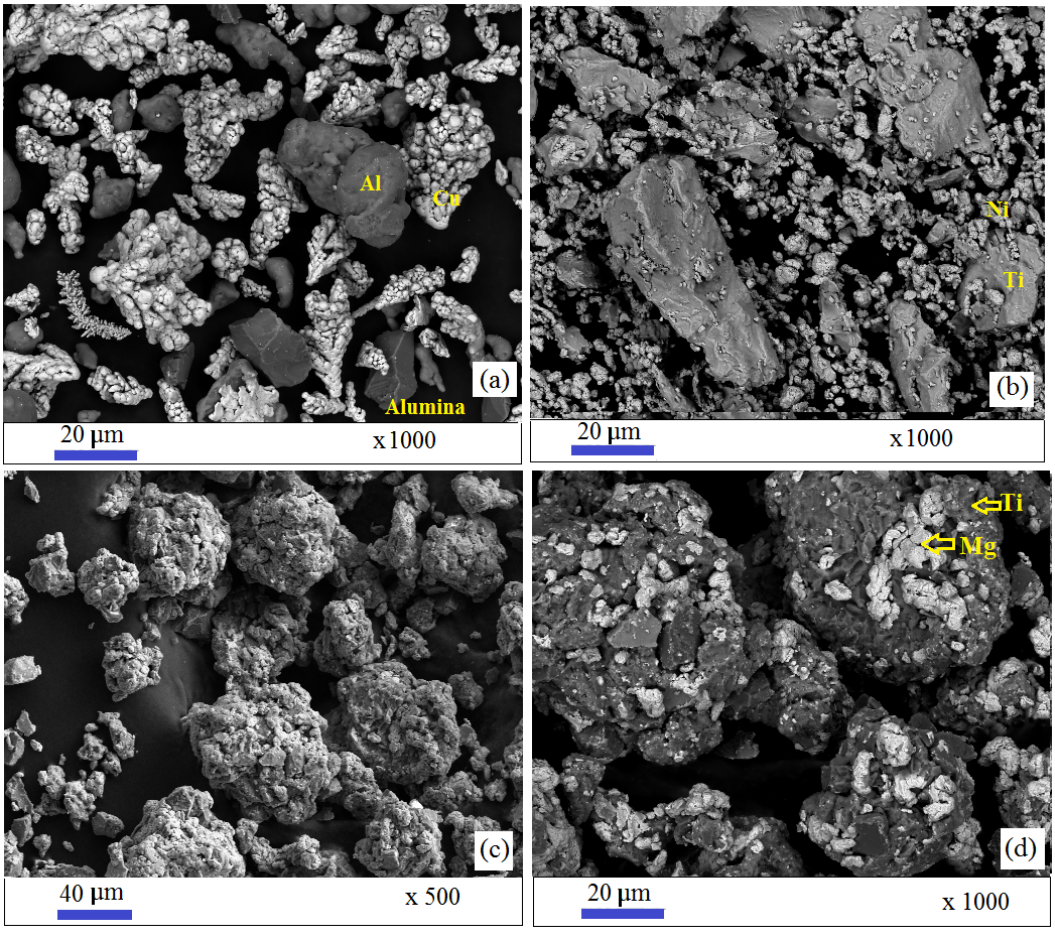


Figure 4.10: Morphology of powder mixtures.
(a) Al-Alumina-Cu, (b) Ti-Ni, (c) Al-Alumina-Zn, and (d) Ti-Mg.

electric conductivity of the coating during gas sensing operation.

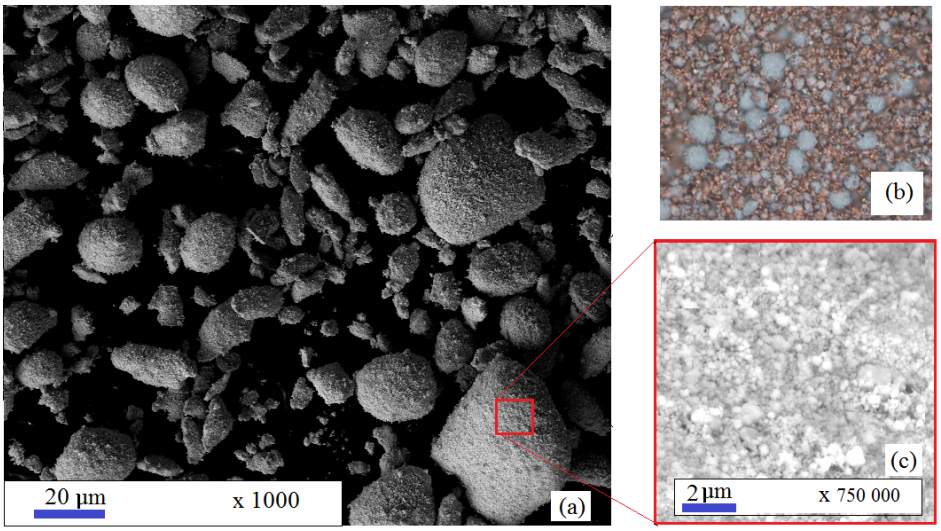


Figure 4.11: Tin-oxide-copper agglomerates.
(a) Agglomerated, (b) Mixture, (c) Magnified view.

4.2.2 The Coatings

Figure 4.12 shows the coatings for the titanium-nickel powder mixture fabricated under varied spray parameter conditions.

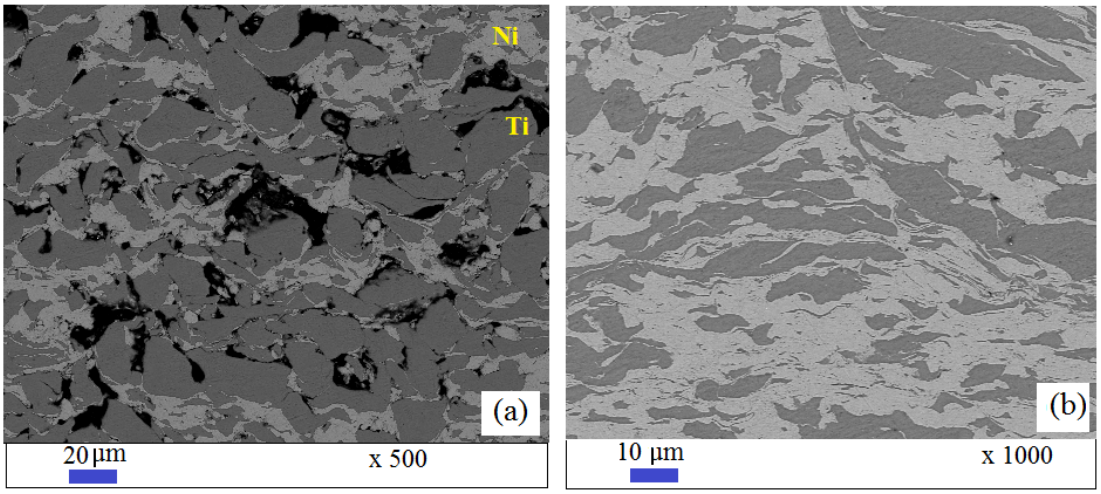


Figure 4.12: Titanium-nickel coatings
(a) Porous, and (b) dense.

The coating shown in Figure 4.12 (a) was fabricated using sub-optimised spray

conditions. This coating had a porosity of 26.5 % which was less than that achieved using titanium powder under similar deposition conditions. This was because the splats from the nickel particles filled up the voids between the titanium particles. On the contrary, a dense coating shown in Figure 4.12 (b) was fabricated using the optimised spray parameters. Equally, the dense coatings shown in Figure P.9 were fabricated using the aluminium-alumina-copper, aluminium-alumina-zinc, copper-chromium and titanium-magnesium powder mixtures. These coatings showed uniform dispersion of constituent particles with good interparticle bonding. The EDX spectrum of the titanium-nickel coating in Figure P.11 shows no peaks for oxygen. This means that the CS process did not oxidise the titanium-nickel coating. The results for the microhardness tests of the titanium, nickel and titanium-nickel coatings are summarised in Table O.1 and shown in Figure 4.13. These indicate that the changes in spray parameter conditions influenced the values for the microhardness as illustrated in the following paragraph.

The increase of gas pressure from 0.75 bars to 9.5 bars (26.7 %) and standoff distance of the nozzle from 14 mm to 26 mm led to increase in the microhardness of the titanium-nickel alloy from 214 Hv to 367 Hv (71.5 %). Similar effect of the change in pressure on the microhardness of the pure titanium coating was observed while the opposite was true for nickel coating. These suggested that the increase in pressure resulted in more drag effect of the gas on the titanium and titanium-nickel particles while a larger standoff distance of the nozzle allowed more time for particles to accelerate. The reduction in microhardness of the nickel coating under these conditions suggested that there was loss of momentum by the smaller nickel particles due to increased standoff distance of the nozzle. Further, the increase in temperature of the gas from 664 K to 782 K (17.8 %) resulted in marginal increase in microhardness from 290 Hv to 292 Hv (0.7 %) for the titanium-nickel coating, while the microhardness for titanium increased from 173 Hv to 222 Hv (28.3 %) and that of Nickel increased from 115 Hv to 176 Hv (53.0 %). These results imply that the variation in temperature could have more effect on microhardness of the coatings for smaller particles when the standoff distance of the nozzle is less. In summary, it could be concluded that the variation in spray parameter conditions have significant effect on the microhardness of the coatings, but, this variation seems to also depend on other factors such as powder sizes and powder mixture.

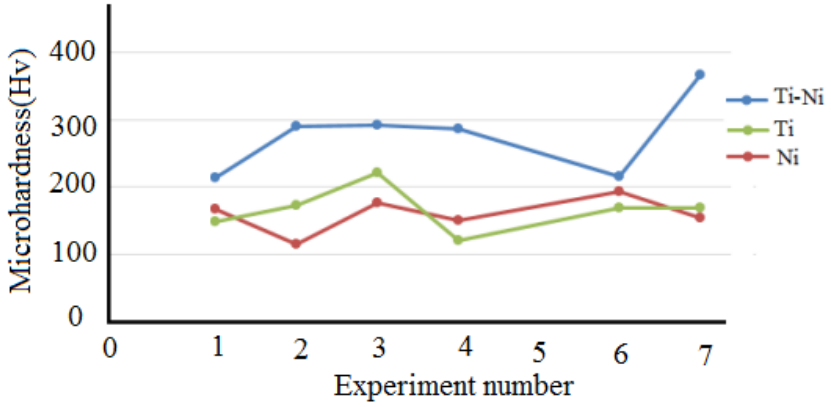


Figure 4.13: Microhardness graphs for coatings.

Further, Figure 4.14 shows the tin-oxide-copper coating. As seen in this figure, the coating adhered to the substrate and maintained the surface porosity shown in Figure 4.15 with a value of 37.6 % which was more that the 10 % minimum required for a good sensitivity of gas sensors (Edelman et al., 2000; Shilova, 2005; Tesfamichael et al., 2007).

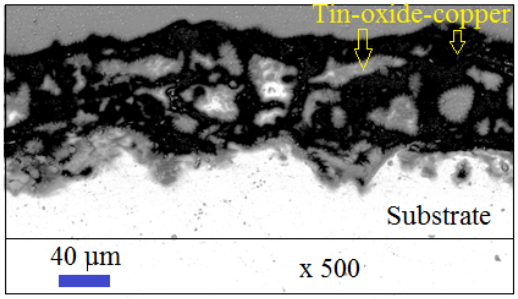


Figure 4.14: Tin-oxide-copper coating.

Furthermore, the peaks for tin (Sn), oxygen (O), and copper (Cu) seen in the EDX spectrum of Figure 4.16 indicate that the tin, copper and oxygen were present in the coating just like in the powder mixture as shown in Figure 4.17. The peak for Al seen in Figure 4.17 is for the aluminium present in the substrate used.

Finally, the tin-oxide-copper coatings for sample 1 and sample 2 were tested for gas sensitivity. Sample 1 refers to the gas sensor in which the tin-oxide-copper coating was fabricated on top of the electrodes and in sample 2 the tin-oxide-copper coating was fabricated on top of the pyramidal fins as shown in Figure 4.18.

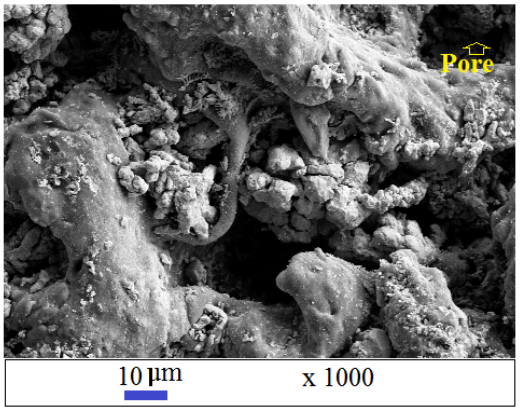


Figure 4.15: Surface porosity of gas sensing layer.

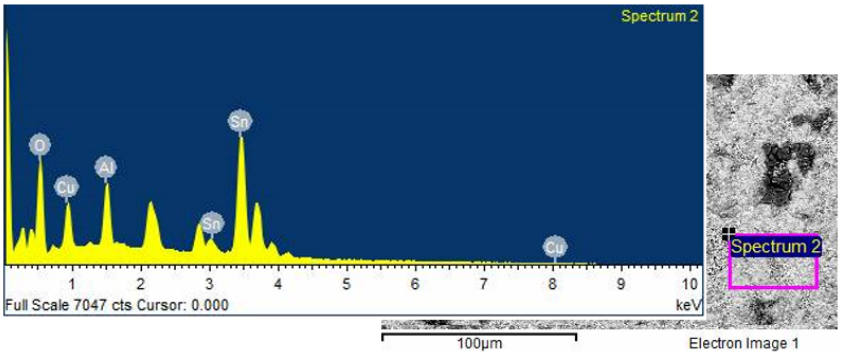


Figure 4.16: EDX spectra for gas sensing layer.

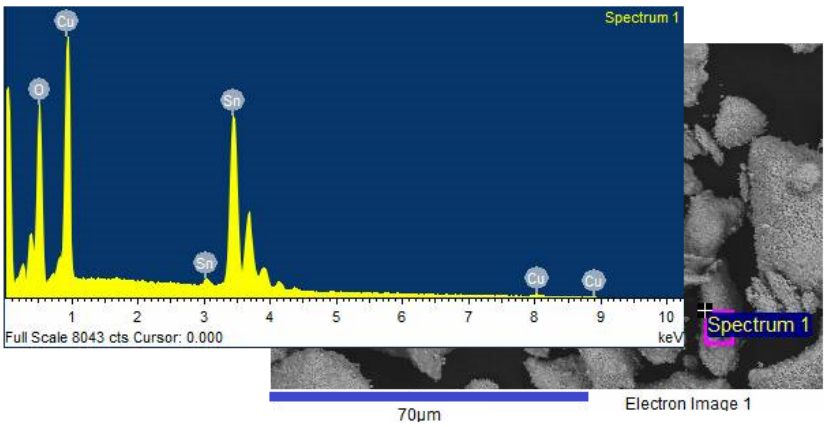


Figure 4.17: EDX spectra for gas sensing layer.

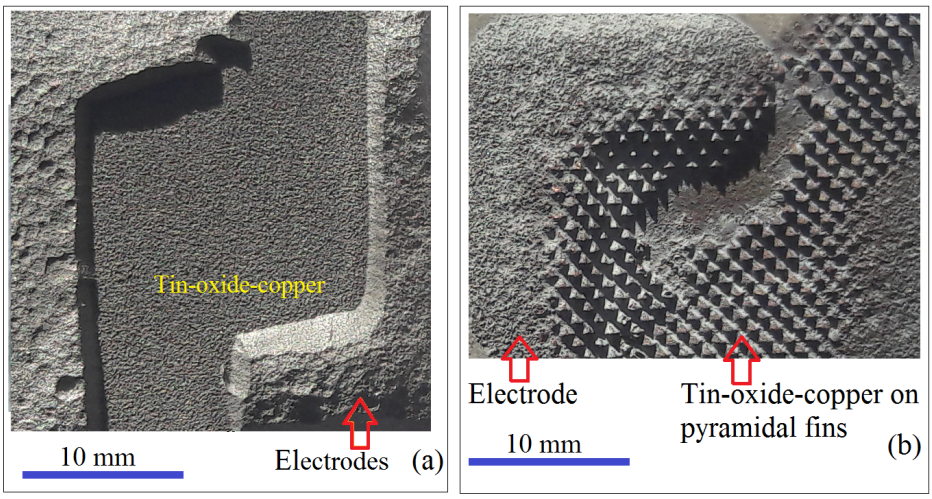


Figure 4.18: Gas sensors.
(a) Sample 1, (b) sample 2.

The results for the resistance in air (R_{air}) and resistance in nitrogen dioxide gas (R_{gas}) for each of these samples are summarised in Table 4.2 and Table 4.3.

Table 4.2: Sensor response for sample 1.

Temperature (°C)	R_{air} (MΩ)	R_{gas}(MΩ)	Sensitivity
21	0.5	4.9	8.8
63	0.49	4.8	8.8
81	0.49	5.4	10.0

Table 4.3: Sensor response for sample 2.

Temperature (°C)	R_{air} (MΩ)	R_{gas}(MΩ)	Sensitivity
26	5.4	4.8	0.0
32	5.39	5.9	0.1
68	5.3	106	19.0

4.2.3 Analysis and Discussion

The homogeneous and un-agglomerated powder mixtures of the aluminium-alumina-copper and titanium-nickel were achieved using the optimum mixing parameters of rotational speed of 250 rev/minute, mixing time of 30 minutes,

and powder to ball mass ratio of 1 to 1. These powders were successfully deposited using the LP-CS process and air as the accelerating gas set to maximum pressure of 9.5 bars. The titanium-nickel powder mixtures reported in literature were strain hardened and could only be deposited using the HP-CS system with air as the accelerating gas set at maximum pressure of 27 bars (Tria et al., 2009). These results confirm that the method of using planetary ball mill, type Retsch PM400 MA, equipped with four stainless steel vials can be used to mix powders.

Further, the titanium-nickel coating with low porosity achieved using sub-optimised spray conditions is a result of the splats of the ductile nickel particles that filled up the voids found between the titanium particles and created a multilayer structure of the flattened titanium and nickel. The low porosity achieved in this microstructure suggests that the strategy of mixing powders with different deformation capability results in lower porosity, and this is contrary to the literature (Zahiri et al., 2006). Consequently, it can be said that the powder mixtures have greater tendency to produce dense structure as observed in the titanium-nickel coating shown in Figure 4.12 (b). Similar results were achieved in the aluminium-alumina-copper, aluminium-alumina-zinc, copper-chromium, and titanium-magnesium coatings shown in Figure P.9. This imply that other techniques are necessary to create porous structures when powder mixtures are used as feedstock. However, these coatings exposed all the individual elements of the initial powders, and the copper-chromium exhibiting excellent interparticle contact. Likewise, similar dense coatings of aluminium-alumina, copper-chromium, and titanium-nickel powder mixtures were reported in literature (Koivuluoto et al., 2008; Tria et al., 2009; Kikuchi et al., 2013; Hamweendo et al., 2016a). But, information about the coatings of the aluminium-alumina-copper, aluminium-alumina-zinc, and titanium-magnesium fabricated using LP-CS system is rare in literature.

Furthermore, the graphs plotted using the results for gas sensitivity tests for sample 1 and sample 2 are presented in Figure 4.19 and Figure 4.20, respectively.

From these graphs it could be noted that the resistance and sensitivity of both samples increased with the temperature. Particularly, sample 2 had the highest increase of the resistance of up to 106 Ω and sensitivity was 20.0 at 70°C

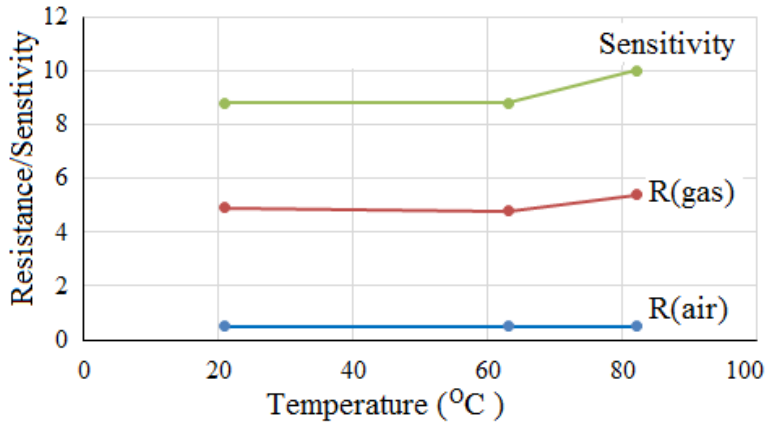


Figure 4.19: Graph for gas sensor sample 1.

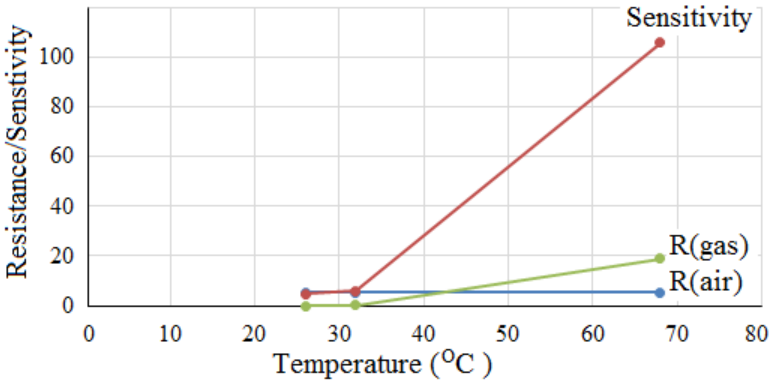


Figure 4.20: Graph for gas sensor sample 2.

compared to the resistance of 5.4 Ω and sensitivity of 10.0 recorded for sample 1 at 81°C. This difference in response is attributed to the increase in surface area of sample 2 (Wang et al., 2010). In addition, both sensing layers were sensitive to nitrogen dioxide gas even at room temperature which is not always the case with the usual gas sensors that require to be heated before sensing could commence (see Appendix F for more information). This suggests that the gas sensing layers fabricated using the LP-CS process have the capability to detect toxic gases even at room temperature and so do not require heating. Moreover, the resistance of the sensing layer fabricated in this study increased along with the gas concentration which was a sign of high sensitivity as shown in Figure 4.21. In this case, the concentration of the nitrogen dioxide gas was increased by adding 2.5 grammes of copper powder to the 100 milliliters of nitric acid each time. This increased performance may be attributed to the fact that the fabricated gas sensing layers had porous top surfaces and firm contact with the electrodes and substrate. Such a structure was difficult to achieve using conventional methods such as sol-gel or screen printing as these methods tended to degrade the porosity during consolidation of the coatings (Shilova, 2005; Graf et al., 2006; Han et al., 2008; Korotcenkov and Cho, 2011).

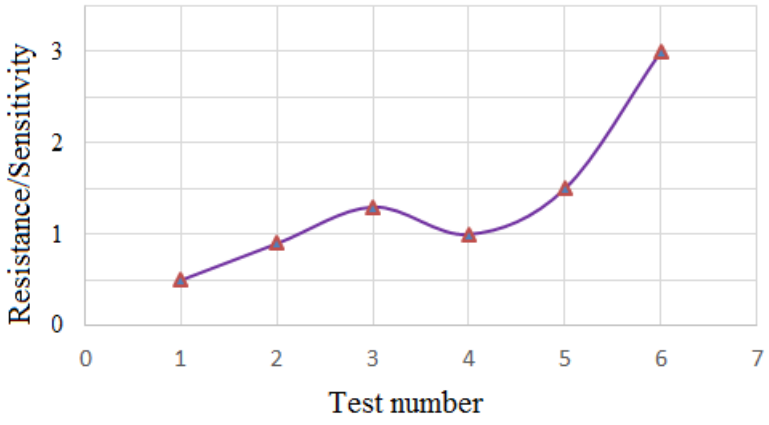


Figure 4.21: Sensitivity variation with gas concentration.

4.2.4 Applications

Bone Implants. The titanium-nickel coatings with near equi-atomic composition could be used as functional materials in many engineering applications such as active, adaptive or smart structures, as well as biomedical applications

such as dental repair (Tria et al., 2009; Tria et al., 2011; Huan et al., 2013). Similarly, the magnesium based alloys such as the magnesium-titanium were identified as potential implant materials because of their excellent mechanical properties such as high strength-to-density ratio and low elastic modulus. In addition, magnesium is an essential component of the enzyme system in humans, and so it is a degradable biomaterial that can be used in medical implants (Tsai et al., 2011).

Antimicrobial Surfaces. Metal coatings made from the aluminium-alumina-copper and aluminium-alumina-zinc powder mixtures can kill bacterial species such as Escherichia coli $O157$, Staphylococcus aureus, and many others. This could prevent the spread of water borne diseases such as kidney failure, skin infections, fever, diarrhea, to mention a few, and ultimately save human life (Mathews et al., 2018; Varkey, 2010; Geoprincy et al., 2012).

Gas Sensors. The tin-oxide powder may be mixed with copper to improve its electric conductivity and adhesion to the substrate during cold spray. The coating fabricated from this powder mixture could be used as gas sensing layer for monitoring pollutant gases such as hydrogen sulphide commonly found in areas of oil and gas commercial-scale extraction and processing (Rumyantseva et al., 1996; Ghimbeu et al., 2008).

In summary, the powder mixtures presented in this study were easily deposited using the LP-CS system, implying that the particles in these powders were less strain hardened compared to those reported in literature (Tria et al., 2009). In addition, these powder mixtures produced coatings with improved properties such as microhardness and, where possible, produced improved porosity of the coating. Finally, the results obtained in section 4.2 proved hypothesis 2 that the CS process could be used to fabricate porous structures when feedstock powders of different mixtures are used.

4.3 Porous Structures through CS and Alloy-De-Alloy

4.3.1 Feedstock Powders

The feedstock powders used in this strategy were the copper, aluminium-alumina and aluminium-alumina-copper mixtures whose morphologies are described in 4.1 and 4.2.

4.3.2 Coatings from CS and Alloy-De-Alloy

The first structure fabricated using this strategy was the antimicrobial surface shown in Figure 4.22. As seen in Figure 4.22 (a), the pores were arranged in a lotus manner (Hamweendo and Botef, 2015). The porosity of this structure was 24.7 % and all the active elements such as the copper, aluminium, and alumina were exposed as shown in the FESEM image of Figure 4.22 (b). The anti-microbial capabilities of these elements were demonstrated in the previous studies (Varkey, 2010; Geoprincy et al., 2012).

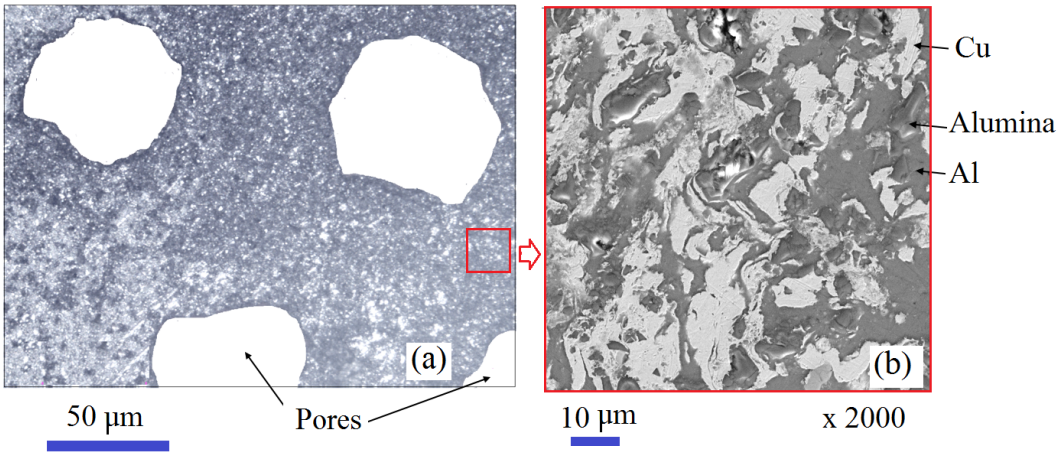


Figure 4.22: Antimicrobial filters.
(a) Pore array (b) FESEM image.

The second structure fabricated from this strategy shown in Figure 4.23 (a) comprised the microchannels with trapezoidal shapes. The porosity of this structure was 40.0 % that is equivalent to that of the sintered porous copper

micro heat sink reported in the literature (Singh et al., 2009). Also, Figure 4.23 (b) shows the aluminium-alumina micro-ridge embedded in the copper matrix that was later de-alloyed and so created the microchannel structures.

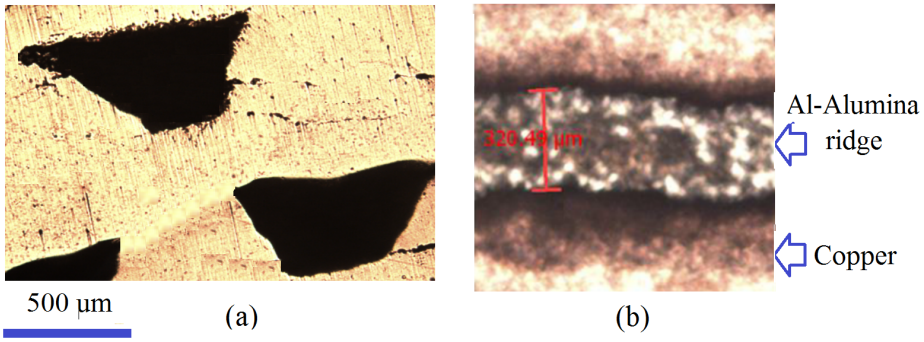


Figure 4.23: Microchannels.
(a) Microchannels (b) Al-Alumina-copper before de-alloy.

The geometric dimensions for these microchannels are summarised in Table 4.4 and indicated in Figure 4.24 (a). Then, Figure 4.24 (b) shows the model of the micro heat sink simulated using these dimensions. In this model, the number of layers for the microchannels was three because previous studies proved that a micro heat sink with three layers of microchannels has the lowest thermal resistance (Wei and Joshi, 2003).

Table 4.4: Geometric dimensions for microchannels.

Dimension	a	b	c	d	e	W^*	S	t
μm	443	1091	459	436	300	1741	543	2708

4.3.3 Analysis and Discussion

Based on the above results, the pores in the antimicrobial structure could be used to make a structures that is permeable to fluids and with active elements that could increase their capability to kill a wide range of bacteria during filtration process as explained in Appendix E. In the case of the microchannels, the calculated mean hydraulic diameter was 336 μm. This diameter falls within the limits of 100 μm and 500 μm recommended for high performance of the micro heat sinks (Bowers and Mudawar, 1994; Gautam et al., 2011). Then,

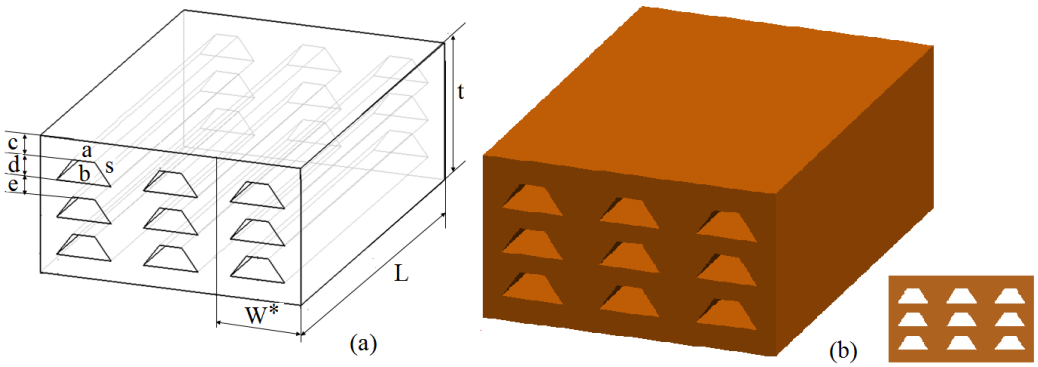


Figure 4.24: Microchannels dimension and model.
Microchannels: (a) dimension (b) model

the analysis of the temperature distribution at the junction and top surface of the micro heat sink was carried out using simulated heat flux that was varied between 100 W/cm^2 and 500 W/cm^2. During simulation, this heat flux was assumed to be applied at the base of the micro heat sink and the results are shown in Table 4.5 and Figure 4.25.

Table 4.5: Simulation temperature distribution for micro heat sink.

Heat flux	100	200	300	400	500
Junction Temperature	22	22	25	27	28
Surface Temperature	20	20	20	20	20

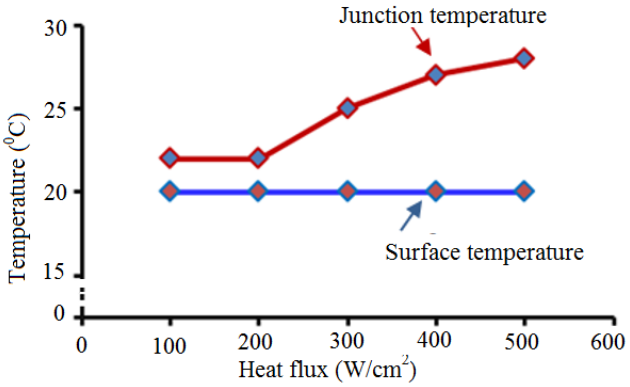


Figure 4.25: Graph of temperature Vs. heat flux.

The results in the above table and graph show that the temperature at the top surface of the micro heat sink remained practically equal to the ambient temperature. Also, the temperature at the junction between the micro heat

sink and the heat source increased marginally to 28°C. This temperature is below the lower minimum of 55°C recommended for the Intel microprocessor currently in use (Mihai, 2011). These results demonstrated that the micro heat sink with trapezoidal shaped microchannels has superior cooling capability. The results are in agreement with the observation made in literature (Gautam et al., 2011; Han et al., 2013; Hamweendo et al., 2014a). Then, Figure 4.26 shows the simulated temperature profile of the micro heat sink when the heat flux of 500 W/cm^2 was applied. According to this figure, the micro heat sink attained an ambient cooling between the first and second layer of the microchannels. Therefore, the third layer of the microchannels may not be necessary.

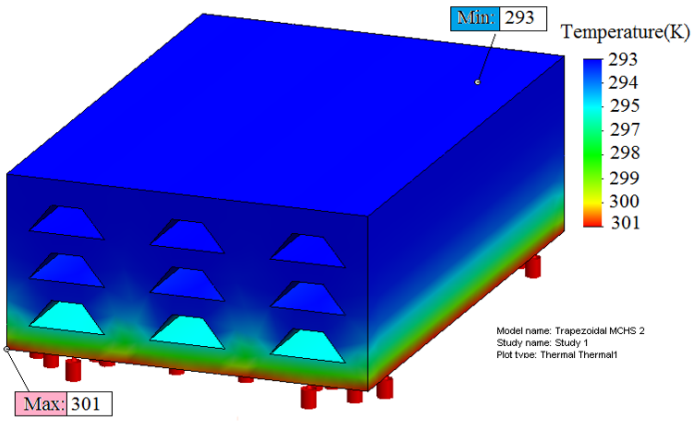


Figure 4.26: Simulated temperature profile for micro heat sink.

Further, the thermal-mechanical test was carried out to analyse the strength of the microchannels. The results of this test shown in Figure 4.27 indicate that the maximum stress induced in the microchannel by 1 bar of fluid pressure was 0.236 MPa. This stress is below the bonding strength of 23.7 MPa reported in Table 4.1 achieved from the copper powder mixed with 20 % chromium sprayed under conditions specified in Table N.6. The calculated factor of safety for this stress was approximately equal to 100.4. This implies that the microchannels fabricated from copper powder mixed with 20 % chromium can withstand maximum pressure of 1 bar when the state-of-the-art micro-pump is used to circulate the cooling fluid inside it.

Furthermore, to compare the above thermal results for the microchannels, thermal-hydraulic performance evaluation of the simulated micro heat sink was carried as explained in Appendix O. In this evaluation, nanofluids made of the

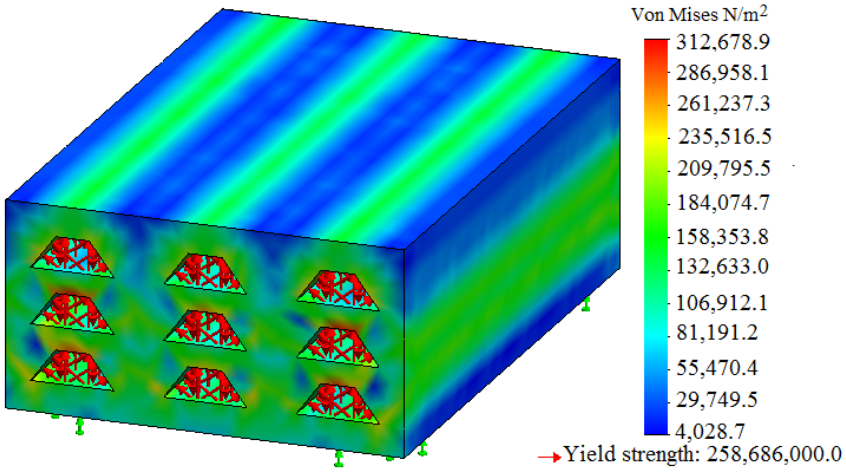


Figure 4.27: Simulated stress profile for micro heat sink.

de-ionised water mixed with 1 % to 5 % by volume of the alumina or copper nanoparticles were assumed to be the cooling fluids. The thermal-physical and thermal resistance data were calculated using the developed empirical equation (4.4).

$$R_{th.} = 0.03137 + Ck_{eff} + D \tag{4.4}$$

Where C and D are given by equation (4.5) and (4.6)

$$C = \frac{113.9949.10^{-6}}{3.1600 + 0.0230Re} \tag{4.5}$$

$$\frac{8.4818}{\mu_{eff} ReC_{pnf}} \tag{4.6}$$

where the effective thermal conductivity of the nanofluid is K_{eff}, the effective dynamic viscosity of the nanofluid is μ_{eff}, and the specific heat capacity of nanofluid is C_{pnf}. The calculated thermal-physical and thermal resistance data were recorded as shown in Figure O.2 and Figure O.3. When plotted, these data produced graphs that were like the one shown in Figure 4.28. The complete graphs plotted using these data are shown in Figure O.4 and Figure O.5.

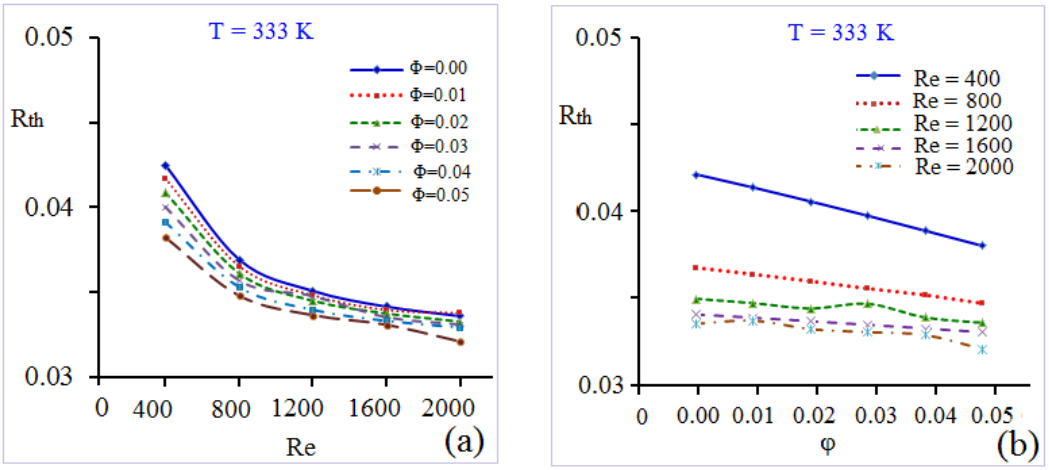


Figure 4.28: Thermal resistance graphs.
Variation with: (a) Re, (b) volume of nanoparticles.

As shown in these graphs, the thermal resistance (R_{th}) of the micro heat sink was reduced when the Reynolds number (Re) and volume fraction of the nanoparticles (φ) were increased. Accordingly, the lowest value of the of the thermal resistance for the water-alumina nanofluid cooling was approximately 0.035 K/W. This value was obtained from Figure O.4 and was lower than the 0.084 K/W reported in the literature (Hung et al., 2012). The thermal resistance value obtained from the graphs of the water-copper nanofluid cooling in Figure O.5 was 0.05 K/W. These results showed that the microchannels could achieve highest cooling capability using water-alumina nanofluids (Ansari et al., 2010; Hung et al., 2012).

Further, Figure 4.28 (a) shows that the decrease of the thermal resistance is limited as the Reynolds number approaches 1200. Therefore, the action of pumping the fluid to increase its speed and Reynolds number beyond 1200 is not beneficial as there is no decrease of the thermal resistance. Moreover, when the Reynolds number is beyond 1200, the flow of the fluid might be turbulent and may reduce the heat removal capability depending on the roughness of the inner walls of the microchannels (Zhang et al., 2014).

In summary, it can be noted that the integration of CS with the alloy-de-alloy process can fabricate new porous structures to be used, for example, as antimicrobial filters and microchannels for micro heat sink. These microchannels are competitive to those made by other technologies mentioned in Appendix

H. Consequently, the results in this section (4.3) proved the hypothesis 3 that the CS process could fabricate porous structures with controlled porosity using the alloy-de-alloy method.

4.3.4 Applications of the Coatings

Cooling of Electronics. The microchannels with trapezoidal shapes made by the CS process and alloy-de-alloy proved to have the lowest thermal resistance. This imply that the micro heat sinks integrated with these microchannels could be applicable in the cooling of the high speed microprocessors (Gautam et al., 2011; Thakre et al., 2014; Xia et al., 2015). The other possible application of these microchannels could be in the fuel cells, microfluidic devices, and drug delivery systems (Yole-Development, 2010).

Antimicrobial Filters. The structure with lotus pores fabricated from mixtures of the aluminium-alumina-copper powders are believed to have increased surface area to volume ratio, greater fluid permeability and capability to kill a wide range of bacteria. Therefore, this structure could be applied in the antimicrobial filtration of contaminated water for rural communities where water reticulation facilities are scarce due to lack of capital and technological know-how (Varkey, 2010; Sanpo et al., 2009; Zang et al., 2013).

4.4 Conclusions

This chapter presented the results for porous structures fabricated and tested according to the methods summarised in Chapter 3. Based on the analysis and discussions of these results, it was proved that all three hypotheses were true and so, the CS technology could be practically and efficiently used in the fabrication of porous materials. This conclusion and their practical implications are illustrated in Figure 4.29. Finally, the conclusions about the research aims, question and hypotheses are presented in Chapter 5.

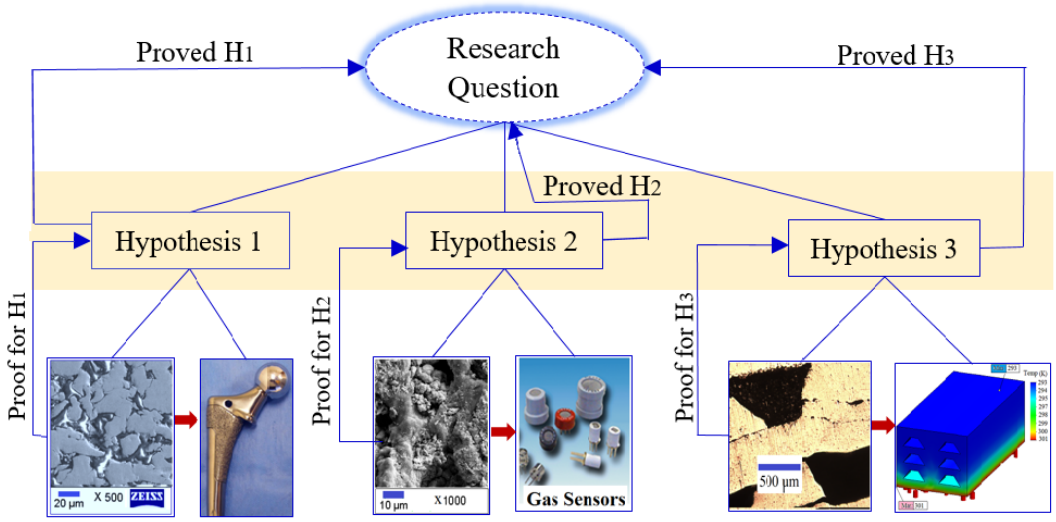


Figure 4.29: Proofs for hypotheses.

5 CONCLUSION

5.1 Introduction

This thesis was organised in five chapters which were structured, unified and focused to answer the research question. Chapter 1 introduced the background to the research problem and the path taken to reach the research objectives. Chapter 2 identified, from literature, the areas of controversy that required to be clarified. Then, Chapter 3 presented the methodologies used to provide data to answer the research question. In Chapter 4, these data were discussed to demonstrate their significance to the research question. Finally, Chapter 5 presents the summary of the previous chapters, followed by conclusions about the hypotheses and research question, contributions of the research to knowledge, and its implications for theory and practice. Also, Chapter 5 presents the research limitations and makes suggestions for further research. Figure 5.1 presents the organization of this Chapter.

5.2 A Brief Overview of Previous Chapters

This thesis aimed to address the following research question:

Could the CS technology be practically and efficiently used in the fabrication of porous materials?

To find the answer to the research question, Chapter 2 described the porous structures and identified their main attributes such as the architecture, size,

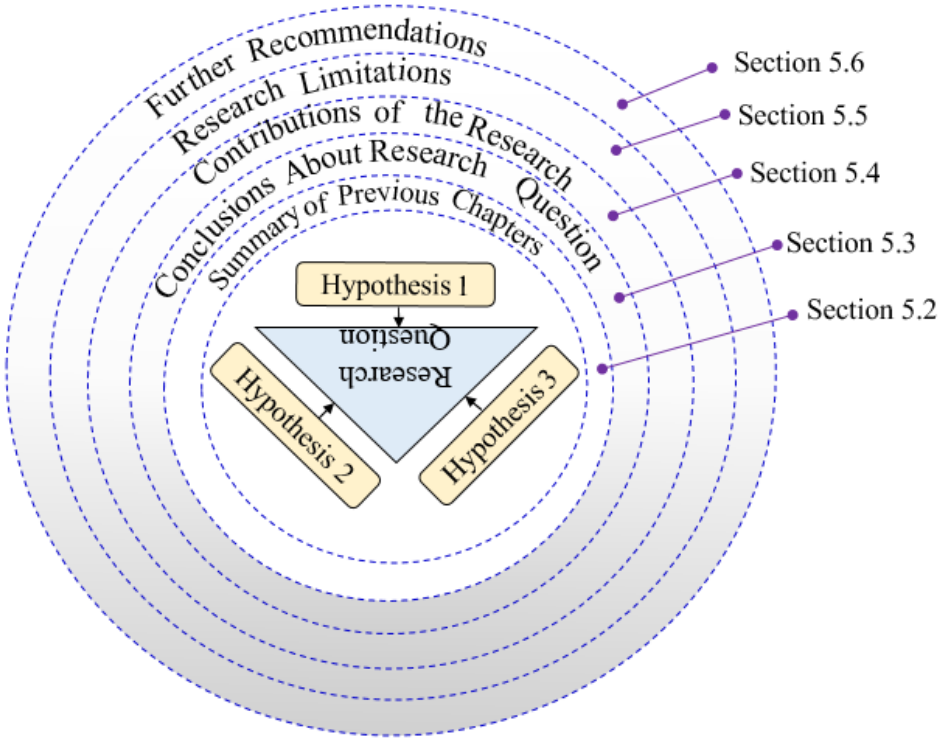


Figure 5.1: Chapter 5's map.

origin of pores, and material used to make the porous structures. These attributes were established to have significant influence on the properties of the porous structures, and so, were used to classify the porous structures. Thereafter, the chapter identified several areas of application for porous structures such as cooling of electronics, medical, and gas sensors, to mention a few. Also, the chapter highlighted the limitations of the current methods used for manufacturing of porous structures and the need for development of a new, efficiency and cost effectiveness method. In this context, the CS process was proposed as a new method for manufacturing of porous structures. However, studies on CS process did not give enough indications on its capability to produce porous structure.

Consequently, Chapter 3 presented the proposed methods for fabrication of porous structures using CS process and their characterisation. Also, the Chapter built the following hypotheses to prove these methods:

Hypothesis 1: CS process could be used to fabricate porous structures through controlling the spray parameters.

Hypothesis 2: CS process could fabricate porous structures when feedstock powders of different mixtures are used.

Hypothesis 3: The CS process could fabricate porous structures with controlled porosity using the method such as alloy-de-alloy.

To answer the above hypotheses, theoretical and experimental studies were conducted and, based on the results, the conclusions were drawn as illustrated in hypotheses loop shown in Figure 5.2.

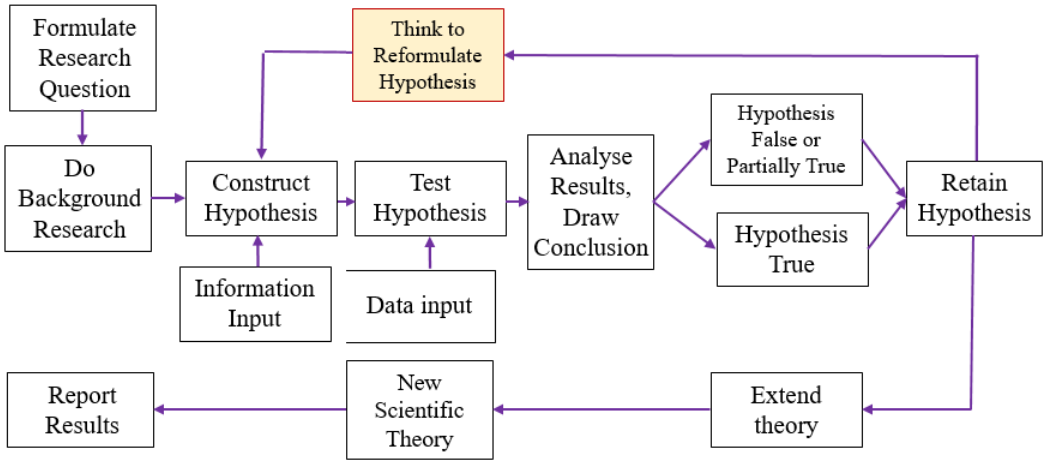


Figure 5.2: Hypotheses loop.

To prove Hypothesis 1, the CS process parameters were varied for a number of selected coatings. These variations proved that the coatings fabricated using aluminium, copper, and zinc powders achieved minimum variation of porosity of up to a maximum of 1 %. This was due to the fact that the particles in these powders were ductile and bonded by interlocking and so, no limited contact was unattainable (Irissou et al., 2007; Legoux et al., 2007; Lubrick et al., 2008). On the other hand, the coatings fabricated using the titanium powder had varied porosity of between 2.8 % and 31.5 %. This variation occurred because titanium particles are reactive and bonded by limited particle contact and interlock that resulted in the inter-particle voids (Cinca et al., 2010; Moy et al., 2010; Dewar et al., 2012). Based on these results, it was concluded that:

CS process could be used to fabricate porous structures through control of spray parameters and the amount of porosity achieved in

the coatings not only depend on the variation of the spray parameters and morphology of the powders, but also on the type of the feedstock powders.

To prove Hypothesis 2, a selected number of soft and hard powders were mixed and then used to fabricate CS coatings. The characterisation of these coatings suggested that there was a reduction in porosity of the coating due to the soft particles in the powder mixtures that deformed more than the hard ones and the fact that the splats from soft particles occupied the voids. This suggested that powders mixtures whose particles had different characteristics had greater tendency to produce dense coatings as reported in literature (Koivuluoto et al., 2009). Based on these results, it was concluded that:

CS process could be used to fabricate structures with controlled porosity when mixtures of different powders are used as feedstock.

To prove Hypothesis 3, a selected number of powders were alternately cold sprayed, then de-alloyed using common acids. Then the coatings were characterised and tested as highlighted in Chapter 4. This process produced microchannels and the structures with lotus pores. The porosity of the microchannels was 40 % and that of the lotus structure was 26.5 %. Based on these results, it was concluded that:

The CS process could fabricate porous structures with controlled porosity using the method such as alloy-de-alloy.

5.3 Conclusions About the Research Question

The purpose of this research was to demonstrate whether the CS technology could be practically and efficiently used in the fabrication of porous materials. To answer the research question, a number of hypotheses were constructed and proved as it was shown above. Based on these results, it was concluded that:

The CS technology can be practically and efficiently used in the fabrication porous structures.

5.4 Contributions of the Research

The contribution and implications of this research could be divided into theoretical and practical aspects.

The implications for theory include:

- a unitary approach of manufacturing porous structures using CS process (see Chapter 3),
- a new method to fabricate microchannels with trapezoidal shape possible to be used in micro heat sink for cooling of electronic components (see section 3.3.3); in this respect, the patent number PCT/IB2015/058721 was issued in 2016,
- a new method to agglomerate the tin-oxide nanoparticles with copper suitable for CS process (see Appendix J.2),
- a new approach for deposition of titanium-nickel, tin-oxide-copper, and magnesium-titanium powder mixtures using CS process (see Chapter 3),
- a new empirical mathematical model for predicting spray parameters and porosity of titanium coatings fabricated by the CS process (see Appendix O.3), and
- the introduction into the CS process theory of the Central Composite Design of Experiments in determination of CS process parameters (Appendix M).

The theoretical and experimental implications of this research for practice may include:

- new method to fabricate micro heat sinks with improved capability that could be applied in the cooling of high speed microprocessors,
- new microchannels with trapezoidal shapes that could be applied in fuel cells, microfluidic devices, and drug delivery systems,

- cost effective gas sensors with high sensitivity for monitoring of pollution, and
- customised porous coated medical implants possible for orthopaedic surgery.

Based on all the above, Figure 5.3 summarises this research contribution to knowledge.

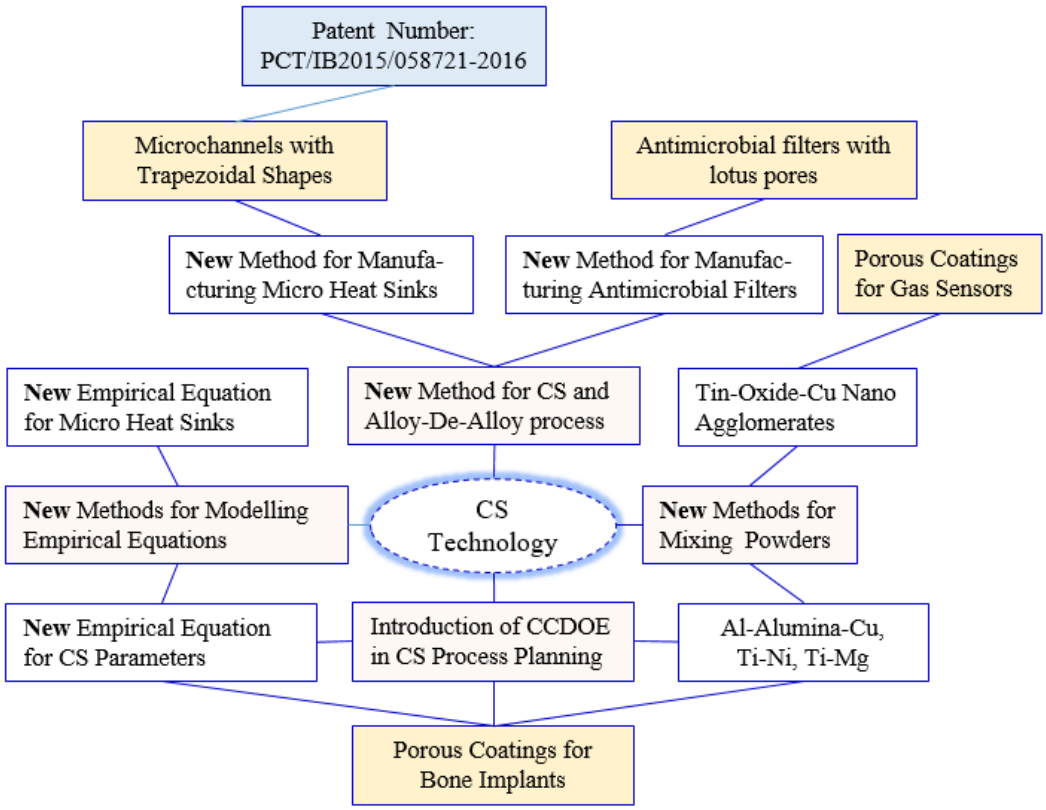


Figure 5.3: Research contributions.

5.5 Research Limitations

Some of the thesis' limitations acknowledged by the author that do not detract the significance of the report findings, refer to the following:

- the experiments used a limited range of CS process parameters (such as gas' pressure between 5.5 bars and 17.2 bars, and gas' temperature between 20 °C and 550 °C) due to the limitations of the CS equipment.

- the need to demonstrate the fabrication processes developed above and the associated products in their actual areas of applications.
- the coatings were evaluated only for porosity, microhardness and, where necessary, the thermal performance; consequently, the coatings were not tested for their bonding with the substrates.
- only limited feedstock powders were used,
- no physical final product was made to practically test various possible applications.

5.6 Further Recommendations and Suggestions

Further research may include:

- theoretical and experimental studies of a micro heat sink for their thermal-mechanical and thermal-hydraulic performance when the de-ionised water and nanofluids are used as cooling liquids,
- theoretical, experimental, and wet and dry medical studies of the antimicrobial surfaces produce via CS process, and
- extension of the modeling of titanium CS process parameters to other materials such as aluminium, copper, zinc, and nickel, and so, develop an empirical model for the manufacturing of porous structures.

REFERENCES

Ackermann, S., Scheffe, J. R., Duss, J. and Steinfeld, A. (2014). Morphological characterization and effective thermal conductivity of dual-scale reticulated porous structures, *Research 7*, Department of Mechanical and Process Engineering, Switzerland. Materials.

Adebiyi, D., Popoola, A. and Botef, I. (2016). Low pressure cold spray coating of Ti-6Al-4V with SiC-based cermet, *Materials Letters* **175**: 63–67.

Adham, A. M., Mohd-Ghazali, N. and Ahmad, R. (2012). Optimization of an ammonia-cooled rectangular microchannel heat sink using multi-objective non-dominated sorting genetic algorithm (nsga2), *Heat and Mass Transfer* **48**(10): 1723–1733.

Adham, A. M., Mohd-Ghazali, N. and Ahmad, R. (2013). Thermal and hydrodynamic analysis of microchannel heat sinks. a review, *Renewable and Sustainable Energy Reviews* **21**: 614–622.

Adham, A., Mohd-Ghazali, N. and Ahmad, R. (2015). Performance optimization of a microchannel heat sink using the improved strength pareto evolutionary algorithm (spea2), *Journal of Engineering Thermophysics* **24**(1): 86–100.

Advance-Coatings (2015). Activitites-Themal Spraying-Principles, *Strategic Research Program*, AMTB GIE Economic Iinterest Group, Rue de l'Avouerie 7, Belgium.

Aghaei, A., Sheikhzadeh, G., Dastmalchi, M. and Forozande, H. (2015). Numerical investigation of turbulent forced-convective heat transfer of Al2O3 -water nanofluid with variable properties in tube, *Shams Engineering Journal* **6**(2): 577–585.

Al-Shabib, W., Habibi, D., Zonghan, X. and Xiaoli, Z. (2012). Identifying smart conducting materials for wi-fi electromagnetic interference shielding, *Electromagnetic Compatibility (APEMC) 2012 Asia-Pacific Symposium on*, pp. 741–744.

Alkhimov, A., Kosarev, V. and Klinkov, S. (2001). The features of cold spray nozzle design, *Journal of Thermal Spray Technology* **10**: 375–381.

Anderson, J. D. (1982). *Fundamentals of Aerodynamics*, McGraw-Hill, United States of America.

Ansari, D., Husain, A. and Kim, K.-Y. (2010). Multiobjective optimization of a grooved micro-channel heat sink, *IEEE TRANSACTIONS ON COMPONENTS AND PACKAGING TECHNOLOGIES* **33**(4): 767–776.

Arai, M. and Suidzu, T. (2013). Porous ceramic coating for transpiration cooling of gas turbine blade, *Journal of Thermal Spray Technology* **22**(5): 690–698.

Arakawa, Y., Kobashi, M. and Kanetake, N. (2012). Effect of elemental powder size on foaming behavior of NiTi alloy made by combustion synthesis, *Research 5*, Graduate School of Engineering, Nagoya University, Nagoya, Japan. Materials.

Arenas, J. P. and Crocker, M. J. (2010). Recent trends in porous sound-absorbing materials, *Materials Reference Issue*, University Austral of Chile, pp. 12–17.

Arjun, R. (2014). Introduction to 3d printing, *Printing New World using 3D Printing*, Kerala, India, pp. 1–27.

Ashby, M. and Medalist, R. E. M. (1983). The mechanical properties of cellular solids, *Metallurgical Transactions A* **14A**: 1755–1769.

Assadi, H., Gartner, F., Stoltenhoff, T. and Kreye, H. (2003). Bonding mechanism in cold gas spraying, *Acta Materialia* **51**(15): 4379–4394.

Assadi, H., Schmidt, T., Richter, H., Kliemann, J., Binder, K., Gartner, F., Klassen, T. and Kreye, H. (2011). On parameter selection in cold spraying, *Journal of Thermal Spray Technology* **20**(6): 1161–1176.

ASTM-International (2012). Standard Test Methods for Tension Testing of Metallic Materials, *E8/E8M-11 1*, American National Standard, Pennsylvania, USA.

Balasubramanian, M., Jayabalan, V. and Balasubramanian, V. (2008). Developing mathematical models to predict grain size and Hardness of Argon Tungsten pulse current arc welded Titanium alloy, *journal of materials processing technology* **196**: 222229.

Bandgar, D., Navale, S., Naushad, M., Mane, R., F.J.Stadler and Patil, V. (2015). Ultra-sensitive polyaniline-iron oxide nanocomposite room temperature flexible ammonia sensor, *Royal Society of Chemistry Advances* **5**: 68964–68971.

Banhart, J. (2001). Manufacture, characterisation and application of cellular metals and metal foams, *Progress in Materials Science* **46**(6): 559–632.

Bari, F. and Morshed, A. (2015). Ultra compact heat exchanger with geometry induced wall jet, *Procedia Engineering* **105**(0): 258–263.

Bartolo, P. (2010). Bio-manufacturing processes for tissue engineering centre for rapid and sustainable product development, *COMA10 International Conference on Competitive Manufacturing Proceedings*, Stellenbosh, South Africa, pp. 89–106.

Bartosiaki, B. G., Pereira, J. A. M., Bielefeldt, W. V. and Vilela, A. C. F. (2015). Assessment of inclusion analysis via manual and automated SEM and total oxygen content of steel, *Journal of Materials Research and Technology* **4**(3): 235–240.

Bereaux, Y., Charmeau, J.-Y. and Balcaen, J. (2010). Optical measurement and numerical simulation of parison formation in blow moulding, *International Journal of Material Forming* **3**(1): 595–598.

Biswas, A. (2005). Porous NiTi by thermal explosion mode of shs:processing, mechanism and generation of single phase microstructure, *Acta Materialia* **53**: 1415–1425.

Bolelli, G., Hulka, I., Koivuluoto, H., Lusvarghi, L., Milanti, A., Niemi, K. and Vuoristo, P. (2014). Properties of wcfecral coatings manufactured by different high velocity thermal spray processes, *Surface and Coatings Technology* **247**(0): 74–89.

Bowers, M. B. and Mudawar, I. (1994). Two phase electronic cooling using minichannel and micro channel heat sinks part 1 design criteria and heat diffusion constraints, *Transactions of the ASME* **116**: 290–297.

Browning, T. R. (2002). Process integration using the design structure matrix, *Systems Engineering* **5**(3): 180–193.

Cadney, S., Brochu, M., Richer, P. and Jodoin, B. (2008). Cold gas dynamic spraying as a method for freeforming and joining materials, *Surface and Coatings Technology* **202**(12): 2801–2806.

Carey, C. and Inderwildi, O. (2009). *Aviation Materials:Review*, Smith School of Enterprise and Environment, University of Oxford, UK.

Casalino, D., Diozzi, F., Sannino, R. and Paonessa, A. (2008). Aircraft noise reduction technologies: A bibliographic review, *Aerospace Science and Technology* **12**(1): 1–17. Aircraft noise reduction.

CenterLine (2010). Portable Spray Machine Spray Manual, *Users' Manual SST-UM-PR-2.0.0-0410*, Supersonic Spray Technology, Windsor, Canada.

Champagne, V. J., Helfritch, D., Leyman, P., Grendahl, S. and Klotz, B. (2005). Interface material mixing formed by the deposition of copper on aluminum by means of the cold spray process, *Journal of Thermal Spray Technology* **14**(3): 330–334.

Champagne, V. K. and Helfritch, D. J. (2013). A demonstration of the antimicrobial effectiveness of various copper surfaces, *Journal of Biological Engineering* **7**(1): 1–6.

Champagne, V. K., Helfritch, D. J., Trexler, M. D. and Gabriel, B. M. (2010). The effect of cold spray impact velocity on deposit hardness, *Modelling and Simulation in Materials Science and Engineering* **18**(6).

Chikarakara, E., Aqida, S., Brabazon, D., Naher, S., Picas, J., Punset, M. and Forn, A. (2010). Surface modification of hvof thermal sprayed wccocr coatings by laser treatment, *International Journal of Material Forming* **3**(1): 801–804.

Chung, D. (2001). Electromagnetic interference shielding effectiveness of carbon materials, *Composite Materials Research Laboratory* **39**: 279285.

Cicek, K. and Celik, M. (2009). Selection of porous materials in marine system design.the case of heat exchanger aboard ships, *Materials and Design* **30**(10): 4260–4266.

Cinca, N., Barbosa, M., Dosta, S. and Guilemany, J. (2010). Study of Ti deposition onto Al alloy by cold gas spraying, *Surface and Coatings Technology* **205**(4): 1096 – 1102.

Corcione, M. (2011). Empirical correlating equations for predicting the effective thermal conductivity and dynamic viscosity of nanofluids, *Energy Conversion and Management* **52**(1): 789–793.

Cordeiro, J. M. and Barao, V. A. (2017). Is there scientific evidence favoring the substitution of commercially pure titanium with titanium alloys for the manufacture of dental implants?, *Materials Science and Engineering C* **71**: 1201–1215.

Cormier, Y., Dupuis, P., Jodoin, B. and Corbeil, A. (2013). Net shape fins for compact heat exchanger produced by cold spray, *Journal of Thermal Spray Technology* **22**(7): 1210–1221.

Cunha, C. A. d., Lima, N. B. d., Martinelli, J. R., Bressiani, A. H. d. A., Padial, A. G. F. and Ramanathan, L. V. (2008). Microstructure and mechanical properties of thermal sprayed nanostructured cr3c2-ni20cr coatings, *Materials Research* **11**: 137–143.

Demirel, M. and Kayan, B. (2012). Application of response surface methodology and central composite design for the optimization of textile dye degradation by wet air oxidation, *International Journal of Industrial Chemistry* **3**(1): 1–10.

Dewar, M., McDonald, A. and Gerlich, A. (2012). Interfacial heating during low-pressure cold-gas dynamic spraying of aluminum coatings, *Journal of Materials Science* **47**(1): 184–198.

Diedericks, G. and du Plessis, J. (1996). Electrical conduction and formation factor in isotropic porous media, *Advances in Water Resources* **19**(4): 225–239.

Dimitrov, D., Bezuidenhout, M. and Marcantonio, G. (2013). Advances in customized medical prostheses through additive manufacturing with an

emphasis on hip replacement and cervical implants, *COMA13 International Conference on Competitive Manufacturing Proceedings*, Stellenbosh, South Africa, pp. 1–6.

Dingal, S., Pradhan, T., Sundar, J., Choudhury, A. and Roy, S. (2008). The application of taguchis method in the experimental investigation of the laser sintering process, *The International Journal of Advanced Manufacturing Technology* **38**(9-10): 904–914.

Durrani, S. (2006). The inuence of electrode metals and its conguration on the response of tin oxide thin lm co sensor, *Sensors and Actuators B, Chemical* **68**: 1732–1735.

Dykhuizen, T. and Smith, M. (1998). Gas dynamic principles of cold spray, *Journal of Thermal Spray Technology* **7**: 205–212.

Edelman, F., Hahn, H., Seifried, S., Alof, C., Hoche, H., Balogh, A., Werner, P., Zakrzewska, K., Radecka, M., Pasierb, P., Chack, A., Mikhelashvili, V. and Eisenstein, G. (2000). Structural evolution of sno2 tio2 nanocrystalline films for gas sensors, *Materials Science and Engineering B* **69-70**(0): 386–391.

Edwards, J., B.Brunski, J. and Higuchi, H. W. (1997). Mechanical and morphologic investigation of the tensile strength of a bonehydroxyapatite interface, *Journal of Biomedical Materials Research* **36**(4): 454–468.

Elahinia, M. H., Hashemi, M., Tabesh, M. and Bhaduri, S. B. (2012). Manufacturing and processing of NiTi implants: A review, *Progress in Materials Science* **57**: 911–946.

Fukamuna, H. and Huang, R. (2009). Development of high temperature gas heater in the cold spray coating syatem, *Proceedings of International Thermal Spray Conference:2009*, ASM, Las Vegas,Nevada,USA, pp. 267–272.

Fukanuma, H., Ohno, N., Sun, B. and Huang, R. (2006). In-flight particle velocity measurements with dpv-2000 in cold spray, *Surface and Coatings Technology* **201**: 1935–941.

Fukumoto, M., Wada, H., Tanabe, K., Yamada, M., Yamaguchi, E., Niwa, A., Sugimoto, M. and Izawa, M. (2007). Effect of substrate temperature on

deposition behavior of copper particles on substrate surfaces in the cold spray process, *Journal of Thermal Spray Technology* **16**(5-6): 643–650.

Galdikas, A., Jasutis, V., Kaciulis, S., Mattogno, G., Mironas, A., Olevano, V., Senuliene, D. and Setkus, A. (1997). Peculiarities of surface doping with Cu in SnO2 thin film gas sensors, *Sensors and Actuators B Chemical* **43**(13): 140–146.

Gartner, F., Schmidt, T., Stoltenhoff, T. and Kreye, H. (2006). Recent developments and potential applications of cold spraying, *Advanced Engineering Materials* **8**(7): 611–618.

Gartner, F., Stoltenhoff, T., Voyer, J., Kreye, H., Riekehr, S. and M (2006). Mechanical properties of cold-sprayed and thermally sprayed copper coatings, *Surface and Coatings Technology* **200**(24): 6770–6782.

Gautam, R., Sharma, A. and Gupta, K. (2011). Performance analysis of non-circular microchannels flooded with cuo-water nanofluid, *3rd Micro and Nano Flows Conference*, Thessaloniki, Greece, pp. 1–8.

Geoprincy, G., Gandhi, N. N. and S.Renganathan (2012). Novel antibacterial effects of alumina nanoparticles on bacillus cereus and bacillus subtilis in comparison with antibiotics, *International Journal of Pharmacy and Pharmaceutical Sciences* **4**(6): 544–548.

Ghelichi, R. and Guagliano, M. (2009). Coating by the Cold Spray Process a state of the art, *Frattura ed Integrita Strutturale* **8**: 30–44.

Ghimbeu, C. M., Schoonman, J. and Lumbreras, M. (2008). Porous indium oxide thin films deposited by electrostatic spray deposition technique, *Ceramics International* **34**(1): 95 – 100.

Glimcher, M. J. (2006). Bone, nature of the calcium phosphate crystals and cellular, structural, and physical chemical mechanisms in their formation, *Reviews in Mineralogy and Geochemistry* **64**(1): 223–282.

Gottlieb, E., Qian, H. and Jin, R. (2013). Atomic-level alloying and de-alloying in doped gold nanoparticles, *Chemistry European Journal* **19**: 4238–4243.

Goyal, T., R.S.Walia and Sidhu, T. (2013). Multi-response optimization of low-pressure cold-sprayed coatings through taguchi method and utility

concept, *The International Journal of Advanced Manufacturing Technology* **64**(5–8): 903–914.

Goyal, T., Walia, R. S. and Sidhu, T. S. (2012). Effect of parameters on coating density for cold spray process, *Materials and Manufacturing Processes* **27**: 193200.

Graf, M., Gurlo, A., Brsan, N., Weimar, U. and Hierlemann, A. (2006). Microfabricated gas sensor systems with sensitive nanocrystalline metal-oxide films, *Journal of Nanoparticle Research* **8**: 823–839.

Gregory, Z. (2006). Fibrous zinc anodes for high power batteries, *Journal of Power Sources* **163**: 591–597.

Grujicic, M., Zhao, C., Tong, C., DeRosset, W. and Helfritch, D. (2004). Analysis of the impact velocity of powder particles in the cold-gas dynamic-spray process, *Materials Science and Engineering A* **368**(12): 222–230.

Gunnasegaran, P., Mohammed, H., Shuaib, N. and Saidur, R. (2010). The effect of geometrical parameters on heat transfer characteristics of microchannels heat sink with different shapes, *International Communications in Heat and Mass Transfer* **37**(8): 1078–1086.

Habijan, T., Haberland, C., Meier, H., Frenzel, J., Wittsiepe, J., Wuwer, C., Greulich, C., Schildhauer, T. and Koller, M. (2013). The biocompatibility of dense and porous nickeltitanium produced by selective laser melting, *Materials Science and Engineering C* **33**(1): 419–426.

Hall, A., Cook, D., Neiser, R., Roemer, T. and Hirschfeld, D. (2006). The effect of a simple annealing heat treatment on the mechanical properties of cold-sprayed aluminum, *Journal of Thermal Spray Technology* **15**(2): 233–238.

Hamweendo, A. and Botef, I. (2015). A Novel Process for Fabricating Aluminium Alloy Porous Structure for Possible Application in Antimicrobial Filtration, *Materials Science Forum*, Vol. 828-829, South Africa, pp. 359–365.

Hamweendo, A. and Botef, I. (2016). *Method for Manufacturing an Object with Microchannels-Patent Application Number PCT IB2015 057821*, World Intellectual Property Organization WIPO.

Hamweendo, A., Malama, T. and Botef, I. (2016a). Titanium-Nickel Alloys for Bone Tissue Engineering Application via Cold Spray, *International Conference on Competitive Manufacturing, COMA-16*, Vol. 2016, South Africa, pp. 273–279.

Hamweendo, A., Malama, T. and Botef, I. (2016b). Titanium-nickel Alloys for Bone Tissue Engineering Application via Cold Spray, *International Conference on Competitive Manufacturing COMA16*, Vol. 2016, Stellenbosch, South Africa, pp. 273–279.

Hamweendo, A., Moloisane, L. and Botef, I. (2015). Bio-Mechanical Compatibility Assessment of Titanium-Nickel Alloy Fabricated Using Cold Spray Process, *Materials Science Forum*, Vol. 828-829, South Africa, pp. 351–356.

Hamweendo, A., Popoola, P. A. I. and Botef, I. (2014a). Computational Modelling and Simulation Analysis of Trapezoidal Channelled Micro Heat Sinks Fabricated using Cold Spray Process, *Mathematical Methods in Science and Engineering*, MMCTSC, Athens, Greece, pp. 186–190.

Hamweendo, A., Popoola, P. A. I. and Botef, I. (2014b). Mathematical Model for Predicting Process Parameters in Cold Pray of Porous Ti Coatings, *Mathematical Methods in Science and Engineering*, MMCTSC, Athens, Greece, pp. 225–229.

Han, B., Kang, J.-S., Kim, H.-J., Woo, C.-G. and Kim, Y.-J. (2015). Investigation of antimicrobial activity of grapefruit seed extract and its application to air filters with comparison to propolis and shiitake, *Aerosol and Air Quality Research* **15**: 10351044.

Han, J. Y., Yu, Z. and Zhou, L. (2008). Hydroxyapatite-titania composite bioactivity coating processed by the solgel method, *Biomedical Materials* **3**(4): 1–4.

Han, Y., Lee, Y. J. and Zhang, X. (2013). Trapezoidal Microchannel Heat Sink With Pressure Driven and Electro Osmotic Flows for Microelectronic Cooling., *IEEE TRANSACTIONS ON COMPONENTS, PACKAGING AND MANUFACTURING TECHNOLOGY* **3**(111): 91851–1858.

Hanson, T. and Settles, G. (2003). Particle temperature and velocity effects on the porosity and oxidation of an hvof corrosion-control coating, *Journal of Thermal Spray Technology* **5**: 403–415.

Hardwicke, C. and Lau, Y.-C. (2013). Advances in thermal spray coatings for gas turbines and energy generation, a review, *Journal of Thermal Spray Technology* **22**(5): 564–576.

Harry, G., Vipender, S. N., Nidhi and Arun, L. K. (2013). Proceedings of the 2013 comsol conference in bangalore, *COMSOL Conference Report*, pp. 1–7.

Heaney, D., Gurosik, J. and Binet, C. (2005). Isotropic forming of porous structures via metal injection molding, *Journal of Materials Science* **40**(4): 973–981.

HEAT (2010). Heating and Temperature Control Applications for Powdered Metal Process, *Powdered Metal Process*, Heat Exchange and Transfer Inc., Carnegie, Pennsylvania, USA.

Hemin, J., Zhiming, Y. and Li, L. (2008). Antibacterial properties and corrosion resistance of cu and ag/cu porous materials, *Journal of Biomedical Materials Research Part A* **87A**(1): 33–37.

Hetsroni, G., Gurevich, M. and Rozenblit, R. (2006). Sintered porous medium heat sink for cooling of high-power mini-devices, *International Journal of Heat and Fluid Flow* **27**: 259–266.

Hirsch, J. and Al-Samman, T. (2013). Superior light metals by texture engineering, optimized aluminum and magnesium alloys for automotive applications, *Acta Materialia* **61**(3): 818–843.

Huan, Z., Fratila-Apachitei, L., Apachitei, I. and Duszczyk, J. (2013). Effect of aging treatment on the in vitro nickel release from porous oxide layers on niti, *Applied Surface Science* **274**: 266 – 272.

Huang, R. and Fukanuma, H. (2009). The influence of spray conditions on deposition characteristics of aluminum coatings in cold spraying, *Proceedings of the International Thermal Spray Conference*, Las Vegas, Nevada, United States of America, pp. 279–284.

Hung, T.-C., Yan, W.-M., Wang, X.-D. and Chang, C.-Y. (2012). Heat transfer enhancement in microchannel heat sinks using nanouids, *International Journal of Heat and Mass Transfer* **55**: 2559–2570.

Husain, A. and Kim, K.-Y. (2010). Enhanced multi-objective optimization of a microchannel heat sink through evolutionary algorithm coupled with multiple surrogate models, *Applied Thermal Engineering* **4**(30): 1683–1691.

IMF (2015). Surface technology, *Information site for Surface Treatment Techniques 70*, Institute of Metal Finishing, Birmingham,UK.

Incropera, F., D.P.Dewitt, T.L.Bergman and A.S.Lavine (2006). *Fundamentals of Heat and Mass Transfer*, John Wiley and Sons.

Intelligence, A.-M. (2014). Global biomedical metal market, *Market Report*, Ratingen, Germany, pp. 1–11.

Irissou, E., Legoux, J.-G., Anatoly, Ryabinin, Jodoin, B. and Moreau, C. (2008). Review on cold spray process and technology: Part i - intellectual property, *Journal of Thermal Spray Technology* **17**: 495516.

Irissou, E., Legoux, J.-G., Arsenault, B. and Moreau, C. (2007). Investigation of Al-Al2O3 Cold Spray Coating Formation and Properties, *Journal of Thermal Spray Technology* **16**: 661–668.

Ismail, M. H., Goodall, R., Davies, H. A. and Todd, I. (2012). Formation of microporous niti by transient liquid phase sintering of elemental powders, *Materials Science and Engineering C* **32**(6): 1480–1485.

Jardini, A. L., Larosa, M. A., de Carvalho Zavaglia, C. A., Bernardes, L. F., Lambert, C. S., Kharmandayan, P., Calderoni, D. and Filho, R. M. (2014). Customised titanium implant fabricated in additive manufacturing for craniomaxillofacial surgery, *Virtual and Physical Prototyping* **9**(2): 115–125.

Jiang, H., Meng, L., Chen, R., Jin, W., Xing, W. and Xu, N. (2013). Progress on porous ceramic membrane reactors for heterogeneous catalysis over ultrafine and nano-sized catalysts, *Chinese Journal of Chemical Engineering* **21**(2): 205 – 215.

Jo, H., Cho, Y.-H., Choi, M., Cho, J., Um, J., Sung, Y.-E. and Choe, H. (2014). Novel method of powder-based processing of copper nanofoams

for their potential use in energy applications, *Materials Chemistry and Physics* **145**(1): 6–11.

Julbe, A., Farrusseng, D. and Guizard, C. (2001). Porous ceramic membranes for catalytic reactors overview and new ideas, *Journal of Membrane Science* **181**(1): 3–20.

Julio, V. (2010). Current and future applications of cold spray technology, *Organic finishing 37*, Centerline Windsor, Ltd., Windsor, Ontario, Canada.

Julio, V. (2014). Considering Cold Spray for Additive Manufacturing, *Advanced materials and processes*, Centerline Windsor, Ltd., Windsor, Ontario, Canada.

Kaladhar, M., Subbaiah, K. V., Rao, C. S. and Rao, K. N. (2011). Application of Taguchi Approach and Utility Concept in solving the Multi-objective Problem when turning AISI 202 Austenitic Stainless steel, *Journal of Engineering Science and Technology Review* **4**(1): 55–61.

Kandlikar, S. and Upadhye, H. (2005). Extending the heat flux limit with enhanced microchannels in direct single-phase cooling of computer chips, *Semiconductor Thermal Measurement and Management Symposium, 2005 IEEE Twenty First Annual IEEE*, pp. 8–15.

Kaneko, K. (1994). Determination of pore size and pore size distribution,1.adsorbents and catalysts, *Journal of Membrane Science* **96**(12): 59–89.

Kaplan, S. J., Hayes, W. C., Stone, J. L. and Beaupre, G. S. (1985). Tensile Strength of Bovine Trabecular Bone, *in* S. J. Kaplan (ed.), *Biomechanics*, Vol. 18, Pergamon Press Ltd., Orthopaedic Biomechanics Laboratory USA, pp. 723–729.

Karthikeyan, S., Balasubramanian, V. and Rajendran, R. (2014). Developing empirical relationships to estimate porosity and microhardness of plasma-sprayed {YSZ} coatings, *Ceramics International* **40**(2): 3171–3183.

Katanoda, H., Fukuhara, M. and Iino, N. (2007). Numerical study of combination parameters for particle impact velocity and temperature in cold spray, *Journal of Thermal Spray Technology* **16**(5-6): 627–633.

Keaveny, T. M., Morgan, E. F. and Yeh, O. C. (2004). *Bone Mechanics*, McGraw-Hill, US.

Kikuchi, S., Yoshino, S., Yamada, M., Fukumoto, M. and Okamoto, K. (2013). Microstructures and Thermal Properties of Cold-Sprayed Cu-Cr Composite Coatings, *Journal of Thermal Spray Technology* **22**(6): 926–931.

Kim, T. B., Yue, S., Zhang, Z., Jones, E., Jones, J. R. and Lee, P. D. (2014). Additive manufactured porous titanium structures: Through-process quantification of pore and strut networks, *Journal of Materials Processing Technology* **214**(11): 2706–2715.

King, H. E., Eberle, A. P. R., Walters, C. C., Kliewer, C. E., Ertas, D. and Huynh, C. (2015). Pore architecture and connectivity in gas shale, *Energy and Fuels* **29**(3): 1375–1390.

Klemperer, C. J. and Maharaj, D. (2009). Composite electromagnetic interference shielding materials for aerospace applications, *Composite Structures* **91**(4): 467–472. Sixth International Conference on Composite Science and Technology.

Koivuluoto, H., Coleman, A., Murray, K., Kearns, M. and Vuoristo, P. (2009). High pressure cold sprayed (HPCS) and low pressure cold sprayed (LPCS) coatings prepared from ofhc cu feedstock: Overview from powder characteristics to coating properties, *Journal of Thermal Spray Technology* **5**: 1–11.

Koivuluoto, H., Coleman, A., Murray, K., Kearns, M. and Vuoristo, P. (2012). High pressure cold sprayed (hpcs) and low pressure cold sprayed (lpcs) coatings prepared from ofhc cu feedstock: Overview from powder characteristics to coating properties, *Journal of Thermal Spray Technology* **21**(5): 1065–1075.

Koivuluoto, H., Lagerbom, J., Lahti, M. K. and Vuoristo, P. (2008). Microstructure and Mechanical Properties of Low-Pressure Cold-Sprayed (LPCS) Coatings, *Journal of Thermal Spray Technology* **17**: 721727.

Koivuluoto, H. and Vuoristo, P. (2010). Effect of powder type and composition on structure and mechanical properties of cu + al2o3 coatings prepared by using low-pressure cold spray process, *Journal of Thermal Spray Technology* **19**: 1081–1092.

Korner, C. and Singer, R. (2000). Processing of metal foamschallenges and opportunities, *Advanced Engineering Material* **2**(4): 159–165.

Korotcenkov, G. and Cho, B. (2011). Instability of metal oxide-based conductometric gas sensors and approaches to stability improvement-short survey, *Sensors and Actuators B Chemical* **156**(2): 527–538.

Kovacik, J. (1999). Correlation between Youngs modulus and porosity in porous materials, *JOURNAL OF MATERIALS SCIENCE LETTERS* **18**(1999): 1007–1010.

Krishna, B., Xue, W., Bose, S. and Bandyopadhyay, A. (2008). Engineered porous metals for implants, *JOM* **60**(5): 45–48.

Kumar, S., Kumar, P. and Shan, H. S. (2008). Density Optimization of Slurry of Coating Material Used in the EPC Process Through Taguchi's Parameter Design Approach, *Materials and Manufacturing Processes* **23**(7): 719–725.

Kwon, E. H., Cho, S. H., Han, J. W., Lee, C. H., and Kim, H. J. (n.d.). Particle Behavior in supersonic Flow during the Cold Spray Process, *Metals and Materials International* **11**(5): 377–381.

Lee, H., Shin, H., Lee, S. and Ko, K. (2008). Effect of gas pressure on al coatings by cold gas dynamic spray, *Materials Letters* **52**: 1579–1581.

Lee, J., Shin, S., Kim, H. and Lee, C. (2007a). Effect of gas temperature on critical velocity and deposition characteristics in kinetic spraying, *Applied Surface Science* **253**: 3512–3520.

Lee, J., Shin, S., Kim, H. and Lee, C. (2007b). Effect of gas temperature on critical velocity and deposition characteristics in kinetic spraying, *Applied Surface Science* **253**: 3512–3520.

Lee, M.-W., Park, J.-J., Kim, D.-Y., Yoon, S. S., Kim, H.-Y., James, S. C., Chandra, S. and Coyle, T. (2011). Numerical studies on the effects of stagnation pressure and temperature on supersonic flow characteristics in cold spray applications, *Journal of Thermal Spray Technology* **20**: 1085–1097.

Legoux, J., Irissou, E. and Moreau, C. (2007). Effect of Substrate Temperature on the Formation Mechanism of Cold-Sprayed Aluminum Zinc and Tin Coatings, *Journal of Thermal Spray Technology* **16**: 619626.

Levine, B. and Fabi, D. (2010). Porous metals in orthopedic applications a review, *Porous metals in orthopedic applications A review* **41**(12): 1001–1010.

Levy, A., Sorek, S., Ben-Dor, G. and Skews, B. (1996). Waves propagation in saturated rigid porous media, analytical model and comparison with experimental results, *Fluid Dynamics Research* **17**(2): 49–65.

Li, C.-J., Yang, G.-J. and Li, C.-X. (2013). Development of particle interface bonding in thermal spray coatings: A review, *Journal of Thermal Spray Technology* **22**(2-3): 192–206.

Li, F., Li, J., Xu, G., Liu, G., Kou, H. and Zhou, L. (2015). Fabrication, pore structure and compressive behavior of anisotropic porous titanium for human trabecular bone implant applications, *Journal of the Mechanical Behavior of Biomedical Materials* **46**: 104–114.

Li, M. and Li, D. (2012). Modular decomposition method based on design structure matrix and application, *TELKOMNIKA* **10**(8): 2169–2175.

Li, W.-Y., Li, C.-J. and Liao, H. (2006). Effect of Annealing Treatment on the Microstrcture and Properties of Cold Sprayed Cu Coatings, *Journal of Thermal Spray Technology* **6**: 206–211.

Li, W.-Y., Li, C.-J. and Liao, H. (2010). Significant influence of particle surface oxidation on deposition efficiency interface microstructure and adhesive strength of cold-sprayed copper coatings, *Applied Surface Science* **256**(16): 4953–4958.

Li, W.-Y., Liao, H., Wang, H.-T., Li, C.-J., Zhang, G. and Coddet, C. (2006). Optimal design of a convergent-barrel cold spray nozzle by numerical method, *Applied Surface Science* **253**: 708–713.

Li, Y., Yang, C., Zhao, H., Qu, S., Li, X. and Li, Y. (2014). New Developments of Ti-Based Alloys for Biomedical Applications, *Materials* **7**(3): 1709–1800.

Liang, X. and Weimer, A. W. (2015). An overview of highly porous oxide films with tunable thickness prepared by molecular layer deposition, *Current Opinion in Solid State and Materials Science* **19**(2): 115–125.

Liang, Y., Wu, D. and Fu, R. (2013). Carbon microfibers with hierarchical porous structure from electrospun fiber-like natural biopolymer, *Scientific Reports* **3**: 1–5.

Lioma, D., Sacks, N. and Botef, I. (2015). Cold gas dynamic spraying of WCNi cemented carbide coatings, *International Journal of Refractory Metals and Hard Materials* **49**: 365–373.

Liu, P. and Liang, K. (2001). Review functional materials of porous metals made by p/m, electroplating and some other techniques, *Journal of Materials Science* **36**(21): 5059–5072.

Lu, C. Q. and Zhao, X. S. (2011). Nanoporous materials-an overview, *Nanoporous Materials-Science and Engineering*, University of Queensland, Australia.

Lubrick, M., Maev, R., Severin, F. and Leshchynsky, V. (2008). Youngs modulus of low-pressure cold sprayed composites-an analysis based on a minimum contact area model, *Journal of Materials Science* **43**(14): 4953–4961.

Ludovic, D., Li, H., Bao, L., Francois-Marie, A., Jean-Baptiste, L., Leonora, V., Fenghua, S., Mikel, D. C., D., O. J., Gilbert, E., D., H. P., Stephen, G. and Lingxue, K. (2013). The fabrication and surface functionalization of porous metal frameworks - a review, *Journal of Materials Chemistry A* **1**: 15185–15206.

Luyten, J., Mullens, S. and Thijs, I. (2010). Designing with pores-synthesis and applications, *Materials Technology VITO*, Blegium, pp. 131–142.

Lynch, M., Gu, W., El-Wardany, T., Hsu, A., Viens, D., A.Nardi and Klecka, M. (2013). Design and topology shape structural optimisation for additively manufactured cold sprayed components, *Virtual and Physical Prototyping* **8**(3): 213–231.

Maev, R. and Leshchynsky, V. (2008). *Introduction to Low Pressure Gas Dynamic Spray*, WILEY-VCH.

Magnabosco, I., Ferro, P., Bonollo, F. and Arnberg, L. (2006). An investigation of fusion zone microstructures in electron beam welding of copperstainless steel, *Materials Science and Engineering: A* **424**(12): 163–173.

Martinez-Orozco, R. D., Antano-Lopez, R. and Rodriguez-Gonzalez, V. (2015). Hydrogen-gas sensors based on graphene functionalized palladium nanoparticles, impedance response as a valuable sensor, *New Journal of Chemistry* **39**: 8044—8054.

Mathews, S., Hans, M., Mucklich, F. and Solioz, M. (2018). *Applied and Environmental Microbiology* **79**(8): 2605–2611.

MBE-International (2015). Thermal Spray Services, *Information site for surface treatment techniques*, Thermal Spraying and Surface Engineering Association (TSSEA), Gloucester, UK.

Meng, X., Zhao, J. Z. J., Liang, Y. and Zhng, Y. (2011). Inuence of gas temperature on microstructure and properties of cold spray 304ss coating, *Journalof Material Science Technology* **27**(9): 809–815.

Mihai, I. (2011). *Heat Transfer in Minichannels and Microchannels CPU Cooling Systems, Heat Transfer - Theoretical Analysis, Experimental Investigations and Industrial Systems*, Intech.

Miller, R. G., Freund, J. E. and Johnson, D. E. (1999). *Probability and Statistics for Engineers*, Prentice Hall, India.

Montgomery, D. C. (2005). *Design and Analysis of Experiments*, John Wiley and Sons, US.

Moy, C. K., Cairney, J., Ranzi, G., Jahedi, M. and Ringer, S. P. (2010). Investigating the microstructure and composition of cold gas dynamic spray (CGDS) Ti powder deposited on Al 6063 substrate, *Surface and Coatings Technology* **204**(1): 3739–3749.

Nakajima, H. (2007). Fabrication, properties and application of porous metals with directional pores, *Progress in Materials Science* **52**(7): 1091–1173.

Nakajima, H. (2010). Review on fabrication, properties, and applications of porous metals with directional pores, *Proc. Jpn. Acad.* **86**(B): 884–889.

Nakajima, H., T.Ikeda and Hyun, S. (2004). Fabrication of lotus-type porous metals and their physical properties, *Advanced Engineering Materials* **6**(6): 377–384.

Neise, W. and Enghardt, L. (2003). Technology approach to aero engine noise reduction, *Aerospace Science and Technology* **7**(5): 352–363.

Ning, X.-J., Jang, J.-H. and Kim, H.-J. (2007). The effects of powder properties on in-ight particle velocity and deposition process during low pressure cold spray process, *Surface and Coatings Technology* **253**: 74497455.

Ning, X.-J., Wang, Q.-S., Ma, Z. and Kim, H.-J. (2010). Numerical study of in-flight particle parameters in low-pressure cold spray process, *Journal of Thermal Spray Technology* **19**(6): 1211–1217.

Nishimura, T., Nomura, D., Sakaguchi, S., Nagayoshi, H. and Hayase, S. (2011). Fabrication of electron passes in nano-tio 2 layer by high-velocity oxy-fuel method for dye-sensitized solar cells, *Japanese Journal of Applied Physics* **50**: 1–4.

OConnor, J., Punch, J., Jeffers, N. and Stafford, J. (2014). A dimensional comparison between embedded 3d-printed and silicon microchannels, *Journal of Physics* pp. 1–11.

Pacheco, M. M. (2007). Self-sustained High-temperature Reactions-Initiation, Propagation and Synthesis, *Strategic Research Program*, Netherlands Institute for Metals Research (NIMR), Netherlands.

Pak, B. C. and Cho, Y. I. (1998). Hydrodynamic and heat transfer study of dispersed fluids with submicron metallic oxide particles, *Experimental Heat Transfer* **11**(2): 151–170.

Pan, M., Zeng, D. and Tang, Y. (2009). Feasibility investigations on multi-cutter milling process: A novel fabrication method for microreactors with multiple microchannels, *Journal of Power Sources* **192**: 562–572.

Papyrin, A. (2006). Cold Spray State of the Art and Applications and Applications, *Cold Spray Technology* pp. 1–21.

Parthasarathy, J., Starly, B. and Raman, S. (2011). A design for the additive

manufacture of functionally graded porous structures with tailored mechanical properties for biomedical applications, *Journal of Manufacturing Processes* **13**(2): 160–170.

Pattison, J., Celotto, S., Khan, A. and O'Neill, W. (2008). Standoff distance and bow shock phenomena in the cold spray process, *Surface and Coatings Technology* **202**(8): 1443–1454.

Paun, F., Gasser, S. and Leylekian, L. (2003). Design of materials for noise reduction in aircraft engines -, *Aerospace Science and Technology* **7**(1): 63–72.

Peerawatt, N., Chatchapol, C., Suparerk, S. and Panadda, N. (2011). The effects of thermally sprayed coating thickness on substrate deformation, experimental investigation and finite element analysis, *Journal of Solid Mechanics and Materials Engineering* **5**(1): 1–13.

Pennig, S., Quehl, J. and Rolny, V. (2012). Effects of aircraft cabin noise on passenger comfort, *Taylor and Francis* **55**(5=10): 12521265.

Persheng, L., Bing, Y., Anmin, H., Karming, L. and Shouren, G. (2001). Development in application of porous metals, *Transactions of Nonferrous Metals Society of China* **11**(5): 629–638.

Phani, P. S., Rao, D. S., Joshi, S. and Sundararajan, G. (2007). Effect of Process Parameters and Heat Treatments on Properties of Cold Sprayed Copper Coatings, *Journal of Thermal Spray Technology* **16**(3): 425–434.

Podshivalov, L., Gomes, C. M., Zocca, A., Guenster, J., Bar-Yoseph, P. and Fischer, A. (2013). Design, analysis and additive manufacturing of porous structures for biocompatible micro-scale scaffolds, *Procedia* {*CIRP*} **5**(0): 247–252.

Prakash, S. and Kumar, S. (2014). Fabrication of microchannels: A review, *Journal of Engineering Manufacturing* pp. 1–16.

Qiao-Sheng, P., Luttge, R., Gardeniers, H. J. G. E. and van den Berg, A. (2003). Comparison of capillary zone electrophoresis performance of powder-blasted and hydrogen fluoride-etched microchannels in glass, *Electrophoresis* **24**: 162171.

Qu, W. and Mudawar, I. (2004). Transport phenomena in two-phase microchannel heat sinks, *Journal of Electronic Packaging* **126**(2): 213–224.

Rimoli, M. G., Rabaioli, M. R., Melisi, D., Curcio, A., Mondello, S., Mirabelli, R. and Abignente, E. (2008). Synthetic zeolites as a new tool for drug delivery, *Journal of Biomedical Materials Research Part A* **87A**(1): 156–164.

Rossella, S., de Filippis, F. L. A. C., Domenico, L. A. and Giancarlo, B. (2010). Application of taguchi method for the multi-objective optimization of aluminium foam manufacturing parameters, *International Journal of Material Forming* **3**(1): 1–5.

Rouquerol, J., Avnir, D., Everett, D. H., Fairbridge, C., Haynes, M., Pernicone, N., Ramsay, J., Sing, K. and Unger, K. K. (1994). Guidelines for the characterization of porous solids, *Characterization of Porous Solids III*, Vol. 87, pp. 1–9.

Roy, R., Brown, J. and Gaze, C. (2003). Re-engineering the construction process in the speculative house-building sector, *Construction Management and Economics* **21**(2): 137–146.

Rumyantseva, M., Labeau, M., Senateur, J., Delabouglise, G., Boulova, M. and Gaskov, A. (1996). Influence of copper on sensor properties of tin dioxide films in h2s, *Materials Science and Engineering: B* **41**(2): 228 – 234.

Ryan, G., Pandit, A. and Apatsidis, D. P. (2006). Fabrication methods of porous metals for use in orthopaedic applications, *Biomaterials* **27**(13): 2651–2670.

Sanpo, N., Ang, S. M., Cheang, P. and Khor, K. (2009). Antibacterial property of cold sprayed chitosan cu-al coating, *Journal of Thermal Spray Technology* **18**(4): 600–608.

Sarkisov, L. (2012). Accessible surface area of porous materials: Understanding theoretical limits, *Advanced Materials* **24**(23): 3130–3133.

Schmidt, T., Gartner, F., Assadi, H. and Kreye, H. (2006). Development of a generalized parameter window for cold spray deposition, *Acta Materialia* **54**: 729–742.

Seetharam, S. and Bhatia, S. (2012). Derivation and development of a mathematical model for long bone growth, *Bioengineering Conference (NEBEC), 2012 38th Annual Northeast*, Philadelphia, PA, pp. 329–330.

Shapovalov, V. I. (2002). Prospective manufacture and aircraft applications of cast metal porous materials, *Technical report*, Sandia National Laboratories, USA.

Shilova, O. (2005). Silicate nanosized films prepared by the sol-gel method for use in planar technology for fabricating semiconductor gas sensors, *Glass Physics and Chemistry* **31**(2): 201–218.

Shirpurkar, P. P., Bobde, S., V.V.Patil and Kale, B. (2012). Optimization of Turning Process Parameters by Using Tool Inserts- a Review, *International Journal of Engineering and Innovative Technology (IJEIT)* **2**(6): 216–226.

Sidambe, A. T. (2014). Biocompatibility of advanced manufactured titanium implants a review, *Materials* **7**(12): 8168–8188.

Simon, I., Brsan, N., Bauer, M. and Weimar, U. (2001). Micromachined metal oxide gas sensors opportunities to improve sensor performance, *Sensors and Actuators B: Chemical* **73**(1): 1–26.

Singh, R., Akbarzadeh, A. and Mochizuki, M. (2009). Sintered porous heat sink for cooling of high-powered microprocessors for server applications, *International Journal of Heat and Mass Transfer* **52**(910): 2289–2299.

Soares, P., Nunes, S., Franco, S., Pires, R., Zanetta-Barbosa, D. and Soares, C. (2014). Measurement of elastic modulus and vickers hardness of surrounding bone implant using dynamic microindentation - parameters definition, *Brazilian Dental Journal* **25**: 385390.

Song, M. and Viskanta, R. (1994). Flow characteristics of anisotropic structures constructed with porous layers, *Transport in Porous Media* **15**(2): 151–173.

Song, T., Yan, M. and Qian, M. (2015). A dealloying approach to synthesizing micro-sized porous tin (sn) from immiscible alloy systems for potential lithium-ion battery anode applications, *Journal of Porous Materials* **22**(3): 713–719.

Sorrentino, L., Aurilia, M., D'Auria, M., Davino, D., Mei, P., Visone, C. and Iannace, S. (2013). Mimicking the Anisotropic Behavior of Natural Porous Structures by Controlling the Reinforcing Particles Distribution in Polymeric Foams, *Advances in Science and Technology*, Vol. 84, Trans Tech Publications, Switzerland, pp. 1–6.

Sova, A., Doubenskaia, M., Grigoriev, S. and Smurov, A. O. I. (2013). Parameters of the gas-powder supersonic jet in cold spraying using a mask, *Journal of Thermal Spray Technology* **22**(4): 551–556.

Stocks, M., Bello-Ochende, T. and J.P.Meyer (2014). Maximum thermal conductance for a micro-channel, utilising newtonian and non-newtonian fluid, *Heat and Mass Transfer* **50**(6): 865–875.

Stoltenhoff, T., Kreye, H. and Richter, H. (2002). An analysis of the cold spray process and its coatings, *Journal of Thermal Spray Technology* **11**(4): 542–550.

Su, J., Kapaca, E., Liu, L., Georgieva, V., Wan, W., Sun, J., Valtchev, V., Hovmller, S. and Zou, X. (2014). Structure analysis of zeolites by rotation electron diffraction (red), *Microporous and Mesoporous Materials* **189**(0): 115–125.

Sun, J., Han, Y. and Cui, K. (2008). Innovative fabrication of porous titanium coating on titanium by cold spraying and vacuum sintering, *Materials Letters* **62**: 3623–3625.

Sundararajan, G., Naveen, C. M., Sivakumar, G. and Sudharshan, P. P. (2010). Evaluation of parameters for assessment of inter-splat bond strength in cold-sprayed coatings, *Journal of Thermal Spray Technology* **19**(6): 1255–1266.

Suo, X., Yu, M., Li, W., Planche, M. and Liao, H. (2012). Effect of Substrate Preheating on Bonding Strength of Cold-Sprayed Mg Coatings, *Journal of Thermal Spray Technology* **5**: 1059–1067.

Suwankamnerd, P. and Wongwises, S. (2015). An experimental study of two-phase airwater flow and heat transfer characteristics of segmented flow in a microchannel, *Experimental Thermal and Fluid Science* **62**: 29–39.

Tamaekong, N., Liewhiran, C., Wisitsoraat, A. and Phanichphant, S. (2010). Flame-Spray-Made Undoped Zinc Oxide Films for Gas Sensing Applications, *Sensors* **10**: 7863–7873.

Tanju, T. and Niyazi, O. (2012). Weldability and joining characteristics of aisi $430/aisi1040$ steels using keyhole plasma arc welding, *The International Journal of Advanced Manufacturing Technology* **63**(1-4): 117–128.

Tesfamichael, T., Motta, N., Bostrom, T. and Bell, J. (2007). Development of porous metal oxide thin films by co-evaporation, *Applied Surface Science* **253**(11): 4853–4859.

Thakre, S. D., Swami, V. B. and Malwe, P. D. (2014). Cooling system of electronic devices using microchannel heat sink, *International Journal of Thermal Technologies* **4**(2): 58–60.

Thirumalaikumarasamy, D., Shanmugam, K. and Balasubramanian, V. (2014). Establishing empirical relationships to predict porosity level and corrosion rate of atmospheric plasma-sprayed alumina coatings on AZ31B magnesium alloy, *Journal of Magnesium and Alloys* pp. 1–14.

Thiruvarudchelvan, S. and Tan, M. (2006). A note on fluid-pressure-assisted deep drawing processes, *Journal of Materials Processing Technology* **172**(2): 174–181.

Thiruvarudchelvan, S. and Travis, F. (2003). Hydraulic-pressure-enhanced cup-drawing processesan appraisal, *Journal of Materials Processing Technology* **140**(13): 70–75. Proceedings of the 6th Asia Pacific Conference on materials Processing.

Tiemann, M. (2007). Porous Metal Oxides as Gas Sensors, *Chemistry European Journal* **13**: 8376–8388.

Tria, S., Elkedim, O., Hamzaoui, R., Guo, X., Bernard, F., Millot, N. and Rapaud, O. (2011). Deposition and characterization of cold sprayed nanocrystalline NiTi, *Powder Technology* **210**(2): 181–188.

Tria, S., Elkedim, O., Li, W. and Liao, H. (2009). Ball milled NiTi powder deposited by cold spraying, *Journal of Alloys and Compounds* **483**(12): 334–336.

Tsai, M.-H., Chen, M.-S., Lin, L.-H., Lin, M.-H., Wu, C.-Z., Ou, K.-L. and Yu, C.-H. (2011). Effect of heat treatment on the microstructures and damping properties of biomedical MgZr alloy, *Journal of Alloys and Compounds* **509**(3): 813 – 819.

Tuckerman, D. and Pease, R. (1981). High performance heat sinking for vlsi, *Electron Device Letters, IEEE* **2**(5): 126–129.

Upadhya, G., Munch, M., Peng, Z., J.Horn, Werner, D. and McMaster, M. (2006). Micro-scale liquid cooling system for high heat flux processor cooling applications, *Semiconductor Thermal Measurement and Management Symposium, 2006 IEEE Twenty-Second Annual IEEE*, pp. 116–119.

USA-Defense (2008). Materials Deposition, Cold Spray, *Manufacturing Process Standards MIL-STD-3021*, Department of Defense, United States of America.

Vankanti, V. K. and Ganta, V. (2014). Optimization of process parameters in drilling of GFRP composite using taguchi method, *Journal of Materials Research and Technology* **3**(1): 35 – 41.

Varkey, A. J. (2010). Antibacterial properties of some metals and alloys in combating coliforms in contaminated water, *Scientific Research and Essays* **5**(24): 3834–3839.

Vasquez, H., Espinoza, L., Lozano, K., Foltz, H. and Yang, S. (2009). Simple device for electromagnetic interference shielding effectiveness measurement, *IEEE* pp. 62–68.

Vayre, B., Vignat, F. and Villeneuve, F. (2012). Designing for additive manufacturing, *Procedia* {*CIRP*} **3**: 632–637.

Venkatesh, L., Chavan, N. M. and Sundararajan, G. (2013). The Inuence of Powder Particle Velocity and Microstructure on the Properties of Cold Sprayed Copper Coatings, *Journal of Thermal Spray Technology* **105**: 121–129.

Vincent, C., Silvain, J., Heintz, J. and Chandra, N. (2012). Effect of porosity on the thermal conductivity of copper processed by powder metallurgy, *Journal of Physics and Chemistry of Solids* **73**(3): 499–504.

Vityaz, P., Sheleg, V., Kaptsevich, V., Savich, V. and Sorokina, A. (1986). Classification of the properties of porous materials, *Soviet Powder Metallurgy and Metal Ceramics* **25**(12): 1006–1010.

Wang, C., Yin, L., Zhang, L., Xiang, D. and Gao, R. (2010). Metal oxide gas sensors: Sensitivity and influencing factors, *Sensors* **10**(3): 2088–2106.

Wang, X., Wei, X., Wen, C. and Han, F. (2011). Fabrication and characterisation of microporous titanium, *Research 1*, Institute of Materials, Minerals and Mining, China. Powder Metallurgy.

Wang, Z., Zheng, H., Lim, R., Wang, F. and Lam, Y. (2011). Improving surface smoothness of laser-fabricated microchannels for microfluidic application, *Journal of Micromechanics and Microengineering* **21**(9): 1–7.

Wei, X. and Joshi, Y. (2003). Optimization Study of Stacked Micro-Channel Heat Sinks for Micro-Electronic Cooling, *IEEE TRANSACTIONS ON COMPONENTS AND PACKAGING TECHNOLOGIES* **26**(1): 62–68.

Wong, W. (2011a). *Understanding the Effects of Process Parameters on the Properties of Cold Gas Dynamic Sprayed Pure Titanium Coatings*, diploma thesis, McGill University, Montreal, Canada.

Wong, W. (2011b). *Understanding the Effects of Process Parameters on the Properties of Cold Gas Dynamic Sprayed Pure Titanium Coatings*, Phd thesis, McGill University, Montreal, Canada.

Wu, J., Fang, H., Yoon, S., Kim, H. and Lee, C. (2005). Measurement of particle velocity and characterization of deposition in aluminum alloy kinetic spraying process, *Applied Surface Science* **252**(5): 1368 – 1377.

Wu, X., Zhang, J., Zhou, X., Cui, H. and Liu, J. (2012). Advanced cold spray technology: Deposition characteristics and potential applications, *Science China Technological Sciences* **55**(2): 357–368.

Wusiman, K., Chung, H., Md, J., Handry, A., Eom, Y., hyo Kim, J. and Jeong, H. (2013). Heat transfer characteristics of nanofluid through circular tube, *Journal of Central South University* **20**(1): 142–148.

Xia, G., Jiang, J., Wang, J., Zhai, Y. and Ma, D. (2015). Effects of different

geometric structures on fluid flow and heat transfer performance in microchannel heat sinks, *International Journal of Heat and Mass Transfer* **80**(0): 439 – 447.

Xie, F., He, X., S.Cao, Mei, M. and Qu, X. (2013). Influence of pore characteristics on microstructure, mechanical properties and corrosion resistance of selective laser sintered porous timo alloys for biomedical applications, *Electrochimica Acta* **105**: 121–129.

Xie, Z., Liu, Z., Wang, Y., Yang, Q., Xu, L. and Ding, W. (2010). An overview of recent development in composite catalysts from porous materials for various reactions and processes, *International Journal of Molecular Sciences* **11**: 2152–2187.

Xiong, Y., Zhuang, W. and Zhang, M. (2015). Effect of the thickness of cold sprayed aluminium alloy coating on the adhesive bond strength with an aluminium alloy substrate, *Surface and Coatings Technology* **270**: 259–265.

Xu, C., Tamaki, J., Miura, N. and Yamazoe, N. (1991). Grain size effects on gas sensitivity of porous sno2-based elements, *Sensors and Actuators B, Chemical* **3**(2): 147–155.

Yan, Z.-F. and Xiao, F.-S. (2008). *Journal of Porous Materials* **15**(2): 115–117.

Yang, R., Hao, Y. and Li, S. (2011). Development and application of low modulus biomedical titanium alloy ti2448, biomedical engineering, trends in materials science, *biomedical engineering trends in materials science* **10**(2): 225–248.

Yang, X., Kuang, J., Lu, T., Han, F. and T.Kim (2013). A simplistic analytical unit cell based model for the effective thermal conductivity of high porosity open-cell metal foams, *Journal of Physics D: Applied Physics* **46**: 1–6.

Yole-Development (2010). Emerging markets for microfluidic applications in life sciences, *Micromachine Summit*, Lyon, France, pp. 1–27.

Yuan, J. and Sunden, B. (2014). On mechanisms and models of multicomponent gas diffusion in porous structures of fuel cell electrodes, *International Journal of Heat and Mass Transfer* **69**(0): 358–374.

Yuan, W., Tang, Y., Yang, X. and Wan, Z. (2012). Porous metal materials for polymer electrolyte membrane fuel cells.a review, *Applied Energy* **94**: 309–329.

Yukselen-Aksoy, Y. (2010). Characterization of two natural zeolites for geotechnical and geoenvironmental applications, *Applied Clay Science* **50**(1): 130 – 136.

Yunlian, Q., Ju, D., Quan, H. and Liying, Z. (2000). Electron beam welding, laser beam welding and gas tungsten arc welding of titanium sheet, *Materials Science and Engineering: A* **280**(1): 177–181.

Zahiri, S., Antonio, C. and M.Jahedi (2008). Elimination of porosity in directly fabricated titanium via cold gas dynamic spraying, *Journal of Materials Processing Technology* **209**: 922–929.

Zahiri, S., Fraser, D., Gulizia, S. and Jahedi, M. (2006). Effect of processing conditions on porosity formation in cold gas dynamic spraying of copper, *Journal of Thermal Spray Technology* **15**(3): 422–430.

Zahiri, S. H., Antonio, C. I. and Jahedi, M. (2009). Elimination of porosity in directly fabricated Titanium via cold gas dynamic spraying, *Journal of Materials Processing Technology* **209**(2): 922–929.

Zahiri, S. H., Mayo, S. C. and Jahedi, M. (2008). Characterization of Cold Spray Titanium Deposits by X-Ray Microscopy and Microtomography, *Microscopy and Microanalysis* **14**(3): 260–266.

Zang, D., Wu, C., Zhu, R., Zhang, W., Yu, X. and Zhang, Y. (2013). Porous copper surfaces with improved superhydrophobicity under oil and their application in oil separation and capture from water, *Chem. Commun.* **49**: 8410–8412.

Zdravkov, B. D., Jirij, Cermark, Sefara, M. and Janku, J. (2007). Pore classification in the characterization of porous materials: A perspective, *Central European Journal of Chemistry* **5**(2): 385–395.

Zhang, D., Shipway, P. and McCartney, D. (2005). Cold gas dynamic spraying of aluminum-the role of substrate characteristics in deposit formation, *Journal of Thermal Spray Technology* **14**(1): 109–116.

Zhang, J., Diao, Y., Zhao, Y., Zhang, Y. and Sun, Q. (2014). Thermal hydraulic performance of multiport microchannel flat tube with a sawtooth fin structure, *International Journal of Thermal Sciences* **84**: 175–183.

Zhang, J., Wang, J. and Ma, J. (2005). Porous structures of natural materials and bionic design, *Journal of Zhejiang University Science A* **6**(10): 1095–1099.

Zhao, Y., He, J., Fan, L., Ran, W., Zhang, C., Gao, D., Wang, C. and Gao, F. (2013). Synthesis and characterization of hierarchical porous LiNiCuZn-oxides as potential electrode materials for low temperature solid oxide fuel cells, *International Journal of Hydrogen Energy* **38**(36): 16558–16562.

Zhou, W., Deng, W., Lu, L., Zhang, J., Qin, L., Ma, S. and Tang, Y. (2014). Laser micro-milling of microchannel on copper sheet as catalyst support used in microreactor for hydrogen production, *International Journal of Hydrogen Energy* **39**: 4884–4894.

Zhou, Y., Li, C.-J., Yang, G. J. and Duo, H. (2010). Effect of self propagating high temperature combustion synthesis on the deposition of NiTi coating by cold spraying using mechanical alloying NiTi powder, *Intermetallics* **18**(11): 2154–2158.

Part I

APPENDICES

APPENDIX A Glossary

Adiabatic. No heat loss or transfer occurs (between the gas–particle mixture and the substrate)

Agglomerate. Several particles adhering together.

Analyte gas. A gas exposed to a sensing layer that change the resistance of the layer.

Antimicrobial filter. A structure permeable to air or water capable of removing impurities and killing bacteria.

Automatic spraying. Spraying with equipment requiring only occasional or no observation and no manual adjustments during its operation. See also manual spraying, mechanized spraying, robotic spraying, and semiautomatic spraying.

Attributes: An intrinsic property of the entity whose value does not depend on other entities.

Bone implant. An artificial structure that mimics the human borne.

Bond. The state of adhesion between the coating and the substrate. Bonding mechanisms may be mechanical, physical, chemical, metallurgical, or a combination of these.

Bond strength. The strength of the adhesion between the coating and the substrate. A number of test methods are in use to measure the bond strength of coatings.

Cladding. The application of a thick (generally above 1 mm) coating which melts or diffuses into the substrate. Processes include weld cladding and plasma transferred arc (PTA).

Cold Gas Dynamic Spraying (CGDS). Process wherein particles are deposited in solid state to form a coating

Composite. Mixture of two or more materials. Nearly all have a reinforcing material (metal, wood, glass, etc.), called filler, and a natural or artificial resin, called matrix to achieve specific characteristics and required properties.

Composite Powder. A powder in which each particle consists of two or more distinct materials joined together. (Not the same as a powder blend.)

Corrosion. Chemical or electrochemical reaction between a material and it's environment which results in deterioration in the properties of the material.

Critical velocity. The velocity of the particle above which bonding is implemented.

CS facility. Configuration of cold spray equipment together with its affiliated equipment.

Debinder. Material used to detach another material from the support or subsstrate.

Deposition efficiency (DE). The weight percentage of particles that are deposited on the substrate to the particles that are accelerated towards it.

Elasticity. The property of certain materials that enables them to return to their original dimensions after an applied stress.

Erosion. Removal of material from a surface due to mechanical interaction between that surface and a fluid, a multicomponent fluid, or impinging liquid or solid particles.

Exothermic reaction or material. Certain materials undergo chemical reactions when thermally sprayed and produce extra heating. This can be useful in improving adhesion of the coating to the substrate.

Fatigue. A cumulative effect causing a material to fail after repeated applications of stress none of which exceeds the ultimate tensile strength. The fatigue strength (or fatigue limits) is the stress that will cause failure after specified number cycles.

Flowability. The powder particles ability to flow evenly, by means of gravity and other forces, from the top to the bottom of a hopper.

Gas sensing layer. A coatings that changes its electrical properties(conductivity) when exposed to an analyte gas. (see definition for analyte gas)

Grit blasting. A pressurised stream of hard metal or oxide grit material used to clean and roughen surfaces prior to coating.

High Velocity Oxy-fuel Spraying (HVOF). A Thermal spray process. The spray powder particles are injected into a high velocity jet formed by the combustion of oxygen and fuel, heated and accelerated to the work piece.

Inert gas. A stable gas that does not support combustion and does not form reaction products with other materials. Included are helium, argon, and sometimes nitrogen.

Isentropic. Adiabatic and frictionless

Mach number. Velocity of the gas divided by the local speed of sound.

Matrix. The continuous phase of a material or coating in which separate particles of another constituent are embedded.

Micro heat sink. A solid or porous structure capable of removing heat from a source.

Micrograph. A micrograph is produced when a section of the coating is taken, polished to show the particulate layers and then photographed through a microscope.

Microhardness. The hardness of a coating as measured on a microscopic scale. Can show the hardness of individual phases within the coating and avoid the effects of porosity.

item[Nanostructured.] A structure with particles that's a few hundred nano-meters in size,

Noble metal. A metal that does not readily tend to furnish ions, and therefore does not dissolve readily, nor easily enter into such reactions as oxidation, etc. The opposite of base metal.

Oxidation. Loss of electrons by a constituent of a chemical reaction. (Also refers to the corrosion of a metal that is exposed to an oxidising gas at elevated temperatures.)

Particle size distribution. The percentage by weight, or by number, of each fraction into which a powder sample has been classified with respect to sieve number or microns.

Particle velocity. A how fast a particle moves when pushed by a gas stream.

Plasma Spraying . A thermal spraying process in which the heat source is a plasma flame.

Porosity. The presence of pores or voids in a coating, usually expressed as a percentage by volume.

Shock Wave. A propagation disturbance within a solid, liquid, or gas medium across which there is a finite decrease in velocity and large and abrupt rise in pressure, temperature, and density of the flow. See also bow shock.

Satelliting particle. A particle used as an attachment for other particles.

Splat. A single thin flattened sprayed particle.

Spray feedstock. Any consumable form of spray material used in the application of a coating. The aperture through which powder is introduced into the spraying apparatus.

Spraying deposition efficiency. The ratio, usually expressed in percent, of the weight of spray deposit to the weight of the material sprayed.

Stagnation pressure. The pressure a gas would exhibit if brought to zero velocity by an isentropic process. Generally used to refer to the fluid pressure in the pre–chamber.

Stagnation temperature. Temperature of the fluid flow at the stagnation point. See also flow stagnation temperature and room stagnation temperature.

Stagnation temperature and pressure. Gas quantities before nozzle entry

Standoff distance. A nonstandard term when used for spray distance. It is the distance between the tip of the nozzle and substrate

Strain. A measure of the extent to which a body is deformed when it is subjected to a stress.

Stress. The force per unit area on body that tends to cause it to deform. It is a measure of the internal forces in a body between particles of the material of which it consists as they resist separation, compression, or sliding.

Subsonic. Having a Mach number of less than 1.0. See also supersonic and hypersonic.

Substrate. The parent or base material to which the coating is applied.

Supersonic. Having a Mach number of greater than 1.0. High supersonic speeds are those between 3 and 5. See also subsonic and hypersonic

Tensile strength. A measure of the resistance that a material offers to tensile stress. It is defined as the stress, expressed as the force per unit cross sectional area, required to break it.

Tensile stress. Axial forces per unit area applied to a body that tend to extend it.

Theoretical density. The density of a solid homogeneous piece of material.

Topography. The geometrical detail of the object, relating particularly to microscopic variations in dimensions

Thermal spraying. Processes wherein particles are deposited in a molten or semi-molten condition to form a coating.

Throat. The point or region in the fluid flow passage having the minimum cross-sectional area.

Two-phase flow. A flow consisting of two different phases of material, for example of both gas and solid phases.

Venturi. A region in a fluid flow passage (e.g. the throat) where flow is constricted to increase the velocity of fluid.

Void. A shrinkage cavity produced during spraying or solidification.

APPENDIX B : Classification Criteria for Porous Structures

Porous structures were classified according to common attributes for their identification, and selection of application areas. The criteria used in the classification of porous structures included the architecture, size, origin of pores, and material used during fabrication (Ashby and Medalist, 1983; Zdravkov et al., 2007). Based on the criterion of architecture of pores, porous structures were classified as closed, open, cellular, foamed, reticulated, isotropic, and anisotropic (Diedericks and du Plessis, 1996; Heaney et al., 2005; Cicek and Celik, 2009; Arenas and Crocker, 2010; Lu and Zhao, 2011; Yang et al., 2013; Ackermann et al., 2014; King et al., 2015). Based on the criterion of size of pores, porous structures were classified as micro-, meso- and macro-porous with pores whose sizes were less than 2 nm, between 2 nm and 50 nm, and greater than 50 nm, respectively (Kaneko, 1994; Cicek and Celik, 2009; Zdravkov et al., 2007; Lu and Zhao, 2011). Then, based on the criterion of origin of pores, porous structures were classified as artificial or natural (Rouquerol et al., 1994; Korner and Singer, 2000; Zahiri et al., 2006; Nakajima, 2007; Ismail et al., 2012; Jo et al., 2014). Finally, based on the criterion of material used during fabrication, porous structures were categorised as metallic, ceramic, polymeric, or paper (Korner and Singer, 2000; Cicek and Celik, 2009; Arenas and Crocker, 2010; Arai and Suidzu, 2013).

Further, the choice of each of the above criteria for classification of porous structures depended on the reason(s) for classifying them (Zdravkov et al., 2007). For instance, the criterion of the origin of the pores was chosen when considering the performance of porous structures (Rouquerol et al., 1994). Similarly, the architecture of pores was chosen as a criterion when the porosity, mechanical properties, and choice of the areas of application were considered

as important characteristics of porous structures (Carey and Inderwildi, 2009). Also, the size of pores became necessary criterion when the choice of the area of application for porous structures was important (Cicek and Celik, 2009). Finally, the criterion of the material used during fabrication of porous structures was chosen only when the fabrication methods, and costs were important (Arenas and Crocker, 2010). Based on this consideration, this study classified porous structures into the sub-groups presented in the taxonomy shown in Figure B.1 constructed based on the literature Vityaz et al. (1986).

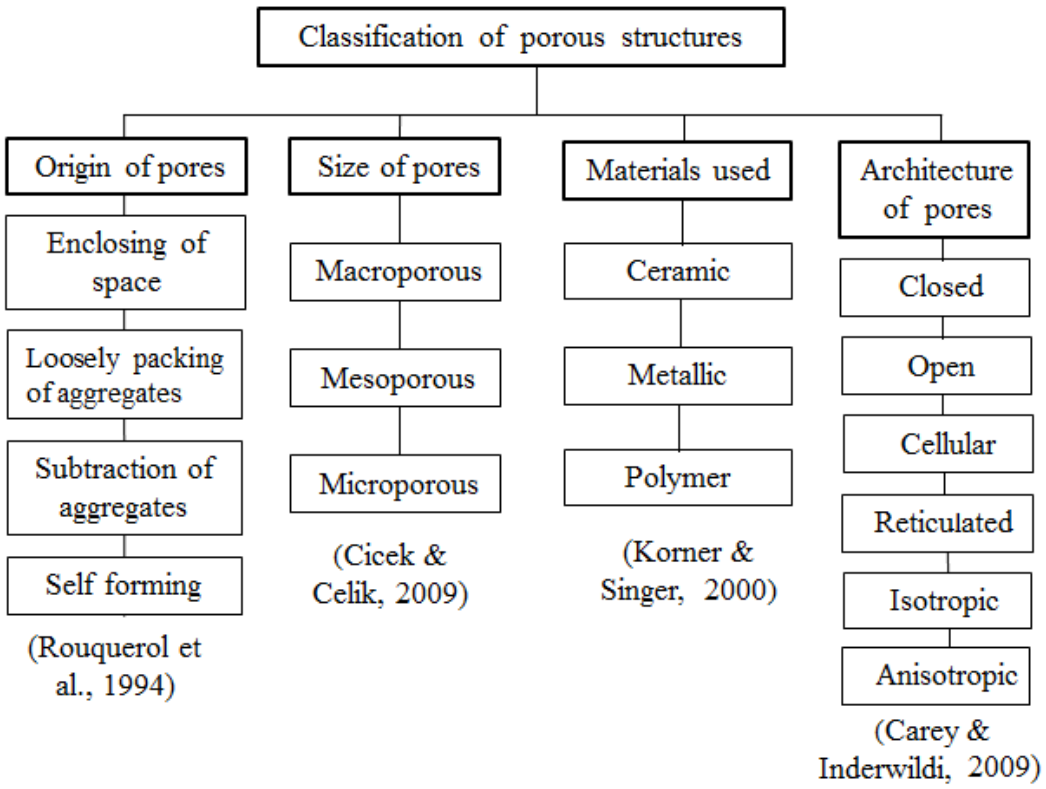


Figure B.1: Classification of porous structures.

APPENDIX C : Porous Structures for Cooling of Electronics

Porous structures such as micro heat sinks (MHSs) characterised with microchannels proved to be efficient heat exchangers in advanced cooling systems such as Microfluidic Cooling Systems (MFCSs) found in cooling high speed electronics devices such as microprocessors (Tuckerman and Pease, 1981; Adham et al., 2013). The microchannels, defined as uni-directional micro pores with uniform cross section area and small hydraulic diameter of between 10 μm and 200 μm, provided high fluid penetration, large surface area to volume ratio, and high cooling capability than any other porous device (Mihai, 2011; Thakre et al., 2014).

Studies showed that MHSs whose microchannels have trapezoidal shapes, and hydraulic diameter was between 100 μm and 500 μm, outperformed the other designs in terms of heat extraction capability when integrated in the Microfluidic Cooling Systems (MFCSs) (Bowers and Mudawar, 1994; Gautam et al., 2011). In addition, their heat removal was superior compared to other cooling technologies as illustrated in Figure C.1. As seen in this figure, the microchannel liquid cooling system surpasses other cooling technologies and able to dissipate enormous heat fluxes of up to $70,000\ W/cm^2$ compared to the forced convection air cooling system capable of dissipating only up to 90 W/cm^2 (Bowers and Mudawar, 1994; Harry et al., 2013; Xia et al., 2015). In this context, the components such as the micro-pump, fan, micro-radiator, and MHS found in the microchannel liquid cooling systems that used microfluidic cooling methods were architectured as shown in Figure C.2.

The superior heat extraction capability of this system was as a result of the micro-pump which circulated the cooling liquid to the microchannels where

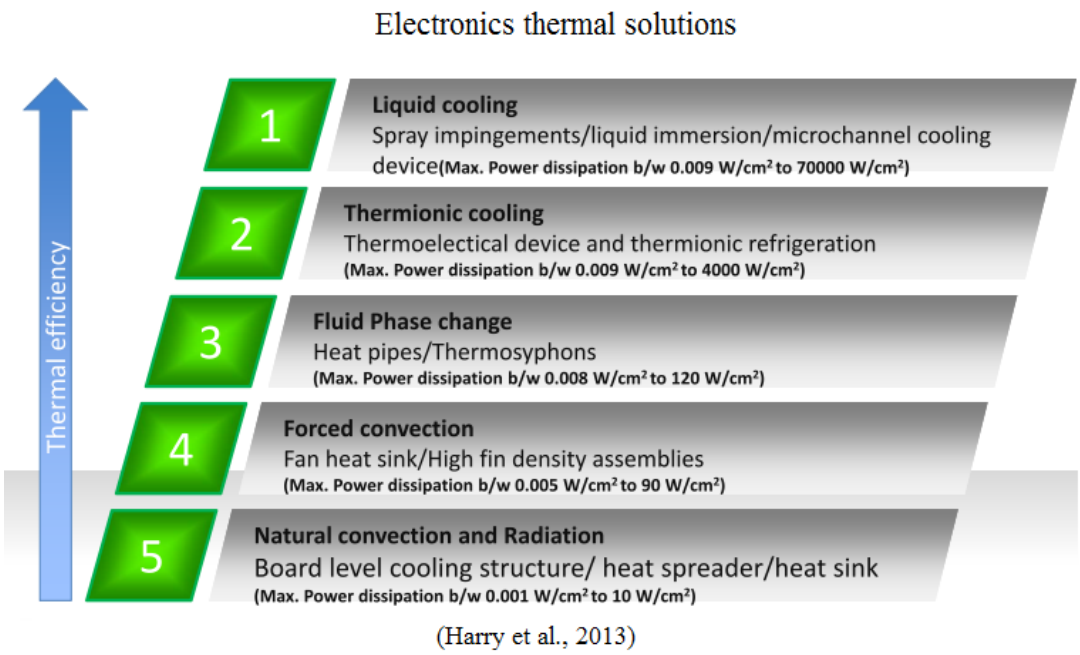


Figure C.1: Thermal solutions hierarchy.
Source: (Harry et al., 2013)

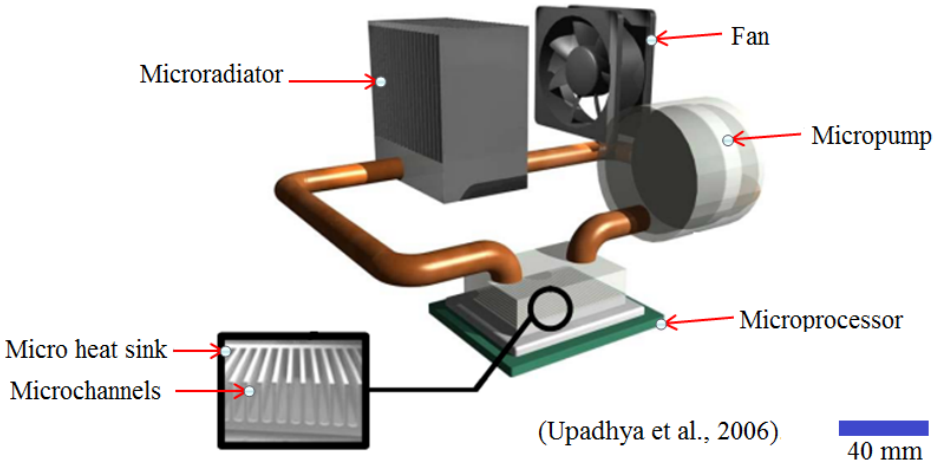


Figure C.2: Microfluidic cooling architecture.
Source: (Upadhya et al., 2006)

the liquid picked up the heat, convected it to the micro-radiator where it was dissipated into the atmosphere with the aid of the fan (Upadhya et al., 2006). The cooling liquid in the MFCSs could be the de-ionised water or nanofluids made of water mixed with metal nanoparticles whose concentration could vary between 1 % and 5 % by volume (Tuckerman and Pease, 1981; Upadhya et al., 2006; Husain and Kim, 2010; Gautam et al., 2011). Because of this superior performance, it is likely that the MFCSs will dominate the next generation micro cooling systems in electronics since the conventional air cooling systems are not capable of dissipating heat fluxes to keep the junction temperature of the microprocessors within permissible limits of 55 °C and 100 °C (Kandlikar and Upadhye, 2005; Mihai, 2011).

Consequently, investigations were carried out to establish the variation of thermal performance of the MHSs with the hydraulic diameter of the rectangular shaped microchannels (Gunnasegaran et al., 2010). The results of this investigation indicated that the heat transfer coefficient of the MHSs is high when the hydraulic diameter of the microchannels is smaller, and vice versa, as illustrated in Figure C.3.

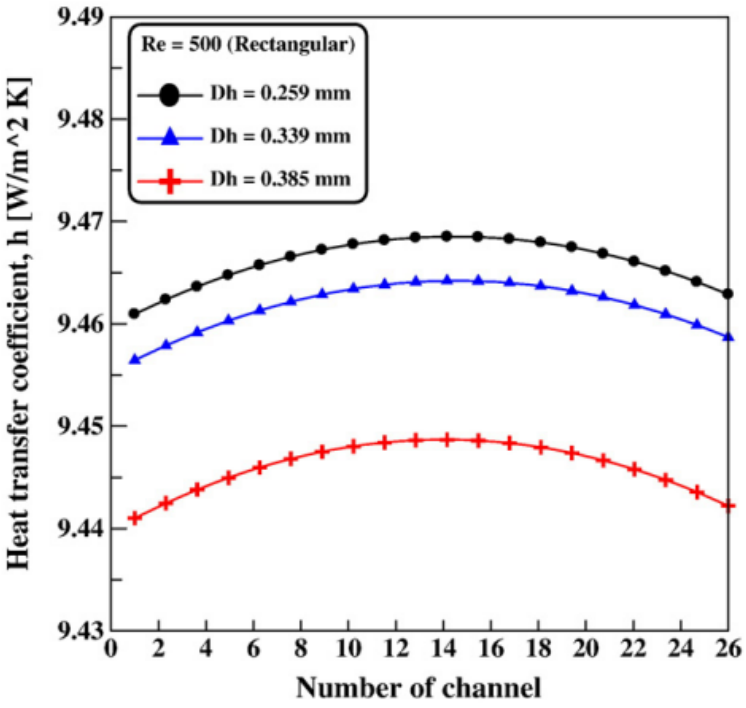


Figure C.3: Heat transfer coefficients.
Source: (Gunnasegaran et al., 2010)

Later, investigation was carried out on the variation of thermal performances

of MHSs with various shapes of non-circular sectioned microchannels shown in Figure C.4 (Gautam et al., 2011). The results of this investigation showed that the variation of the normalised heat exchange rate with Reynolds number (R_e) was more for the microchannels with trapezoidal shapes compared to different designs (Gautam et al., 2011), as illustrated in Figure C.5.

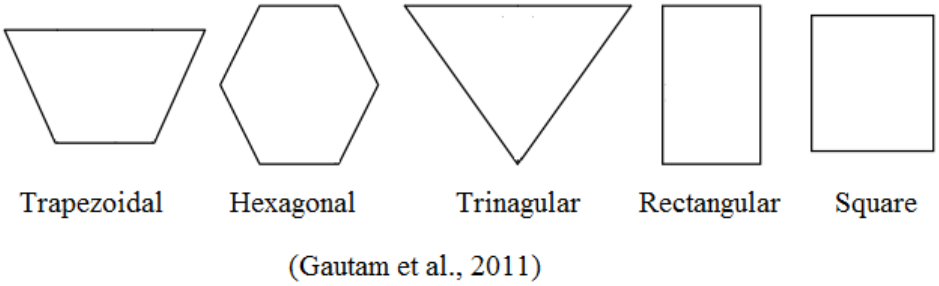


Figure C.4: Non-circular shapes for microchannels.
Source: (Gautam et al., 2011)

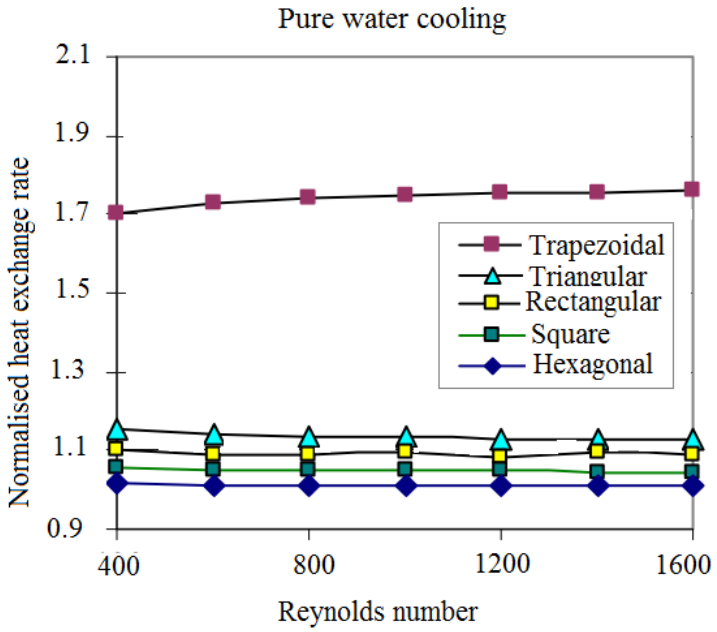


Figure C.5: Heat exchange rate Vs. Re for water cooling.
Source: (Gautam et al., 2011).

Moreover, the normalized heat exchange rate for trapezoidal shaped microchannels cooled by Copper-water nanofluids was 14.7 % higher than the normalized heat exchange rate for similar microchannels cooled by deionised water as summarised in Figure C.6 (Gautam et al., 2011).

In summary, the MHSs with trapezoidal shaped microchannels integrated in MFCSs proved to be a solution to the thermal problems associated with

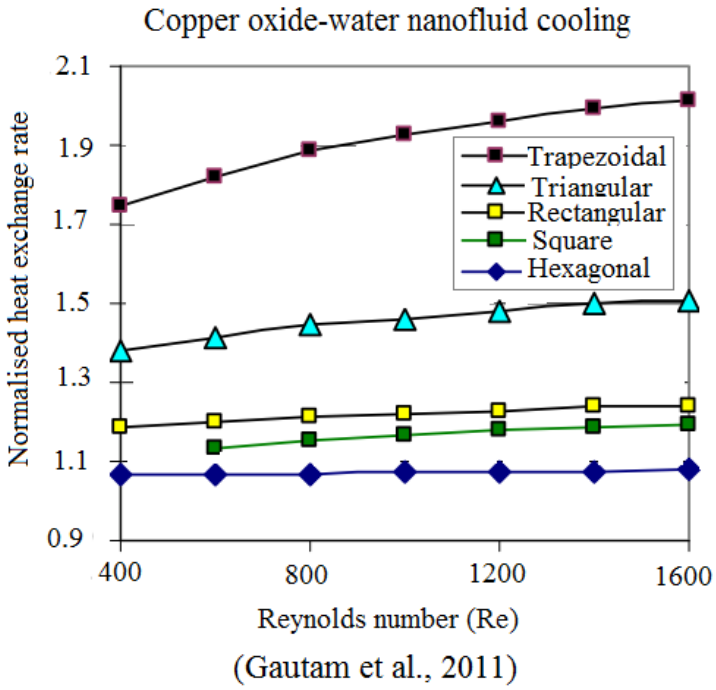


Figure C.6: Heat exchange rate Vs. Re for nanofluid cooling.
Source: (Gautam et al., 2011)

Ultra-Large-Scale-Integrated-Circuit (ULSIC). This solution could improve the performance and service life of the electronics equipment (Tuckerman and Pease, 1981; Singh et al., 2009; Husain and Kim, 2010; Mihai, 2011; Stocks et al., 2014; Thakre et al., 2014; Adham et al., 2015; Bari and Morshed, 2015; Suwankamnerd and Wongwises, 2015; Xia et al., 2015). In addition, the application of nanofluids as cooling liquid could enhance the cooling capability of MFCSs (Gautam et al., 2011). Further increase in thermal properties and high-temperature strength of the heat sink was achieved when the copper powder was mixed with chromium powder during cold spray process (Kikuchi et al., 2013). However, the problem hampering the wide-scale application of the MHSs with trapezoidal shaped microchannels in electronics cooling is the scarcity of these devices due to lack of reliable and cost effective method of manufacturing (Gunnasegaran et al., 2010; Prakash and Kumar, 2014; Zhou et al., 2014; OConnor et al., 2014). On this account, there is need to develop a new low cost method for fabrication of MHSs with trapezoidal shaped microchannels since these structures could also be applied in micro reactors, fuel cells, and many other micro-electromechanical systems (MEMS) (Yole-Development, 2010)

APPENDIX D : Porous Structures for Medical Implants

The demand for porous structures in medical application is rising specifically in orthopaedic operations where bone implants are required for repair or replacement of degraded bones resulting from increased number of aging people, bone diseases and traffic related bone injuries (Levine and Fabi, 2010; Yang et al., 2011; Intelligence, 2014; Sidambe, 2014). It was projected that the market growth rate for the bone implants, in Billions of US Dollars, will remain between 20 % and 25 % in the next decade as illustrated in Figure D.1 (Intelligence, 2014; Li et al., 2014). Bone implants with porous coatings are necessary to support the structure of the body, bone in-growth and cell attachment (Krishna et al., 2008; Levine and Fabi, 2010). Examples of porous coated bone implants are shown in Figure D.2.

Despite increase in demand for these medical devices, there is still a gap between the supply and demand due to lack of cost effective and efficient method od manufacturing (Dimitrov et al., 2013; Li et al., 2014; Hamweendo et al., 2016b). This gap makes the research on development of new fabrication methods an important topic (Zahiri et al., 2009; Elahinia et al., 2012; Li et al., 2014; Jardini et al., 2014). In this respect, porous coated titanium (Ti) and its alloys were extensively studied because of their favourable properties such as high specific strength, high corrosion resistance, super-elasticity, low elastic modulus, bio-inertness, porosity of $30-60$ %, tensile strength of $3.7-140$ MPa, Youngs Modulus of $0.16-18.1$ GPa, and microhardness of $45-200$ Hv (Ryan et al., 2006; Levine and Fabi, 2010; Yang et al., 2011; Elahinia et al., 2012; Habijan et al., 2013; Li et al., 2014; Sidambe, 2014; Soares et al., 2014). In addition, studies proved that it was difficulty and costly to fabricate porous coatings on bone implants using powder metallurgy (PM), electron beam melting (EBM),

graph.png

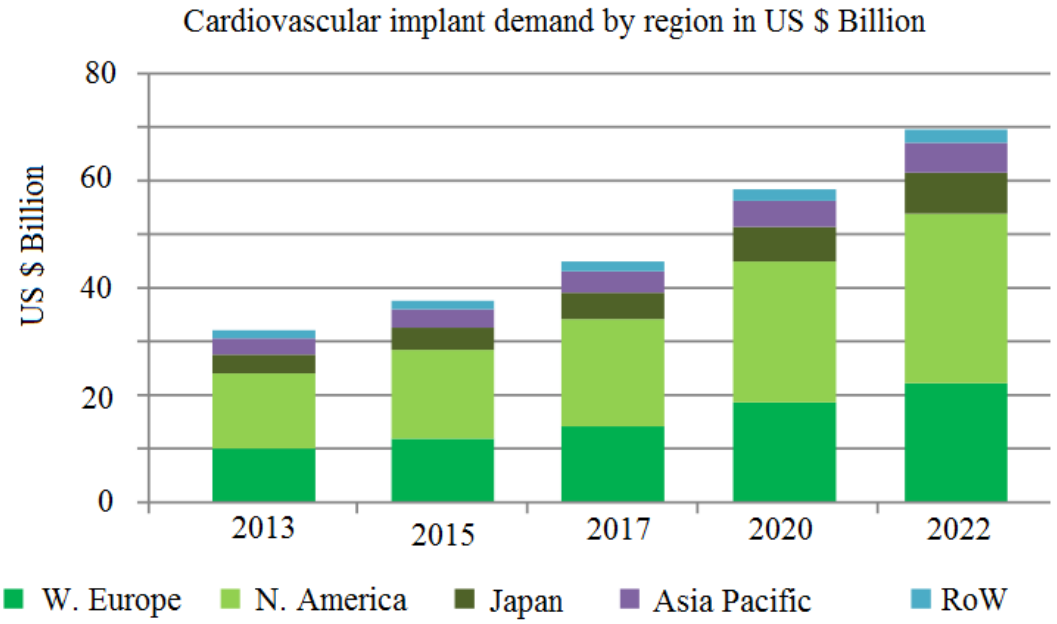
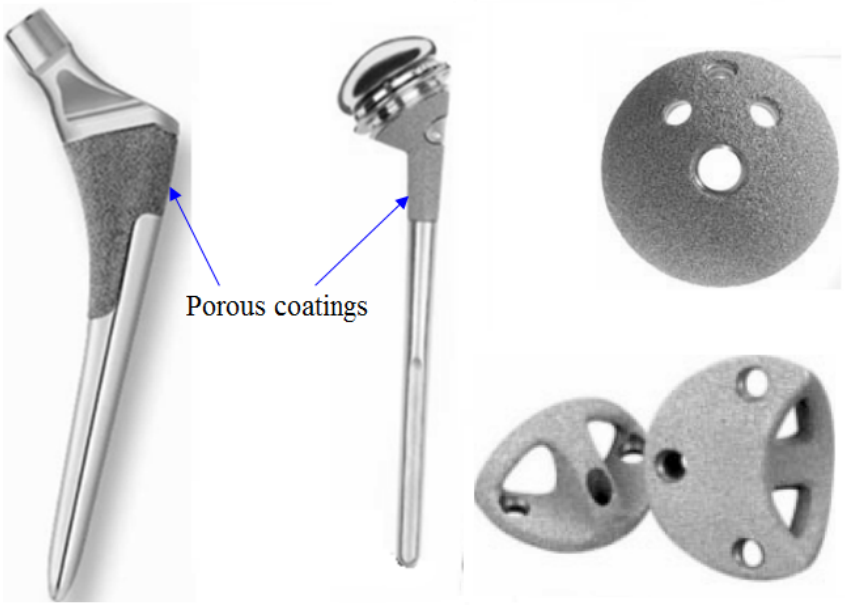


Figure D.1: Demand for bone implants.
Source: (Intelligence, 2014).



implants.png

Figure D.2: Porous coated bone implants.
Source: (Levine and Fabi, 2010).

selective laser melting (SLM) processes, and thermal spraying (TS) processes (Levine and Fabi, 2010; Yunlian et al., 2000; Magnabosco et al., 2006; Krishna et al., 2008; Tanju and Niyazi, 2012). Consequently, new methods for manufacturing bone implants and their surface coatings are required (Zahiri, Antonio and M.Jahedi, 2008).

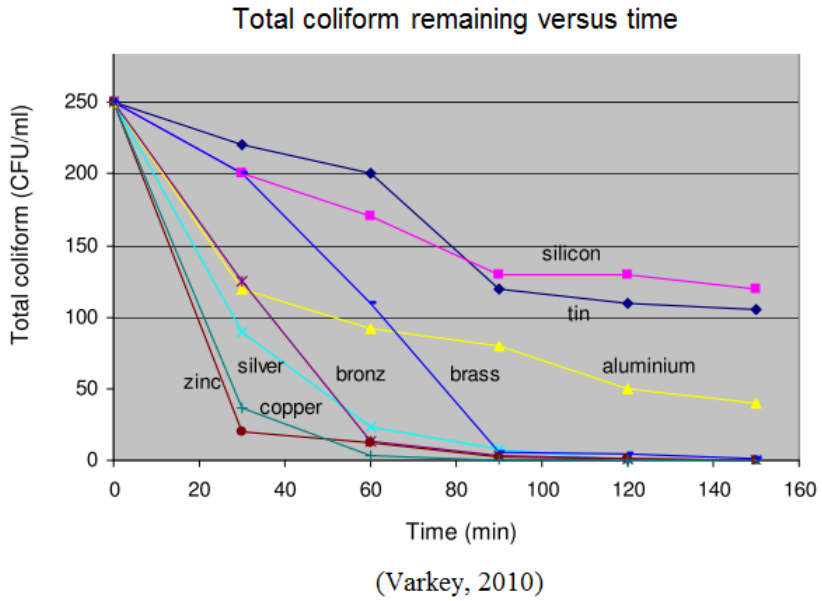
APPENDIX E : Porous Structures for Medical Filters

Medical filtration is a process used to purify air or drinking water by trapping microorganisms using adsorption or mechanical straining of those microorganisms that are too large to pass through the microscopic holes of the filter (Varkey, 2010; Han et al., 2015). This process could be used to clean drinking water in rural communities where there is scarcity of modern water reticulation facilities due to lack of capital and technological know-how. The major sources of drinking water in these areas are: rivers, dams and streams. However, the water from these sources is usually contaminated with pathogenic micro-organisms, mainly the coliforms, the most prevalent strain of these is the Escherichia coli bacteria, called E.Coli 0157:H7. This strain causes water borne diseases such diarrhea and kidney damage that are responsible for death of millions of people each year (Varkey, 2010).

Studies showed that simple and affordable antimicrobial filters could decontaminate drinking water in rural areas using selected metals foams as filters (Hemin et al., 2008; Varkey, 2010). These filters could be made from metals such as copper, aluminium, and zinc or their alloys, as they were proved to be capable of killing several bacterial species such as Escherichia coli $O157$, Staphylococcus aureus, Salmonella enterica, Campylo-bacter jejuni, Clostridium difficile, Listeria monocytogenes, and My-cobacterium tuberculosis. These bacteria cause water borne diseases such as kidney failure, skin infections, fever, gastroenteritis, diarrhea, and tuberculosis (Mathews et al., 2018; Varkey, 2010). Likewise, alumina was demonstrated to be capable of inhibiting the infectious effects of bacteria such as Bacillus cereus, Bacillus subtilis, Vibrio cholerae and Klebsiella pneumoniae. These bacterial cause ailments such as diarrhea,

food poisoning, meningitis, bloodstream, and wound infections (Geoprincy et al., 2012).

Consequently, investigations were carried out to establish the rate at which these metals can kill the bacteria (Varkey, 2010). The results of these investigations proved that metals such as copper, zinc and silver have the highest antimicrobial capabilities since they could kill over 90 % of the bacteria in less than 60 minutes, and the aluminum and tin showed moderate antimicrobial capabilities, as illustrated in Figure E.1. These metals killed or inhibited the bacteria by emitting the ions that rapidly degraded the Deoxyribonucleic acid (DNA) cell and membranes of the bacteria (Mathews et al., 2018).

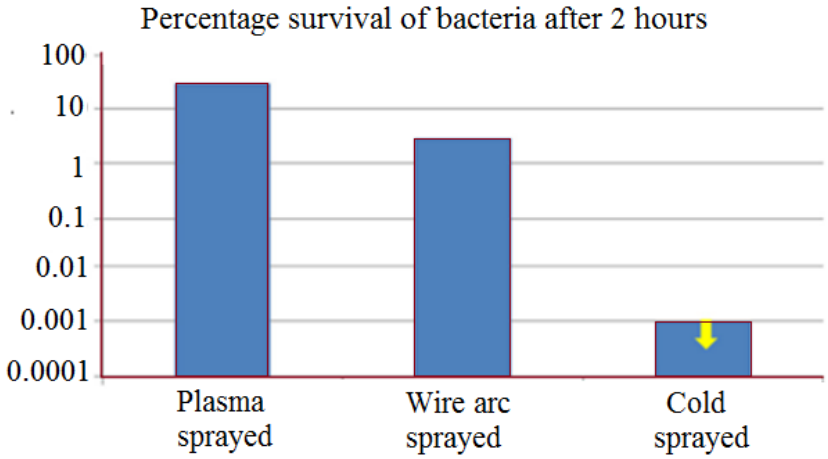


metals.png

Figure E.1: Antimicrobial capability of metals.
Source: (Varkey, 2010).

Further, a study was carried out to compared the antimicrobial capabilities of the Copper coatings fabricated using various technologies such as plasma spray, wire arc spray and cold spray (CS) (Champagne and Helfritch, 2013). The results of study, presented in Figure E.2, proved that the coatings fabricated using CS technique have superior antimicrobial effectiveness compared to those fabricated by other techniques. This is mainly due to the high impact velocity of the particles which resulted in high dislocation density and high ionic diffusivity (Champagne and Helfritch, 2013). Further enhancement of antimicrobial capabilities of structures were obtained when two or more metals were mixed (Sanpo et al., 2009). In addition, porous structures could improve the

antimicrobial results due to increased surface area (Hemin et al., 2008). The challenge with these results was to fabricate porous structures with two or more metals mixed together. Consequently, there is need for development of a low-cost method for manufacturing antimicrobial medical filters with these characteristics (Hemin et al., 2008; Sanpo et al., 2009; Varkey, 2010; Champagne and Helfritch, 2013).



coatings.png

Figure E.2: Antimicrobial capability of CS coatings.
Source: (Champagne and Helfritch, 2013)

APPENDIX F : Porous Structures for Gas Sensors

A gas sensor is a device that detects the presence of gases in an area. In these devices, porous surfaces, with improved gas selectivity, sensitivity and immunity to poisoning, made from semi-conductive metal oxides are necessary as sensing layers (Edelman et al., 2000; Simon et al., 2001; Tiemann, 2007; Tesfamichael et al., 2007; Wang et al., 2010). The components of a typical gas sensor are: the sensing layer usually positioned on top of the electrodes, the substrate to support the electrodes and gas sensing layer, and the heaters deposited beneath the substrate. Figure F.1 shows the configuration of these components in a typical gas sensor.

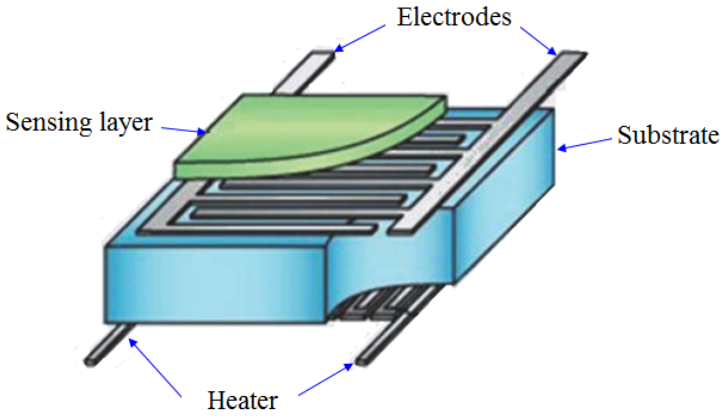


Figure F.1: Gas sensor configuration.
Source: (Tiemann, 2007)

During the gas sensing operation, the analyte gas comes into contact with the sensing layer where the gas adds Oxygen atoms and subtracts the electrons from the sensing layer (if the analyte gas is an oxidising agent) or removes oxygen atoms or adds electrons (if the gas is a reducing agent). This action results

in the change of resistance of the sensing layer that is measured at the terminal of the electrodes to signify the presence or change of concentration of the analyte gas (Xu et al., 1991; Wang et al., 2010; Bandgar et al., 2015; Martinez-Orozco et al., 2015). This mechanism is called transduction (Tiemann, 2007). Then, the sensitivity of the gas sensing layer can be calculated using equation (F.1) (Wang et al., 2010).

$$Se = \frac{R_g - R_a}{R_a} \tag{F.1}$$

where Se is the sensitivity of the sensing layer, R_g is the resistance of the gas sensing layer exposed to the gas and R_a is the resistance of the gas sensing layer when exposed to air.

Studies showed that the sensitivity of the gas sensor depended on surface area, pore size, and porosity of the gas sensing layer. All these factors affected the number of oxygen atoms or free electrons exchanged between the sensing layer and the analyte gas (Wang et al., 2010). As shown in Figure F.2, the pores not only served as channels for transportation of analyte gas into the sensing material and evacuation of the gas during recovery, but also increased the surface area of gas sensing layers.

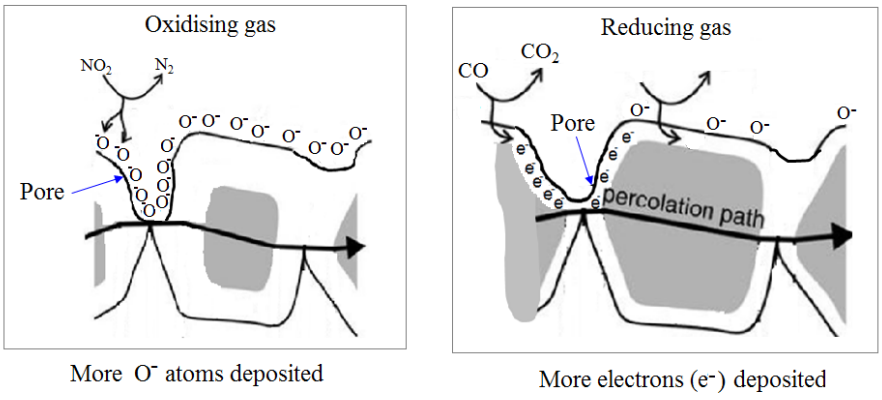


Figure F.2: Gas sensing mechanism.
Source: (Edelman et al., 2000).

In this context, several experiments showed that the surface porosity of between 10 % and 20 % resulted in favourable sensitivity and selectivity of the gas sensors (Edelman et al., 2000; Shilova, 2005; Tesfamichael et al., 2007). In addition, high responses of gas sensor was realised when the electrodes were

positioned with a good inter-metallic cohesion beneath the gas sensing layers as illustrated in Figure F.3 (Durrani, 2006; Korotcenkov and Cho, 2011). However, there is a challenge faced by the current manufacturing of porous gas sensors whereby the deposition of the sensors' electrodes can take place with maximal adhesion between the electrodes and the sensing layers without degradation of the the porosity of the sensing layers. Addressing this challenge could enhance sensors' sensitivity and stability during operation (Shilova, 2005; Graf et al., 2006; Korotcenkov and Cho, 2011).

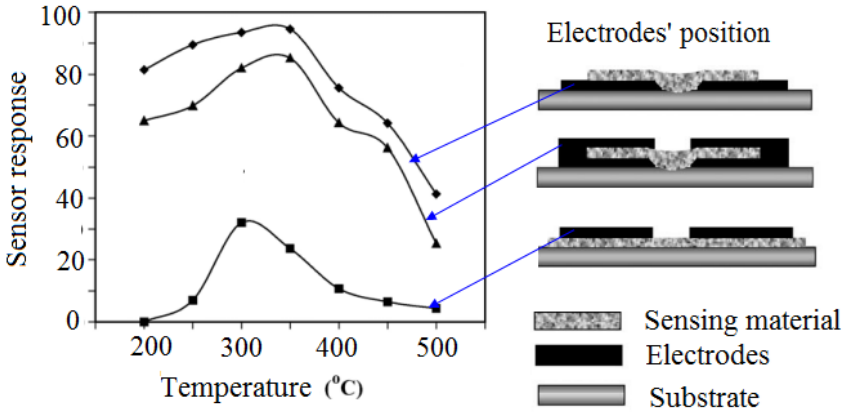


Figure F.3: Effects of electrodes position.
Source: (Durrani, 2006).

APPENDIX G : Additional Advantages of Porous Structures

The additional advantages of porous structures which make them suitable in several other applications but are not discussed further in this thesis, include the following:

1. *Less mass density* which makes porous structures necessary in the construction of light weight structures for aircrafts, automobiles, and marine vessels to reduce their mass and fuel-burn, and so improve their fuel economy (Liu and Liang, 2001; Shapovalov, 2002; Rossella et al., 2010; Hirsch and Al-Samman, 2013).

2. *Radiation capability* associated with porous metal foams which makes them necessary in the shielding of electromagnetic radiation waves emanating from electronic devices to minimise the interference of these waves with the navigation and communication equipment of the aircrafts (Persheng et al., 2001; Chung, 2001; Klemperer and Maharaj, 2009; Vasquez et al., 2009; Al-Shabib et al., 2012).

3. *Sound proof capability* of porous or foamed structures are required in the filtration of the noise produced by propulsive and non-propulsive components of aircrafts (Paun et al., 2003; Neise and Enghardt, 2003; Casalino et al., 2008; Pennig et al., 2012).

4. *Improved efficiency* emanating from increased surface area of porous metal foams, sinters, or meshes are necessary in catalyst supports for petro-chemical refinery processes (Julbe et al., 2001; Yan and Xiao, 2008; Xie et al., 2010; Jiang et al., 2013; Liang and Weimer, 2015).

5. *Enhanced Chemical reactivity* of electrodes as a result of increased surface area improves the performance of fuel cells in energy generation facilities (Gregory, 2006; Zhao et al., 2013; Yuan and Sunden, 2014; Jo et al., 2014).

APPENDIX H : Fabrication of Porous Structures

This appendix presents the principles behind the creation of pores in the structure using either natural or artificial means. This is followed by description of the selected methods for fabrication of porous structures aligned with these principles, highlighting their key steps and, the limitation inherent with them. Thus, the appendix endevours to justify the development of the new, cost effective, and efficient method for fabrication of porous structures.

H.1 Porous Structures Fabrication Principles

Fabrication of porous structures in not a new concept since nature, people and other living organisms have been creating pores for growth, accommodation, and transportation (Zhang, Wang and Ma, 2005; Sorrentino et al., 2013). For this reason, studies were carried out to identify the principles by which pores were created in the structures (Banhart, 2001). These studies established that pores were created by the following principles: loosely packing of aggregates, subtraction of aggregates, construction of materials around spaces, and self-forming processes (Rouquerol et al., 1994; Korner and Singer, 2000; Roy et al., 2003; Jo et al., 2014). These principles are briefly described in the following paragraphs.

In the principle of loosely packing of aggregates (LPA), the pores were created by loosely consolidation of particles such that they were less deformed during packing and therefore were surrounded by voids (Rouquerol et al., 1994; Zahiri et al., 2006; Singh et al., 2009). In this case, the two possible packing

strategies, illustrated in Figure H.1, that resulted in higher porosity were cubic and rhombohedral that resulted in maximum porosity of 48 % and 26 %, respectively.

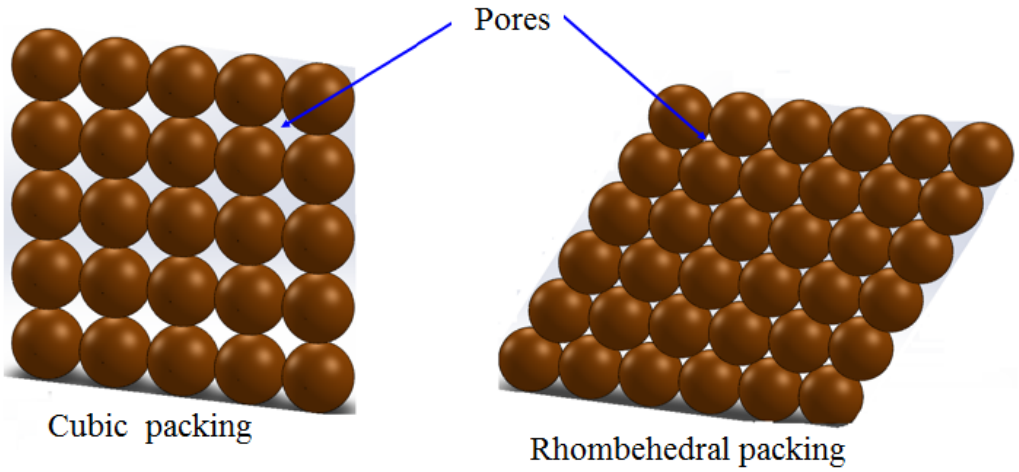


Figure H.1: Loosely packing of aggregates

In the principle of subtraction of aggregates, the pores were created by infiltration of the pattern elements with a matrix forming material follwed by removal of pattern elements using any physical means such as melting, sublimation, and leaching. This principle, illustrated in Figure H.2, resulted in new methods of making pores of micrometer or nanometer sizes in the structures by directly removal of the material (Rouquerol et al., 1994; Korner and Singer, 2000; Ryan et al., 2006; Wang, Zheng, Lim, Wang and Lam, 2011; Prakash and Kumar, 2014).

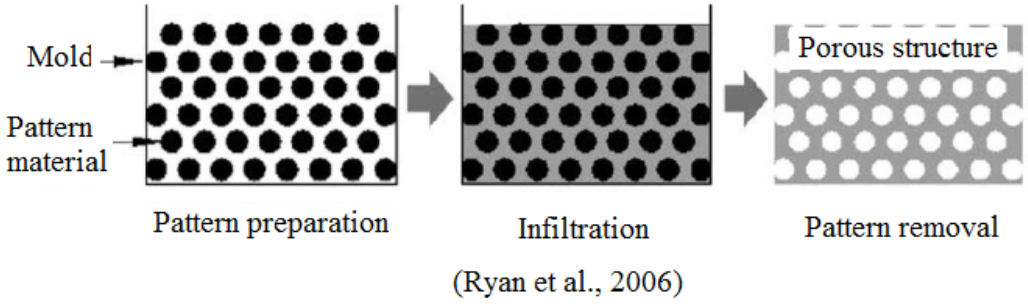


Figure H.2: Subtraction of aggregates.
Source: (Ryan et al., 2006).

In the principle of self-forming principle, the pores were created in the structure by self-evolution manner of the gas in accordance to the physical principle. In this case, the gas was introduced in the matrix by admixing the feedstock

powder with gas forming agent or by gas bubbling during molding. The gas dissolved into the material up to the equilibrium concentration under a given gas pressure and temperature to create the necessary pores (Ashby and Medalist, 1983; Banhart, 2001; Korner and Singer, 2000; Nakajima, 2007).

In the principle of construction of material around space, microscopic pores were fabricated using additive manufacturing and created products such as cup, pot, and bottle, illustrated in Figure H.3 (a), (b) and (c) made by casting, deep drawing or vacuuming forming processes (Thiruvarudchelvan and Travis, 2003; Thiruvarudchelvan and Tan, 2006; Bereaux et al., 2010). Similarly, the larger pores such as rooms in a building or cabins in the fuselage of aircrafts in (d)[1] and (e) were created by construction of materials around space (Roy et al., 2003). Natural processes such as growth and volcanic actions resulted in porous products such as bones and zeolites shown in (f) and (g) (Ashby and Medalist, 1983; Glimcher, 2006; Rimoli et al., 2008; Yukselen-Aksoy, 2010; Seetharam and Bhatia, 2012; Su et al., 2014).

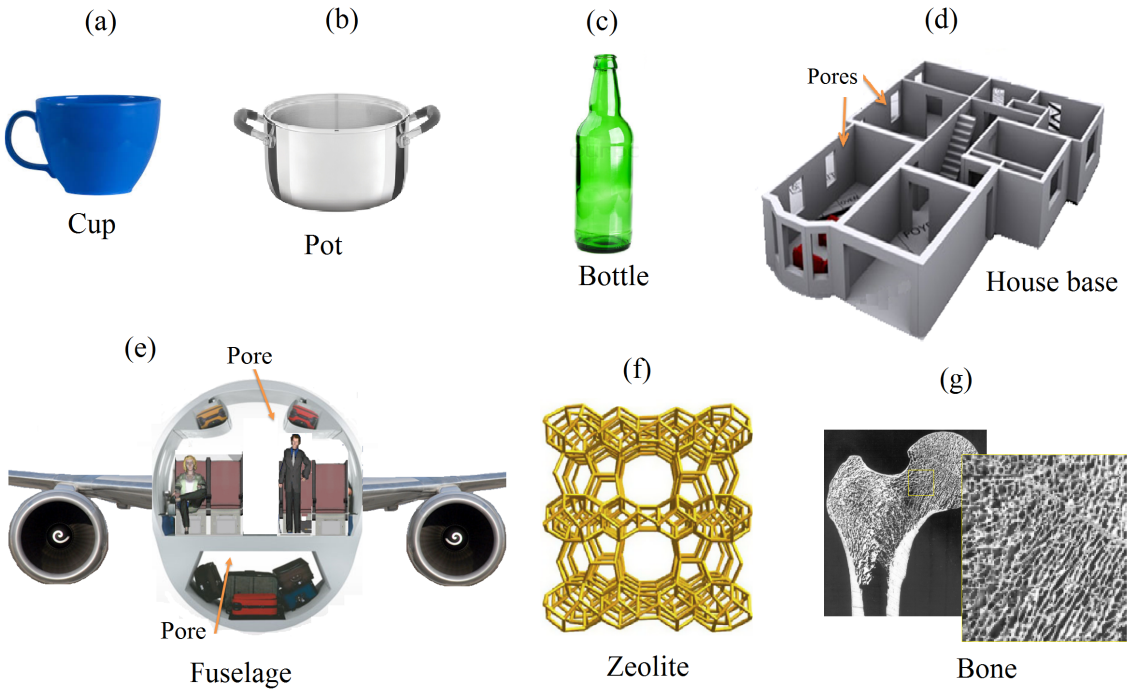


Figure H.3: Selected pore structures

[1]Modeled.

H.2 Porous Structures Fabrication Methods

Methods for fabrication of porous structures base on the principles presented above are discussed in the following subsections, and their limitation are highlighted.

The Sol-gel method, illustrated in Figure H.4, is a wet-chemistry-synthesis, based on principle of loosely packing of aggregates, with the following critical steps: the synthesis of gel from sol, deposition of gel on substrate, and finally heating to dry and consolidate the gel (Shilova, 2005; Graf et al., 2006; IMF, 2015). Although, this method was proved in many industrial applications, it failed to achieve maximal adhesion of the coatings to the substrate without degradation of the porosity (Shilova, 2005; Graf et al., 2006; Han et al., 2008; Korotcenkov and Cho, 2011).

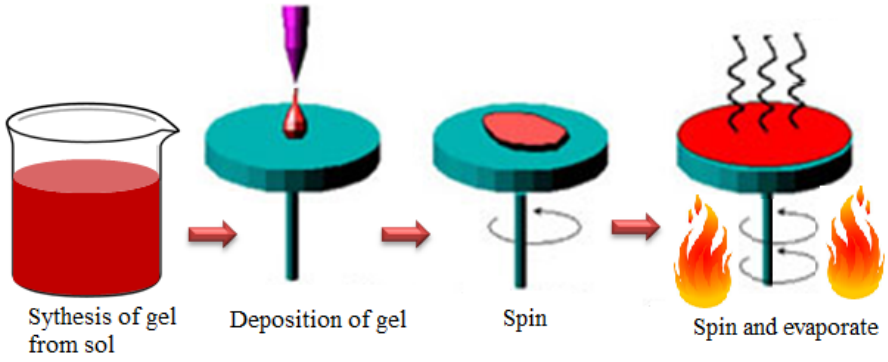


Figure H.4: Sol-gel method.
Source: (IMF, 2015).

Powder metallurgy illustrated in Figure H.5is another process that is based on loosely packing of aggregates. Its basic steps include mixing of feedstock powders, die-compaction at high pressure, and sintering at elevated temperatures (Persheng et al., 2001; Hetsroni et al., 2006; Ryan et al., 2006; HEAT, 2010). Despite its successful application in industry, powder metallurgy has limitations such as high costs, production of brittle products due to formation of cracks and oxides inside the material, and poor workability due to high pressure and temperature application during processing. These problems rendered this process unsuitable for fabrication of porous coatings on surfaces that are delicate or with complex geometries (Hetsroni et al., 2006; Ryan et al., 2006; Krishna et al., 2008; Wang, Wei, Wen and Han, 2011; Sidambe, 2014).

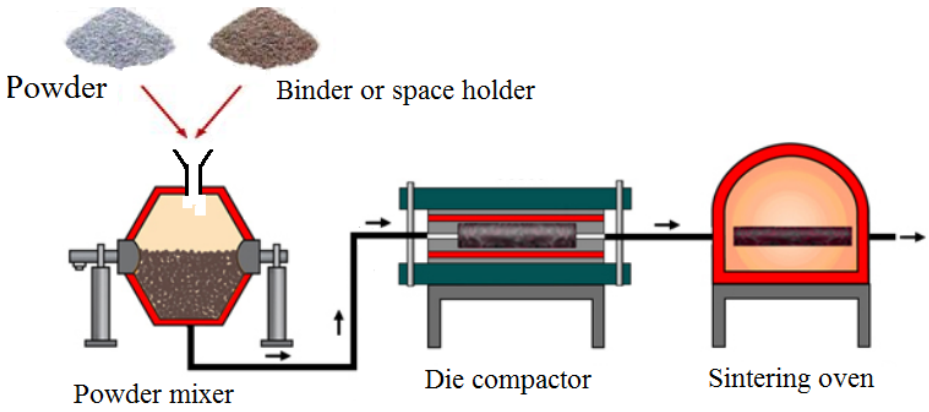


Figure H.5: Powder metallurgy process.
Source: (HEAT, 2010).

Thermal spray processes are also based on principle of loosely packing of aggregates and involve preheating to melt the feedstock powders, supersonically accelerate the melted metal powder towards a prepared substrate where the particles impacted, cooled, solidified and rapidly built a coating. These steps are illustrated in a generic thermal spray process in Figure H.6 (Julio, 2010; Julio, 2014). The distinction among the thermal spray processes is based on the sources of heat, and the common types are the plasma spray, and high velocity oxy-fuel (Lynch et al., 2013; MBE-International, 2015), discussed further in the following sections.

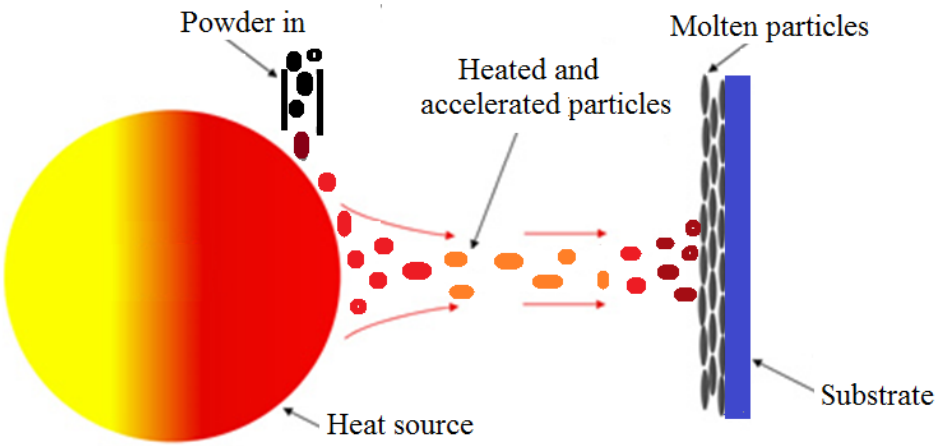


Figure H.6: Thermal spray process.
Source: (MBE-International, 2015).

Plasma spray is a metal coating technology in which an electric arc is generated between two water-cooled electrodes in a gun to heat a gas to extremely high temperatures (up to $20,000°C$) and forms a plasma jet. The feedstock powder

is injected into this plasma jet using a carrier gas and the particles in the powder are heated, melted, and accelerated to a high speed towards a prepared substrate where they impact with high kinetic energy and adhere. The physics of the plasma process is illustrated in Figure H.7. Through this process, porous coatings for titanium shown in Figure H.8 were fabricated when the parameters were set so as to limit the particle velocity and impact to create a loosely packed coating (Ryan et al., 2006). Even though plasma spray process achieved porous coatings, its major setback was that it took place at very high temperature and therefore required a vacuum to limit oxidation of the powder making it very costly (Hanson and Settles, 2003; Papyrin, 2006).

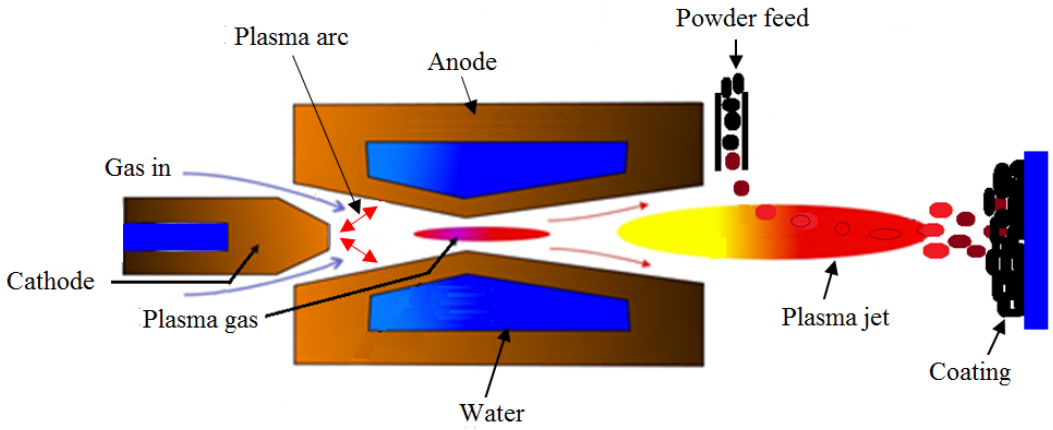


Figure H.7: Plasma spray process.
Source: (MBE-International, 2015).

The high velocity oxy-fuel (HVOF), schematically shown in Figure H.9, involved feeding of mixture of gaseous or liquid fuel and oxygen into a combustion chamber, where they were ignited and combusted continuously. The, the feedstock metal powder were injected into the hot gas stream that resulted from the hot gas which emanated at a supersonic velocity through a convergingdiverging nozzle. These hot gases partially melted and supersonically accelerated the powders towards the substrate where they deposited to form a coating (Nishimura et al., 2011). Similarly, even though the HVOF has been demonstrated in many industrial applications (), the excessive heating of the powders during deposition resulted in deleterious effects such as cracking, oxidisation, decarburisation, decomposition, crystallisation, particle melting, evaporation, gas release, grain growth, residual stress and delamination of the coating (Papyrin, 2006; Cunha et al., 2008; Chikarakara et al., 2010; Nishimura et al., 2011; Wang, Wei, Wen and Han, 2011; Li et al., 2013; Bolelli et al., 2014).

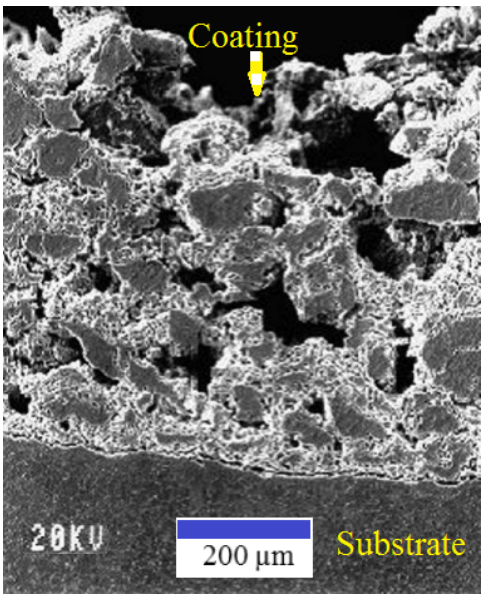


Figure H.8: Plasma spray coating
Source: (Ryan et al., 2006).

As such, HVOF is not an ideal process for coating temperature and phase sensitive materials such as titanium, copper and aluminium.

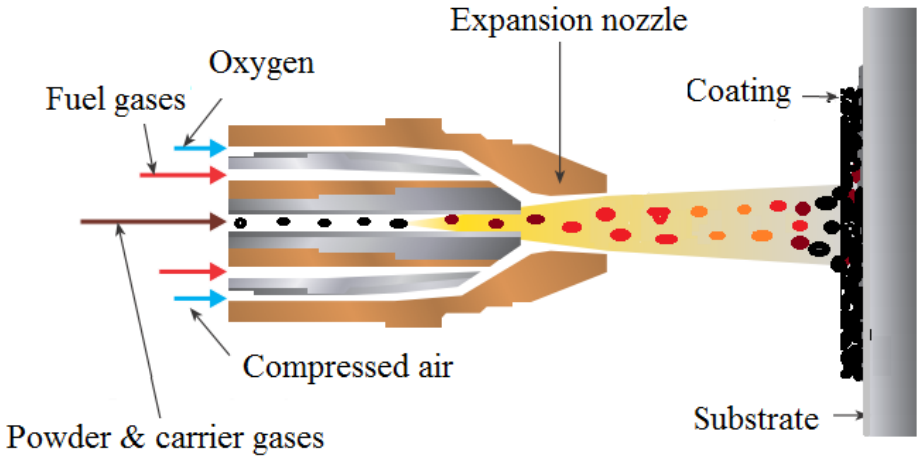


Figure H.9: HVOF process
Source: (Ryan et al., 2006).

Chemical etching is based on principle of subtraction of aggregates, and was used to make microchannels such as those shown in Figure H.10(a). This method involved formation of pores in the material through removal of the unmasked surfaces of the substrate using common acids. This process resulted in uni-directional pores illustrated in Figure H.10(b) (Qiao-Sheng et al., 2003).

Also, the pores fabricated using chemical etching exhibited irregular topography and rough inner surfaces as shown in Figures H.10(b). Although this method was demonstrated in the laboratory setup, its commercial application is hampered by the slow pace of removing the material and the failure to control the shape and surface roughness of the pores (Wang, Zheng, Lim, Wang and Lam, 2011; Prakash and Kumar, 2014; OConnor et al., 2014).

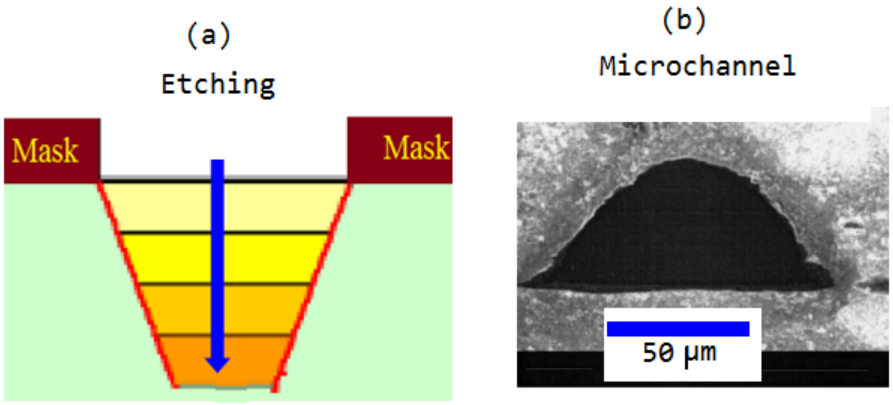


Figure H.10: Chemical etching method.
Sources : (a) (Prakash and Kumar, 2014), (b)(Qiao-Sheng et al., 2003)

Micro-mechanical cutting process used a single or multiple cutting tool of microscopic design, shown in Figure H.11(a), to remove materials and resulted in the formation of microchannels with profile illustrated in Figure H.11 (b) (Pan et al., 2009). Although this method was demonstrated in the fabrication of microchannels with regular shapes and reasonably smooth inner profiles, it proved to be unsuitable for mass production due to high tool and setup costs (OConnor et al., 2014; Prakash and Kumar, 2014).

Laser cutting technology, schematically shown in Figure H.11(c), applied a collimated laser beam to cut microchannels and achieved rough inner surfaces shown in Figure H.11 (d) (Wang, Zheng, Lim, Wang and Lam, 2011; Zhou et al., 2014). However, this technology is not yet developed for commercial production of porous parts because it is slow and cannot fabricate desired shapes due to inconsistent interaction between the laser jet and the material being cut. This inconsistence resulting in the pores with irregular topography and rough inner surfaces as seen in Figure H.11(d) (Wang, Zheng, Lim, Wang and Lam, 2011; Zhou et al., 2014; OConnor et al., 2014). Consequently, these processes do not suit the modern requirement for production of microchannels

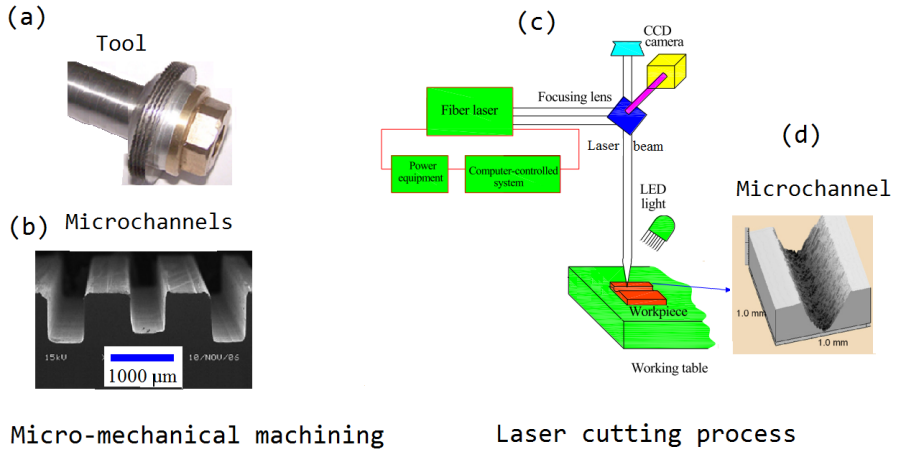


Figure H.11: Micro-mechanical and laser cutting.
Sources: (a),(b) (Pan et al., 2009), (c) (Zhou et al., 2014), (d) (Wang, Zheng, Lim, Wang and Lam, 2011)

in which the balancing between surface texture, low cost, and high productivity are cardinal and, the top surfaces of the microchannels fabricated by these methods were open and required extra processes to enclose them (Prakash and Kumar, 2014).

Additive manufacturing method applied the principle of enclosing of material around space to create pores in the structures using computer aided design (CAD), part modeling, and layer-by-layer deposition of feedstock material (Vayre et al., 2012; Julio, 2010; Julio, 2014; Kim et al., 2014). The cutting-edge technology based on this concept is the $3D$ Printing, also called stereolithography (Arjun, 2014), and is illustrated in Figure H.12(a). In this technology, the pattern was transferred from a digital $3D$ model, stored in the CAD file, to the object using a laser beam scanned through a reactive liquid polymer which hardened to create a thin layer of the solid (Arjun, 2014). In this manner, the microchannels were fabricated in the polymer (OConnor et al., 2014). Although this method was proved in the laboratory setup, its setback is the slow pace of building layers, high initial costs and the microchannels produced had irregular topography as shown in Figure H.12(b) (Zhou et al., 2014).

Electron beam melting shown in Figure H.13(a), applied the principle of enclosing of material around space to create pores in the structures. This method involved melting and layer-by-layer deposition of metal powders using a magnetically directed electron beam. Although this method was proved to

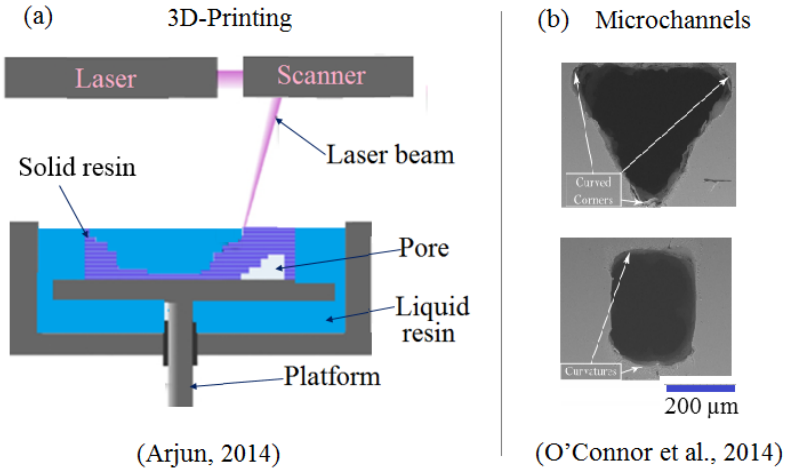


Figure H.12: 3*D*-printing process.

be successful in the laboratory trials, it had a problem of high setup costs due to the requirement of high vacuum atmosphere around the beam of electrons and the workpiece (Sidambe, 2014). Similarly, the **Selective Laser Melting** method, shown in Figure H.13(b) deposited the materials by completely melting the metal powders using a high-power laser beam. Similarly, this method proved to be costly due to need of advanced cooling systems, and the fluctuations of temperatures during processing negatively affected the density of the products (Bartolo, 2010; Sidambe, 2014).

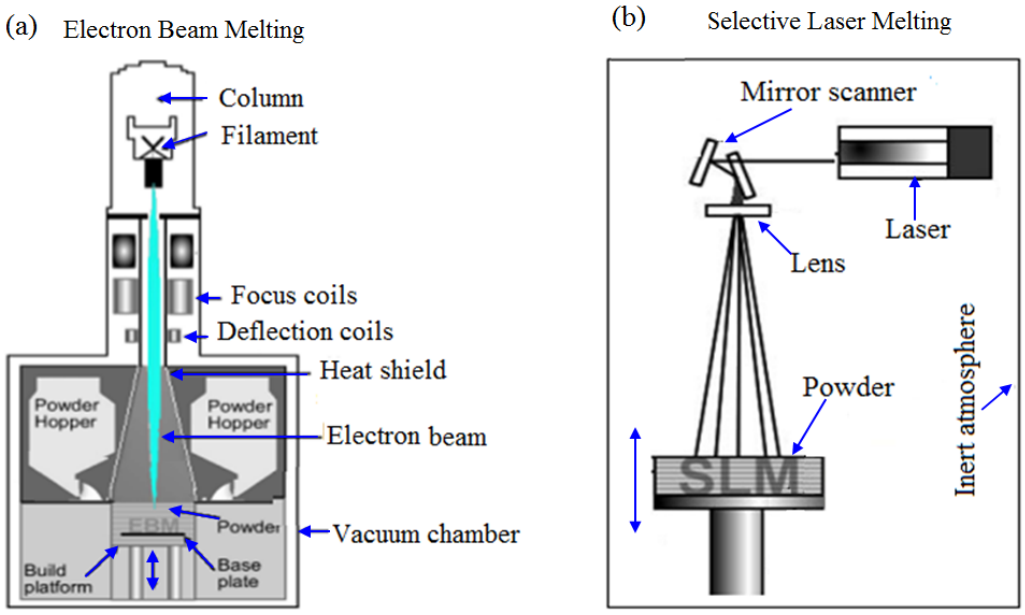


Figure H.13: Electron beam and selective laser melting.
Source: (Sidambe, 2014)

The two common methods based on principle of self-evolution were the gas-bubbling and self propagating high-temperature synthesis. In the **gas-bubbling method**, the pores were created in the structures by either directly bubbling the gas in the materials or indirectly by admixing of the feedstock powder with gas forming agent and reacted it to form a gas in the material (Banhart, 2001; Korner and Singer, 2000). The major challenge with this method was its inflexibility during processing and it only manufactured porous solids, and not porous coatings on substrates (Nakajima, 2007).

Then, the **self propagating high-temperature synthesis** involved mixing of reagents, cold compaction, and finally ignition to initiate a spontaneity self-sustaining exothermic reaction to transform the cold compacted structure into a desired porous structure as illustrated in Figure 2.6. Although this method proved to be of low cost due to exothermic nature of the reaction, it produced undesirable inter-metallic compounds owing to high temperature reaction (Biswas, 2005; Arakawa et al., 2012).

APPENDIX I : Introduction to Cold Spray Process

Cold spray (CS) process, originally called the Cold Gas Dynamic Spray (CGDS) process, is the newest member of the thermal spray processes (see Figure I.1), capable of depositing a variety of powders, and composites using compressed and preheated gases (Zahiri et al., 2006; Parthasarathy et al., 2011). Unlike other thermal spray process which implement bonding only at elevated temperature, CS can deposit materials at low temperatures and moderate deposition efficiency (Papyrin, 2006; Irissou et al., 2007; Zahiri et al., 2009; Wong, 2011a; Julio, 2014; Advance-Coatings, 2015).

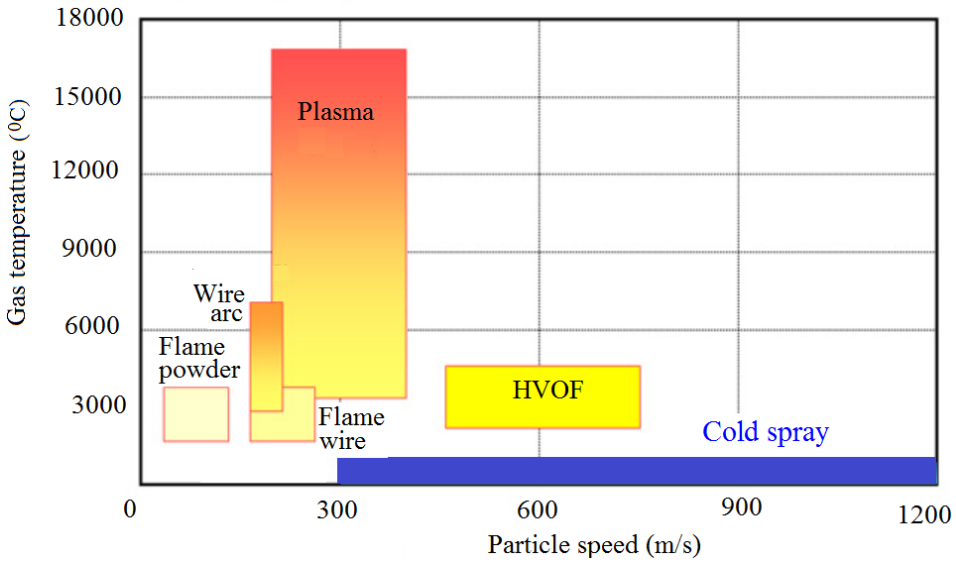


Figure I.1: Comparison between CS and thermal spray processes. Source: (Advance-Coatings, 2015).

I.1 Evolution of CS (CS) process

CS was discovered in mid-1980s by Dr. A.N. Papyrin and his colleagues during the supersonic wind tunnel test (Figure I.2 (Papyrin, 2006)) which was carried out at the Institute of Theoretical and Applied Mechanics of the Russian Academy of Sciences in Novosibirsk.

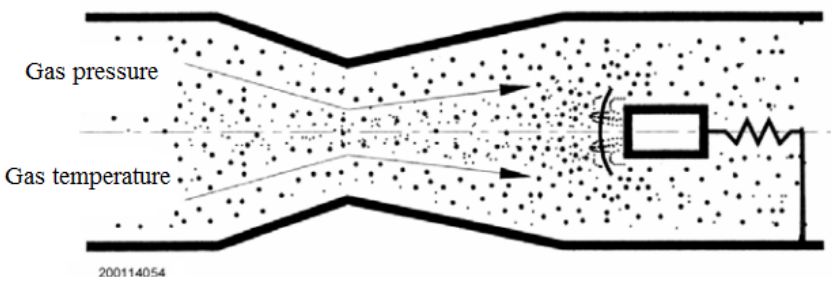


Figure I.2: Wind tunnel test

During this test, the pressurised and pre-heated gas was directed through a convergent/divergent duct. The purpose of this test was to establish the interaction of a two-phase flow (gas and solid particles) with the surface of immersed bodies in which a new gas dynamics diagnostic tool was used to study the gas and solid particles flow around the bodies. The small tracer particles of aluminium were rapidly deposited on the surface of the target when their velocity was above a transition value. However, when these particles were projected at a velocity below this transition value, erosion of the surface of the target occurred. The continued bombardment of the solid target by these particles resulted in a thick and highly bonded coating (Dykhuizen and Smith, 1998; Papyrin, 2006; Goyal et al., 2012).

After Papyrin and his colleagues invented the CS process, they presented their findings in the United States in 1994, which led to the first research on cold spray at the National Centre for Manufacturing Sciences of Ann Arbor. Thereafter, a U.S.patent on the CS process was issued in 1994, while the European patent was issued in 1995 (Wong, 2011a). Before these results, engineers assumed that in the two-phase flow, the particles would need to be heated to high temperatures (near or at melting point) in order to create a coating (Wong, 2011a). However, the discovery of CS process dawned new ways of thinking by engineers about metal coating processes. Thus, realising the potential of this new cold (creating a coating near room temperature) method,

Papyrin and his colleagues performed more experiments in order to thoroughly investigate this phenomenon. These additional experiments studied the importance of particle velocity which led to the idea of critical velocity and the effect of gas temperature on deposition efficiency. In these experiments, metals, metal alloys, and composites were successfully deposited on various substrates (Wong, 2011a).

Currently, CS has undergone a full technological evolution cycle and is emerging as the cutting-edge surface engineering innovation and is currently receiving a lot of research attention in the deposition of a wide range of materials such as pure metals, metal alloys, polymers, ceramics, composite materials, and nanocrystalline powders (Dykhuizen and Smith, 1998; Goyal et al., 2012; Papyrin, 2006; Irissou et al., 2008). In this regard, two CS systems (see I.2) were developed and are available on the market.

I.2 CS Systems

The two CS systems are the lower pressure CS system (LP-CS) and the high pressure CS system (HP-CS). The main components of a generic CS system include the source of compressed gas, gas heater, powder feeder, spray nozzle assembly, and sensors for gas pressure and temperature. The source of compressed gas acquires the gas from an external reservoir, compresses it to desired pressure and delivers it into the gas heater. Then, the gas heater preheats the compressed gas in order to increase its enthalpy energy. The preheated gas is delivered into the spray nozzle assembly whose convergent/divergent geometry not only converts the enthalpy energy of the gas into kinetic energy but also mixes the powder and the gas proportionately. The powder feeder meters and injects the powder in the spray nozzle assembly. The sensors for the gas pressure and temperature are responsible for regulating the preset pressure and temperature of the gas stream. The powder injection point in the spray nozzle assembly, the gas pressure, and gas temperature distinguish the HP-CS system from the LP-CS system. Several other parameters which contribute towards this distinction are summarised in Table I.1 (USA-Defense, 2008).

Further, in the HP-CS, a high pressure powder injection system is required in

Table I.1: Operation parameters for CS systems

Parameters	**HP-CS**	**LP-CS**
Working gas	nitrogen, air, helium	nitrogen, air, helium
Gas pressure, Mpa	$0.5 - 5.0$	$0.5 - 1.7$
Gas temperature, °C	$20 - 1000$	$20 - 600$
Gas flow rate, m^3/h	$2 - 200$	$15 - 78$
Maximum gas match no.	$1 - 3$	$1 - 3$
Powder flow rate, g/s	$0.1 - 2.0$	$0.1 - 1.0$
Particle size, μm	$5 - 100$	$5 - 50$

order to propel the powder particles from the powder feeder into the nozzle. Using the process parameters summarised in Table I.1, the HP-CS system can achieve a high deposition efficiency for a wider range of feedstock powders and the resultant coatings are dense (Papyrin, 2006). Figure I.3 shows the architecture of the components in a HP-CS system (Fukamuna and Huang, 2009). As can be seen from this figure, the feedstock powder is injected in the convergent section of the nozzle assembly.

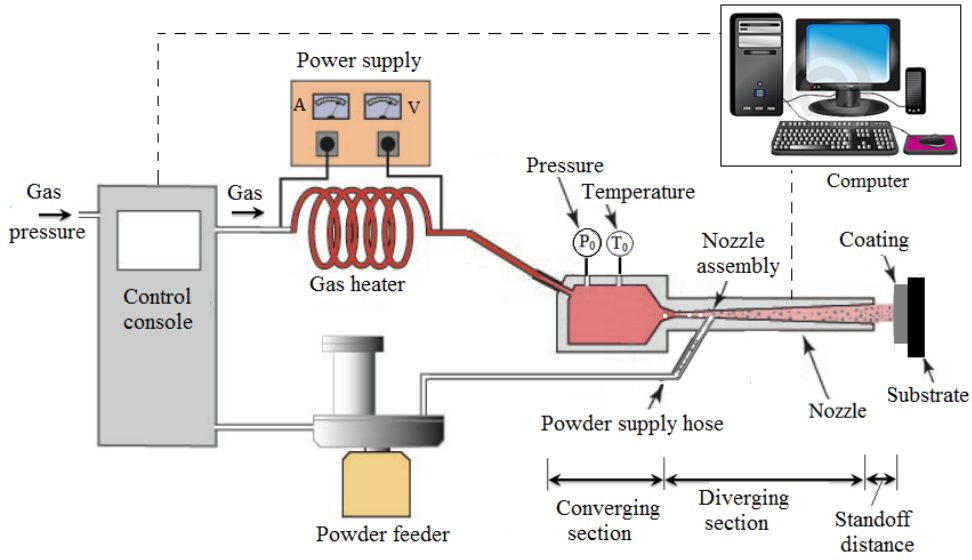


Figure I.3: CS process configuration.
Source : Modified from (Fukamuna and Huang, 2009).

I.3 Deposition by CS Process

To deposit the metal powders, the CS system injects the powder particles in the supersonic stream of compressed and preheated gas that accelerates the particles to supersonic speeds towards the substrate where they bond due to impact (Dykhuizen and Smith, 1998; Papyrin, 2006; Zahiri et al., 2006; Goyal et al., 2012). To achieve a uniform thickness of the coating, the spray jet is scanned parallel to the surface of the substrate using manual or robotic arm control system. The traversing speed of the spray gun is controlled by a program inputted via the computer in the case of the automated system. The spray parameters such as powder feed rate, gas temperature and gas pressure are entered in the control console, while the standoff distance is altered by offsetting the nozzle from the substrate (CenterLine, 2010).

I.4 Bonding Mechanisms in CS Process

In order to improve the quality of coatings fabricated by the CS process, studies were carried out to ascertain the nature of bonding. Two types of bonding that were identified included the particle-onto-substrate, which is necessary for the formation of an initial mono-layer of particles and determined the adhesive strength of the final coating on the substrate; and particle-onto-particle, which allowed a thickness of the deposit to build up, and affected the cohesive strength of the deposit (Wu et al., 2012). In this respect, several theories were developed to explain the bonding mechanisms in CS .

According to first theory, the bonding was modelled as a plastic deformation of the particle-substrate or particle-particle interaction using finite element analysis. Based on this theory, it was established that the bonding of particles was attributed to adiabatic shear instabilities which occurs at the particle-substrate or particle-particle interfaces. This modelling also showed a non-uniform development of strain and temperature at the interface and suggested that this bonding is confined to a fraction of the interacting surfaces (Assadi et al., 2003).

Then, the second theory applied dynamic finite element analysis to study the

interactions between the particles and the substrate during the CS process. Similarly, this study revealed that the plastic deformation occurs at a localized thin region adjacent to the particle-substrate interface. At this interface, the thermal-softening effects caused the adiabatic shear instability. This resulted in the injection of an interfacial jet consisting of the highly deformed material, and removed the oxide films from the surfaces of the particle and the substrate that enabled an intimate contact of clean metallic surfaces and hence promoting particle-substrate bonding. Figure I.4 illustrates the temporal evolution of the particle and the substrate materials during the particle collision. From this figure, the growth of the metal jet between the substrate and the particle progressed from the point of initial contact. However this theory did not relate the particle deformation with process parameters (Grujicic et al., 2004).

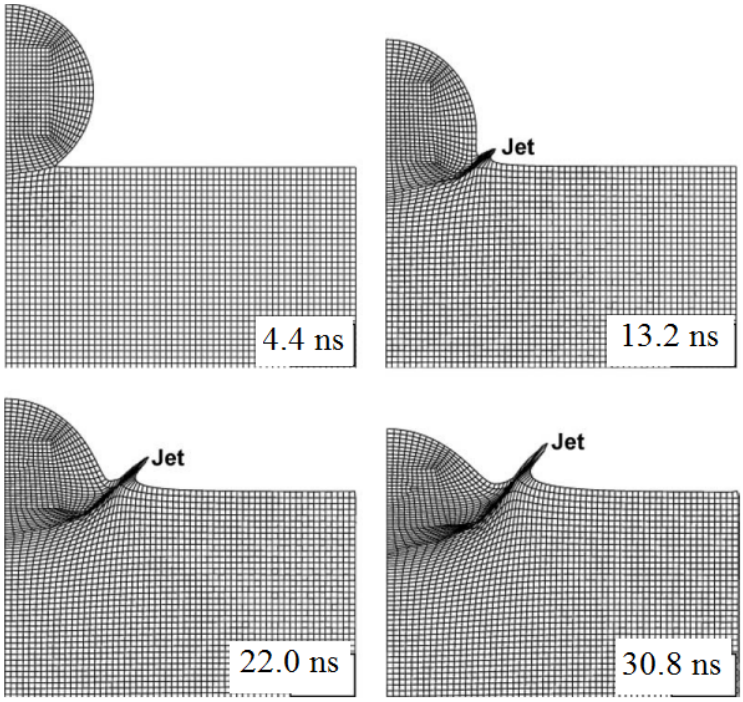


Figure I.4: Particle evolution during bonding

The third theory was proposed that the bonding of particles was largely caused by melting of the particle at the contact which resulted in the formation of a jet of material at the interface when the velocity of the particle is greater than 700 m/s by (Schmidt et al., 2006). However when particle velocity was lower than 700 m/s system, it was argued that the inter-facial melting was not likely to occur, and so the bonding of particles is caused by inter-facial heating during impact (Schmidt et al., 2006; Dewar et al., 2012). Therefore, a study

to examine the heat generation and deformation mechanisms during LP-CS process of pure aluminium powder was conducted by (Dewar et al., 2012). This study revealed that the interparticle bonding was caused by deformation and recrystallisation that occur in the interior of the splat than resulted in inhomogeneity due to presence of ultra-fine grain structures in a matrix of course grained powders (Dewar et al., 2012). These results agreed with those of a simulation and experimental studies. Therefore, nano-recrystallization contributed majorly to the bonding in LP-CS where there is limited interparticle contact due to limited particle velocity and deformation (Dewar et al., 2012). In summary, the theories that suggested that the causes of bonding in CS are adiabatic shear instability and nano-recrystallization seemed to be convincing to justify the particle bonding that occurred in both LP-CS and HP-CS systems.

I.5 Research Works on CS Process

CS process was proposed as a method for making porous structures since the actual technologies used to fabricate the porous products have limitations in meeting some of the modern manufacturing requirements such as flexibility, efficient and cost effectiveness (Zahiri et al., 2006; Zahiri et al., 2009; Elahinia et al., 2012; OConnor et al., 2014; Zhou et al., 2014; Prakash and Kumar, 2014). The CS process has several advantages such as capability to fabricate thermally and electrically conductive, dense, thin or thick coatings, with reasonable bond strength at moderate to high deposition efficiency (Champagne et al., 2005; Sundararajan et al., 2010; Li et al., 2010; Venkatesh et al., 2013; Kikuchi et al., 2013; Xiong et al., 2015). Due to its low temperature deposition, the CS process was proved to be capable of depositing Oxygen sensitive and thermally degradable materials such as Titanium, and other nano-, micro-, or macro-phased alloy materials (Grujicic et al., 2004; Gartner, Stoltenhoff, Voyer, Kreye, Riekehr and M, 2006; Papyrin, 2006; Cinca et al., 2010; Lioma et al., 2015). The flexibility during selection of process parameters and low gas consumption at moderated deposition efficiency enabled CS to achieve lower operational costs (Zhang, Shipway and McCartney, 2005; Irissou et al., 2007; Zahiri et al., 2009). Finally, the coatings fabricated by CS process exhibited higher

hardness than the bulk materials due to the high degree of plastic deformation of the particles at impact (Papyrin, 2006; Lioma et al., 2015). However, the CS process exhibited some limitations such as low ductility of coatings, and incapability to spray pure ceramics or nanostructured powders without blending and/or agglomerating them (Hall et al., 2006; Lioma et al., 2015). In addition, there is limited selectivity of substrates because these required minimum ductility to produce well bonded coatings (Zhang, Shipway and McCartney, 2005). Finally, the HP-CS system proved to have higher operations costs compared to LP-CS system due to high consumption of process gases (Irissou et al., 2007).

Because of the advantages that outweighed the disadvantages, few investigations using CS process were carried out to establish the process conditions that minimise porosity in the structures, using copper as feedstock, and the spray parameters such as temperature and pressure of the gas, and nozzle offset from substrate (standoff distance) were varied so as to eliminate porosity in the coatings (Zahiri et al., 2006). The results of these investigations indicated that an increase in gas temperature and pressure, and reduction in standoff distance resulted in the reduction in the porosity of the coatings as illustrated in Figure I.5 (a), (b) and (c), while large particles resulted in increased porosity of the coatings (Zahiri et al., 2006).

Further investigations were carried out to establish the influence of the type of the gas and the process parameters on the porosity of titanium coating. In this study helium and nitrogen gases were used as process and powder carrier gases. According to this study, the increase in temperature and pressure of the gas, and reducing the stand-off distance resulted in reduction of the porosity of the titanium coating. Also, helium gas instead of nitrogen or air as powder carrier gas led to reduction in the porosity of the coatings (Zahiri et al., 2009). Based on this premise, it was believed that when these process conditions were applied in the opposite way, then the porosity of the coating could be enhance.

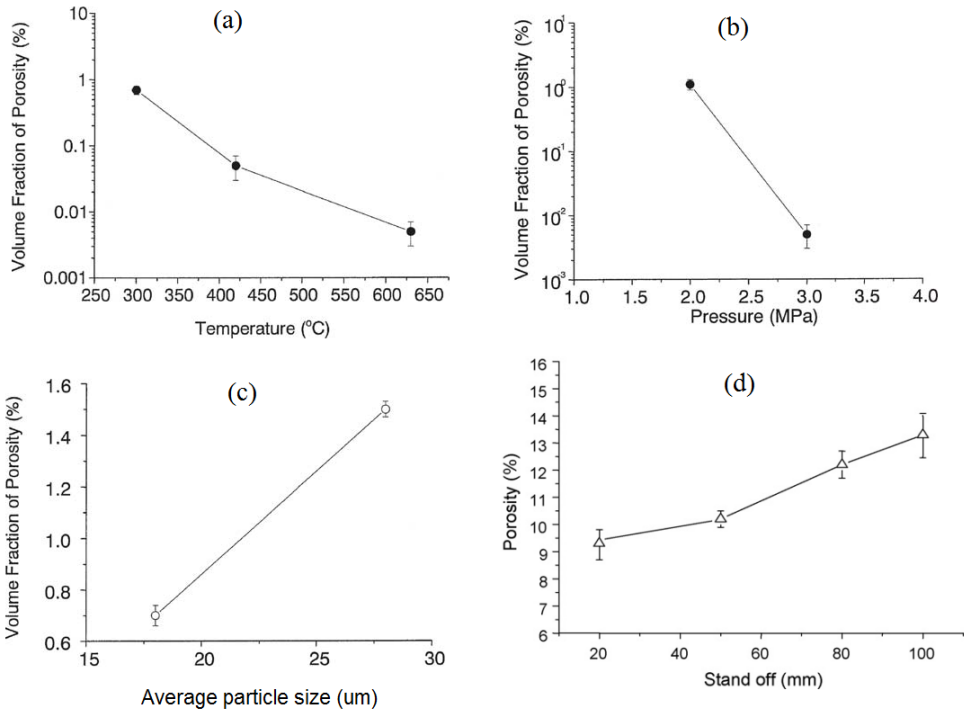


Figure I.5: Porosity minimisation in CS coatings.
Source: (Zahiri et al., 2006)

APPENDIX J : Methodological Processes

This appendix explains the selection of powders and equipment, powder mixing process, calculation and optimisation of spray parameters, and fabrication of microchannels and antimicrobial filters.

J.1 Selection of Powders and Equipment

The feedstock powders were selected such that they were sprayable using the LP-CS process and the material properties were compatible for micro heat sinks, antimicrobial filters, bone implants and gas sensors (Tuckerman and Pease, 1981; Edelman et al., 2000; Levine and Fabi, 2010; Varkey, 2010). On this basis, the following powders were selected: alumina or aluminium Oxide (Al_2O_3), aluminium (Al)-alumina (Al_2O_3), copper (Cu), chromium (Cr), magnesium (Mg), nickel (Ni), tin-oxide (SnO_2), titanium (Ti) and zinc (Zn). The supply codes, area of application, mesh sizes and suppliers of these powders are summarised in Table J.1.

where EC stand for electronics cooling, BI for bone implants, AMF for antimicrobial filtration, and GS for gas sensors. Then, the equipment and software, summarised in Table J.2, were selected for characterisation the powders, fabrication of porous coatings, characterisation and test of specimens.

Table J.1: Selected powders.

Powders	**Code**	**Application**	**Mesh** (μm)	**Suppliers**
Alumina	SST G0002	Activation	$-300+100$	Centreline
Al-alumina	SST A0050	EC, AMF	$-45+5$	Centreline
Chromium	$266299-500G$	EC	$-75+10$	Sigma Aldrich
Copper	SST C5003	EC, AMF	$-45+5$	Centreline
Magnesium	$13112-1KG$	BI	$-75+10$	Sigma Aldrich
Nickel	SST N5001	BI	$-45+5$	Centreline
Tin-oxide	$244651-100G$	GS	< 0.1	Sigma Aldrich
Titanium	SST T5001	BI	$-45+5$	Centreline
Zinc	SST T5001	AMF	$-45+5$	Centreline

Table J.2: Selected equipment and software.

Equipment/software	**Specification**	**Purpose**
Cold spray facility	SST series P	Powder deposition
Cutting machine	-	Sectioning
Infra red thermometer	Top-Tronic300 °C	Temp. Measure.
Fume hood	Esco	Fume protection
Hot press	SimpliMet3000	Hot mounting
Polishing Machine	Struers Tegramin-20	Polishing
Powder Size Analyser	Marven Mastersizer-2000	Size analysis
Optical Microscope	LEICA CTR -6000	Microanalysis
Planetary ball mill	Retsch PM-400 MA	Powder mixing
Pressure booster	Festo DPA-63	Amplify pressure
FE Scanning E.Microscope	Carl Zeis SIGMA	Microanalysis
microhardness Tester	Vickers FM-700	Microhardness
Scale	Satorius -1mg	Measuring mass
Sieve shaker Fritch	Analysettes3 PRO	Sieving powders
Tensile testing machine	Shimadzu AG20kN/50kNIC	Tensile testing
Software ImageJ	ImageJ 1.45	Porosity Testing
MATLAB	MATLAB R2010b 1.45	Simulation
Solid Edge	Solid Edge	Simulation
Soldering iron	40W	Heating coatings

J.2 Mixing of Powders

Mixing of powders, was carried out to study the influence of powder composition on process conditions and the coatings. The powder that were mixed were: aluminium-alumina and copper, aluminium-alumina and zinc, copper and chromium, titanium and nickel, tin-oxide and copper, and magnesium and titanium. These powders were mixed according to the percentages summarised in Table J.3.

Table J.3: Powder mixtures.

Composition	**Percentages**	**Application**	**Substrates**
Al:Al-alumina:copper	60 : 20 : 20	Antimicrobial	Cu
Al:Al-alumina:zinc	60 : 40	Porosity test	Al
Copper:chromium	80 : 20	Heat sinks	Cu
Titanium:nickel	50 : 50	Bone implant	Cu,Fe,Ti
Tin-Oxide:copper	70 : 30	Gas sensors	Al_2O_3
Magnessium:titanium	60 : 40	Bone implant	Fe

Prior to mixing the powders, optmisation of mixing parameters was necessary since the only mixing parameters provided in literature were for milling to re-size the particles in the feedstock powders (Tria et al., 2009; Zhou et al., 2010; Tria et al., 2011). During optmisation, the planetary ball mill, type Retsch PM400 MA, equipped with four stainless steel vials was used. The mixing media were the stainless steel balls of diameter 15 mm each. In the initial mixing trial, the parameters used were from literature and included the following: rotational speed of 300 revolutions/minute, mixing time of 2 hours and the powder to ball mass ratio (PBR) of 1 to 3 (Tria et al., 2009; Zhou et al., 2010). However, these mixing parameters favourably agglomerated the tin-oxide and Copper mixture, but the rest of the powders were excessively agglomerated as shown in Figure J.1 and were not suitable for CS process.

Therefore, starting with the above mixing parameters, several mixing trials were carried out in which the values for the rotational speed, mixing time and PBR were cautiously reduced in steps of 25, 15 and 1, respectively, until optimum values were found. In each trial, the mixing process was stopped every 15 minutes and small powder samples were taken and viewed under the optical microscope to examine their homogeneity and agglomeration.

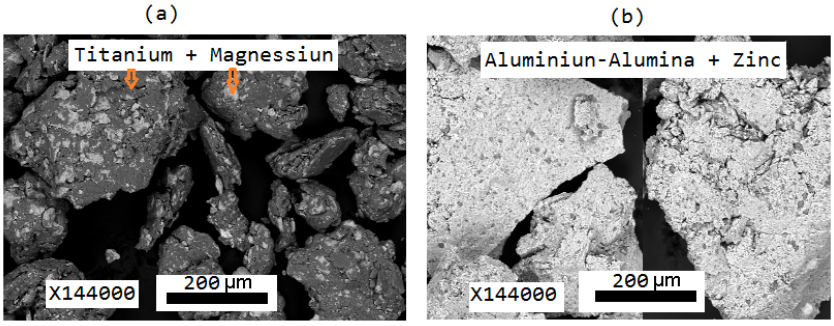


Figure J.1: Enlarged particles.

In this process, optmisation was attained when the powder mixtures were homogenised, without agglomeration of the particles, and the corresponding parameters were the optimal ones. For most powder mixtures, it was found that the optimal mixing parameters were as follows (i) rotational speed of 250 revolutions/minute, (ii) mixing time was between 15 minutes and 30 minutes, and (iii) the PBR was 1 to 1. Using these parameters, the rest of the powders were mixed, in exception of the tin-oxide nanoparticles which were initially agglomerated by mixing with (5 % by weight) copper powder and milled at rotational speed of 300 revolutions/minute for 2 hours and PBR of 1 to 3. Then, the agglomerated tin-oxide particles were mixed with 30 % by weight copper powder using the optimised mixing parameters stated above. After mixing, selected powder mixtures such as aluminium-alumina and zinc, titanium and nickel, and magnesium and titanium were sieved using a sieve with apertures of 53 μm in diameter to remove the excessively enlarged particles and prevent clogging of the delivery pipe during cold spraying. The sieve was fitted on the Fritch sieve shaker which was set to vibrate at an amplitude of 1.8 mm, the sieving time was set at 10 minutes and the sieving interval at 3 seconds. Finally, the sieved powders were characterised for morphology using FESEM. The results from this powder mixing process and characterisation are presented in Chapter 4.

J.3 Calculation of Spray Parameters

Calculation of process parameters was carried out to quantify their values during design and preparation of the CS process. The temperature (T_0) and pressure (P_0) of the working gas (air) were the fundamental parameters which

were calculated by equating the empirical model for estimating the velocity of the particle (equation (L.1)) to the empirical model for determining the critical velocity of the particle (equation (L.3)) (Alkhimov et al., 2001; Schmidt et al., 2006). Under this condition, the deposition of the particles was presumed to have occurred (Dykhuizen and Smith, 1998; Zahiri et al., 2006). These calculations were carried out using the isentropic gas flow models, outlined in Appendix K. The following assumptions were applied during these calculations:

- the sizes of the particles in the feedstock powders were normally distributed,
- the process gas was perfect with constant specific heat capacity,
- the effect of the bow shock waves on particles' deposition was neglected,
- the velocity of the particles was constant in the gap between the exit of the nozzle and the substrate.
- the gas flow process in the nozzle was isentropic, thus reversible, frictionless and one dimensional with no exchange of heat with the environment.

Considering the assumptions mentioned above, the values for T_0 were varied between 200 °C and 550 °C in steps of 25 °C. In this case the 200 °C was taken as the lower sprayable limit for the selected powders and the 550 °C was the upper limit for the LP-CS equipment. The values for T_0 were also used in the estimation of critical velocity for the powders. Then, the values for P_0 were estimated iteratively using equation (L.1) until a point where the value for the velocity of the particle was equal to that of the corresponding critical velocity. The initial values for the standoff distance (S) were provided in the technical data sheets for the respective feedstock powders from which the permutations for T_0 , P_0 and S were made using the Taguchi L_8 Orthogonal Array Design of Experiment (TOADE) as explained in Appendix M. According to this process, the permutations for the parameters were based on Three-factors, Three-levels, Eight-runs factorial experiments (Dingal et al., 2008). To validate the selected permutations of the spray parameters, the deposition trials were carried out using constant feed rate setting of 45 % and traversing speed of the gun set at 10 m/s. During these trials, the parameters which resulted in rapid build up of the coatings were selected as viable ones. Based on this approach, the spray

parameters for aluminium -alumina, copper, zinc and titanium powders were determined and the results are summarised in Table N.1, Table N.2, Table **??** and Table N.4.

However, the values for spray parameters given by the above method could not be used for validation of the CS process (Lioma et al., 2015). As such, an additional method such as the Central Composite Design of Experiment-Response Surface Methodology (CCDOE-RSM) was necessary. This method has the advantage that its results are compatible for development of empirical mathematical model using polynomial regression modeling necessary for validation of the fabrication process (Hamweendo et al., 2014b; Karthikeyan et al., 2014; Thirumalaikumarasamy et al., 2014). To calculate the process parameters for titanium powder using this method, the empirical model (J.1) was used.

$$X = \frac{X_i}{3.364}[X_{max} - X_{min}] + \frac{[X_{max} + X_{min}]}{2} \tag{J.1}$$

where X is the process parameter, X_i is the coded level, X_{max} and X_{min} are the maximum and minimum values of the process parameters which were determined from the capability of the process or the specification limits for the feedstock material, respectively. In this study, the maximum and minimum limits for the temperature and pressure, and the standoff distance were 200 °C and 550 °C, 5.5 bar and 15.0 bar, and 10 mm and 40 mm, respectively. These values were based on sprayable limits for the feedstock powders and capability limits of CS process. The values for the coded levels were -1.682, -1, 0, $+1$, and $+1.682$, which are the coordinates of the location points on the corners of the cube enclosed by the response surface and its intersection with the principal axes T, P, and S as shown in Figure J.2 (Miller et al., 1999; Karthikeyan et al., 2014).

By listing the above coded levels and collating them with the calculated process parameters, the permutations for the process parameters were made in the design matrix as reported in (Hamweendo et al., 2014b; Karthikeyan et al., 2014; Thirumalaikumarasamy et al., 2014). To validate these process parameters, deposition trials were carried out at optimised powder federate percentage of 45 % and traversing velocity of 10 mm/s for the automated gun.

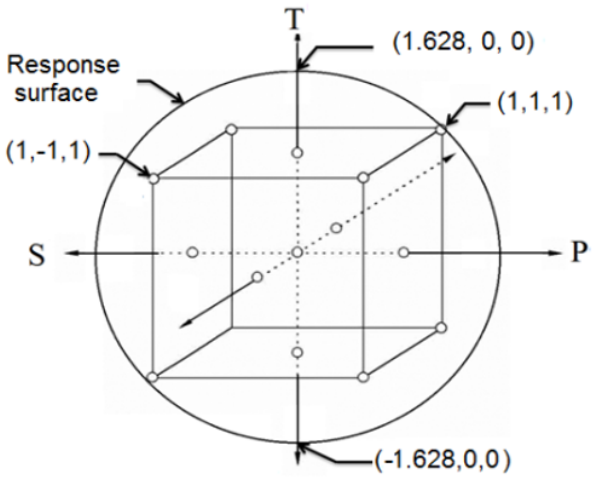


Figure J.2: Response surface

The results obtained from these trials are summarised in Table N.3. Further information about the TOADE and CCDOE-RSM methods is presented in Appendix M.

J.4 Optimisation of Spray Parameters

The spray parameters for fabrication of coatings using powder mixtures were optimised from those in Table N.1, Table N.2 and Table N.3, in which the aluminum-alumina, copper, and titanium were used as the binding powders. During optimisation, these spray parameters were adjusted until there was rapid build up of the coating and there was no clogging of the powder in the feeding system. The spray parameters for fabrication of microchannels and antimicrobial filters were optimised as explained in the respective fabrication steps below. The optimised spray parameters are summarised in Appendix N.

J.5 Fabrication of Microchannels

To fabricate the microchannels alloying using CS process followed by de-alloying using common acids was carried out. The Copper and aluminium-alumina powders were selected as matrix former and pore forming agent, respectively. Then the substrates were cut to size of 40 mm long, 40 mm wide, and 5 mm thick from the copper slab because it hardly reacts with hydrochloric ((acid (HCL). Thereafter, the process parameters, namely the temperature and pressure of the gas and the powder feed rate were optimised for deposition of Copper by inputting their values in the control console of the CS machine. The optimised spray parameters were selected if the copper powder sprayed without a mask did not change its colour. Similarly, the process parameters for aluminium-alumina powder mixtures, namely the temperature and pressure of the gas, powder feed rate, velocity of the gun and the standoff distance between the spray gun and the mask (SOD_{GM}), standoff distance between the mask and substrate (SOD_{MS}), standoff distance between the spray gun and substrate (SOD_{GS}) were optimised by adjusting their values such that the resultant coating did not over spray and the bottom widths of the ridges were between 600 μm and 1000 μm, and their geometric profiles were consistently triangular (Cormier et al., 2013). During this optmisation process, the aluminium-alumina powder was sprayed through a slotted mask with slit size of 600 μm. This mask was optimal because it allowed easy passage of spray jet and resulted in microchannels whose hydraulic diameters were between 100 μm and 500 μm , recommended for high performance of the micro heat sinks necessary for cooling high speed microprocessors for computers (Bowers and Mudawar, 1994; Harry et al., 2013; Xia et al., 2015). *This optmisation process was the critical part of developing the new method for fabricating microchannels reported here for the first time.* The optimised CS process parameters for fabrication of microchannels are reported in Appendix N.

After optimisation, the fabrication process for microchannels started by grit blasting to activate the surface of the substrates using Alumina powder followed by deposition of a thin layer of aluminium-alumina as a de-binder. Then, three layers of Copper were deposited as a base using optimised process parameters as indicated in 3.3.3. Thereafter, through a slotted mask with slit size of 600 μm, positioned at optimised standoff distances (SOD_{GM} and SOD_{MS}

) shown in the Figure J.3 and using the spray parameters in Appendix N, one layer of aluminium-alumina was deposited to fabricate the microchannels.

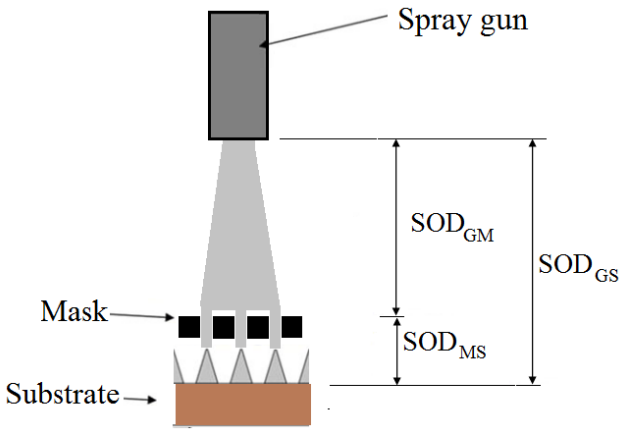


Figure J.3: Cold spray through mask

The deposition of aluminium- powder was followed by deposition of three layers of Copper powder without the mask to embed the bottom of the aluminium-alumina micro ridges. The depth of the copper layer was around 446 μm so that the hydraulic diameter of the microchannels was between 100 μm and 500 μm. After depositing the Copper powder, the protruding tips of the microchannels were ground to the level of the copper coating. Thereafter, one layer of aluminium-alumina was deposited via the mask to fabricate the second layer of the micro ridges that were later embedded by depositing three layers of copper powder. This process was repeated until three layers of microchannels were fabricated inside the Copper matrix. The three layers of microchannels were preferred because they were optimal for effective removal of the heat from the microprocessors using the micro heat sinks (Wei and Joshi, 2003; Qu and Mudawar, 2004).

After this fabrication, the specimens were lightly ground around to expose the cross sections of the microchannels, which were dipped in 50 % dilute HCL for about 30 minutes to dissolve aluminium-alumina micro ridges. This dipping was repeated until no bubbles were seen forming around the specimen, and signified that all the aluminium-alumina micro ridges were preferentially dissolved and through pores were created leaving behind the copper walls standing. The above process is illustrated in Figure J.4 and summarised in Table J.4.

Table J.4: Steps in fabrication of microchannels.

Step	Action
1	Grit blast the substrate using alumina
2	Spray three layers of Cu powder
3	Through mask spray one layer of alumina powder to make microchannels
4	Without mask spray 3 layers of copper to embed microchannels
5	Grind off the protruding tips of microchannels
6	Repeat steps 2 to 5 until three layers of microchannels are embeded
7	Without mask spray 3 layers of copper to cover microchannels
8	Lightly grind the peripheral of specimen
9	Submerge specimen in 50 % HCL to de-alloy alumina
10	Repeat step 9 until through pores are formed in specimen
11	Rinse the specimen in distilled water
12	Dry the specimen in air

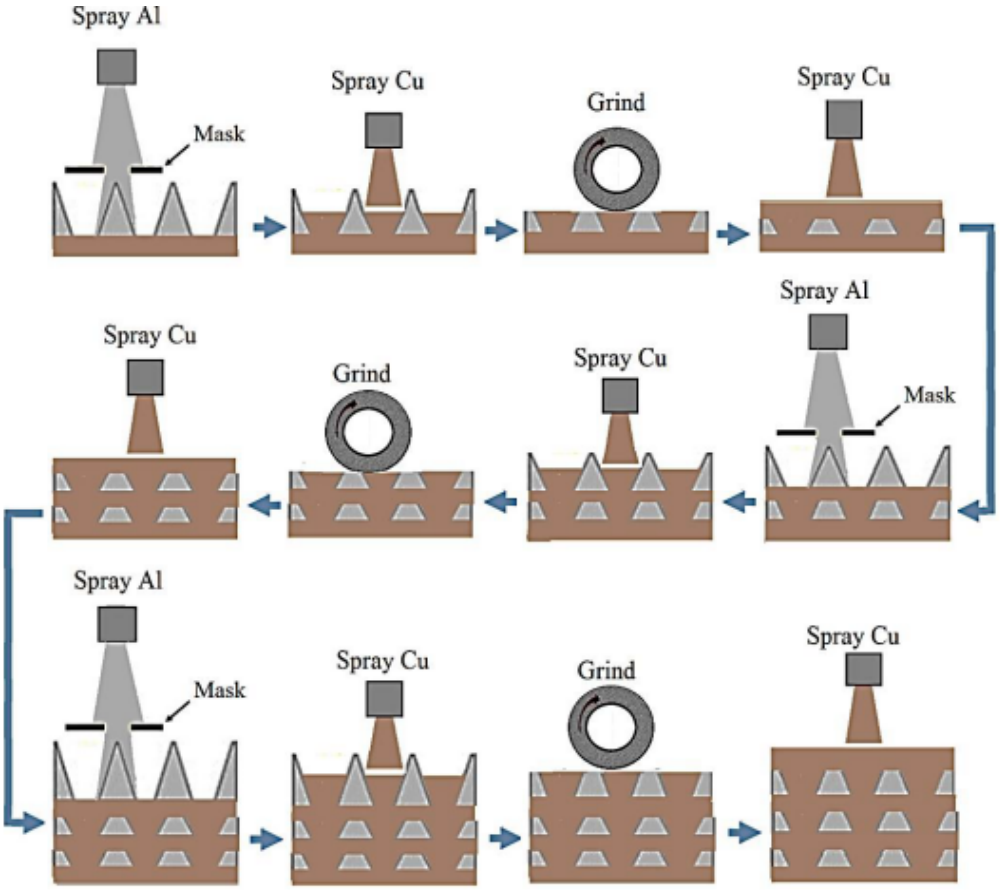


Figure J.4: Fabrication process for microchannels.

J.6 Fabrication of Antimicrobial Filters

To fabricate the antimicrobial filters, the alloying process using CS process followed by de-alloying using common acids was carried out. The powders which were used in this task were the aluminium-alumina-copper powder mixtures for antimicrobial surfaces and the copper powder as pore-forming agent. These powders were mixed as described in J.2. The substrates which were used in this experiment were of sizes 40 mm long, 40 mm wide, and 5 mm thick, and were cut from the aluminium slab. Aluminium was chosen for this purpose because it does not react with nitric acid. The selected spray mask for this task was perforated mild steel with round holes of radius 400 μm each. This mask was chosen because it created a lotus porous structure with the porosity which is good for fluid permeability (Hetsroni et al., 2006; Singh et al., 2009; Zang et al., 2013). The optmisation of spray parameters before fabrication was necessary just like in the fabrication of microchannels. In this process, the temperature and pressure of the gas, powder feed rate, velocity of the gun, and the standoff distances (SOD_{GM}, SOD_{MS}, SOD_{GS}) were varied such that the Copper powder was deposited via the mask without over spray and the resultant discs were separated at the base. Similarly, optmisation of spray parameters for aluminium-alumina-copper powder mixture involved adjusting the values for temperature and pressure of the gas, powder feed rate, velocity of the gun and standoff distance such that deposition of one layer of this powder embedded three quarter of the height of the copper discs. *Like in microchannels, this optmisation process constituted the critical part of developing the new method for fabricating antimicrobial filters, and it is reported here for the first time.* The optimised spray parameters for Copper powder and the aluminium-alumina-copper powder mixture are as in 3.3.3.

After this optmisation process, the aluminium substrates were activated by grit blasting using alumina powder. Then, a thin layer of de-binder (copper) was deposited on the entire surface of the grit blasted substrate. Thereafter, via a perforated mask positioned at the optimal distance, three layers of Copper powder were deposited to fabricate the discs, followed by deposition of one layer of aluminium-alumina-copper powder mixture without a mask to embed the copper discs. Then, the copper power was deposited via the mask to make

another layer of the copper discs, followed by deposition of the aluminium-alumina-copper powder mixture. This process was repeated for three times until a coating with a thickness of between 2 mm and 3 mm was fabricated. To de-alloy the Copper discs from this coating, the specimens were dipped in dilute Nitric acid for 24 hours at room temperature. After de-alloying the Copper discs, the specimens were rinsed in de-ionised water followed by dipping them in 50 % dilute HCL for up to 5 seconds to dissolve some aluminium-alumina particles and expose the copper particles. Then, the specimens were rinsed in deionised water again and dried in still air at ambient temperature.

The fabricated micro filters had the exposed aluminium, copper and alumina particles all with antimicrobial capability. The results of the developed fabrication processes are presented and discussed in Chapter 4.

Table J.5: Optimised CS parameters for antimicrobial filters.

Powder	T_0 (°C)	P_0 (bar)	SOD_{GM} (mm)	SOD_{MS} (mm)	SOD_{GS} (mm)	V_{gun} (mm/s)	F %
Cu	400	9.5	12	3	15	10	40
Al-Al_2O_3	400	8.3	-	-	20	10	5

Table J.6: Steps in fabrication of antimicrobial filters.

Step	**Action**
1	Grit blast the aluminium substrate
2	Spray a thin layer of copper on grit blasted surface
3	Through mask spray copper to make discs
4	Without mask spray aluminium-alumina-copper leaving discs protruding
5	Repeat steps 3 to 4 to achieve 2-3 mm thickness
6	Dip specimen in nitric acid to delaminate coating
7	Rinse the coatings in distilled water
8	Dip specimen in 50 % HCL for 5s to expose copper
9	Rinse the specimen in distilled water

APPENDIX K : Isentropic Gas Models

One of the main tasks in the CS process design was the selection of the appropriate spray parameters to deposit the feedstock powders (Alkhimov et al., 2001; Stoltenhoff et al., 2002). Studies showed that the velocity of the particle is dependent and limited by the velocity of the gas (Dykhuizen and Smith, 1998; Zahiri et al., 2009; Ning et al., 2010). Consequently, the analytical mathematical models for the isentropic gas flow in CS process were reported in literature (Anderson, 1982; Dykhuizen and Smith, 1998; Grujicic et al., 2004). The isentropic gas flow is an adiabatic, reversible and frictionless flow of the gas which takes place in one dimension. In this case, the flow of the gas in CS process using a convergent/divergent nozzle is analogous to the isentropic flow of perfect gas through a variable cross section area (Dykhuizen and Smith, 1998) shown in Figure K.1. In this figure, the flow is subsonic in the convergent section of the nozzle where the gas is preheated and compressed. At the throat of the nozzle, the velocity of the gas is sonic. Due to stead expansion of the nozzle in the divergent section, the velocity of the gas increases to supersonic value while the gas temperature and pressure drop (Anderson, 1982).

The important parameters which describe the motion of the gas in the isentropic gas flow are the temperature (T), pressure (P), velocity (V) of the gas, the cross section area (A) of the nozzle, local Mach number (M), and the specific heat ratio of the gas (γ). In modelling these parameters, the flow of the gas was assumed to originate from a large chamber where its pressure was equal to the stagnation pressure (P_0), the temperature of the gas was the stagnation temperature (T_0), and the velocity of the gas was zero (V_0). For practical purposes, this situation matches the upstream conditions for the nozzle throat in

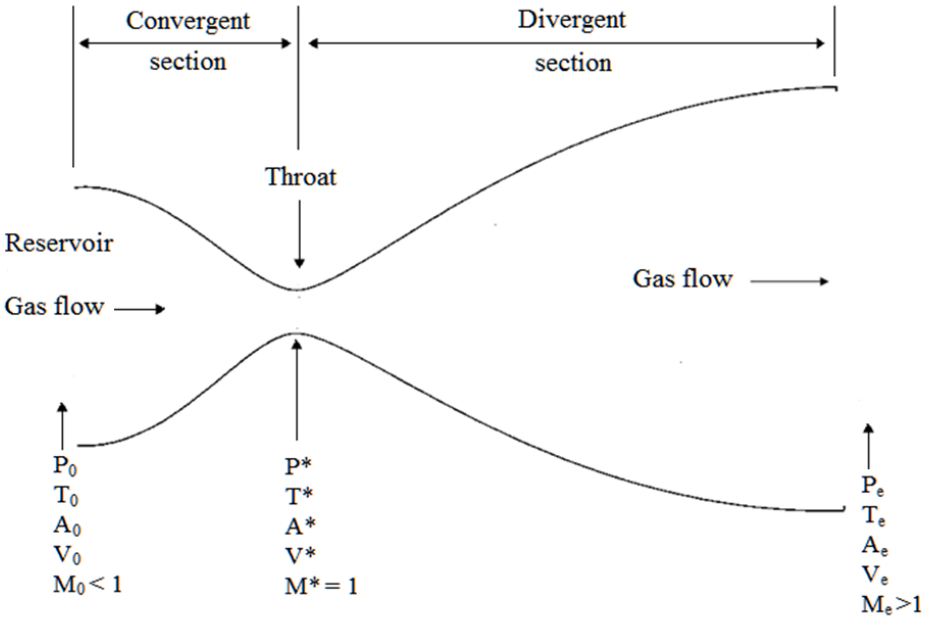


Figure K.1: Converging-diverging supersonic nozzle
Source: (Anderson, 1982).

CS processes, since the flow area is three times greater than the throat area. It was also assumed that (T_0), and the mass flow rate (and not P_0) are set by the operator (Dykhuizen and Smith, 1998). Then the mathematical models for these parameters were as following:

The sonic velocity (v^*) of the gas at the throat of the nozzle is given by equation (K.1)[1].

$$V^* = \sqrt{\gamma R T^*} \tag{K.1}$$

where γ is the specific heat ratio of the gas, R is the specific gas constant (J/kg.K), and T^* is the temperature of the gas at the throat of the nozzle (K). For monatomic gases such as helium, γ is 1.66, and for diatomic gases such as nitrogen and air, γ is typically 1.4 (Dykhuizen and Smith, 1998). Because of large value of γ, monatomic gases such as helium achieved high velocity (Zahiri et al., 2009; Ning et al., 2010).

Equation (K.2)[2] was used to estimate the velocity of the gas at the exit of the

[1]Note that all quantities marked with (*) are throat or sonic conditions.
[2]Note that all quantities marked with ($_e$) are nozzle exit conditions.

nozzle (v_e) if the Mach number M_e and temperature of the gas T_e are given (Dykhuizen and Smith, 1998).

$$V_e = M_e\sqrt{\gamma RT_e} \tag{K.2}$$

The stagnation temperature of the gas in the convergent section of the nozzle (T_0) related to the temperature of the gas at the throat of the nozzle T^* as given in equation (K.3).

$$T_0/T^* = 1 + (\gamma - 1)/2 \tag{K.3}$$

Equation (K.4) provided the relationship for the stagnation temperature of the gas in the convergent section of the nozzle (T_0) and the temperature of the gas at the exit of the nozzle (T^*).

$$T_0/T_e = 1 + M_e^2(\gamma - 1)/2 \tag{K.4}$$

The ratio of the area of the nozzle at the exit and throat (A_e/A^*) related with the Mach number (M), and the specific heat ratio of the gas (γ) as stated in equation (K.5). This equation was used to calculate the exit Mach number when the exit area is specified (Dykhuizen and Smith, 1998).

$$\frac{A_e}{A^*} = (\frac{1}{M_e})[(\frac{2}{\gamma+1})(\frac{\gamma-1}{2})M_e^2]^{\frac{\gamma+1}{2(\gamma-1}}) \tag{K.5}$$

Where M_e is the Mach number at the exit of the nozzle, A^*, and A_e, is the area at the exit and throat of the nozzle, respectively.

The pressure (P) of the gas stream at any point in the nozzle was estimated using equation (K.6) when the stagnation pressure of the gas (P_0) was known.

$$\frac{P_0}{P} = [1 + (\frac{\gamma-1}{2})M_e^2]^{\frac{\gamma}{\gamma-1}} \tag{K.6}$$

Equations (K.1) through to (K.6) can be used to compute the pressure, temperature and velocity of the gas at the exit nozzle so long the throat and exit cross-sectional areas were given. However, it must be noted that the calculated pressure, temperature and velocity values will reflect the true conditions of the gas at the nozzle exit only if a normal shock does not take place inside the nozzle. To determine if the normal shock takes place inside the nozzle, the ambient pressure (P_a) should be compared with the following shock pressure (P_s) using (K.7).

$$\frac{P_s}{P_e} = 1 + (\frac{2\gamma}{\gamma+1})M_e^2 - \frac{(\gamma-1)}{(\gamma+1)} \tag{K.7}$$

If the shock pressure, P_s, is lower than the ambient pressure (P_a), then a shock will occur inside the nozzle and the subsequent gas flow is subsonic so that the exit conditions cannot be calculated using equations (K.1) through to (K.6). Under normal CS operation conditions, the shock pressure is maintained above the ambient pressure so that no shock occurs inside the nozzle and the exit conditions can be estimated using equations (K.1) through to (K.6). At the same time, the exit gas pressure, P_e is generally lower than the ambient pressure in an effort to maximize the exit velocity of the gas and thus, the average velocity of the feed-powder particles, referred to as the particle velocity. Under such conditions, the one-dimensional gas dynamic equations (K.1) through to (K.6), developed by (Dykhuizen and Smith, 1998), and briey reviewed above can be used to analyze the gas flow inside the nozzle (Grujicic et al., 2004). The above analysis of equations enabled the reader to understand real gas flow conditions surrounding the estimation of the spray parameters.

APPENDIX L : Cold Spray Parameters

Cold spray (CS) parameters affect the quality of the coatings. The knowledge of existence, types, quantities, and interaction of spray parameters assist process engineering with fore knowledge about process control and quality of the product (Hamweendo et al., 2014b). Consequently, this section introduces the various types and interaction of the spray parameters studied in this thesis. These parameters include: temperature of the gas and particle, pressure of the gas, standoff distance, particle and critical velocity, type of the nozzle, type of the gas, and powder characteristics. These spray parameters were categorised as independent if the values were altered by the operator of CS equipment, or dependent if their values change according to process interactions (Lee et al., 2007a; Assadi et al., 2011; Goyal et al., 2012).

L.1 Analysis of Spray Parameters

The analysis of spray parameters was carried out to identify the primary and secondary parameters, their interactions and effects on the cold sprayed coatings. The primary spray parameters were defined as those with profound influence on the properties of sprayed coatings, and these were temperature of the gas (T_0), pressure of the gas (P_0), and standoff distance (S) (Zahiri et al., 2006). The secondary process parameters with influence only on the primary spray parameters included the molecular weight of the process gas (M_w), nozzle expansion ratio (ϵ), diverging length of the nozzle (x_d), diameter of powder particles (d_p), powder angularity (P_{ang}), and temperature of substrate (T_{sub}). The interaction of all these process parameters and their effects

on the characteristics of the coatings are summarised in Table L.1. This table was constructed using Design Structures Matrix (DSM) theory and the precedence rules as described in literature (Browning, 2002; Meng et al., 2011; Li and Li, 2012).

Table L.1: Analysis of CS process parameters.

Inputs/outputs	Particle temperature	Particle velocity	Critical velocity	Deposition efficiency	Microhardness	Bonding strength	Porosity of coating	**References**
T_0	+	+	-	+	+	+	-	(Meng et al., 2011)
P_0	( )	+	( )	+	-	+	-	(Lee et al., 2008)
S	-	-	( )	-	-	-	+	(Li, Li and Liao, 2006)
M_w	( )	-	( )	-	-	-	+	(Ning et al., 2010)
ϵ	( )	+	( )	+	+	+	-	(Li, Li and Liao, 2006)
x_d	+	+	( )	+	+	+	-	(Li, Li and Liao, 2006)
d_p	-	-	+	-	-	-	+	(Schmidt et al., 2006)
P_{ang}	( )	+	( )	+	+	+	+/-	(Wong, 2011a)
T_{sub}	+	( )	-	+	+	+	-	(Suo et al., 2012)

In this table, the spray parameters wer listed in the first column and their effects were presented in the first row. The effect of increasing each of the spray parameters were indicated as +, -, +/-, or ( ) in the intersection boxes of the table. These signs meant increase, decrease, variable and undefined effects of input process parameters on the output variables, respectively. This analysis, reported here for the first time, assisted in identifying the effect of Primary spray parameters on the secondary ones and on the coatings and made it easier to decide whether to increase or decrease a given primary spray parameters in order to achieve desired change in porosity of the coating.

L.2 Description of Spray Parameters

The temperature of the gas:, T_0, is independently altered parameters using the gas heater which is an integral part of the spray gun assembly (see Figure I.3) (Fukamuna and Huang, 2009). In this case, when the stagnation temperature of the gas was increased, the velocity of the gas jet also increased as shown in Figure L.1 (a) (Kwon et al., n.d.; Lee et al., 2007a; Assadi et al., 2011). Also, the bonding strength and microhardness of the coating increased as shown in Figure L.1(b) and (c) respectively, and the porosity of the coating reduced (Figure L.1(d)) (Zahiri et al., 2006; Meng et al., 2011).

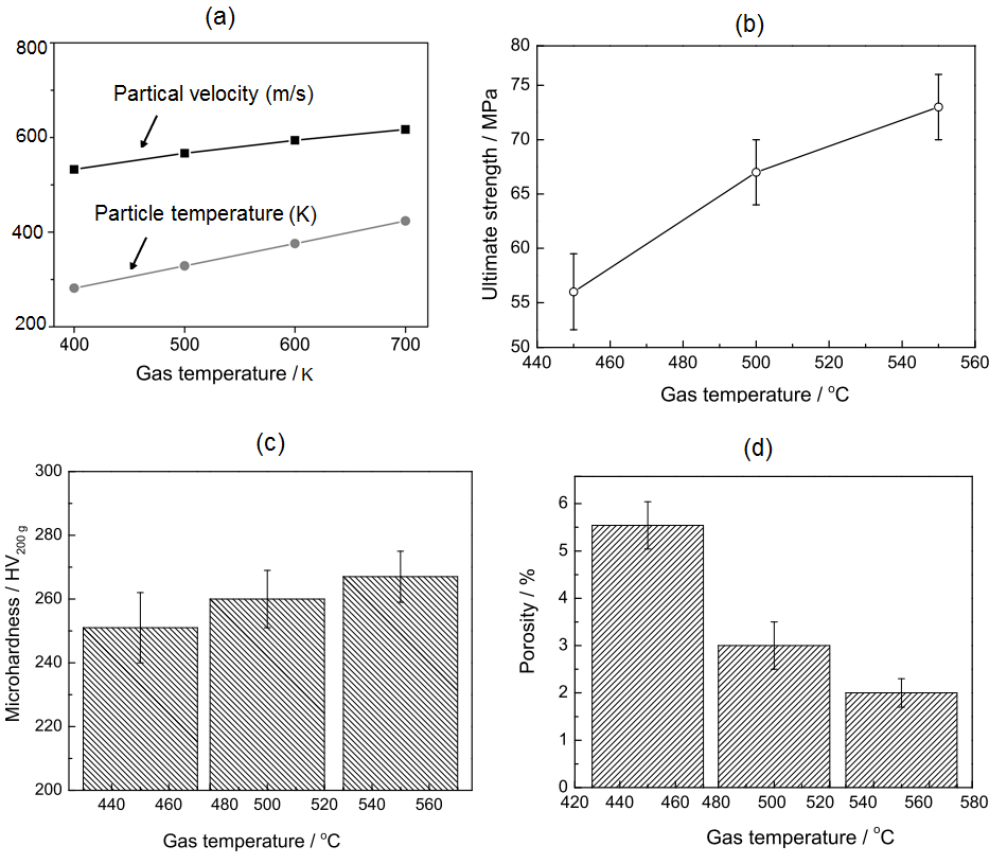


Figure L.1: Effect of stagnation gas temperature.
Sources: (a) (Li, Liao, Wang, Li, Zhang and Coddet, 2006), (b),(c) and (d) (Meng et al., 2011).

The increase in gas temperature enhanced the thermal softening, plastic deformation and deposition efficiency of the feedstock powder (Lee et al., 2007a). However, when the stagnation temperature of the gas was reduced, the velocity of the gas and that of the particles reduced as well. Under such conditions,

the deposition of the particles was lessened due to reduced kinetic energy and plastic deformation during impact. As a consequence, a porous structure was deposited (Zahiri et al., 2009). Further, if the gas temperature, hence the particle temperature was too low or too high, then the particle momentum (or impact energy) was equally too low or too high, resulting in the particle becoming too brittle or ductile, respectively. Both of these extreme conditions resulted in unfavourable erosion of the substrate or coating as illustrated in Figure L.2 (Lee et al., 2011). The knowledge of these extreme conditions is critical in CS process design. In this sense, it was critically important to set the temperature of the gas within the optimal limits to avoid erosion of the substrate or coating.

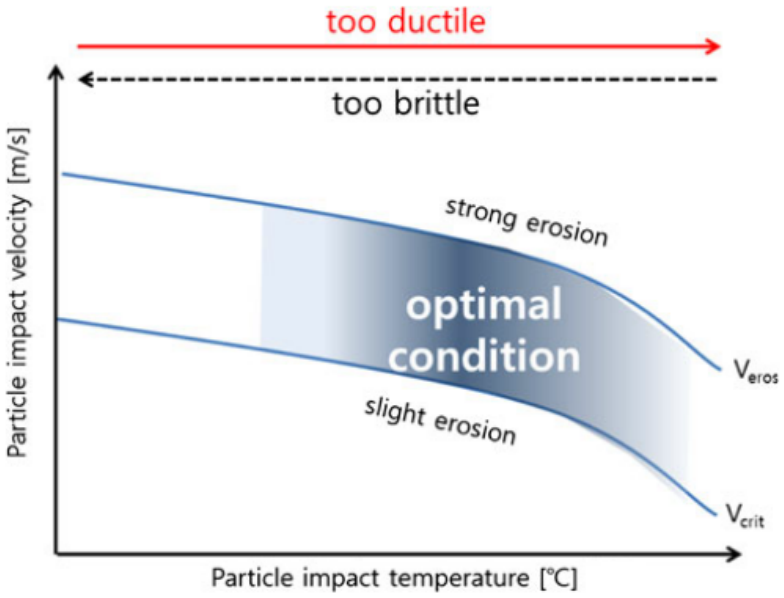


Figure L.2: Optimal CS conditions.
Source: (Lee et al., 2011)

In addition, it was demonstrated that an increase in the stagnation temperature of the gas led to a significant reduction in impact velocity as the critical velocity is the material property that is dependent on particle temperature of the powder as illustrated in Figure L.3. In this case, an increase in the gas temperature resulted in increased velocity of the gas jet and particle impact velocity. This condition resulted in high deposition efficiency and denseness of the coatings (Lee et al., 2007a).

The pressure of the gas:, P_0, is the second independent spray parameter. Studies of this parameter showed that an increase in its value while holding the

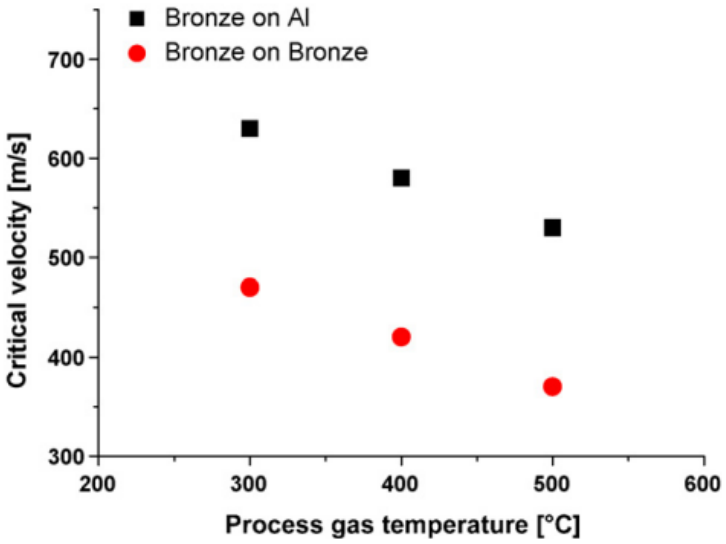


Figure L.3: Critical velocity Vs. process gas temperature.
Source: (Lee et al., 2007b)

temperature of the gas constant resulted in increased velocity of the particles and the deposition efficiency as illustrated in Figure L.4 (a) and (b), respectively (Lee et al., 2008; Stoltenhoff et al., 2002). The high pressure setting increased the drag effect of the gas on the particles, hence their deformation at impact (Li, Li and Liao, 2006). However, reduction of the gas pressure tended to limit the velocity of the particles, their plastic deformation at impact, leading to formation of porous coatings (Koivuluoto et al., 2009; Zahiri et al., 2009).

The standoff distance: ,S, is the third independent process parameters, defined as the offset or gap between the exit of the nozzle and the surface of the substrate or coating during CS process. Studies showed that an increase in standoff distance led to enhancement of porosity in the coating (Zahiri et al., 2009). However Li, Li and Liao (2006) observed that standoff distance has little effect on coating microstructure except for the deposition efficiency (Goyal et al., 2012). To the contrary, Pattison et al. (2008) proved that the deposition efficiency (DE) of the particles varied with the standoff distance as shown in Figure L.5. As seen in this figure, the DE increase along with S between 0 mm and 60 mm, due to accompanying decrease in bow shock waves. When the standoff distance was between 60 mm and 120 mm, the DE was almost constant since the bow shock waves had completely disappeared. Thereafter, the DE declined along with increase in standoff distance above 120

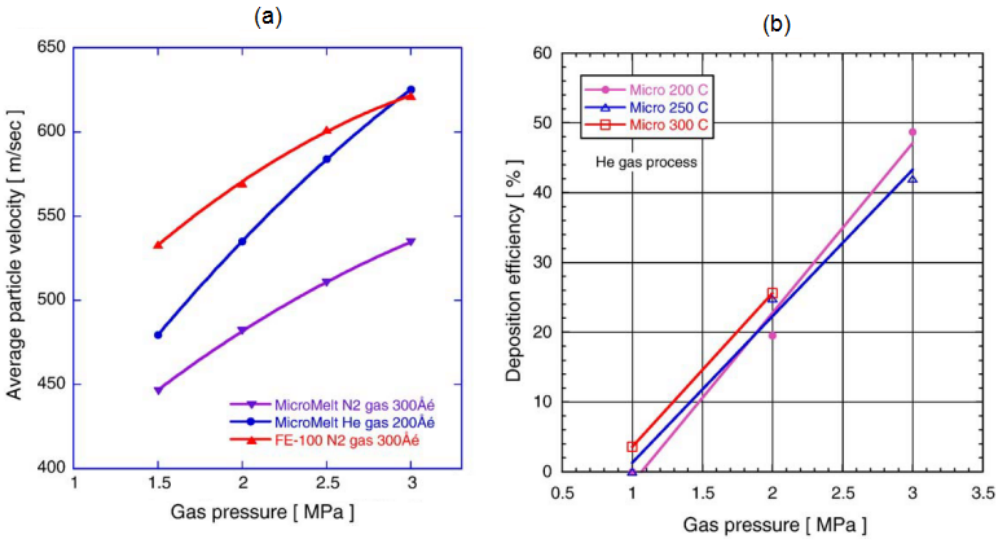


Figure L.4: Effect of gas pressure.
Source: (Fukanuma et al., 2006)

mm because of the particles retardation (Pattison et al., 2008). From these results, it appeared that there was an optimum standoff distance at which DE is optimal which is a necessary condition to be known during process design.

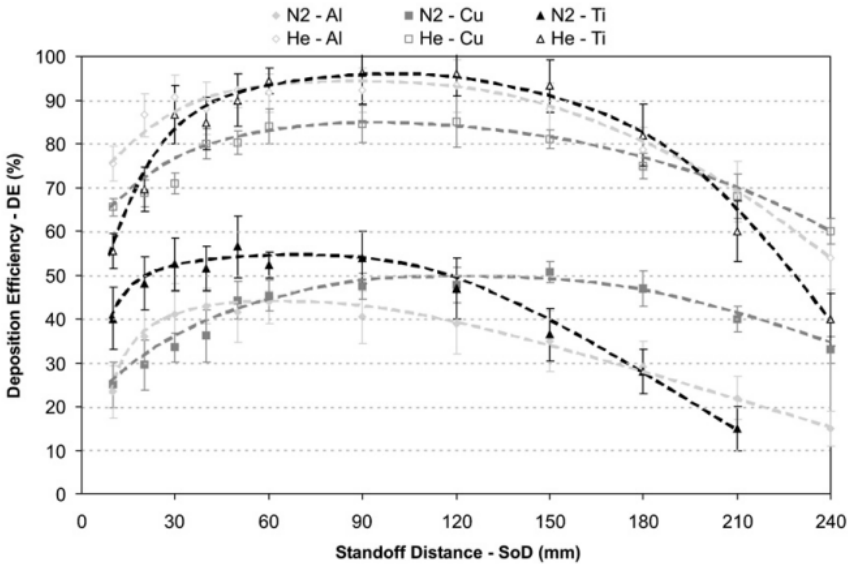


Figure L.5: Effect of standoff distance on deposition.
Source : (Pattison et al., 2008).

The velocity of the particle at impact:, v_p, is the first dependent spray parameter found to have profound influence of the microstructure of the coatings (Zahiri et al., 2006; Zahiri et al., 2009). The v_p increased with (T_0) and

pressure (P_0) of the gas. Consequently, in CS process design, the prior knowledge of T_0 and P_0 was cardinal in controlling the quality of the coatings for anticipated applications (Champagne et al., 2010). In light of this, Alkhimov et al. (2001) developed an empirical model (L.1) for calculating the v_p at the exit of the nozzle.

$$v_p = \frac{v_g}{1 + 0.85\sqrt{\frac{d_p}{x_d}}\sqrt{\frac{\rho_p v_g^2}{P_0}}} \tag{L.1}$$

Where v_p is the velocity of the particle (m/s), v_g is the velocity of the gas (m/s), d_p is the diameter of the particle (μm), ρ_p is the density of the particle (kg/m^3), x_d is the nozzle axial length (mm), and P_0 is the gas inlet pressure (MN/m^2). v_g is given by (L.2), obtained by substituting (K.4) into (K.2) after dropping the subscript e.

$$v_g = M\sqrt{\frac{\gamma R T_0}{1 + \frac{1}{2}M^2(\gamma - 1)}} \tag{L.2}$$

Where M is the Mach number at the exit of the nozzle, $\gamma - 1$ is the specific heat of a given gas, R is the specific gas constant (J/kgK). Models (L.1) and (L.2) express the v_p and v_g in terms of the independent CS process parameters which were analysed in Appendix L.1. These parameters include T_0, P_0, M, d_p, and γ (Alkhimov et al., 2001). Therefore, equation (L.1) was used to calculate the v_p in the gas stream of CS process for given T_0, P_0, M, d_p, and γ values. A number of experiments demonstrated that the calculated v_p using (L.1) correlated very well with the measured values (Wu et al., 2005; Phani et al., 2007) as demonstrated in Figure L.6, in which the coefficient of determination was 98.24 %. Consequently, model (L.1) could be used to predict process parameters which was an important requirement in CS process design (Hamweendo et al., 2014b).

Critical velocity of the powder:, $v_{crit.}$, is the second dependent spray parameters which influences the deposition of particles. The $v_{crit.}$ was defined as the velocity of the particle at or above which bonding of powders is implementable, and below which the particles erode the substrate or coating (Dykhuizen and Smith, 1998). Thus, deposition of cold sprayed particles only

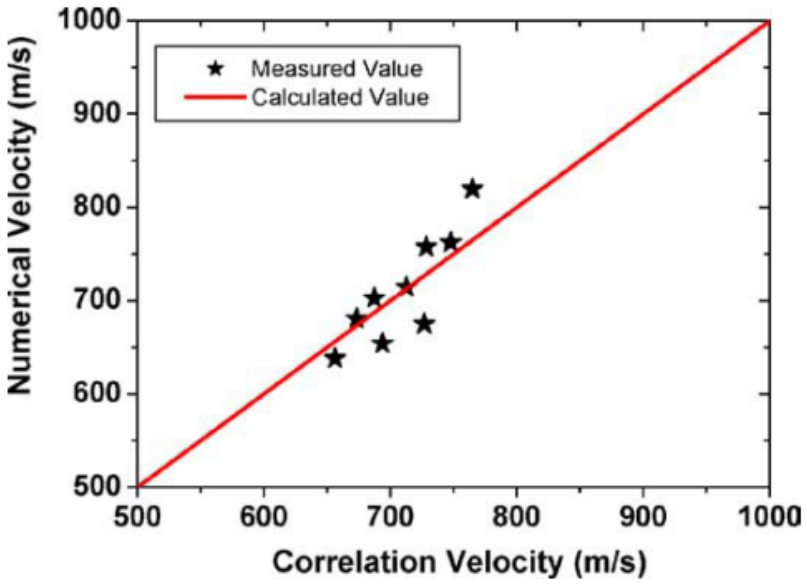


Figure L.6: Comparison of particle velocities.
Source: (Wu et al., 2005)

occurs when their velocity reached or exceeded the critical velocity. The more the particle impact velocity exceeds the critical velocity, the higher was the resulting deposition efficiency (Gartner, Schmidt, Stoltenhoff and Kreye, 2006), as schematically represented in Figure L.7.

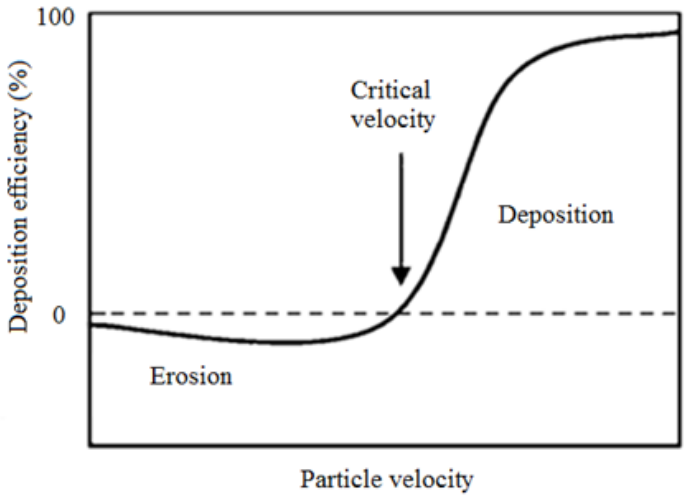


Figure L.7: Critical velocity Vs. deposition efficiency.
Source: (Gartner, Schmidt, Stoltenhoff and Kreye, 2006)

As seen in this figure, deposition of powders commenced when v_p was equal to the $v_{crit.}$ and improves as the v_p increased (Gartner, Stoltenhoff, Voyer, Kreye,

Riekehr and M, 2006; Lee et al., 2011). Since the higher particle impact velocity led to higher deposition efficiency, the factors that affected particle impact velocity also affected the deposition efficiency. For instance, higher inlet gas temperature results in higher inlet gas velocity, which in turn increased the particle acceleration and particle impact velocity due to greater drag effects (Wong, 2011b). The studies by Assadi et al. (2011) revealed that the deposition efficiency of the particles improved with the increase in the ratio $v_p/v_{crit.}$. Therefore, knowing the the magnitude of the $v_{crit.}$ of the feedstock powder was important in CS process design because in reality there is a window of cold sprayability that is dependent on the material properties and temperature of the particle outside which erosion instead of deposition of the particles occur (Schmidt et al., 2006; Champagne et al., 2010; Lee et al., 2011). For this reason, investigations were carried out to establish the factors that affect the ($v_{crit.}$ of the particles. These investigations revealed that the impact temperature of the particle, tensile strength of the feedstock material, the ambient temperature and specific heat were the fundamental factors that influence the $v_{crit.}$ (Assadi et al., 2003; Schmidt et al., 2006; Assadi et al., 2011). Based on these results, Schmidt et al. (2006) developed a fundamental empirical model (L.3) for calculation of the $v_{crit.}$ of specific materials.

$$v_{crit.} = [4f_1\sigma_{ut}(1 - \frac{T_i - T_R}{T_m - T_R})/\rho + f_2c_p(T_m - T_R)]^{\frac{1}{2}} \tag{L.3}$$

Where $v_{crit.}$ is the critical velocity (m/s), f_1 and f_2 are empirical factors, σ_{ut} is the tensile strength of the powder material (MN/m^2), T_i is the impact temperature (K), T_m is the melting temperature for the powder material (K), T_R is the ambient temperature (K), c_p is the specific heat of the powder material (J/kg^0C), and ρ is the density of the powder material (kg/m^3). From equation (L.3) it was evident that the $v_{crit.}$ reduced as temperature of the particle increase. The pressure term was completely absent in this equation and implied that it did not affect the $v_{crit.}$. This was in agreement with the assertion by Fukanuma et al. (2006) that the $v_{crit.}$ of the material is independent of the stagnation pressure of the gas. Unlike the model which were developed by Assadi et al. (2003) which overstated the $v_{crit.}$ values for selected materials, equation (L.3) predicted the $v_{crit.}$ values for a wide range of materials that were (nearly) in agreement with the experimental results as illustrated in Figure L.8 (Schmidt et al., 2006; Assadi et al., 2011).

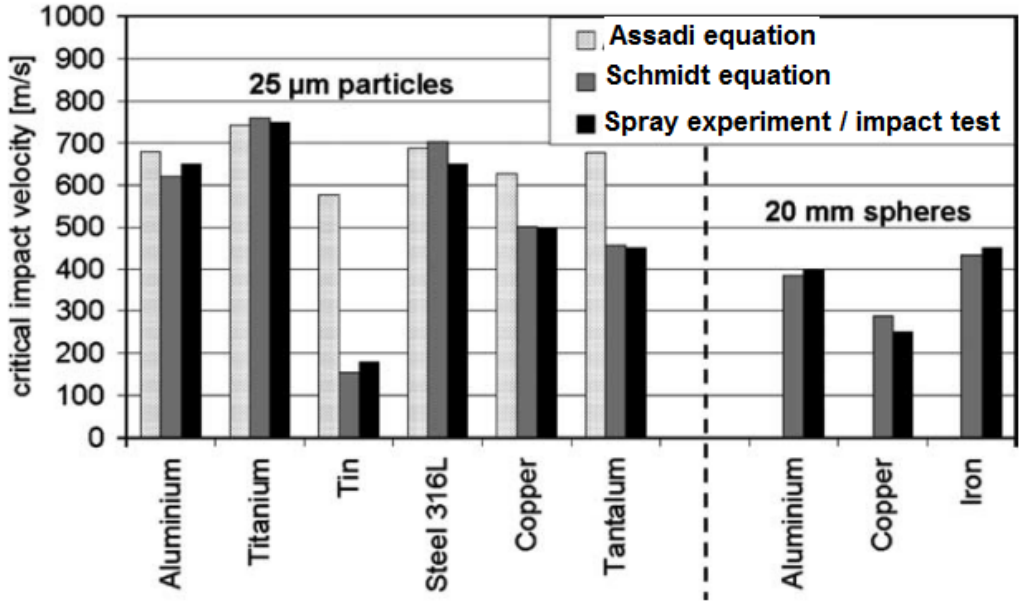


Figure L.8: Calculated and experimental critical velocities
Source: (Schmidt et al., 2006)

For mixed powders, the mean critical velocity was calculated using equation (L.4) in which the respective fraction distributions and critical velocities for constituent powders were accounted.

$$v_{critm} = (fr1)(v_{crit1}) + (fr2).(v_{crit2}) \tag{L.4}$$

where v_{critm} is the mean critical velocity for the powder mixture, $fr1$ and $fr2$ are the respective fraction distributions of the constituent powders in the mixture and, v_{crit1} and v_{crit2} are the critical velocities for the constituent powders, respectively.

Temperature of the particle:,T_p, is another dependent parameter whose value increases with the stagnation temperature of the gas and the length of the nozzle (Dykhuizen and Smith, 1998; Katanoda et al., 2007; Dewar et al., 2012). Figure L.9 shows the variation of temperature of the particle with that of the process gas that is based on modeling since the actual measurement of this parameter is still challenging (Huang and Fukanuma, 2009).

From this figure, it can be seen that the temperature of the particles increases exponentially with the temperature of the gas. Such a variation resulted in

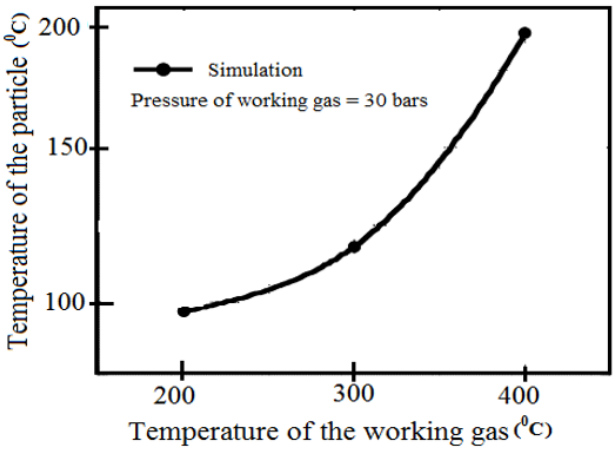


Figure L.9: Variation of particle temperature.
Source: (Huang and Fukanuma, 2009)

more dense coatings due to thermal softening, improvement in the ductility, and reduction in the $v_{crit.}$ (Zahiri et al., 2006; Katanoda et al., 2007; Li, Li and Liao, 2006; Huang and Fukanuma, 2009; Dewar et al., 2012). As indicated above, controlling the stagnation temperature of the process gas is a useful means of controlling the quality and deposition of CS process. In addition, the estimation of the temperature of the particles at the exit of the nozzle could assist in prediction of the microstructure of the coatings. Since the temperature of the particle tend to have stable values between exit of the nozzle and impact, it could be possible to predict the temperature of the particle at impact using the theories proposed by Katanoda et al. (2007), and Huang and Fukanuma (2009).

Molecular weight of process gas: This plays an important role in CS deposition. For instance, process gases with small molecular weight such as Helium, have large specific heat ratio (γ) of 1.66 and therefore attained higher velocity, while heavy gases such as air or nitrogen have large molecular weight and smaller specific heat ratio of 1.4. Figure L.10 illustrates the simulated results of the aerodynamic properties of helium and nitrogen during CS deposition (Ning et al., 2010).

According to this figure, the helium gas accelerated the particles more than nitrogen gas due to lower molecular weight. Consequently, the choice of gas in CS process design is important as this has direct influence on the properties of the coatings. According to studies, nozzles with rapidly expanding

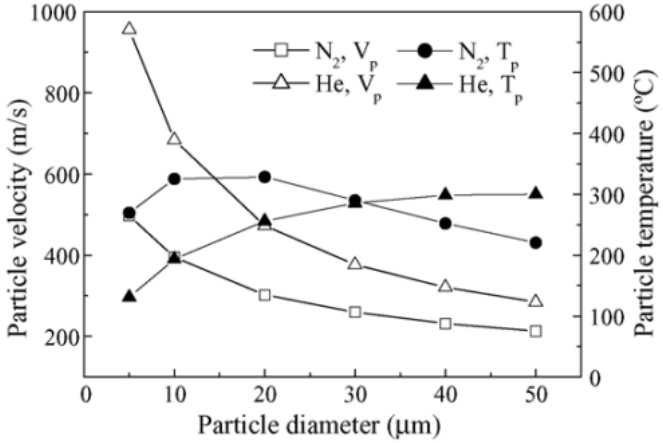
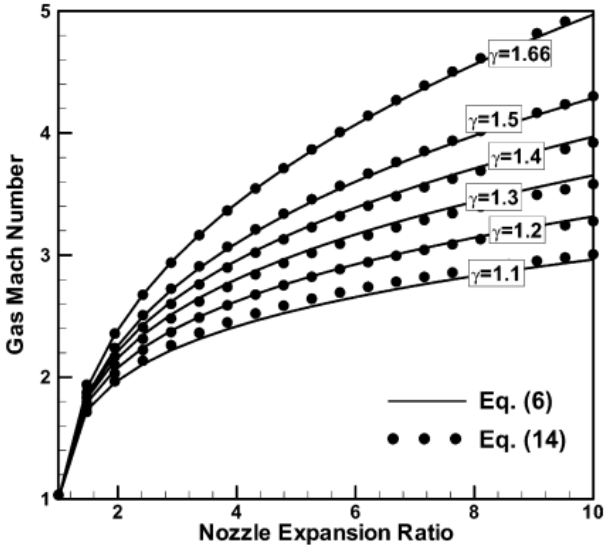


Figure L.10: Particle velocity Vs. nozzle diameter.
Source: (Ning et al., 2010)

shapes and longer axial length speedily increased the local Mach numbers and efficient converts the pressure and heat energy of the gas into kinetic energy, and the velocity of the gas in the diverging section of the gas stream increases to supersonic (Dykhuizen and Smith, 1998). Figure L.11 illustrates this phenomenon (Grujicic et al., 2004). According to this figure, an increase in nozzle expansion ratio resulted in corresponding increase in the local Mach number, which also increased along with the γ values. Therefore, in CS process planning, the choice of the nozzle geometry and type of gas matter since these have combined effect of increasing the velocity of the gas as depicted by Figure L.11 and (K.2)

Diameter of the powder:,d_p, This is another important independent CS process parameters which cannot be ignored by the CS process designer. In this context, the simulation and experimental studies carried out revealed that the diameter of the particles influenced the deposition of CS process and the microstructure of the coating (Li, Li and Liao, 2006). This is so because particles with smaller diameter of between 5 μm and 20 μm were propelled at higher inflight velocities so that they endured larger deformation at impact leading to dense coatings. On the contrary, particles with diameters which were larger than 30 μm achieved lower inflight velocities due to large inertia and low drag, and landed on the target with less impact which resulted in less or no deposition or formation of porous coatings (Ning et al., 2010). Figure L.10 illustrates the effects of particle diameter on particle velocity and temperature (Li, Li and Liao, 2006).



nozzle expansion.png

Figure L.11: Variation of Mach with nozzle expansion.
Source: (Grujicic et al., 2004)

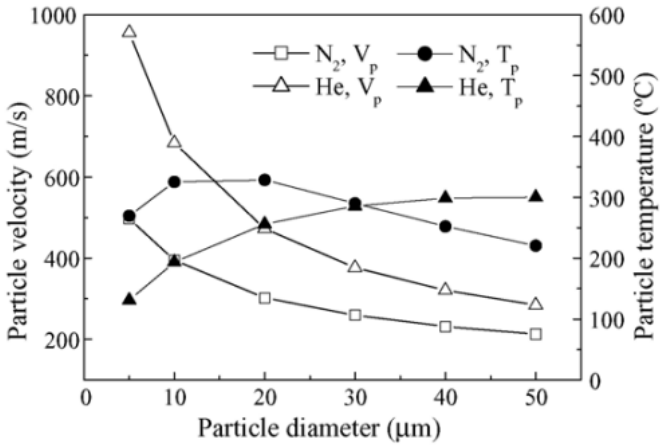


Figure L.12: Particle velocity Vs. particle diameter.
Source: (Li, Li and Liao, 2006)

As seen in this figure, the decrease in particle diameter to below 30 μm led to a noticeable increase in the velocity of the particle using Helium as process gas. This situation has positive effects of increasing deposition and denseness of coatings. On the other hand, when Nitrogen was used as the process gas, the increase in diameter of the particle led to the moderate reduction in velocity of the particle while its temperature initially increased and later decreased (Li, Li and Liao, 2006). Therefore, according to these results, a powder with a relatively small particle size could achieve high deposition with CS process. Consequently, the choice and knowledge of the diameter of the powder is cardinal as this affected the CS process and the characteristics of the microstructure of the coating (Zahiri et al., 2009).

Angularity of the powder: This refers to extent of angular morphology of the powder. CS experiments which were carried out demonstrated that powder with irregular (angular) morphology achieved higher particle velocities and formed more compact coatings due to increased inflight velocities and intense plastic deformation on impact (Ning et al., 2007). Figure L.13 (a) and (b) illustrates the angular and spherical shaped particles, respectively. Based on this explanation, the choice of the morphology of the particle in CS process was also cardinal as this had direct influence on the deposition behavior and microstructure of the coatings (Koivuluoto and Vuoristo, 2010).

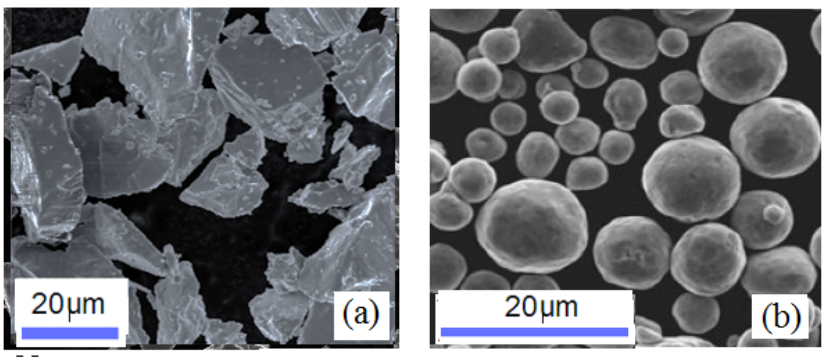


Figure L.13: Particle morphology.
(a) Angular, (b) round. Source: (Koivuluoto and Vuoristo, 2010)

Temperature of the substrate surface: (T_{sub}).Studies showed that the surface temperature of the substrate or coating at impact have effect on the deposition efficiency of different powders. In this context, Legoux et al. (2007) found that the deposition efficiency of aluminium particles increase with the surface temperature at impact, while the opposite was true for zinc, and there

was no signicant change on the deposition efficiency for tin. This behaviour was attributed to the low melting point of zinc which compromised the deposition efficiency at high impact temperature. Figure L.14 illustrates the variation of deposition efficiency as a function of the ratio of surface temperature of substrate and melting temperature of the particle.

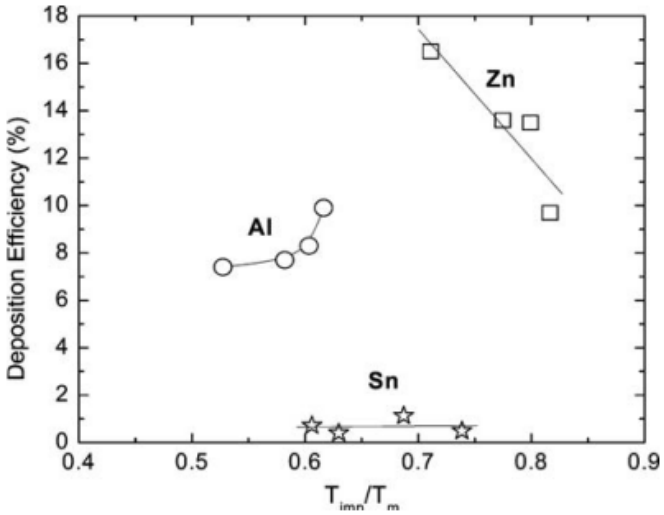


Figure L.14: Deposition efficiency Vs. melting temperature.
Source : (Legoux et al., 2007).

From this figures it is clear that there was variation in the deposition of different powders. However, other studies indicated that an increase in the substrate temperature increased the bonding strength between the coating and substrate due to the increase of particles' interlocking areas and metallurgical bonding of the first coating layer (Fukumoto et al., 2007; Suo et al., 2012).

APPENDIX M : Parameters Selection Tools

In the past, the selection of process parameters was left to the discretion of machine operators. In such cases, the experience of the operators played a major role in deciding the optimum mix of process parameters. But, due to complexity of new job processes and advancement in machine technologies, selection of process parameters became difficult even to the most skilled operators (Shirpurkar et al., 2012). For this reason, the selection strategies were proposed and studied. For instance, Taylor (1907) pioneered selection of machining parameters to improve the life of cutting tools. Later, Gilbert (1950) studied the selection of machining parameters to maximise production rate and minimise production cost in turning processes. Thereafter, Armarego and Brown (1969) investigated selection of unconstrained machine parameter using differential calculus. Finally, Brewer and Rueda (1963) applied simplified optimum analysis of machining parameters in order to reduce the machining cost (Shirpurkar et al., 2012).

From this background, it was evident that selection of parameters preoccupied the process engineers for a long time as this was believed to be a prerequisite for achievement of targeted product quality at optimum costs. On account of this, there has been proliferation of selection strategies for process parameters. In this context in the last two decades, the Taguchi Orthogonal Arrays Design of Experiment (TOADE) and the Central Composite Design of Experiments (CCDEO) methods emerged to be the most popular methods (Kaladhar et al., 2011). These techniques are briefly discussed in the subsequent paragraphs. The TOADE is a systematic method for selection of parameters during planning of experiments, whose fundamental steps are as follow (Kumar et al., 2008; Kaladhar et al., 2011; Vankanti and Ganta, 2014):

- identification of the parameters and their interaction levels,
- selection of the number of levels for each of these parameters,
- construction of the orthogonal array matrix with all possible process parameters,
- carrying out of experiments to determine the optimum level for each process parameters to establish the relative importance of individual process parameters, and
- transformation of experimental results into a signal-to-noise (S/N) ratio to measure the quality characteristics deviation from or nearn to the desired values.

Studies showed that the TOADE have the following advantages: reduced numbers of trials, lessens costs of experiments, accurate determination of optimum values of parameters, easy assessment of experimental and qualitative estimation process parameters (Shirpurkar et al., 2012). Therefore, the TOADE was applied in optimisation of spray process by selected authors. For example Goyal et al. (2013) applied a simplified model of the TOADE method and utility concept to analyze the multi-response optimization of the deposition of copper powder using the LP-CS process. In this study, all the input parameters were observed to have significantly improved the utility function and signal to noise (S/N) ratio comprising three quality characteristics of coating thickness, density, and surface roughness. However, this analysis did not consider the influence of the spray parameters of the microstructure of the coatings.

Later, Lioma et al. (2015) applied the TOADE method in the determination spray parameters for deposition of tungsten-carbide-nickel coatings with an objective of establishing the optimum spray conditions for each powder composition (Lioma et al., 2015). In this study, although the selection and optimisation of spray parameters were successful, the TOADE was unable to successfully predict the coating hardness and thickness values because this method does not account for the occurrence of strain hardening that takes place during deposition. More, these studies were among the very few cases were TOADE method was applied in CS process. Also, these studies did not focus on the optimisation and/or sub-optimisation of spray parameters so as to achieve coatings with different percentage of porosity (Goyal et al., 2012; Goyal

et al., 2013; Lioma et al., 2015). On account of this, this thesis intends to apply the TOADE during selection of process parameters for fabrication of porous structures with different percentage of porosity.

The central composite design of experiments-response surface methodology (CCDOE-RSM) is an emerging and robust method for selection and optimisation of spray parameters. CCDOE-RSM is a response surface optmisation method which applies mathematical techniques to determine the relative significance of spray parameters and their optimum conditions (Demirel and Kayan, 2012). In this method, the spray parameters with profound influence on the characteristics of the product needed to be identified. This was followed by determination of the the working limits for these parameters using either the material supply data sheets, manuals of the equipment or carrying out of experiments. Then, these working limits were used to calculate the parameter values necessary for the construction of the experimental design matrix using RSM (Balasubramanian et al., 2008; Karthikeyan et al., 2014; Thirumalaikumarasamy et al., 2014).

In addition, the CCDOE-RSM was established to be most efficient tool for establishment of the rigorous mathematical models for spray parameters. This method gave accurate results even when the smallest number of experiments were carried out (Karthikeyan et al., 2014). Therefore, Balasubramanian et al. (2008) applied the CCDOE method to optimise parameters and developed the mathematical model for predicting grain size and hardness of argon tungsten pulse current arc welded titanium alloy. Similarly, Demirel and Kayan (2012) applied response surface methodology with CCDOE-RSM for the optimization of textile dye degradation by wet air oxidation. Similarly, Thirumalaikumarasamy et al. (2014) applied CCDOE-RSM together with second-order regression polynomial modelling technique to optimise the process parameters on alumina coatings fabricated by plasma spraying process. However, there has been no report on the application of CCDOE-RSM in optimisation and/or sub-optimisation of CS process parameters so as to achieve structures with varied porosity for selected applications. On this basis, this thesis applied the CCDOE-RSM in optimisation of CS process parameter for the first time.

APPENDIX N : Tables of Parameters

The estimated values for spray parameters for the aluminium-alumina, copper, zinc and titanium powders, and powder mixture, microchannels and antimicrobial filters used in this research are summarised in Table N.1, Table N.2, Table N.4, Table N.3. The spray parameters in the rest of the tables were optimised as explained in Appendix J.

Table N.1: Spray parameters for aluminum-alumina.

Specimen	T_0 (°C)	P_0 (bar)	SOD (mm)
1	275	7.0	16
2	300	6.0	16
3	375	7.0	16
4	400	6.0	16
5	375	7.4	25
6	375	7.4	35
7	375	7.4	45

Table N.2: Spray parameters for copper.

Specimen	T_0 (°C)	P_0 (bar)	SOD (mm)
1	325	7.0	16
2	400	6.0	16
3	525	9.5	16
4	550	9.5	10
5	400	9.5	16
6	400	8.0	16
7	400	8.0	10

Table N.3: Spray parameters for titanium.

Specimen	T_0 (°C)	P_0 (bar)	SOD (mm)
1	509	8.3	14
2	509	9.2	14
3	509	8.3	26
4	509	9.2	26
5	550	8.8	20
6	450	9.5	20
7	550	9.5	20

Table N.4: Spray parameters for zinc.

Specimen	T_0 (°C)	P_0 (bar)	SOD (mm)
1	375	8.0	16
2	375	14.5	25
3	375	14.5	35
4	375	14.5	45
5	450	13.0	25
6	450	13.0	35
7	450	13.0	45
8	550	9.5	20

Table N.5: Optimised spray parameters for powder mixtures.

Powder mixtures	Substrate	T_0 (°C)	P_0 (bar)	SOD (mm)	F %
Al-Alumina-Copper	Al	400	8.3	20	5
Al-Alumina-Zinc	Al	400	8.3	16	5
Copper-Chromium	Cu	400	9.7	10	45
Tin-Oxide-Copper	Ceramic	400	9.7	10	5
Magnesium-Titanium	Mild steel	500	9.7	14	5

Table N.6: Optimised spray parameters for microchannels.

Powder	T_0 (°C)	P_0 (bar)	SOD_{GM} (mm)	SOD_{MS} (mm)	SOD_{GS} (mm)	V_{gun} (mm/s)	F %
Al-Alumina	400	8.3	25	2	27	10	5
Copper	400	9.5	–	–	10	10	40

Table N.7: Optimised spray parameters for antimicrobial filters.

Powder	T_0 (°C)	P_0 (bar)	SOD_{GM} (mm)	SOD_{MS} (mm)	SOD_{GS} (mm)	V_{gun} (mm/s)	F %
Al-Alumina-Copper	390	8.3	–	–	20	10	5
Copper	400	9.5	15	3	18	10	40

APPENDIX O : Analysis and Validation of Data

This appendix presents the calculation of tensile strengths and Young's Moduli; evaluation of thermal-mechanical and thermal-hydraulic performance of the micro heat sink; development, analysis and validation of the mathematical model relating spray parameters with the porosity of cold sprayed Titanium coating; and analysis of gas sensors.

O.1 Calculation of Tensile Strength and Young's Modulus

The strain (ϵ) and Young's Modulus (Y) (Gpa) for the titanium, titanium-nickel, and copper chromium coatings were calculated using equation O.1, equation (O.2), and (O.3), respectively. The results from these calculations are presented in Table 4.1.

$$\epsilon = \Delta l / l_0 \tag{O.1}$$

where l_0 is the original length, Δ is the change in length.

$$\sigma = \sigma_0 (1 - p)^k \tag{O.2}$$

where σ is the tensile strength at porosity p, σ_0 is tensile strength of dense material, and K is a constant that depends on the materials and fabrication

method, and k = 2. Equation (O.3) is for tensile strength and porosity of metals with moderate plasticity such as titanium, copper and nickel. The calculated results of these properties for the titanium, copper and copper nickel alloy are tabulated in Table 4.1 (Nakajima, 2010).

$$Y = Y_0(1 - p/p_c)^f \tag{O.3}$$

where Y is the effective Youngs Modulus of the porous material with porosity p, Y_0 is Youngs modulus of the solid material, p_c is the porosity at which the effective Youngs modulus becomes zero (p_c=0, for practical purposes), and f, whose value is 2.1 for particles with size ranging between 4 μm and 44 μm), is the parameter dependent on the grain morphology and pore geometry of porous material (Kovacik, 1999).

O.2 Evaluation of Micro Heat Sink

Calculation of hydraulic diameter for microchannels. The hydraulic diameter (d_h) for the microchannel was calculated using equation (O.5) where A is the cross section area and P is the perimeter of the microchannel, and the values for a, b, c and s are given in Table 4.4. Then the (d_h) = 336 μm, and is between 100 μm and 500 μm with trapezoidal shape, so its heat extraction capability when integrated in the Microfluidic Cooling Systems (MFCSs) may be good, as explained in Appendix C.

$$d_h = \frac{4A}{P} = \frac{4c(a+b)/2}{a+b+2S} \tag{O.4}$$

The hydraulic diameter (d_h) for the microchannel was calculated using equation (O.5) where A is the cross section area and P is the perimeter of the microchannel, and the values for a, b, c and s are given in Table 4.4. Then the (d_h) = 336 μm, and is between 100 μm and 500 μm with trapezoidal shape, so its heat extraction capability when integrated in the Microfluidic Cooling Systems (MFCSs) may be good, as explained in Appendix C.

$$d_h = \frac{4A}{P} = \frac{4c(a+b)/2}{a+b+2S} \tag{O.5}$$

thermal-hydraulic performance tests: The test for thermal-hydraulic performance of fabricated microchannels involved using nanofluidics and analytical methods. The low thermal resistance was used as the criterion to signify high cooling performance, and equations (O.6) up to equation (O.10), shown below, were used to generate thermal-physical data to establish the flow characteristics of the nanofluids.

In this case, equation (O.6) relates the density of the nanofluids to the density of the base fluid and nanoparticles.

$$\rho_{nf} = (1-\varphi)\rho_{bf} + \varphi)\rho_{np} \tag{O.6}$$

where the density of the nanofluid is ρ_{nf}, the volume fraction of nanoparticles in the base fluid is φ, the density of the base fluid is ρ_{bf}, and the density of nanoparticles is ρ_{np}.

The equation for calculating the heat capacity of the nanofluids is given by (O.7)

$$C_{npf} = (1-\varphi)C_{pbf} + \varphi)C_{pnp} \tag{O.7}$$

where the specific heat capacity of nanofluid is C_{npf} , the specific heat capacity of base fluid is C_{pbf}, and the specific heat capacity of nanoparticle is C_{pnp}.

Equation (O.8) which relates the effective thermal conductivity (k_{eff}), to the normalised thermal conductivity of the base fluid, k_f, was used to calculate the thermal conductivity of the nanofluid. This equation was derived from the experimental data related to the nanouids consisting of alumina, copper-oxide, titania and copper nanoparticles whose diameters were between 10 nm and 150 nm, and were suspended in water or ethylene glycol. The best-fit of the data enumerated by this model was within the experimental results with a mean empirical correlation of 98.16%, signaling an excellent performance of this model as compared to the classical models from Maxwell and Brinker which largely

failed to predict the accurate values for the effective thermal conductivity. In equation (O.8), the Reynolds number (Re') is given by equation (O.9) which is a modification of the bulk Reynolds number using the Brownians and Keblinskis theories under the assumption that there is no agglomeration of the nanoparticles in the nanofluids (Corcione, 2011; Aghaei et al., 2015).

$$\frac{K_{eff}}{K_f} = 1 + 4.4(Re')^{0.4} Pr^{0.66} (\frac{T}{T_{fr}})^{10} (\frac{k_P}{k_f})^{0.03} \varphi^{0.66} \tag{O.8}$$

$$Re' = \frac{2\rho_f k_b T}{\pi \mu_f^2 d_p} \tag{O.9}$$

where the effective thermal conductivity of the nanofluid is K_{eff}, the conductivity of the base fluid is K_f, the Reynolds number for the nanoparticle is Re', the Prandtl number for the base liquid is Pr, the temperature of nanofluid is T, the freezing point of the base liquid is T_{fr}, the thermal conductivity of nanoparticle is k_P, and the volume fraction of the nanoparticles is φ, the Boltzmann constant is $k_b$and the dynamic viscosity of base fluid is μ_f. Then, the effective dynamic viscosity of the nanofluid (μ_{eff}) is given by equation (O.10)

$$\mu_{eff} = \frac{1}{1 - 34.87(d_p/d_f)^{-0.3} \varphi^{1.03}} \tag{O.10}$$

where the diameter of the nanoparticle is d_p, the equivalent diameter of a base fluid molecule is d_f, and this diameter is given by equation (O.11), and was proposed for nanouids consisting of alumina, titanium, silica-oxides, copper nanoparticles with diameters ranging between 25 nm and 200 nm, suspended in water, ethylene glycol, propylene glycol or ethanol. In these fluids, the volume fraction for the nanoparticles ranged between 0.01 % and 7.1 %, and the temperature of the nanofluids ranged between 293 K and 333 K.

$$d_f = 0.1(\frac{6M}{N\pi\rho_{f0}})^{1/3} \tag{O.11}$$

Where the molecular weight of the base fluid is M, the Avogadro number is N and the mass density of the base fluid calculated at temperature T_0 equal to 293 K is ρ_{f0}.

Development of a new empirical equation: In this process, equations (O.6) through to equation (O.10) were used to develop a new empirical equation (O.19) for predicting thermal resistance of the micro heat sink by inserting the thermal-physical and geometrical data presented in Figure O.1 into the above equations and simplifying. Then these simplified equations were again used to simplify equation (O.12) through to equation (O.18) according to the theory of heat transfer in the micro heat sinks under constant heat flux and with a finite difference between the highest and lowest temperature (Adham et al., 2012).

$$R_{th.} = R_{cond.} + R_{conv.} + R_{capa.} + R_{const.} \tag{O.12}$$

Thermal-physical data for nanoparticles and water

Properties	Alumina nanoparticles	Copper nano- suspensions
$\rho(Kg/m^3$	3970	8933
$c_{p\,(J/KgK)}$	765	385
$k(W/mK)$	40	401

The physical properties for water

T (K)	ρ (Kg/m^3)	c_p $(J/KgK$	$\mu \times 10^6$ *(Pa.s)*	k $(W/mK$	Pr
293	998.2	4182	993	0.597	6.99
313	992.2	4175	658	0.633	4.33
333	983.2	4181	672	0.658	3.00
353	971.8	4194	352	0.673	2.57
373	958.4	4211	278	0.682	1.73

Thermal-physical parameters for Copper micro heat sink

Parameters	*Value*
A_c	0.6688 x 10^{-6} m
α	4.716
d_h	336 x 10^{-6} m
K_{hs}	401 W/m.K
L	25,000 x 10^{-6} m
μ	6.31 x 10^{-6} kg/s.m
n	45
p	2.62 x 10^{-3}m
Pr	5
R_e	100 to 1700

Figure O.1: Thermal physical data schedules.

then;

$$R_{cond.} = \frac{t}{k_{hs}LW} = 0.01080 \tag{O.13}$$

$$R_{conv.} = \frac{d_h}{N_u k_f LW\alpha} = \frac{113.9949 * 10^{-6}}{3.61 + 0.023Re} \tag{O.14}$$

$$R_{capa.} = \frac{1}{C_{pf}npRe\mu} = \frac{8.4818}{\mu_{eff}ReC_{pnf}} \tag{O.15}$$

$$R_{const.} = (\frac{w_c + w_w}{k_{hs}LW\pi})ln(\frac{1}{sinQ})w_c = 0.02052 \tag{O.16}$$

$$Q = \frac{w_w\pi}{2(w_w + w_e)} \tag{O.17}$$

where Q is given by equation (O.17) and the Nusselt number (N_u) was simplified as in equation (O.18) (Zhang et al., 2014).

$$N_u = 3.61 + 0.023Re \tag{O.18}$$

where, the width of the micro heat sink is w (m), the width of microchannel is w_c (m), width of the wall for microchannel is w_m (m). Then, equation (O.13), equation (O.14), equation (O.15), equation (O.16) and (O.18) were repalced in equation (O.12) and simplified resulted in equation (O.19).

$$R_{th.} = 0.03137 + Ck_{eff} + D \tag{O.19}$$

where C and D are given by equation (O.20) and (O.21)

$$C = \frac{113.9949.10^{-6}}{3.1600 + 0.0230Re} \tag{O.20}$$

$$\frac{8.4818}{\mu_{eff} Re C_{pnf}} \tag{O.21}$$

Graphs for thermal performance of microchannels: Then equation (O.19) was used to calculate the thermal resistance of the micro heat sink while equation (O.6) through to equation (O.10) where used to calculate the thermal-physical data for water-alumina and water-copper nanofluids using selected values of temperature and Reynoldss number and, the results were recorded as shown in Figure O.2 and Figure O.3. The graphs for variation of the thermal resistance (R_{th}) with Reinolds number (Re) and percentage concentration of nanoparticles (φ) for water-alumina are shown in Figure O.4 and in Figure O.5 for water-copper nanofluids.

From these plots, it is apparent that the lowest thermal resistance of the micro heat sink with trapezoidal shaped microchannels is 0.035 K/W when water-alumina nanofluid is used as cooling media. This value was obtained from Figure O.4 and was lower than 0.084 K/W reported in the literature (Hung et al., 2012). The lowest thermal resistance value obtained above signifies a high thermal conductivity and an excellent thermal cooling capability of the micro heat sinks using water-alumina as coolant. These results suggest that this micro heat sink could provide solutions to the challenge of cooling microprocessors in order to maintain low junction temperature of high speed microprocessor. Also in Figure O.4, the values for the thermal resistance tend to reduce as the volume fraction of the nanoparticles increase. Further, there is minimal reduction in the thermal resistance when the Reynolds number is increased beyond 1200. This implies that there is no much benefit of increasing fluid speed and hence pumping power when the fluid attains Reynolds number of more than 1200. Moreover, studies show that as the Reynolds number increases beyond 1200, the flow of the fluid changes from laminar to unfavorable turbulent condition depending on the roughness of the inner wall of the microchannels (Zhang et al., 2014).

From the plots in Figure O.5 (a), (b) and (c), the thermal resistance of the micro heat sink decreased exponentially as the Reynoldss number and volume fraction of the Copper nanoparticles increased in the water, and the lowest value was 0.05 K/W Comparing (a), (b) and (c), it can be said that thermal resistance which was initially high at 293 K, drops to lower value at 333 K

Thermal-Physical properties for water-Alumina nanofluid

Nanoparticles = Al_2O_3, Ø =36nm, T = 293K, Pr = 6.96, $Re^{'}$ =7.2436*10^{-5}						
Properties	φ = 0.00	φ =0.01	φ =0.02	φ =0.03	φ =0.04	φ =0.05
ρ_{nf}	998.2	1027.918	1057.636	1087.354	1117.072	1146.790
c_{pnf}	4182.0	4147.830	4113.660	4079.490	4045.320	4011.150
k_{eff}	0.597	0.6200	0.6334	0.6445	0.6544	0.6636
μ_{eff}	993E-6	1076.847 E-6	1180.735 E-6	1309.019 E-6	1470.412 E-6	1678.996 E-6
R_{th} at Re = 400	0.03649	0.03613	0.03575	0.03535	0.03495	0.03453
R_{th} at Re = 800	0.03393	0.03375	0.03356	0.03336	0.03316	0.03295
R_{th} at Re = 1200	0.03308	0.03296	0.03283	0.0327	0.03256	0.03243
R_{th} at Re = 1600	0.03265	0.03256	0.03247	0.03237	0.03227	0.03216
R_{th} at Re = 2000	0.0324	0.03232	0.03225	0.03217	0.03209	0.03200

Nanoparticles = Al_2O_3, Ø =36nm , T = 333K , Pr = 2.57, $Re^{'}$ =3.5890*10^{-4}						
Properties	φ = 0.00	φ =0.01	φ =0.02	φ =0.03	φ =0.04	φ =0.05
ρ_{nf}	983.200	1013.068	1042.936	1072.804	1102.672	1121.710
c_{pnf}	4181	4146.840	4112.680	4078.520	4044.360	4010.200
k_{eff}	0.658	0.7309	0.7731	0.8084	0.8399	0.8688
μ_{eff}	472E-6	511.855E-6	561.236E-6	622.213E-6	698.927E-6	798.072E-6
R_{th} at Re = 400	0.04213	0.04137	0.04057	0.03974	0.03888	0.03801
R_{th} at Re = 800	0.03675	0.03637	0.03597	0.03555	0.03518	0.03469
R_{th} at Re = 1200	0.03496	0.03471	0.0344	0.03467	0.03388	0.03358
R_{th} at Re = 1600	0.03406	0.03387	0.03367	0.03346	0.03325	0.03303
R_{th} at Re = 2000	0.03352	0.0337	0.03321	0.03304	0.03287	0.03207

Nanoparticles = Al_2O_3, Ø =36nm , T = 353K, Pr = 1.72, $Re^{'}$ =6.7423*10^{-4}						
Properties	φ = 0.00	φ =0.01	φ =0.02	φ =0.03	φ =0.04	φ =0.05
ρ_{nf}	971.800	1001.782	1031.764	1061.746	1091.728	1121.710
c_{pnf}	4194	4159.710	4125.420	4091.130	4056.840	4022.550
k_{eff}	0.673	0.8833	1.0053	1.1073	1.1981	1.2814
μ_{eff}	352E-6	381.722E-6	418.549E-6	464.023E-6	521.234E-6	595.173E-6
R_{th} at Re = 400	0.04575	0.04473	0.04366	0.04255	0.04141	0.04024
R_{th} at Re = 800	0.03856	0.03805	0.03752	0.03696	0.03639	0.03581
R_{th} at Re = 1200	0.03616	0.03583	0.03547	0.0351	0.03472	0.03433
R_{th} at Re = 1600	0.03496	0.03471	0.0344	0.03417	0.03388	0.03359
R_{th} at Re = 2000	0.03425	0.03404	0.03383	0.03361	0.03338	0.03314
R_{th} at Re = 2000	0.03425	0.03404	0.03383	0.03361	0.03338	0.03314

Figure O.2: Thermal physical data for water-alumina nanofluids.

Thermal-Physical properties for water-Copper nanofluid

Nanoparticles = Cu Ø =50nm , T = 293K, Pr = 6.96, Re' =4.86E-05						
Properties	φ = 0.00	φ =0.01	φ =0.02	φ =0.03	φ =0.04	φ =0.05
ρ_{nf}	998.2	1027.918	1057.636	1087.354	1117.072	1146.790
c_{pnf}	4182.0	4144.030	4106.060	4068.090	4030.120	3992.150
k_{eff}	0.597	0.597	0.6180	0.6301	0.6403	0.6494
μ_{eff}	993E-6	1075.404E-6	1177.200E-6	1302.436E-6	1459.268E-6	1660.772E-6
R_{th} at Re = 400	0.049	0.04822	0.04686	0.04546	0.04402	0.04255
R_{th} at Re = 800	0.04043	0.0398	0.03912	0.03842	0.0377	0.03696
R_{th} at Re = 1200	0.03741	0.03699	0.03654	0.03607	0.03559	0.0351
R_{th} at Re = 1600	0.0359	0.03558	0.03524	0.03489	0.03453	0.03416
R_{th} at Re = 2000	0.035	0.03474	0.03447	0.03419	0.0339	0.03361

Nanoparticles = Cu, Ø =50nm, T = 333K , Pr = 2.57, Re' =2.58E-04						
Properties	φ = 0.00	φ =0.01	φ =0.02	φ =0.03	φ =0.04	φ =0.05
ρ_{nf}	983.200	1013.068	1042.936	1072.804	1102.672	1121.710
c_{pnf}	4181	4143.040	4105.080	4067.120	4029.160	3991.200
k_{eff}	0.6631	0.633	0.6790	0.7056	0.7279	0.7478
μ_{eff}	472E-6	511.169E-6	559.555E-6	619.083E-6	693.630E-6	789.410E-6
R_{th} at Re = 400	0.04213	0.0414	0.0406	0.0398	0.03897	0.03811
R_{th} at Re = 800	0.03675	0.03638	0.03599	0.03559	0.03517	0.03474
R_{th} at Re = 1200	0.03496	0.03471	0.03445	0.03418	0.0339	0.03362
R_{th} at Re = 1600	0.03406	0.03388	0.03368	0.03348	0.03327	0.03306
R_{th} at Re = 2000	0.03352	0.03338	0.03322	0.03306	0.03289	0.03272

Nanoparticles = Cu, Ø =50nm , T = 353K , Pr = 1.72, Re' =4.87E-04						
Properties	φ = 0.00	φ =0.01	φ =0.02	φ =0.03	φ =0.04	φ =0.05
ρ_{nf}	971.800	1001.782	1031.764	1061.746	1091.728	1121.710
c_{pnf}	4194	4155.910	4117.820	4079.730	4041.640	4003.550
k_{eff}	0.7836	0.673	0.8707	0.9853	1.0811	1.1664
μ_{eff}	352E-6	381.211E-6	417.296E-6	461.689E-6	517.283E-6	588.713E-6
R_{th} at Re = 400	0.04575	0.04477	0.04372	0.04264	0.04152	0.04037
R_{th} at Re = 800	0.03856	0.03807	0.03755	0.037	0.03645	0.03587
R_{th} at Re = 1200	0.03616	0.03584	0.03549	0.03513	0.03475	0.03537
R_{th} at Re = 1600	0.03496	0.03472	0.03446	0.03419	0.03391	0.03362
R_{th} at Re = 2000	0.03425	0.03405	0.03384	0.03362	0.0334	0.03317

Figure O.3: Thermal physical data for water-copper nanofluids.

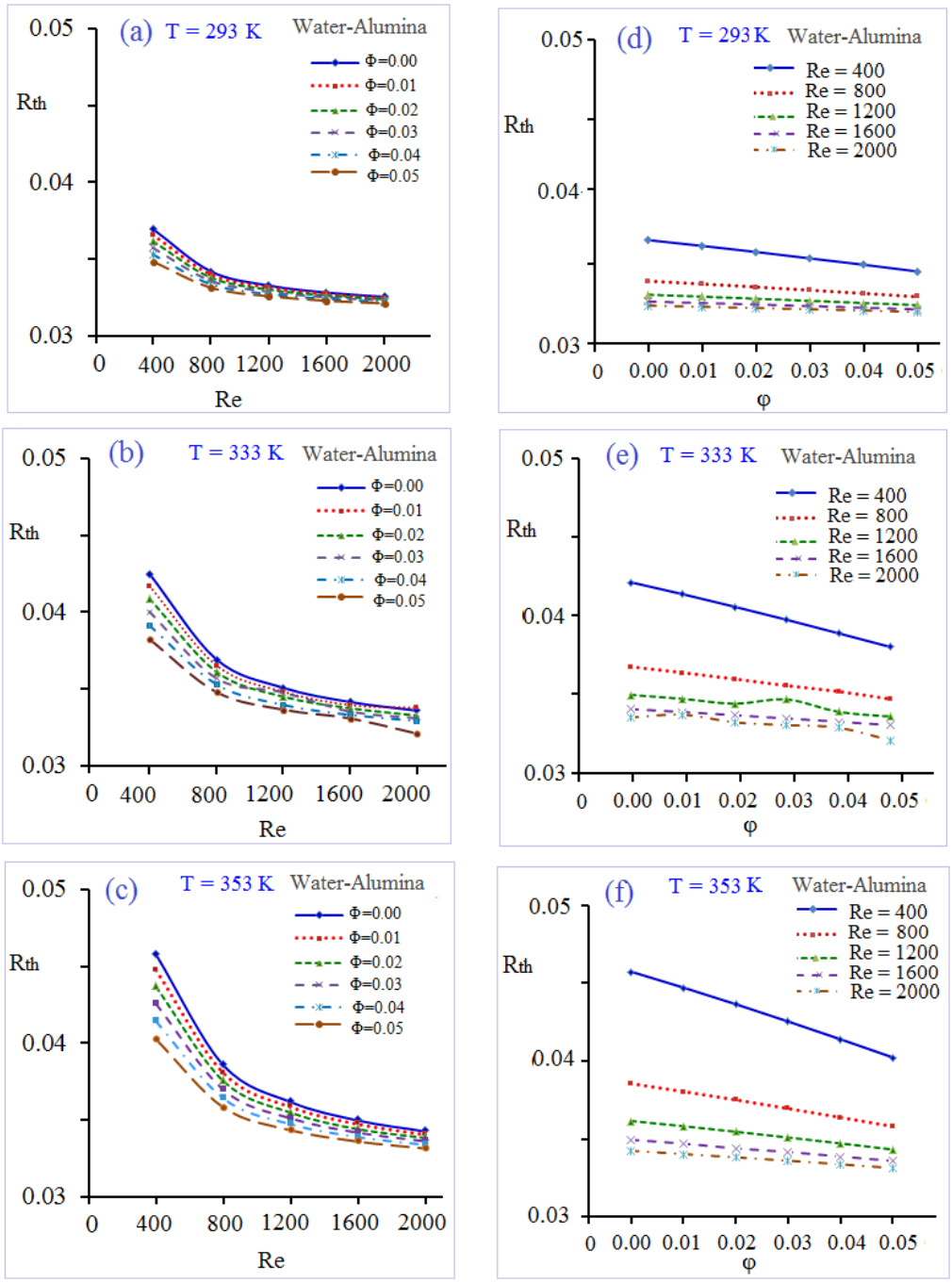


Figure O.4: Variation of thermal resistance for alumina nanofluids.

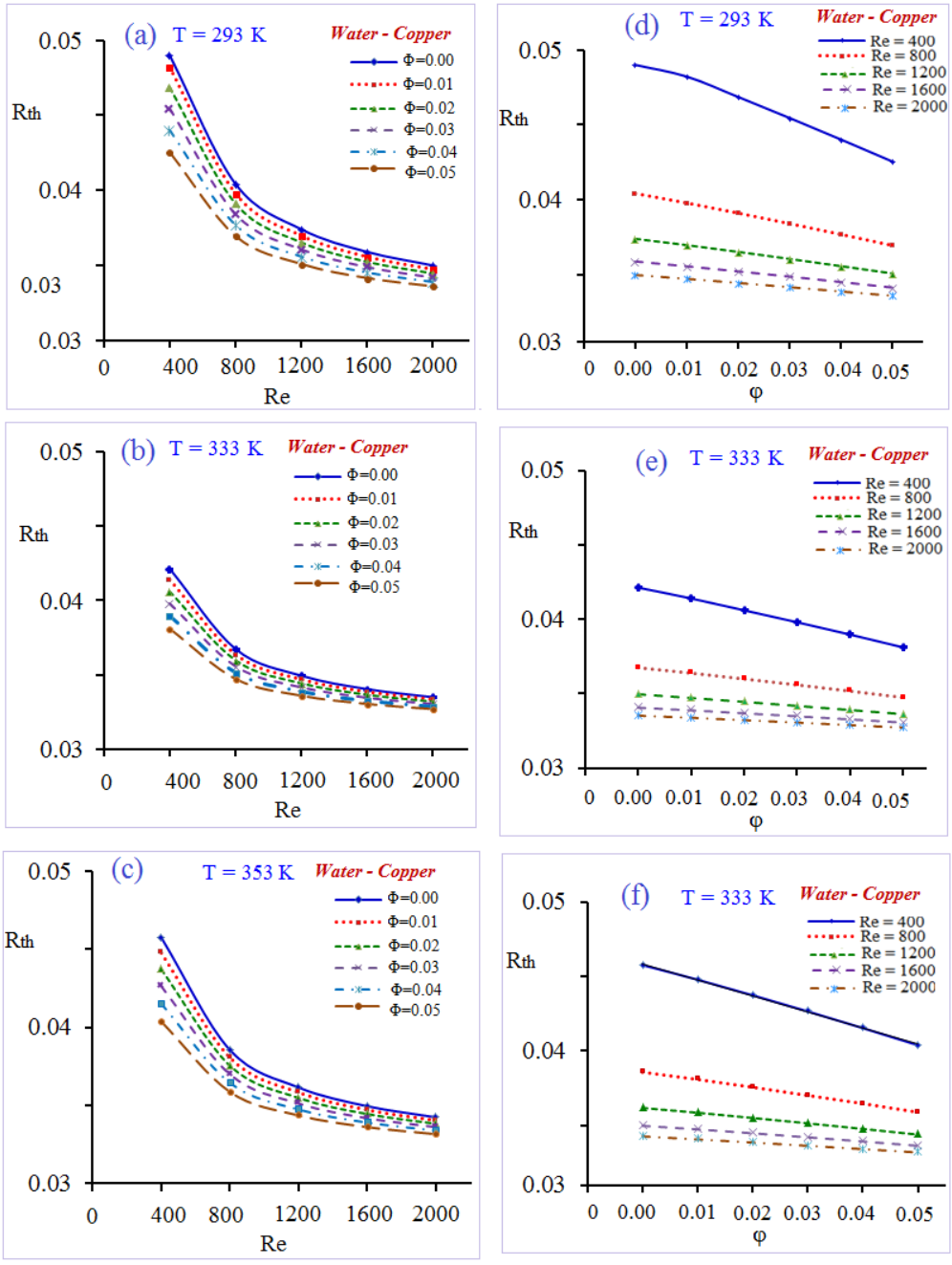


Figure O.5: Variation of thermal resistance for copper nanofluids.

and increase at 353 K, suggesting that the optimum operation temperature of the water-copper nanofluidics cooling systems is a 353 K (60°C). Like in the water-alumina nanofluidics cooling, there is no much benefit of increased pumping power when the fluid velocity attains Reinolds number which is more than 1200, also the flow of the water-copper nanofluids can change from lamina to unfavorable turbulent conditions. Figure O.5 (d), (e) and (f), shows that the thermal resistance reduces with the increase in volume fraction and the Reynoldss number, as well as with temperature and rises again.

O.3 Modelling of CS Parameters

The development of the mathematical model for predicting process parameters in cold spray of porous titanium coatings described here is a modification of the steps followed in (Thirumalaikumarasamy et al., 2014) with new key steps such as: the selection of process parameters; development of experimental design matrix; conduction of experiments; and the building and verification of the model. The selection of process parameters was based on the literature survey and the working limits of the CS equipment, supplied by Centreline, Canada. Consequently, for this study, three process parameters which have predominant influence on the porosity of titanium coatings were selected, namely: the stagnation temperature (T), stagnation pressure (P), and the standoff distance (S). The working limits for these parameters, which were determined from the deposition trials conducted in the CS laboratory at the University of the Witwatersrand, Johannesburg were as follows: stagnation temperature between 623 K and 873 K; stagnation pressure between 0.7 MPa and 9.5 MPa; and standoff distance between 10 mm and 30 mm.

To develop the design matrix, five coded levels, namely 1.682; −1; 0; +1; and +1.682 were used. These coded levels are coordinates of the location points where possible values of process parameters could be found (Montgomery, 2005). The process parameters were calculated using equation (O.22), which relates the given coded level, X_i, with respective the process parameters X, and X_{max} and X_{min} are the upper and lower limits of process parameters (Miller et al., 1999).

$$X = \frac{X_i}{3.364}[X_{max} - X_{min}] + \frac{[X_{max} + X_{min}]}{2} \tag{O.22}$$

The process parameters and the coded levels in Table O.1 were used to developed an empirical mathematical model, expressed by (O.23) using the Central Composite Design of Experiments-Response Surface Methodolgy, polynomial regression modelling, matrix algebra and MATLAB software to analyse and validate the CS process (Thirumalaikumarasamy et al., 2014; Hamweendo et al., 2014b).

$$Porosity = 11.6656 + A - B \tag{O.23}$$

where A and B are given by equation (O.24) and equation (O.25), respectively.

$$A = 299.8704P + 11.0097S + 0.0333S^2 + 1.3389TP \tag{O.24}$$

$$B = 0.2866T + 0.00057T^2 + 788.452P^2 + 0.01014TS + 4.4700PS \tag{O.25}$$

where, T is temperature of the gas (K), P is pressure of the gas (bars) and S is the standoff distance (mm). Then, equation (O.23) was used to predict porosity for titanium coating when T varied between 623 K and 823 K, P varied between 0.7 bars and 0.95 bars and S varied between 10 mm and 30 mm, and these values were recorded alongside the measured values porosity, and mean and standard deviation values microhardness for titanium-nickel (Ti-Ni), titanium (Ti) and nickel (Ni) coatings are summarised in the Table O.1 and Table O.2.

Table O.1: Porosity and microhardness values for coatings.

Specimen	T(°C)	P(bar)	SOD(mm)	Measured porosity for Ti	Predicted porosity	Microhardness for Ti-Ni	Microhardness for Ti	Microhardness for Ni
1	782	0.75	14	4.6	6.8	214	149	167
2	664	0.9	14	9.6	10.2	290	173	115
3	782	0.9	14	2.8	4.3	292	222	176
4	664	0.825	14	25.8	27.7	286	120	151
5	782	0.75	26	19.3	19.3	-	139	231
6	664	0.9	26	31.5	29.2	216	162	194
7	782	0.9	26	9.1	9.1	367	170	153
8	823	0.825	20	0.8	0.8	-	-	-
9	723	0.95	20	1.4	0.0	-	-	-

Table O.2: Standard deviation for microhardness.

Coating	Mean Hv	Standard deviation Hv
Ti-Ni	278	± 26
Ti	169	± 32
Ni	169	± 33

APPENDIX P : Graphs and Pictures

This Appendix shows the additional information on powder morphology and size distributions, Energy Dispersive X-ray Spectroscopy (EDX), and coatings for individual and mixed powders.

P.1 Powder Size Distributions

The PSD for the aluminum-alumina in P.1 showed a (nearly) normal distribution with less scatter, and each with mean particle size of 24.2 μm.

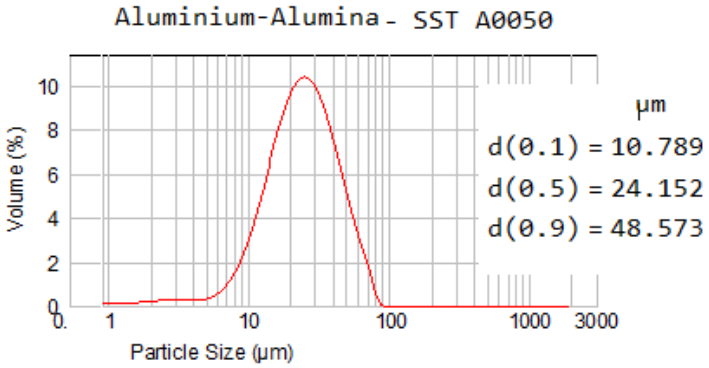


Figure P.1: Particle size distributions for aluminum-alumina

Also, the PSD for the chromium in Figure P.2 showed a (nearly) normal distribution with less scatter, and each with mean particle size of 36.3 μm.

Similarly, the PSD for the zinc in Figure P.3 showed a (nearly) normal distribution with less scatter, and each with mean particle size of 36.3 μm .

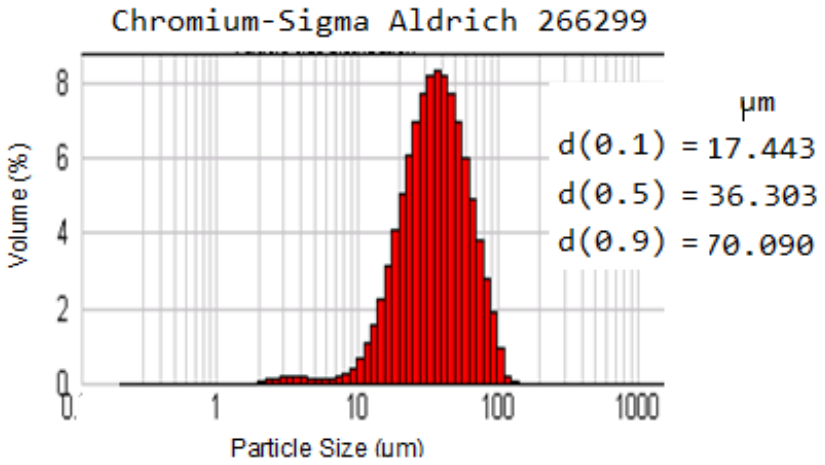


Figure P.2: Particle size distributions for chromium powder

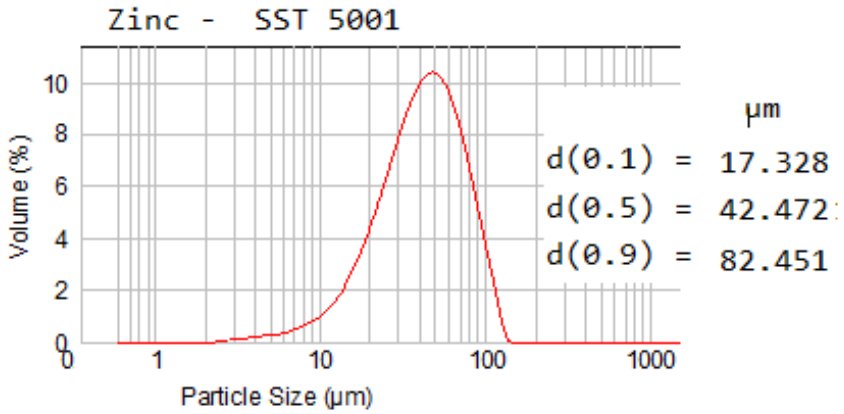


Figure P.3: Particle size distribution for zinc powder

As one can see from above, the PSD for the aluminum-alumina, chromium and zinc powders fall within the cold sprayable limits of 5.0 μm to 50.0 μm. In addition, these (nearly) normal PSDs entail uniform in-flight particle velocity distribution and homogenous deposition characteristics of the powders for these powders (Ning et al., 2007).

On the contrary, the PSD for the magnesium in Figure P.4 exhibited bi-mode in which the particle sizes had two mean values; the first being 44.4 μm and was within the cold sprayable limits stated above. The second mean value of particle size was 200.0 μm and was large than the upper cold sprayable limit of 50.0 μm.

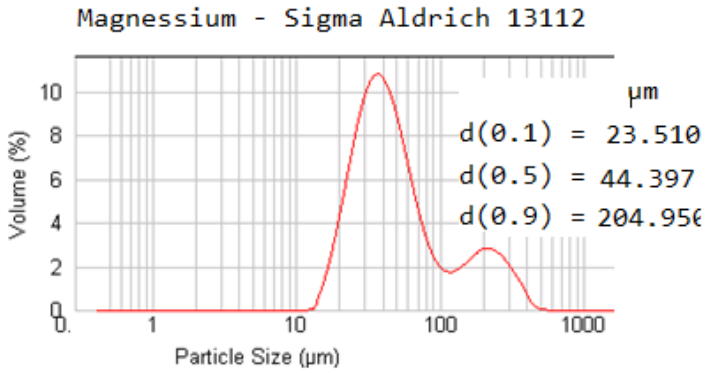


Figure P.4: Particle size distribution for magnesium Powder

Finally, the PSD for the nickel powder in Figure P.5 shows left skewed distribution, with mean sizes of 12.9 μm.

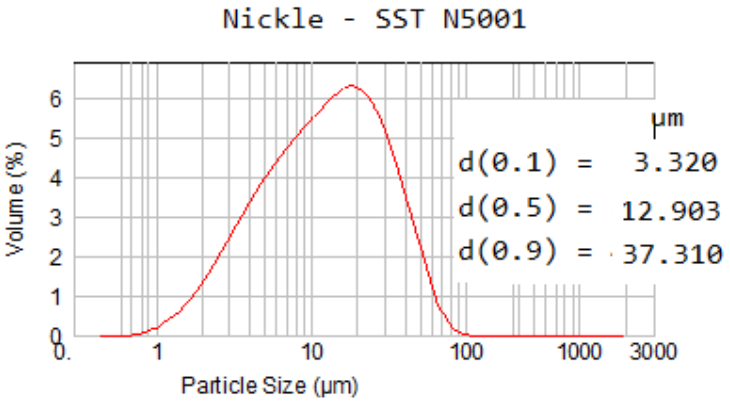


Figure P.5: Particle size distribution for nickel powder.

P.2 EDX Spectra for Powders

The elemental compositions of the as received powders with high affinity for oxygen were analysed using the Oxford Energy Dispersive X-ray Spectroscope (EDX) detector coupled with FESEM. This analysis was meant to monitor the change in oxygen content of the powders and coating before. The result of this analysis is displayed in the spectra for copper, magnesiun and nickel are shown in Figure P.6, Figure P.7, and P.8, respectively.

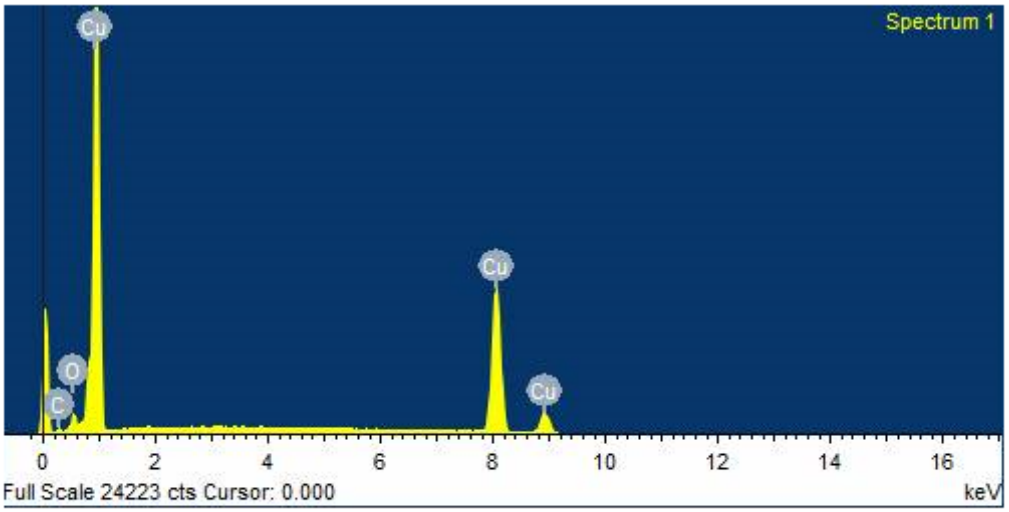


Figure P.6: EDX spectrum for copper powder.

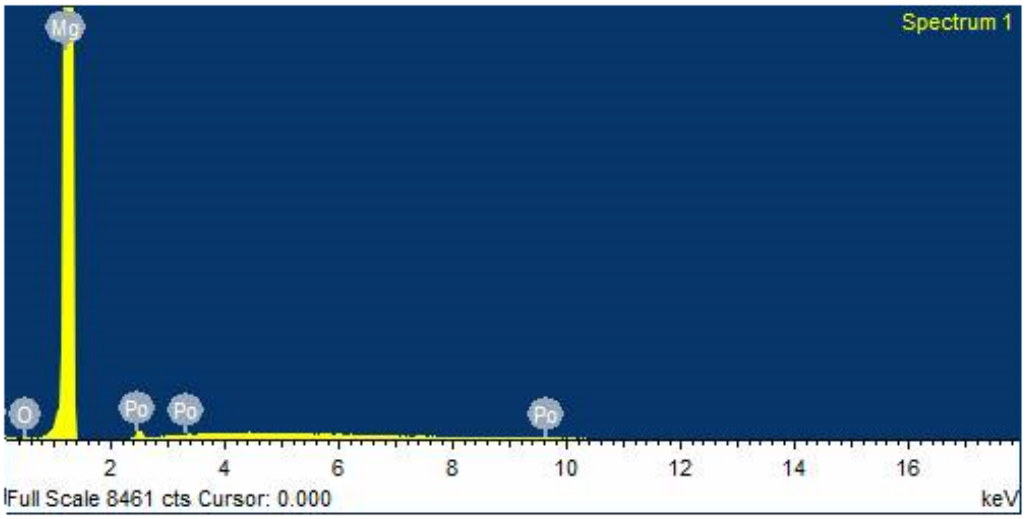


Figure P.7: EDX spectra for magnesium powder.

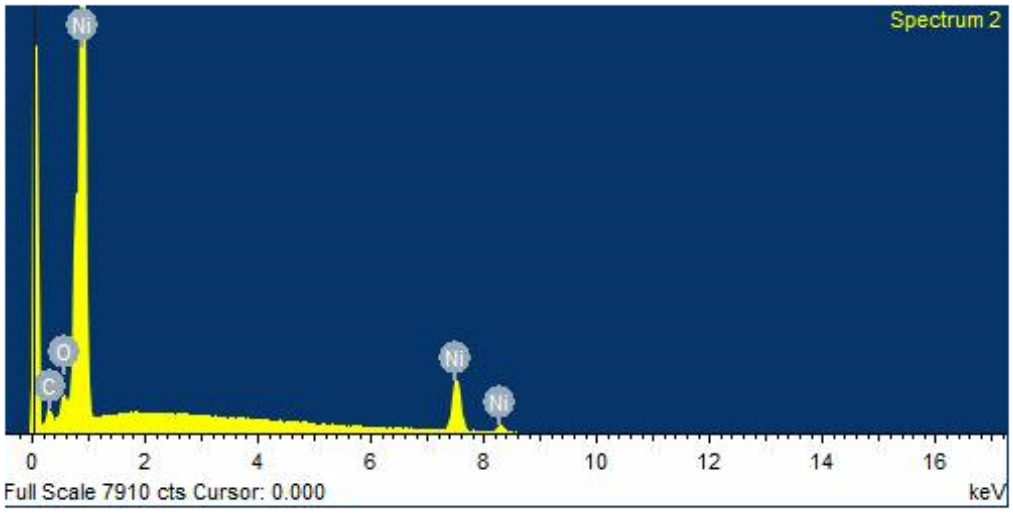


Figure P.8: EDX spectra for nickel powders.

As seen in these spectra, there is negligible peak for oxygen in the powder. This means that the oxygen content in each of these as received powders was negligible (Bartosiaki et al., 2015). After this characterisation, the selected powders were mixed as described in Chapter 3 and the resultant mixtures of the powder are presented below.

P.3 Coatings

Figure P.9 shows the dense coatings fabricated using the aluminium-alumina-copper (Al-Alumuna-Cu), aluminium-alumina-zinc (Al-Alumuna-Zn), copper-chromium (Cu-Cr) and titanium-magnesium (Ti-Mg) powder mixtures.

Figure P.10 shows the coatings for aluminium, copper, and zinc powders. As seen in this figure, these coatings had no pores.

P.4 EDX Spectra for Coatings

Figure P.11 indicate that there was there were no peaks for oxygen (O) in the titanium (Ti) and (Ni) EDX spectrum. Therefore, the CS process did not

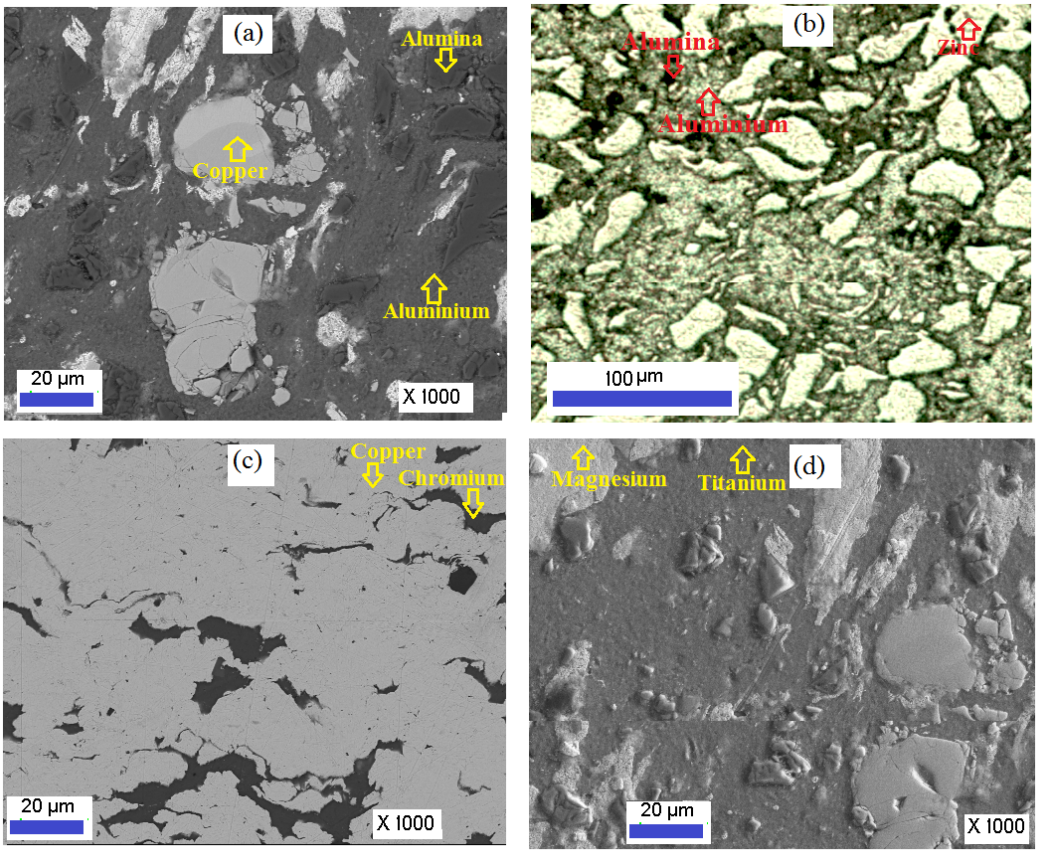


Figure P.9: Mixed powder coatings.
(a) Al-Alumina-Cu, (b) Al-Alumina-Zn, (c) Cu-Cr, and (d) Ti-Mg.

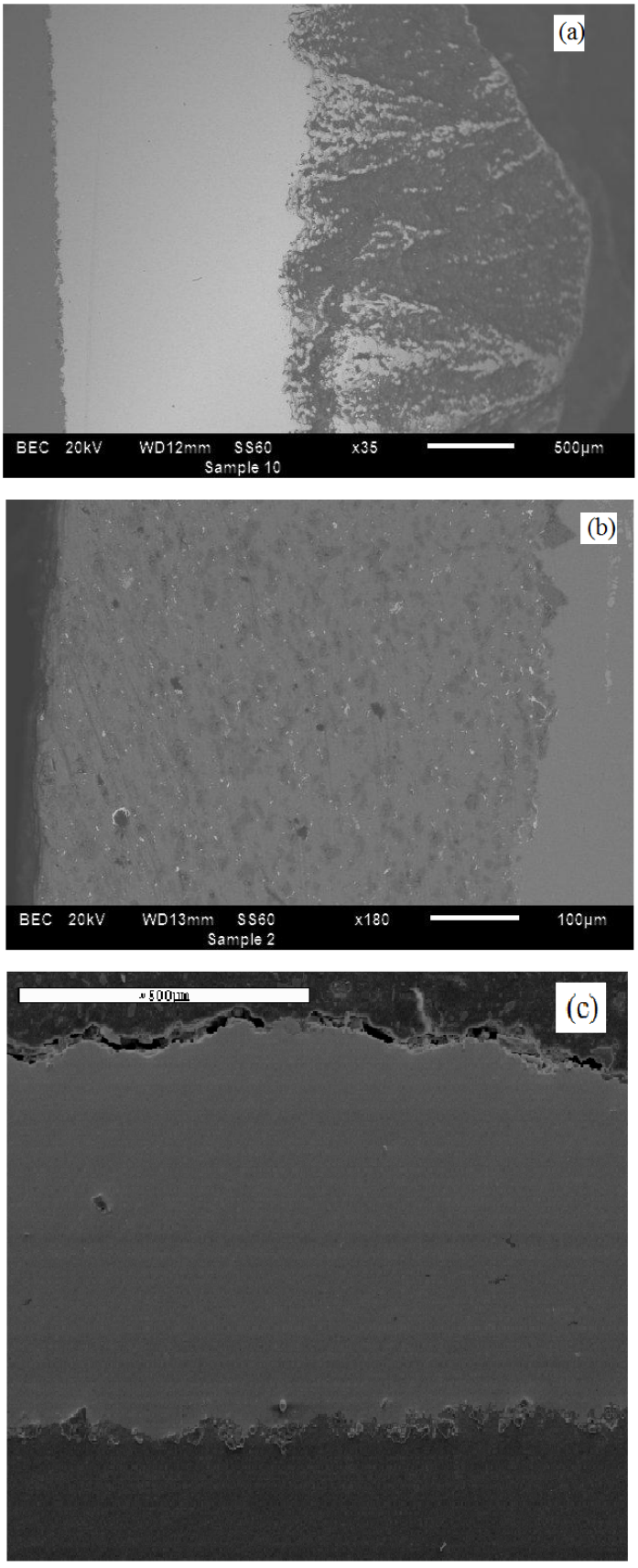


Figure P.10: Coatings for individual powders.
Coatings: (a) Aluminium (b) copper (c) zinc

oxidise the coatings.

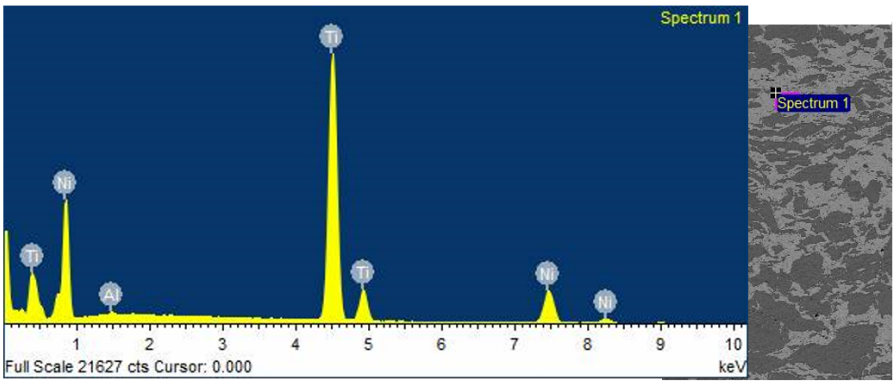


Figure P.11: EDX Spectrum for titanium-nickel coatings.